UNIVERSIDAD COMPLUTENSE DE MADRID

FACULTAD DE CIENCIAS FÍSICAS

Departamento de Física Atómica, Molecular y Nuclear

TESIS DOCTORAL

Implementation and validation of ultra-fast dosimetric tools for IORT

Implementación y validación de herramientas de dosimetría ultra-rápida para IORT

MEMORIA PARA OPTAR AL GRADO DE DOCTOR

PRESENTADA POR

Paula Beatriz Ibáñez Cuenca

Director

José Manuel Udías Moinelo

Madrid, 2018

UNIVERSIDAD COMPLUTENSE
MADRID

UNIVERSIDAD COMPLUTENSE DE MADRID

FACULTAD DE CIENCIAS FÍSICAS

Departamento de Física Atómica, Molecular y Nuclear

TESIS DOCTORAL:

Implementation and validation of ultra-fast dosimetric tools for IORT

Implementación y validación de herramientas de dosimetría ultra-rápida para IORT

Realizada por:
Paula Beatriz Ibáñez García

Director:
Dr. José Manuel Udías Moinelo

A mis padres

Por plantar la semilla de la curiosidad en mi mente desde niña.

Felix, qui potuit rerum
cognoscere causas.

Virgilio

Agradecimientos

Bueno, pues parece que ya está. Resulta que todos estos años, cuando los que ya habían pasado por esto me decían *"parece imposible, pero acaba llegando"*, en el fondo no estaban desencaminados... Debe ser eso de hacerse doctor, que igual te hace un poquito más listo.

Ha sido un viaje largo y en ocasiones modivito, con sus triunfos (y sus correspondientes bailes de la victoria) y sus tropiezos (y sus *"¿Y si monto una librería y me olvido de todo?"*). Pero al final el esfuerzo ha tenido recompensa, y esta tesis lo demuestra.

Sois muchos los que habéis hecho posible esta tesis, ya sea por ayudarme en el ámbito investigador o en el personal, y tenéis que saber que, sin vosotros, todo esto no habría salido adelante.

En primer lugar debo darle las gracias a José Manuel. Él confió en mí a pesar de no tener el expediente más brillante y me hizo ver que yo valía para la investigación. Si no hubiera sido por esa oportunidad que me dio en forma de beca de verano, esta aventura jamás habría ni siquiera empezado.

También quiero dar las gracias a la gente con la que he colaborado todos estos años. Al equipo de GMV, con Carlos Illana, Raúl Rodríguez, Manlio Valdivieso y Samuel Rodríguez. Sin ellos, ***radiance*** sería solamente una idea borrosa en la cabeza de algún oncólogo. A Pedro Guerra, María Jesús Ledesma y Juan Ortuño, de la UPM, por su trabajo indispensable en este proyecto.

Quiero agradecer también su ayuda a Laure Parent, Frank Schneider y, especialmente, a Sven Clausen, por darme la oportunidad de ir a realizar medidas a sus centros y ayudarme en todo lo que necesitaba cuando me encontraba perdida por los pasillos del hospital.

Y como no, un grandísimo gracias a Marie, mi franchutilla, la mejor compañera de batallas que alguien podía tener. Y a Elena, por ayudarme y enseñarme todo lo que sabía cuando era una recién llegada.

Pero la lista acaba de empezar. Cuando llegué al GFN no sabía bien qué esperar. Nunca había estado en un grupo de investigación, así que me imaginaba muchos escenarios en mi cabeza (y os aseguro que tengo una gran imaginación). Pero lo que me encontré fue un grupo de gente estupendo, algo raritos pero maravillosos cada uno en su estilo. Estaba Jacobo, que vivía en

sus mundos de Cal, Vadym con sus liebres de 50 kg, Bruno, ese chico callado (al principio) que siempre nos olvidábamos al bajar a comer, Pablo y sus bromas y concursos, Armando, nuestro meteorólogo con alma de nuclear, Elena, la pequeña dictadora con habilidad para hacer que Iron Maiden sonara como los pitufos maquineros, Esteban, nuestro tico, Richichop, la persona con más motes en la historia, Esther, la inauguradora de bares, Luis Mario y su bate, César, experto en IPs, y Cris, que cada día intenta hacer del mundo un sitio un poquito más agradable.

Al poco de estar aquí llegaron Vicky con sus derrapes por el pasillo y May, acompañada de sus rayos y centellas. Y con ellas surgió el gallinero, que pasó a ser el gallinero 2.0 con la incorporación de Marie y sus *tirejas* y *parajitos*. Quiero dar las gracias especialmente a mis nuclear hens, por haber estado siempre ahí todos estos años, y porque, aunque cada una esté ahora en una parte distinta del mundo, nuestras reuniones hacen que no pase el tiempo. ¡Os quiero!

Y pasaron los años, los *"más viejos"* se fueron y llegaron los nuevos (y no tan nuevos). Jaime, Víctor, Amaia, Pablo y Alex, que aunque no sepan cómo pegar un sello, son gente maja. Y Dani y Joaquín, los hijos pródigos que han vuelto al grupo. Gracias a todos por seguir haciendo del GFN un grupo tan divertido.

Y cómo olvidar a la gente que he conocido gracias a mis GFNitos: Edu, Borja Peropapi, Alex, Dimitri, Vincent "25", Simon, Tarek, Oli y Natalia. Con vosotros las cañas y los viajes se volvían mucho más emocionantes.

También hay gente que le tengo que agradecer el haber estado siempre ahí. Y cuando digo siempre, es SIEMPRE. Desde niñas. Blanca, Agos y Rachel. Crecimos juntas y áun nos queda por crecer mucho más, juntas, claro. Celes y Leti, mis hermanísimas favoritas y compañeras de mil aventuras, Marion, echaré de menos nuestros cafés durante la tesis, y nuestra no tan nueva adquisición, Angelita. Y Josus y Pumirris, porque aunque pasen los años hay cosas que nunca cambian.

Y no me quiero olvidar de mi familia swing. Vita, Estela, Eva, Isa (mis ladies), Urko, Adri, NachoS, Maite, AlbertoS y muchos más. Habéis hecho del miércoles mi día favorito de la semana.

Y finalmente, mi mayor agradecimiento es para mi familia. A mis tíos, primos y a mi abuelo. A mi abuela, por todas esas velas que ha puesto durante años para que el trabajo fuera bien, y sobre todo, a mis padres. Gracias a ellos crecí rodeada de libros y curiosidad. Desde experimentos (a veces con final desastroso) en la cocina, visitas casi semanales al museo de ciencias naturales, y preguntas infantiles incómodas que respondieron siempre con paciencia y veracidad. Ellos me enseñaron que la ciencia era algo asombroso y que la investigación era *"jugar siendo adulto"*. Me contagiaron su pasión y sin ellos no estaría aquí. Muchas gracias.

En definitiva, a todos vosotros, y a los que me he olvidado, **¡muchas gracias!**

Contents

Table of contents vii

Summary xi

Resumen en castellano xv

Motivation, objectives and outline of this thesis xix

1 Fundamentals of radiotherapy 1
- 1.1 The role of radiotherapy in oncology . . . 1
- 1.2 Interaction of radiation with matter . . . 3
  - 1.2.1 Interaction of photons with matter . . . 3
  - 1.2.2 Interaction of electrons with matter . . . 5
- 1.3 Intraoperative radiation therapy (IORT) . . . 7
  - 1.3.1 Intraoperative electron radiation therapy (IOERT) . . . 8
  - 1.3.2 Low energy X-rays intraoperative radiation therapy (XIORT) . . . 9
- 1.4 Dose delivery in IORT . . . 10
  - 1.4.1 Linear accelerators for IOERT . . . 10
  - 1.4.2 Mobile devices for XIORT . . . 18
- 1.5 Dosimetry in an IORT treatment . . . 21
  - 1.5.1 Ionization chambers . . . 22
  - 1.5.2 Radiochromic films . . . 23
- 1.6 Dosimetric characteristics of electron beams . . . 26
  - 1.6.1 Energy and angular distributions . . . 26
  - 1.6.2 Depth dose profiles . . . 27
  - 1.6.3 Transverse dose profiles . . . 28
  - 1.6.4 Isodose contours . . . 29
- 1.7 Dosimetric characteristics of low energy X-rays . . . 30
  - 1.7.1 Energy and angular distributions . . . 30
  - 1.7.2 Depth dose profiles . . . 31
  - 1.7.3 Transverse dose profiles . . . 32
  - 1.7.4 Isodose contours . . . 33
- 1.8 Radiance®, a treatment planning system for IORT . . . 33

1.9 Gamma evaluation . . . 36

2 Monte Carlo methods in radiotherapy **39**
2.1 Introduction . . . 39
2.2 Monte Carlo technique. Basic concepts . . . 40
2.2.1 Modeling of particle transport . . . 41
2.2.2 Random number generator . . . 42
2.2.3 Probability distribution functions and sampling method . . . 42
2.2.4 Error estimation . . . 45
2.2.5 Monte Carlo optimization . . . 45
2.3 Main Monte Carlo codes in radiotherapy . . . 48
2.4 PENELOPE . . . 49
2.5 PenEasy . . . 51
2.5.1 Source models . . . 52
2.5.2 Tallies . . . 52
2.6 DPM . . . 53
2.6.1 Source model . . . 54
2.6.2 Tallies . . . 54

3 Detailed simulations of IORT systems **55**
3.1 Introduction . . . 55
3.2 Intrabeam® applicators . . . 56
3.2.1 MC characterization of Intrabeam® X-ray source . . . 56
3.2.2 MC characterization of Intrabeam® Spherical applicators . . . 60
3.2.3 Simulation of Intrabeam® flat and surface applicators . . . 63
3.3 Dedicated electron accelerators . . . 65
3.3.1 LIAC® . . . 65
3.3.2 NOVAC® . . . 67
3.3.3 MOBETRON® . . . 69
3.4 Phase Space parameterization . . . 71
3.4.1 Parameterization of PHSP files in the IOERT accelerators . . . 71
3.4.2 Parameterization of PHSP files in the Intrabeam® spherical applicators . . . 74
3.4.3 Parameterization of PHSP file in the Intrabeam® flat and surface applicators 77
3.5 Conclusion . . . 79

4 Phase space optimization process **81**
4.1 Introduction . . . 81
4.2 Database generation . . . 83
4.2.1 Intrabeam® applicators . . . 83
4.2.2 IOERT accelerators . . . 84
4.3 Optimization of energy spectrum . . . 84
4.3.1 Energy spectrum for Intrabeam® applicators . . . 85
4.3.2 Energy spectrum for IOERT accelerators . . . 86
4.3.3 Treatment of the experimental data . . . 87

4.4 PHSP weighting algorithm . . . 87
4.4.1 Weighting approach for DDPs with the same number of histories . . . 88
4.4.2 Weighting approach for DDPs with different number of histories . . . 89
4.5 Results . . . 90
4.6 Conclusion . . . 91

5 Validation of the phase space optimization process with experimental data 93
5.1 Introduction . . . 93
5.2 Validation for XIORT applicators . . . 94
5.2.1 Experimental measurements for Spherical applicators . . . 94
5.2.2 Experimental measurements for Flat and surface applicators . . . 99
5.2.3 Dose comparison for spherical applicators . . . 102
5.2.4 Dose comparison for flat and surface applicators . . . 105
5.3 Validation for IOERT accelerators . . . 108
5.3.1 Experimental measurements for IOERT accelerators . . . 108
5.3.2 Dose comparison for IOERT accelerators . . . 110
5.4 Conclusion . . . 115

6 Hybrid Monte Carlo for dose calculation 117
6.1 Introduction . . . 117
6.2 MC simulations . . . 119
6.3 Code description . . . 120
6.3.1 Photoelectric effect . . . 122
6.3.2 Compton effect . . . 122
6.3.3 Study of the zero range approximation for electrons . . . 124
6.3.4 Flow chart of the code . . . 124
6.4 Dose normalization . . . 126
6.4.1 Calculation of the expected fluence for spherical applicators . . . 128
6.4.2 Calculation of the expected fluence for flat and surface applicators . . . 130
6.5 Validation of the Hybrid Monte Carlo against MC simulations . . . 132
6.5.1 Hybrid Monte Carlo for spherical applicators . . . 132
6.5.2 Hybrid Monte Carlo for flat and surface applicators . . . 141
6.5.3 Validation in clinical situations . . . 149
6.6 Conclusion . . . 153

Conclusions of this thesis 155

A Appendix: Generation of the material list for the Hybrid Monte Carlo 161

Main contributions of this thesis 163

List of figures 171

List of tables 179

Bibliography **181**

Summary

Introduction and objectives

Intraoperative Radiation Therapy (IORT) is a special modality for cancer treatment that delivers a single high dose of radiation directly to the exposed tumor bed during the tumor resection surgery [Palta et al., 1995, Beddar et al., 2006, Calvo et al., 1993, 2013, Lamanna et al., 2012]. One of the main limitations in IORT lies in the difficulties that the planning process entails, which limits the use of this technique [Lamanna et al., 2012, Pascau et al., 2012], and a treatment planning has not been available in IORT up to now. Recently, a new tool has been introduced: ***radiance***®, the first Treatment Planning System (TPS) specifically designed for IORT [Pascau et al., 2012, Valdivieso-Casique et al., 2015].

The main goal of this thesis has been the development, implementation and evaluation of a dosimetric tool capable of providing a realistic dose distribution from any intraoperative electron radiotherapy (IOERT) dedicated accelerator or Intrabeam® applicator that can be used for dose treatment planning in the operating room (OR) during an IORT treatment.

This dosimetric tool has been separated in three phases. First, a database of monoenergetic phase space (PHSP) files and depth dose profiles (DDPs) in water was computed with penEasy [Sempau et al., 2011, Badal Soler et al., 2008] from detailed simulations of each IOERT accelerator and Intrabeam® applicator. Then, the energy spectrum of these monoenergetic simulations was tuned for each device using simple experimental DDPs provided by the manufacturer to the user, obtaining an optimized PHSP file that reproduces the user's data [Ibáñez et al., 2015, Vidal et al., 2015]. Finally, dose was calculated from this optimized PHSP file with an accelerated version of DPM [Sempau et al., 2000, Guerra et al., 2014] in the case of electrons, or with the Hybrid Monte Carlo (HMC) code we have developed [Vidal et al., 2014b,a, Udías et al., 2017b], in the case of the Intrabeam®.

Materials and methods

Detailed simulations and database generation

We have simulated the most relevant dedicated accelerators employed in IOERT treatments (ie. NOVAC®, LIAC® and MOBETRON®) with their corresponding applicators, and Intrabeam® needle, spherical, surface and flat applicators. These simulations will represent a reference accelerator or applicator, and will be used to create a database of monoenergetic PHSP and DDPs in water that will be employed to generate a PHSP file tuned to each user machine in a dose treatment planning procedure.

Phase space optimization process

First, a generic spectrum, whose general features were derived from the realistic MC simulations, is fine-tuned by means of a genetic algorithm [Fernandez-Ramirez et al., 2008] until it describes the experimental DDP provided by the user of any given applicator. Afterwards, the monoenergetic PHSP files are combined with weights given by the energy spectrum, to build a PHSP file optimized to describe the experimental dose distribution [Ibáñez et al., 2015, Vidal et al., 2015, Udías et al., 2017a].

Hybrid Monte Carlo

Dose with the Intrabeam® device is calculated from the optimized PHSP file by means of an in-house developed code, the **Hybrid Monte Carlo (HMC)** [Vidal et al., 2014b,a, Udías et al., 2017b]. This code calculates deposited dose within minutes, fully taking into account the different tissues and structures of the patient. It incorporates all the relevant physical processes at Intrabeam® working energies, and the savings in calculation time are possible thanks to taking to the extreme some variance reduction techniques, such as the use of meta-histories, each one representing the fate of many particles, or the dose normalization, which allows statistic noise-free dose distributions with a low number of initial meta-histories.

Results

Detailed simulations and database generation. We could compare dose distributions against experimental data and a good agreement was reached. The optimization process only fits the DDPs, which is why it is essential that the rest of the dose distribution behaves correctly. By simulating in detail the different accelerators we guarantee a precise shape of the transverse profiles.

Phase space optimization process. We have done a broad validation of this process against

experimental data in homogeneous and heterogeneous situations. For the validation of dose distributions in water with spherical applicators, we found some discrepancies between simulations and measurements due to the anisotropy of the dose in the backward direction. However, the area presenting the anisotropy has no clinical interest. Regarding the dose distributions in water with flat and surface applicators, we found a good agreement for the cases studied, with more than 95% of the voxels fulfilling the gamma criteria at the 2%-2 mm level. In the dose comparisons inside heterogeneous phantoms, either with Intrabeam® applicators or IOERT accelerators, we reached a reasonable agreement at the 2%-2 mm level, specially considering the uncertainties in the measurements.

Hybrid Monte Carlo. We have validated the HMC against penEasy in homogeneous and heterogeneous phantoms. We have also compared dose distributions in clinical situations. In general, good results were obtained with the gamma evaluation with the 2%-1 mm criterion. In a few cases we had to go to a 5%-1 mm criterion to achieve a good agreement. However, the gamma criteria for the Intrabeam® has not been stipulated, and values of previous studies can go from 2%-1 mm [Nwankwo et al., 2013], 2%-2 mm [Clausen et al., 2012] to even 10%-1 mm [Chiavassa et al., 2014].

Conclusion

The phase space optimization process works correctly, reproducing dose distributions in clinical situations for both electrons or X-rays beams. It has proven to be fast, flexible and precise enough for IORT planning.

The HMC provides soft dose distributions accurately and within minutes. It can be used as a dose calculation tool in the operating room, as its high speed allows an on-the-fly dose calculation which includes the realistic effects of the beam in the different tissues within the patient's body.

The phase space optimization process and the HMC have been integrated into ***radiance***®.

Resumen en castellano

Introducción y objetivos

La radioterapia intraoperatoria (IORT) es una modalidad de tratamiento que consiste en irradiar directamente el lecho tumoral expuesto durante la cirugía con una dosis única y localizada [Palta et al., 1995, Beddar et al., 2006, Calvo et al., 1993, 2013, Lamanna et al., 2012]. A pesar de las ventajas que ofrece esta técnica, hasta hace poco la IORT carecía de las herramientas de planificación y dosimetría que se emplean regularmente en radioterapia externa. Para remediar esta carencia, se creó ***radiance***®, el primer planificador de tratamientos para IORT [Pascau et al., 2012, Valdivieso-Casique et al., 2015].

El principal objetivo de esta tesis ha sido el desarrollo, implementación y validación de una herramienta de cálculo de dosis capaz de proporcionar una dosis realista de cualquier acelerador dedicado de IORT con electrones o con el sistema Intrabeam® que pueda ser usada para planificar el tratamiento dentro del quirófano durante una intervención de IORT.

Esta herramienta dosimétrica se ha separado en tres fases. Primero, se ha generado una base de datos con penEasy [Sempau et al., 2011, Badal Soler et al., 2008] a partir de simulaciones detalladas de aceleradores de electrones y aplicadores de Intrabeam®, compuesta por espacios de fase (PHSP) monoenergéticos y perfiles de dosis en profundidad (DDPs) en agua. Después, con un proceso de ajuste en el que necesitamos únicamente la DDP experimental de cada máquina, obtenemos un PHSP optimizado que reproduce la dosis experimental. Finalmente, la dosis se calcula a partir de este PHSP, bien con una versión acelerada de DPM [Sempau et al., 2000] en el caso de trabajar con electrones, o bien con el Monte Carlo Híbrido (HMC) que hemos desarrollado [Vidal et al., 2014b,a, Udías et al., 2017b] para el Intrabeam®.

Materiales y métodos

Simulaciones detalladas y generación de la base de datos

Hemos simulado los aceleradores dedicados para IORT de electrones más relevantes con sus aplicadores correspondientes, así como los distintos aplicadores del ®. Estas simulaciones servirán para crear la base de datos de PHSP y DDPs monoenergéticos que alimentarán nuestro algoritmo de optimización.

Proceso de optimización del espacio de fases

Primero, ajustaremos un espectro de energías genérico, derivado de las simulaciones detalladas de los aceleradores, mediante un algoritmo genético [Fernandez-Ramirez et al., 2008], hasta que describa la DDP experimental introducida por el usuario. Después usaremos el espectro optimizado para pesar los PHSP monoenergéticos y obtener un espacio de fases que reproduzca la dosis experimental [Ibáñez et al., 2015, Vidal et al., 2015, Udías et al., 2017a].

Monte Carlo Híbrido

Para el cálculo de dosis con la máquina Intrabeam® hemos desarrollado el **Monte Carlo Híbrido (HMC)** [Vidal et al., 2014b,a, Udías et al., 2017b]. Este código calcula la dosis depositada en minutos, y tiene en cuenta el efecto de los distintos tejidos y estructuras en el interior del paciente. Incorpora los procesos físicos relevantes a las energías de trabajo del Intrabeam® y lleva al extremo técnicas de reducción de varianza para acelerar los cálculos, tales como el uso de meta-historias, cada una de ellas representando el destino que miles de partículas, o la normalización de la dosis, que permite la obtención de dosis sin apenas ruido estadístico a partir de pocas meta-historias iniciales.

Resultados

Simulaciones detalladas y generación de la base de datos. Las distribuciones de dosis obtenidas se han comparado contra medidas experimentales y se ha observado un buen acuerdo entre ellas. El proceso de optimización del PHSP sólo ajusta la dosis a las DDP experimentales, por lo que es esencial que el resto de la dosis tenga la distribución adecuada. Al simular en detalle todos los aceleradores, garantizamos que la forma de los perfiles transervales sea la correcta.

Proceso de optimización del espacio de fases. Se ha llevado a cabo una amplia validación del proceso con medidas experimentales en medios homogéneos y heterogéneos. Al realizar la comparación de dosis con los aplicadores esféricos del Intrabeam® en agua encontramos algunas discrepancias debidas a la anisotropía que presentan las medidas experimentales en la parte de detrás del aplicador. Sin embargo, la localización de la anisotropía está en una zona sin interés clínico. En el caso de la comparación de dosis con los aplicadores planos y de superficie del Intrabeam® en agua vimos que había buen acuerdo entre medidas y simulaciones, con más del 95% de los vóxeles cumpliendo el criterio gamma con límites 2%-2 mm para todos los casos. Y lo mismo observamos al comparar las dosis en heterogeneidades tanto en IORT de electrones

como en Intrabeam®, donde el acuerdo es razonable, especialmente si tenemos en cuenta las incertidumbres asociadas a la medida experimental.

Monte Carlo Híbrido. El HMC ha sido validado contra penEasy en maniquíes homogéneos y heterogéneos. También se han comparado las distribuciones de dosis en CTs de pacientes. En términos de criterio gamma, al nivel del 2%-1 mm se ha obtenido un buen acuerdo en general entre ambos códigos, aunque en algunos casos se tuvo que aumentar a 5%-1 mm. Sin embargo, los límites del criterio gamma para las dosis del Intrabeam® no se han establecido aún, y los valores que se han usado en estudios previos pueden ir desde 2%-1 mm [Nwankwo et al., 2013], 2%-2 mm [Clausen et al., 2012] hasta incluso 10%-1 mm [Chiavassa et al., 2014].

Conclusiones

El proceso de optimización de espacios de fase funciona correctamente, obteniendo PHSP que reproducen distribuciones de dosis experimentales tanto para electrones como para el Intrabeam®. Se ha demostrado que es rápido, flexible y suficientemente preciso para planificación en IORT.

El HMC proporciona distribuciones de dosis suaves y precisas en minutos. Puede usarse como herramienta de cálculo de dosis en la sala de operaciones, ya que su alta velocidad permite realizar un cálculo de dosis en el momento que además incluye los efectos realistas del haz al atravesar las distintas estructuras del cuerpo.

Tanto el proceso de optimización de espacios de fase como el Monte Carlo Híbrido han sido incorporados en ***radiance***®.

Motivation, objectives and outline of this thesis

Intraoperative radiotherapy (IORT) is a modality of cancer treatment that combines the effort of two disciplines, surgery and radiotherapy, in order to increment the rate of tumor control. In this treatment technique a high and localized dose of radiation is administrated directly to the exposed tumor bed during the surgery performed to extract the tumor [Beddar et al., 2006, Lamanna et al., 2012, Calvo et al., 1993]. The direct visualization of the tumor allows a more precise definition of the volume that has to be irradiated and the protection of the surrounding healthy tissues, by retraction of the tissue or by placing shields. Furthermore, IORT eliminates the time between surgery and radiotherapy and offers an alternative to those patients in which external radiotherapy is not indicated. Finally, IORT is also used as the boost radiation of multidisciplinary treatment approaches, including external radiotherapy.

The first reported IORT clinical treatments date back to the early 1900s, just a few years after the discovery of the X-rays, but the development of this technique really started in the late 1960s with the incorporation of the high-energy electrons as the optimal radiation beam for IORT treatments [Calvo et al., 1993]. Since then, the technology involved in IORT has been optimized and several dedicated linear accelerators and X-rays devices, such as Intrabeam® (Carl Zeiss Meditec, Dublin, CA, USA) or Axxent® (Xoft, San Jose, CA, USA) have been developed, and the number of institutions carrying out this treatment modality has been increasing in all countries.

However, IORT is, in spite of the years that it has been around, still considered an *experimental* procedure. This is mostly due to the fact that no commercial or certified/approved solution existed covering the aspects that one is used to find in conventional (external or brachytherapy) radiotherapy. Although treatment planning is a necessary step in external radiotherapy, the corresponding procedure has not been available in IORT up to now. There are several reasons to this: There is usually no image for therapy planning, and a basic planning is sketched based on preoperatory imaging. There are a few places where intraoperatory image is available, thanks to magnetic resonance imaging (MRI) [Shah et al., 2012], in-room computed tomography (CT) imaging [Jones et al., 2014] or ultrasounds [Lindner et al., 2006], but it is not at all commonplace.

Moreover, the position where the applicator is going to be placed, its size and the possible protections are decided *in situ*, after examining the surgical results [Lamanna et al., 2012, Pascau et al., 2012, Beddar et al., 2006]. This means that there is a short time window to perform and/or tune the treatment plan. Furthermore, there is no actual record of the position of the applicator, patient or shields during treatment, other than the memory of the people present, and pictures or videos of the intervention, from which one could only roughly infer the treatment setup. This prevents the post study of treatments and complicates the quality control. In view of these inconveniences, planning has been based on isodose curves in water, measured for each applicator and energy, and from this information, oncologists and medical physics set the radiotherapy plan.

The need of a tool that allows the radiation oncologist to plan an IORT treatment and to obtain an estimation of the dose distribution deposited in the volume of interest led the Unidad de Medicina y Cirugía Experimental and the Servicio de Oncología Radioterápica from the Hospital General Universitario Gregorio Marañón (HGUGM) in Madrid into developing a tool capable of simulating an IORT process with electron beams from patient images. The Laboratorio de Imagen Médica from the HGUGM developed a prototype of a treatment planning system (TPS) that allowed the positioning of the IOERT applicators superimposed on the patient's CT or MRI images, and painted the isodose lines in water for each applicator diameter, bevel and energy [Desco et al., 1997]. The HGUGM contacted then with GMV company in order to transform this prototype software into a commercial TPS for IOERT. As a result of this collaboration a project was approved by the Ministry of Industry (FIT-300100-2007-53) to develop the first TPS for IORT: ***radiance***®.

radiance® appeared in 2007. In its first implementation, simple isodose curves in water were still used, but ***radiance***® allowed to load a CT (or any other modality image) of the patient (either intra-, pre- or post-operatory). This image could be edited to reflect better the surgical findings and patient situation, and the applicator and energy of the electrons could be changed and the resulting water isodose could be seen on the screen, co-registered with the patient image, so that the doctors could then have a more clear picture of the setup and the radiation of the tumor bed and organs at risk. ***radiance***® made also possible a much more precise documentation of the procedure. However, although water measurements were a good starting point towards providing a planning tool to IORT, they did not take into account the behavior of electrons in tissues with densities different than water.

Since 2009, a collaboration of several universities, companies and hospitals in Madrid have taken ***radiance***® to a new level, building a research consortium composed of private companies (GMV, Técnicas Radiofísicas), medical institutions (Hospital Universitario Gregorio Marañón, Consorcio Hospitalario Provincial de Castellón, Clínica La Luz, Hospital Ramón y Cajal) and universities (Universidad Politécnica de Madrid, Universidad Complutense de Madrid, Universidad Rey Juan Carlos, Universidad de Valencia, Universidad de Granada) [Valdivieso-Casique et al., 2015]. In 2012 the project was extended to include low-energy X-rays intraoperative radiotherapy (IPT-2012-0401-300000) and early in 2016, ***radiance***®, including its MC TPS, obtained EU and

FDA marking and approval for use as TPS in human radiotherapy. Finally, in October 2016 the companies Carl Zeiss and GMV signed a commercial collaboration agreement, and now every Intrabeam® device is being sold with ***radiance***®, incorporating the codes described in this thesis, fully taking into account patient's anatomy.

In the new version of ***radiance***®, intraoperative images are being obtained and incorporated, as well as a fully registration of the patient and the radiotherapy applicator thanks to video cameras and reference marks in the OR, with real time visualization and offering the oncologist a similar control as the one it is customarily achieved in external radiotherapy (ERT). Estimating dose from isodose curves in water was not longer sufficient in this context. It was called for a TPS tool of similar accuracy and precision as the ones available for ERT, and this means a full Monte Carlo (MC) based TPS.

Now this proved to be an extremely challenging goal. A MC TPS requires the two following tasks to be accomplished:

- Detailed simulation of the accelerator and applicators to obtain a complete description of the radiation being applied to the patient. If repeatability among different units of the same model is not good enough, the detailed simulations should be performed for each accelerator deployed on the field. Commissioning of the unit must include the comparison to measurements and the validation of the results. Ideally, commissioning has to be an approach amenable to any user with little knowledge of MC simulations. And it should be done in a very short time, hours at most. We have tackled this need employing phase space (PHSP) files containing the complete description of the particles emitted by the accelerator, meaning that the simulation of the accelerator and applicator does not need to be repeated for each case. With regards to tuning to the machine, the chosen procedure consisted in the pre-computing of a number of virtual monochromatic accelerators, being described in Chapter 4 [Ibáñez et al., 2015, 2016, Vidal et al., 2015, Udías et al., 2017a].

- A fast calculation of the dose on the patient, taking into account the different tissues seen in the planning or intraoperative CT, once the PHSP file is given. Dose calculation must be very fast because it should be possible to repeat the calculations once the patient situation after surgery is known, and it should be even possible to compute the dose under different scenarios (energy, applicator size or angle, different shielding) so that the oncologist and the medical physicist can tune the setup within minutes, in order to not delay the procedure and allow an as fast as possible end of the surgical intervention. For the electron case, a modification of the DPM code [Sempau et al., 2000] was incorporated [Herranz et al., 2014, Guerra et al., 2014, Guerra Gutiérrez et al., 2012] in ***radiance***®. For Intrabeam®'s kilo-voltage X-rays, we have developed [Vidal et al., 2014b,a, Udías et al., 2017b] a new algorithm for dose calculation aiming to preserve the accuracy of MC approaches, but avoiding as much statistical noise as possible. This is going to be described in Chapter 6.

This Ph.D. thesis has been carried out inside the Grupo de Física Nuclear from the Universidad

Complutense de Madrid, which is a component of the ***radiance***® collaboration. The main goal of this thesis has been the development, implementation and evaluation of a dosimetric tool capable of providing a realistic dose distribution from any IOERT dedicated accelerator or Intrabeam® applicator that can be used for dose treatment planning in the OR during an IORT treatment. To do this we have done two mayor contributions to the dose calculation algorithms implemented in ***radiance***®. First, we have developed a fast tuning tool to generate PHSP files optimized to any user's device providing as input only an experimental DDP in water. Second, we have developed a dose calculation code suitable for the Intrabeam® working energies that includes the accuracy of a MC method and calculates dose distributions in a fraction of time. The combination of both contributions allows the user to obtain a dose distribution from a PHSP file tuned to reproduce his device within minutes.

The objectives of this thesis can be summarized as follows:

- Development of a complete database of detailed IOERT accelerators and Intrabeam® applicators by simulating in detail the different geometries of the devices and comparing dose distributions with experimental measurements to assure a correct behavior of every simulation.

- Development of a phase space tuning procedure to generate a PHSP file that reproduces experimental dose distributions from any given DDP in water.

- Validation of the previous procedure against experimental measurements for Intrabeam® applicators and IOERT accelerators.

- Development and validation of a dose computation tool, called **Hybrid Monte Carlo**, for the Intrabeam® applicators that calculates accurate dose distributions within minutes.

Therefore, in this thesis we describe the tools developed for the incorporation of realistic dose calculations into ***radiance***®, taking into account the heterogeneous composition of the treatment volume. Such a complex project is the result of a collaboration between several researchers. However, the specific contributions of this PhD student to the ***radiance***® project are listed below:

- Elaboration of the detailed MC models with penEasy of the different IOERT accelerators, Intrabeam® X-ray source and spherical, needle, flat and surface applicators.

- Generation of the PHSP and DDP database for all IOERT and XIORT devices.

- Significant contribution in the development of the HMC algorithm and the phase space optimization tools.

- Measurements with radiochromic films for the spherical, flat and surface Intrabeam applicators in Mannheim and Toulouse.

- Complete validation of the phase space optimization process against reference simulations and experimental measurements.

- Complete validation of the HMC against reference simulations.

This thesis is organized in six chapters:

In **Chapter 1** we present the fundamentals of radiotherapy. First, we introduce the role of the radiotherapy in the treatment of cancer and the main modalities of administration. Then, we make a brief introduction of the interaction of photons and electrons with matter, and afterwards, we focus on the intraoperative radiation therapy and its two modalities: Intraoperative electron radiotherapy (IOERT) and low energy X-rays intraoperative radiotherapy (XIORT). We describe the dedicated accelerators used in IOERT and the Intrabeam® device, we introduce the dosimetric tools used in an IORT treatment, such as ionization chambers and radiochromic films and we finally present the dosimetric characteristics of electrons and kilo-voltage photon beams. We finally describe the main characteristics of ***radiance***®.

In **Chapter 2** we summarize the main concepts of the Monte Carlo methods, as well as some of their mathematical and probabilistic bases. We present the main MC codes used in radiotherapy and we focus on the characteristics of the codes used in this thesis: penEasy, DPM, and the main MC code in which these two codes are based, PENELOPE.

In **Chapter 3** we present the detailed simulations we have done to generate the database that will be used in Chapter 4. We describe the characteristics of each simulation and geometry, as well as the resulting dose distributions compared to experimental measurements. We start with the Intrabeam® device. We characterize the X-ray source and its energy spectrum, and we use it to simulate all spherical, flat and surface applicators. In the case of IOERT accelerators, we describe the geometries and source models for the LIAC®, NOVAC® and MOBETRON® dedicated accelerators. Finally we present the different parameterizations performed to the phase space files of the simulations in order to make them easy to handle.

In **Chapter 4** we describe the optimization method used to tune a PHSP file so it reproduces any given experimental dose. We explain the different parts of the optimization tool, starting with the generation of the database with monochromatic PHSP files and DDPs from the detailed simulations of the previous chapter, the optimization of the energy spectrum by means of a genetic algorithm and the final PHSP weighting algorithm that generates the optimized PHSP file. We also include some of the results of the genetic algorithm, the comparison of the fitted DDPs against experimental data and the optimized energy spectra.

In **Chapter 5** we perform a complete validation of the fitting procedure described in the previous

chapter against experimental measurements. For the Intrabeam® spherical applicators, we compare against radiochromic films that we measured in the Universitätsklinikum of Mannheim and for the Intrabeam® flat and surface applicators we compare against measurements we did in the Institut Universitaire du Cancer in Toulouse. We describe the different experimental setups and the calibration procedure, and we compare dose distributions in water and in heterogeneous phantoms. For the IOERT accelerators, we use experimental transverse profiles measured with a NOVAC® at the Universitätsklinikum in Düsseldorf, and we extend the validation to the LIAC® and MOBETRON® against detailed simulations.

In **Chapter 6** we present the Hybrid Monte Carlo (HMC) developed to calculate dose for the different Intrabeam® applicators in a short period of time. We describe the physics incorporated to the code and the accelerating approaches. We incorporate also a dose normalization to avoid artifacts and to generate statistical noise-free distributions with a low number of initial particles. We finally validate the HMC against penEasy simulations for all applicators, in homogeneous and heterogeneous media and in two clinical cases.

At the end we present the general conclusions of this thesis and the publications and conference proceedings derived from this work.

Chapter 1

Fundamentals of radiotherapy

1.1 The role of radiotherapy in oncology

Nowadays, cancer is one of the leading causes of death worldwide, accounting for 8.2 million deaths in 2012 [World Health Organization, 2014]. Its high mortality, increasing incidence and affection to all humankind turn cancer into one of the diseases with higher social impact. World Cancer Report 2014 [World Health Organization, 2014] highlighted the increasing incidence of cancer from 12.7 million in 2008 to 14.1 million in 2012, and its trend is projected to continue, with the number of cancer cases close to 25 million over the next two decades. Furthermore, approximately 39.6 percent of men and women will be diagnosed with cancer at some point during their lifetimes (based on 2010-2012 data) [World Health Organization, 2015]. These data justify that fighting cancer has become one of the principal objectives in developed countries.

There has been a great improvement in cancer treatments during the last decades. Thanks to constant investigation, important progress has been achieved in early diagnosis and treatment [Mackie et al., 2003, Mageras and Yorke, 2004, Herman, 2005, Jaffray, 2005], increasing recover expectancy in cancer patients.

Fighting cancer is a multidisciplinary task of high complexity due to the increment of combined treatments. There are three main techniques which are used alone or in combination for treating cancer: surgery, chemotherapy and radiotherapy. This last technique, radiotherapy, has an essential role in cancer treatment, specially for localized tumors. Around 50% cases of cancer will receive radiotherapy at least once during the course of their illness [Delaney et al., 2005], for either tumor control or palliative treatment.

Radiotherapy arose soon after the discovery of X-rays by Röntgen in 1895 when ionizing radiation was established as a powerful therapeutic agent, and has been evolving since then together with

the advances in physics and oncology. This technique consists in the application of ionizing radiation on the tumor in such a way that the interaction of these particles within the medium may kill or prevent the malignant cellular proliferation.

Ideally, a radiotherapy treatment would only irradiate tumor cells, leaving healthy tissue unaffected. However, these two objectives cannot be fully achieved simultaneously, and a compromise between beneficial and detrimental effects of radiation must be achieved. Therefore, in order to deliver the correct quantity of radiation dose, the oncologist must consider not only the effects of treatment on the tumor but also the consequences on normal tissues. For that, the final objective of radiotherapy is to deliver a lethal dose to the tumor while limiting radiation damage to healthy tissue. The development of new techniques to limit the radiotherapy effects in healthy areas is a constant challenge, where medicine, biology, physics and engineering meet.

Since the first radiotherapy treatments until now, treatment techniques have become more and more sophisticated [Jaffray, 2005, Mackie et al., 2003, Halperin et al., 2008, Lamanna et al., 2012, Hogstrom and Almond, 2006, Sadeghi et al., 2010]. In order to obtain the best results, different types of radiation and different ways to deliver them are used. For example, certain types of radiation can penetrate more deeply into the body than others. In addition, some types of radiation can be very finely controlled to treat only a small area without damaging nearby tissues and organs. Other types of radiation are better for treating larger areas. In general, the various radiotherapy techniques can be classified in the following two categories:

External beam radiotherapy or teletherapy: The radiation source is located at a certain distance of the patient. Teletherapy is typically carried out in the radiation oncology unit of a hospital using photons or electrons from a linear accelerator (LINAC). The LINAC is a device that uses high-frequency electromagnetic waves to accelerate charged particles such as electrons to high energies (typically 5-25 MeV) through a linear tube [Sadeghi et al., 2010, Khan, 2009]. The high-energy electron beam itself can be used for treating superficial tumors, or it can be made to strike a target to produce X-rays for treating deep-seated tumors.

Internal radiotherapy or brachytherapy: Brachytherapy is a method of treatment in which sealed radioactive sources are used to deliver radiation at a short distance by interstitial, intracavitary, or superficial application. With this mode of therapy, a high radiation dose can be delivered locally to the tumor with a rapid dose fall-off in the surrounding normal tissue [Sadeghi et al., 2010]. This involves placing implants in the form of seeds, wires or pellets directly into the tumor. Such implants may be temporary or permanent depending on the implant and the tumor itself. The typically used radioactive sources are Iridium-192, Cesium-137, Iodine-125 and Palladium-103.

A special type of treatment is the **intra-operative radiotherapy (IORT)**, considered half way between external and internal radiotherapy. IORT treatment consists in directly irradiating the tumor bed with a high, localized dose during surgery. The tumor is removed surgically and the radiation beam is directly delivered to the the tumor cavity, in order to kill residual cancer

cells to prevent recurrence. A high-dose radiation is given to the patient in only one fraction. Since the radiation is given directly to the tumor bed, the surrounding healthy tissues and organs can be protected and excluded. It can be either considered teletherapy, as the radiation source is located outside the patient, and brachytherapy, as the applicators are introduced inside the patient or in direct contact.

This thesis presents an extensive study about this last technique, IORT, so its main characteristics and applications will be described in detail in the following sections.

1.2 Interaction of radiation with matter

Ionizing radiations are characterized by their ability to excite and ionize atoms of matter with which they interact. Since the energy needed to cause a valence electron to escape an atom is of the order of 4-25 eV, radiations must carry kinetic or quantum energies in excess of this magnitude to be called “ionizing" [Attix, 2008].

Ionizing radiation may be classified into two main groups: Directly ionizing radiation and indirectly ionizing radiation [Attix, 2008, Knoll, 2010, Martin, 2006]. The first group includes the charged particle radiations that continuously interact with the electrons present in the medium through the coulomb force, gradually losing their energy. On the other side, indirectly ionizing radiations are uncharged, so they undergo a probabilistic and catastrophic interaction that radically alters the properties of the incident radiation. In a single encounter, these particles can loose an important percentage of their energy, or all of it. In this case, the energy transfer to the medium is a two-step process: The photons (or neutrons) transfer energy to the charged particles which are responsible of the bulk of the ionization effects.

1.2.1 Interaction of photons with matter

When a clinical photon beam goes through a medium, different interactions with matter take place. All these processes (except for the Rayleigh scattering) lead to the partial or complete transfer of the photon energy to electron energy. They result in sudden and abrupt changes in the photon history, in which the photon either disappears or its scattered through a significant angle and secondary charged particles are emitted. These resulting particles can produce ionizations, excitations or electromagnetic radiations in the medium.

We limit our considerations to the clinical energy range (keV-MeV), where the dominant interaction processes are the photoelectric effect, coherent (Rayleigh) scattering, incoherent (Compton) scattering and electron-positron pair production (Figure 1.1).

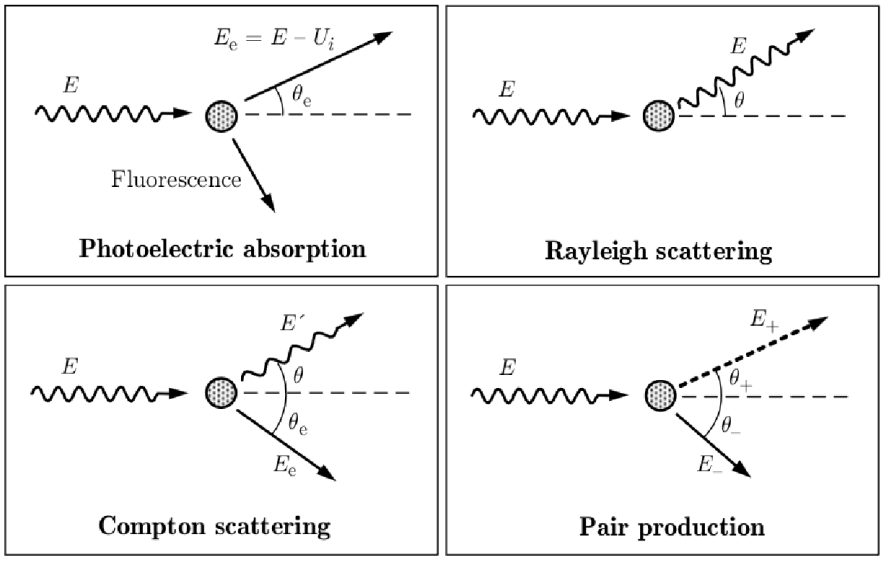

Figure 1.1: Basic interactions of photons with matter [Salvat et al., 2006].

Photoelectric effect: A low-energy photon gives up all of its energy to a bounded orbital electron and ejects it from the atom. The electron is ejected with an energy equal to the energy of the incoming photon, hν, minus the binding energy of the electron in its particular orbit. Since a vacancy is created in the electron shell, a characteristic X-ray, typically from filling the K-shell, will also be emitted. The photoelectric effect is most pronounced in high-Z materials and for low-energy photons (less than 0.5 MeV).

Compton scattering: The interaction process of Compton scattering takes place between an incoming photon and an electron in the absorbing material. The incident photon transfers a fraction of its energy to an electron which is ejected from the atom. As a result, the photon is deflected through an angle θ with respect to its original position. The Compton scattering is the predominant interaction mechanism for low-Z materials and for energies employed in external beam radiotherapy (around several MeV).

Rayleigh scattering: Also called "coherent" because the photon is scattered by the combined action of the whole atom. The photon loses essentially none of its energy; the atom moves just enough to conserve momentum. The photon is usually redirected through only a small angle. Rayleigh scattering contributes nothing to dose, since no energy is given to any charged particle, nor is any ionization or excitation produced.

Pair production: When a high-energy (>1.022 MeV) photon interacts with the strong electromagnetic field surrounding a nucleus, the photon may disappear and be replaced by an electron-positron pair. All the excess energy carried in by the photon above the 1.022 MeV required to create the pair goes into kinetic energy shared by the electron and the positron. Pair

production is predominantly confined to high-energy gamma rays.

The relative importance of Compton effect, photoelectric effect, and pair production depends on both the photon quantum energy ($E, = h\nu$) and the atomic number Z of the absorbing medium. Figure 1.2 shows the relative importance of the three major types of photon interaction. The line at the left represents the energy at which Compton scattering and photoelectric effect are equally probable as a function of the absorber atomic number. The line at the right represents the energy at which pair production and Compton scattering are equally probable.

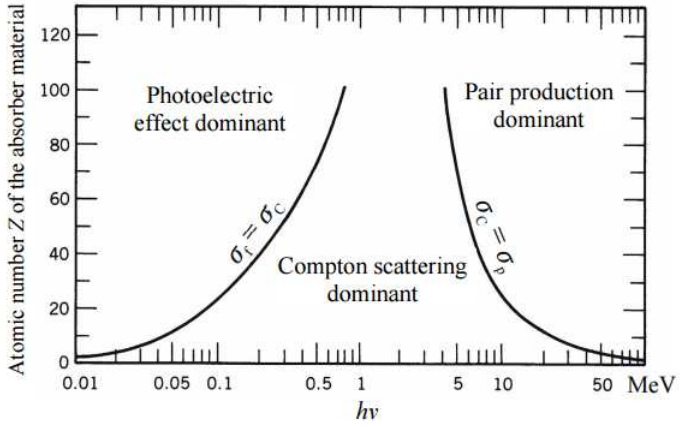

Figure 1.2: The three major types of photon interaction [Evans and Noyau, 1955].

1.2.2 Interaction of electrons with matter

An incident electron interacts with one or more electrons or with the nucleus of practically every atom it passes. Most of these interactions transfer only a fraction of the incident particle's kinetic energy in each interaction, gradually losing its kinetic energy as they go through the medium (a 1-MeV charged particle would typically undergo $\sim 10^5$ interactions before losing all of its kinetic energy), so this mechanism is often called the *"continuous slowing-down approximation" (CSDA)*. When electrons interact with other electrons, they produce excitations and ionizations. When interacting with the atomic nuclei coulomb fields, they generate radiative collisions. In these processes electrons undergo abrupt changes in their trajectories.

The possible interactions of electrons and positrons with the medium are, as shown in figure 1.3: elastic scattering, inelastic collisions and bremsstrahlung emission; positrons can also undergo annihilation, either in flight or at rest [Attix, 2008, Knoll, 2010, Martin, 2006, Cherry et al., 2012].

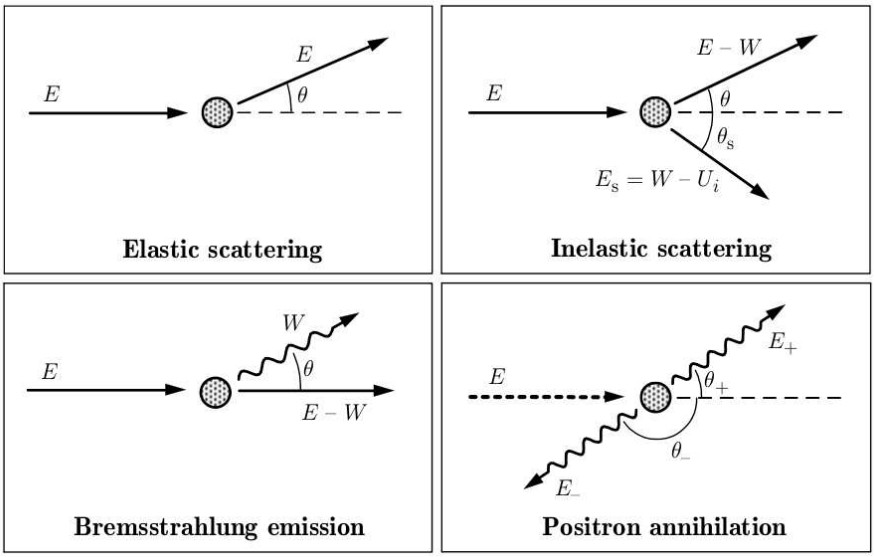

Figure 1.3: Basic interactions of electrons with matter [Salvat et al., 2006].

1.2.2.1 Collisions with atomic electrons

Soft collisions

When an electron passes at a certain distance of an atom, the particle's Coulomb force field affects the atom as a whole, exciting it to a higher energy level, or ionizing it by ejecting a valence-shell electron. In this process, the net effect is the transfer of a very small amount of energy (a few eV) to an atom of the absorbing medium.

For low and intermediate electron energies (non relativistic energies), this scattering is the main energy transfer process, causing either excitation or ionization of the atoms.

Hard collisions

When the electron passes near the atom, it becomes more likely that the incident particle will interact with a single atomic electron, which is then ejected from the atom with considerable kinetic energy.

Ionization involving an inner shell electron eventually leads to the emission of characteristic X-rays or Auger electrons. The ejected electrons might have enough energy to create further ionization. That electron is called a *delta ray*. The delta rays dissipate their energy along a separate path, so some of the energy transferred to the medium may be transported some distance away from the primary particle track.

The probability of hard collisions depends of the nature of the incident particle, and although these kind of collisions are less in number than the soft ones, the energy fraction of the primary particle lost in both processes is comparable.

1.2.2.2 Interactions with the external nuclear field

These interactions occur when the incident particle actually penetrates the orbital electron cloud and interacts with its nucleus. In most of the cases (97%−98%) the electron is scattered *elastically*, losing just a negligible amount of energy due to the nucleus recoil. Hence this is not a mechanism for the transfer of energy to the absorbing medium (the electron does not emit X-rays or excite the nucleus), but it is the reason why the path of the electrons is very tortuous.

In the other 2-3 % of the cases in which the electron passes near the nucleus, an inelastic radiative interaction occurs in which an X-ray photon is emitted. The electron is not only deflected in this process, but gives a significant fraction (up to 100%) of its kinetic energy to the photon, slowing down in the process. Such X-rays are called *bremsstrahlung* (German word for "braking radiation"). The energy of the bremsstrahlung photons can range anywhere from nearly 0 (events in which the particle is only slightly deflected) up to a maximum equal to the energy of the incident particle (events in which the particle is virtually stopped in the collision).

Bremsstrahlung is an important resource for dissipating energy in high Z media, but it is relatively insignificant for tissue-like (low Z) materials for electrons below 10 MeV.

1.2.2.3 Positron annihilation

When a positron is combined with an electron in an annihilation reaction, their masses are converted into energy. This energy appears in the form of two 0.511 MeV annihilation photons that travel in opposite directions. However, if the annihilation takes place before the positron stops, the resulting photons may be emitted in directions slightly off the ideal.

1.3 Intraoperative radiation therapy (IORT)

Once described how the different types of radiation interact with matter, let's focus on describing the main characteristics of intraoperative radiotherapy (IORT), because this treatment technique will be the main subject of this thesis.

Intraoperative radiation therapy is a special radiation modality that allows the administration

of a high localized dose (in the range of 10 to 25 Gy) in a single fraction during surgery, alone or as a boost technique [Calvo et al., 1993, Lamanna et al., 2012, Beddar et al., 2006, Abe, 1984, Rich, 1986, Gunderson et al., 2011, Debenham et al., 2013, Palta et al., 1995]. This modality permits direct visualization of the region to be irradiated after the removal of the lesion and it allows healthy tissue to be protected, by displacement or by shielding [Oshima et al., 2009, Russo et al., 2012, Martignano et al., 2007].

Although IORT was first introduced as a treatment technique at the beginning of the XX century [Beck, 1909], it was not until the earlies 1970s and 1980s that modern IORT with electron beams was developed [Abe et al., 1971, Abe and Takahashi, 1981]. Nowadays, IORT is widely used and its benefits in certain types of cancer (breast, gastrointestinal, prostate, pancreatic, brain, vertebral, etc) have been widely achieved [Calvo et al., 1993, Orecchia et al., 2003, Orecchia and Veronesi, 2005, Vaidya et al., 2001, Rich, 1986, Kraus-Tiefenbacher et al., 2005, Beatty et al., 1996, Bodner et al., 2003, Wenz et al., 2010, Schneider et al., 2011].

IORT can combine the benefits of the surgery with the benefits of the radiotherapy in the following aspects:

- Reduction of the possibility of a residual tumor regeneration, eliminating the microscopic tumor focal points.
- Allowance of a better definition of the treatment area, minimizing the damage to the healthy tissue.
- Maximization of the radiobiological effect with a high, localized dose.
- Fewer side effects, including rashes and skin irritation, that are commonly experienced during traditional radiation therapy.
- Shortening of the external radiation therapy treatment time when combined with IORT.

IORT requires a complex organizing system specifically designed for this treatment, that includes the collaboration of a multidisciplinary team made up by surgeons, oncologists, radiotherapists, radiophysicists, anaesthetists, nursing staff and assistants, among others.

There are two different types of IORT treatment, depending of the radiation used: **Intraoperative electron radiation therapy (IOERT)** and **Low energy X-rays intraoperative radiation therapy (XIORT)**.

1.3.1 Intraoperative electron radiation therapy (IOERT)

IOERT is the most common intraoperative radiation modality. Megavoltage electrons, when comparing to megavoltage photons, release the maximum dose at a similar depth as the photons. However, while the dose of electrons is released in a few cm from the entry point, the dose of photons is released at greater depths, as shown in figure 1.4 [Lamanna et al., 2012]. This fact

makes electrons the most suitable particles to give the required dose of radiation directly to the tissues displayed during surgery, thus protecting the underlying healthy tissues.

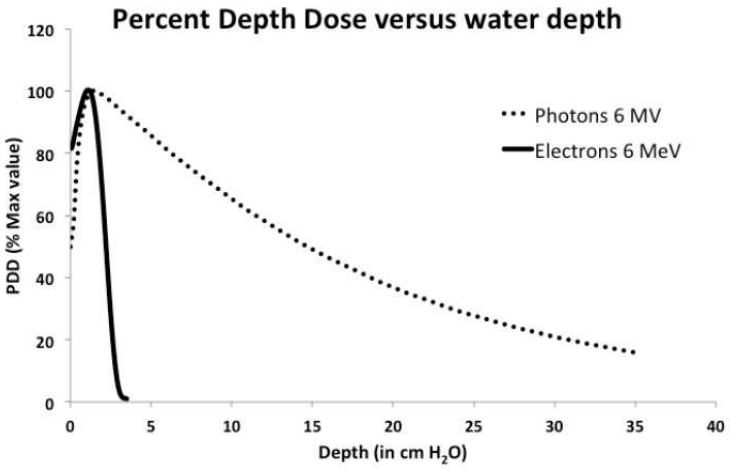

Figure 1.4: Percent Depth Dose (PDD) as a function of depth in water. The photon behavior is compared to the electron delivered dose. [Lamanna et al., 2012]

There are two application possibilities for IOERT, regarding the used radiation equipment: Using the linear accelerator treatment room, where the patient is carried from the operating room, or using mobile accelerators [Beddar et al., 2006] and treat the patient directly in the operating room. Both possibilities will be described in due course.

1.3.2 Low energy X-rays intraoperative radiation therapy (XIORT)

Intraoperative radiotherapy using electrons has been the favorite approach over orthovoltage beams because of better dose homogeneity, decreased treatment time and less bone absorption attributed to the photoelectric effect [Park et al., 2010]. However, XIORT (also called electronic brachytherapy because it uses X-rays produced by linear accelerators instead of using radioactive materials) has advantages in some clinical settings and is more cost-effective in most cases. The potential major advantages of XIORT are disposability of the source after use and a lesser requirement for protective shielding during the procedure [Eaton et al., 2011].

Intraoperative radiotherapy with low-energy X-rays (30-50 keV) is an innovative technique that can be either used as a single treatment or as a boost radiation. Inmediately after tumor resection the tumor bed can be treated with a low-distance X-rays by a single high dose [Kraus-Tiefenbacher et al., 2005]. At such low energies, the dose fall-off from the effective beam source is extremely rapid. The highest dose is at the applicator surface and it decreases with increasing tissue distance from the applicator. This allows a high irradiation to the surgical cavity (up to a depth of 1-2 cm) preserving the healthy tissue underneath.

XIORT is increasingly used since clinical results for breast cancer irradiation showed a similar local control [Veronesi et al., 2013], less toxicity, especially chronic skin toxicity [Sperk et al., 2012], and a overall survival benefit [Vaidya et al., 2014] for patients treated with XIORT in comparison to patients treated with external beam radiotherapy.

There are currently two commercial devices dedicated to low energy X-rays IORT (XIORT) treatments: the Axxent® Electronic Brachytherapy System (Xoft Inc., Fremont, California) and the INTRABEAM® device (Carl Zeiss Surgical Gmbh, Oberkochen, Germany). In this thesis we will study the INTRABEAM® device, so further description of this device can be found in the next sections.

1.4 Dose delivery in IORT

1.4.1 Linear accelerators for IOERT

There are two IOERT types of linear accelerators (LINAC), as previously mentioned: Conventional linear accelerators and dedicated mobile accelerators. The main characteristics of both systems will be found below.

1.4.1.1 Stationary linear accelerators

The available clinical linear accelerators can produce either photon or electron beams. In general, the generated radiation with this kind of devices is a high energy radiation with an energy spectrum from a few keV to several MeV, depending on the model.

A linear accelerator is a device that uses high radio-frequency (10-100 MHz) electromagnetic waves to accelerate charged particles (i.e. electrons) to high energies in a linear path, inside a tube-like structure called the accelerator waveguide [Khan, 1994, Karzmark and Morton, 1981]. The most basic configuration of a linear accelerator consists in using electron acceleration between two electrodes by means of the electric gradient within them. The electron beam is accelerated until it reaches kinetic energies between 4 and 25 MeV.

The LINAC has two working modes depending on the particles used for the treatment (figure 1.5):

In the **X-ray therapy mode** the electron beam hits a high-Z target, like tungsten. As a result, the electron energy is converted into a spectrum of X-ray energies with maximum energy equal to the incident electron energy.

In the **electron mode therapy**, the target is replaced by a scattering foil that spreads the beam.

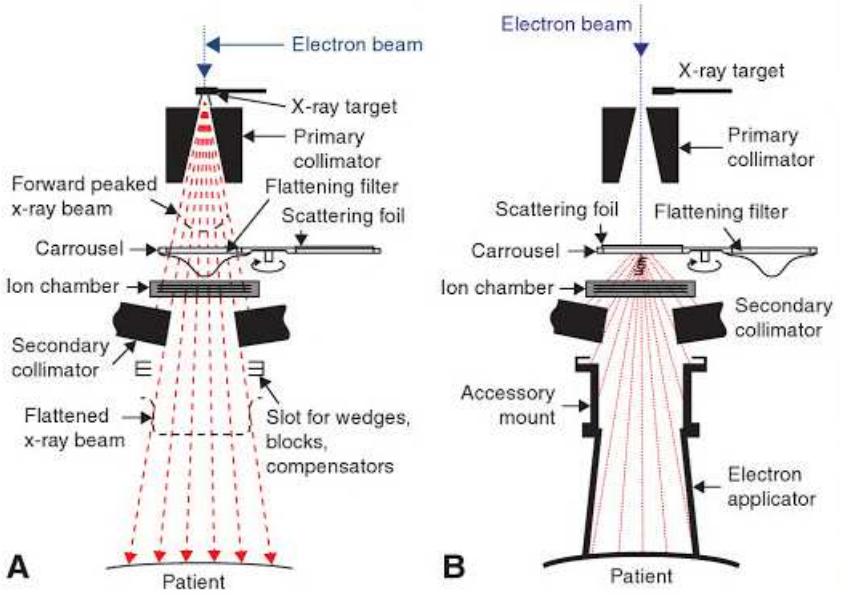

Figure 1.5: Components of the treatment head of A: X-ray therapy mode and B: Electron therapy mode [Khan, 1994].

The treatment head contains the collimation, stabilization and monitoring systems. The treatment unit and the acceleration structure are held inside the gantry, which can rotate 360° around its axis. As the gantry rotates, the collimator axis (coincident with the central axis of the beam) moves in a vertical plane. The point of intersection between the collimator axis and the rotation axis of the gantry is known as the isocenter.

The final dose distribution strongly depends on the beam modifier systems:

Scattering foils: The electron beam, as it exits the window of the accelerator tube, is a narrow pencil beam of about 3 mm diameter. In the electron mode of LINAC operation, this beam is made to strike an electron scattering foil to spread the beam as well as get a uniform electron fluence across the treatment field. The scattering foil consists of a thin metallic foil, usually lead. The thickness of the foil is such that most of the electrons are scattered instead of suffering bremsstrahlung. However, a small fraction of the total energy is still converted into bremsstrahlung and appears as X-ray contamination of the electron beam.

Flattening filter: The beam intensity is peaked in the forward direction. To make the beam intensity uniform across the field, a flattening filter is inserted. This filter is made of a metallic material (usually lead) and it is thicker in the center than in the sides.

Collimators: The emerging beam needs to be shaped to fit the treatment area. This is done by metallic jaws that change the beam area and size and focus the radiation.

IOERT applicators: All IOERT treatments need a specific collimator system [Nevelsky et al., 2010, Björk et al., 2000, Pimpinella et al., 2007]. Besides primary and secondary collimators, there are other systems called applicators that also collimate the beam.

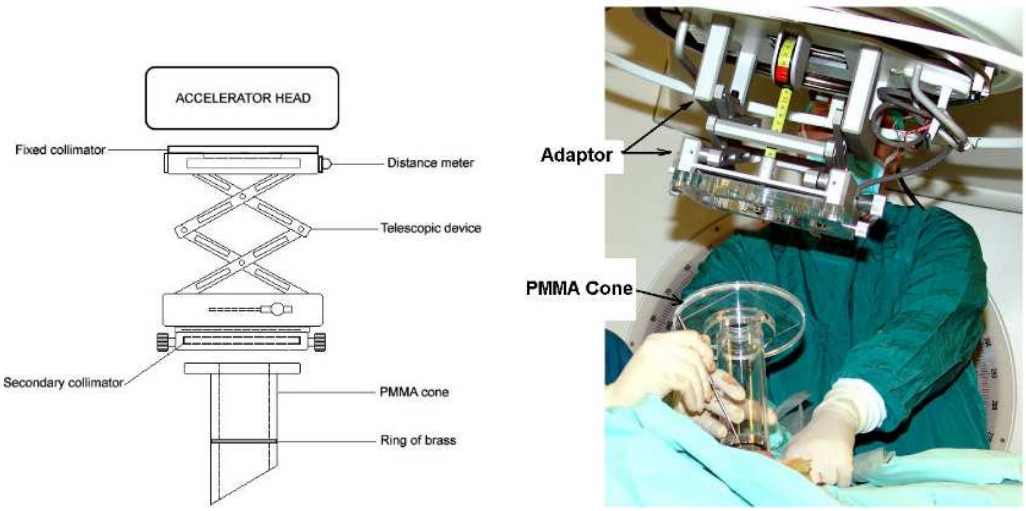

Figure 1.6: Main components of an ELEKTA PRECISE device [Nevelsky et al., 2010]

An IOERT applicator has three main functions: Collimation of the electron beam, definition of the treatment volume and detraction of the healthy tissue [Björk et al., 2000].

The main characteristics of applicators (used in both stationary and mobile linear accelerators) are [Pimpinella et al., 2007, Björk et al., 2000]:

- Applicators have, in general, cylindrical shape, although some of them may be rectangular.
- Applicators can be beveled or non-beveled.
- They are usually made of PMMA or brass.
- Applicator thickness varies between 3 mm and 8 mm.
- They present different lengths (from 30 cm to more than 1 m) and diameters (5-10 cm or more).

When a conventional accelerator is used for IOERT treatments, specific designed applicators must be employed [Nevelsky et al., 2010]. A telescopic device is attached to the accelerator head to change the source-to-applicator-end distance in the range up to 100–110 cm (figure 1.6).

The use of conventional accelerators for IOERT has several disadvantages. In this case, the anesthetized patient must be moved from the operating room (OR) to a sanitized treatment

Figure 1.7: IOERT procedure with a stationary linear accelerator. The treatment room changes temporarily into an operating room with all the needed equipment for monitoring the anesthetized patient [Calvo et al., 2013]

room, accompanied by OR personnel, as shown in figure 1.7. This is technically difficult and relatively inefficient, with the LINAC often unavailable for conventional treatment for a considerable time due to room preparation and waiting for the patient. [Beddar et al., 2006]. Most of the technical problems can be overcome with specialized operating rooms with integrated accelerators. However, the dedicated IORT facility in an OR is quite expensive and the OR needs to be properly shielded. To solve these problems mobile accelerators have been designed.

1.4.1.2 Mobile linear accelerators

The development of mobile linear accelerators has encourage the use of IOERT over the last decade. These kind of machines can be directly used in the OR, without the need of any other special shielding requirements.

Furthermore, the specific design of these mobile units can lead to advantages over conventional units adapted to IORT. For example, electron beams can have flatter beam profiles than conventional LINACs, and the range of motion of the treatment head allows more flexibility in setting up the patient. On the other hand, limitations on these units are imposed by practical concerns of storage, transport, treatment setup, and radiation protection [Beddar et al., 2006].

Actually there are several types of mobile LINACs:

Mobetron®

The Mobetron® (IntraOp Medical, Inc.) is a lightweight linear accelerator mounted on a C-arm gantry. The gantry is attached to a stand that contains the accelerator cooling system and a transportation system [Lamanna et al., 2012].

The gantry may be rotated ±45° in the transverse plane, and ±30° in the radial plane. Also, the gantry may be moved in the horizontal plane, ±5 cm. These movements are unique features not found in conventional accelerators used for IOERT.

Figure 1.8: Mobetron® linear accelerator (extracted from www.md51.com).

Applicator sizes range from 3 to 10 cm diameter for flat applicators, and 3 to 6 cm diameter for 30° beveled applicators, and produces electron beams of nominal energies 4, 6, 9, and 12 MeV. The system is designed to deliver a large, uniform dose from 10 Gy to 25 Gy in a single fraction at a dose rate of 10 Gy/min.

The Mobetron® uses a soft-docking system [Beddar et al., 2006, Björk et al., 2000] in which the treatment applicator is connected to a special rigid clamp system attached to the surgical bed and the gantry is optically guided to the docking position above the applicator (Figure 1.9).

As the unit is designed to operate only in the electron mode, beam currents are low, producing less inherent radiation leakage. The accelerator design allows the system to be used in rooms with no additional shielding.

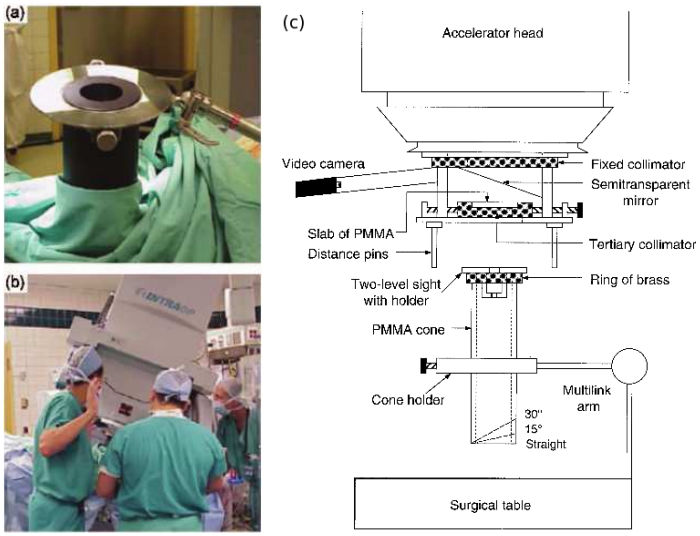

Figure 1.9: The soft-docking system used by the Mobetron®. (a) The electron applicator, in contact with the tumor bed, is rigidly clamped to the surgical bed [Beddar et al., 2006].(b) The gantry being moved for soft docking to the applicator [Beddar et al., 2006]. (c) Schematic diagram of the soft-docking system [Björk et al., 2000].

Novac7®

Novac7® (Hitesys SpA (LT) Italy 1997), is a dedicated accelerator with four nominal electron energy levels: 3, 5, 7 and 9 MeV [Lamanna et al., 2012, Mihailescu et al., 2006, Pimpinella et al., 2007, Righi et al., 2013].

The most important characteristic of this accelerator is the very high dose-per-pulse, ranging from 2.5 to 12 cGy/pulse, values up to 100 times greater than the doses per pulse produced by a conventional accelerator.

Novac7® has both a mobile and a fixed unit. The mobile unit is a stand structure on a motorized base, which supports the accelerator and modulator. The stand structure has the form of an articulated arm with four rotational joints, allowing movements similar to those of human arms. The base permits the entire structure to move without modifying the head orientation.

The beam collimation is performed through PMMA applicators consisting of two separated sections: the upper is fastened to the accelerator's head, and the lower is in contact with the patient (Hard-docking system, see figure 1.11). The applicator's set consists of cylindrical tubes with a wall thickness of 5 mm, diameter ranging from 4 to 10 cm, and face angles of 0°–45°. The

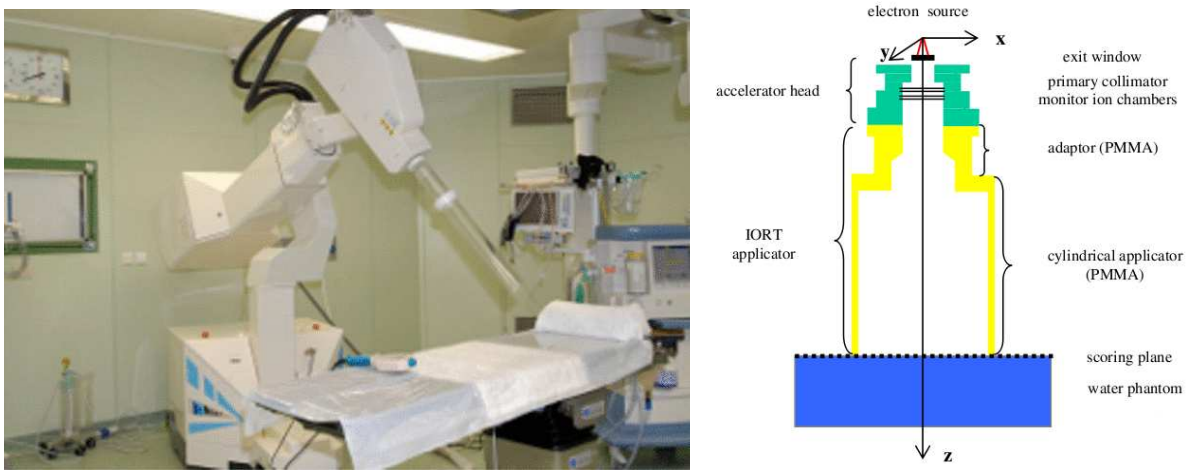

Figure 1.10: On the left, the mobile accelerator Novac7® in the operating room [Russo et al., 2012]. On the right, scheme of the accelerator head [Pimpinella et al., 2007].

length of the applicators varies according to the diameter: 80 cm for diameters up to 8 cm and 100 cm for those up to 10 cm.

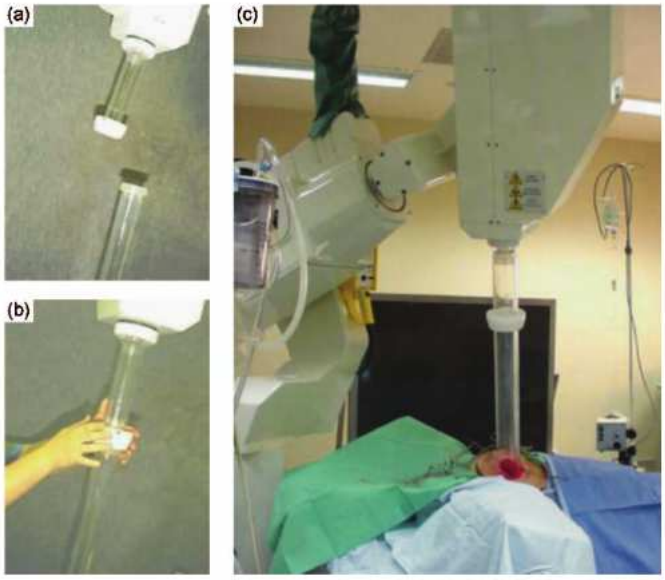

Figure 1.11: Hard-docking system employed in Novac7®. (a) The collimation system fixed to the accelerator and the electron applicator before docking. (b) The hard-docking mechanism. (c) The unit ready for treatment with the applicator in contact with the tumor [Beddar et al., 2006].

The Novac7® does not employ scattering filters which in conventional machines are the main

source of stray radiation. The accelerator head has just a primary collimator and the exit window (see figure 1.10). For this reason Novac7® has a low photon contribution: The total bremmstrahlung photon dose for conventional accelerators is at least 2-3% of the dose at the PDD (Percentage Depth Dose) maximum, mainly due to head scatter. For Novac7® with a 9 MeV nominal energy this value is 0.2% of the dose value at the PDD maximum.

Liac®

Liac® (SORDINA SpA Italy) is a dedicated IOERT linear accelerator, which produces electrons with energies of 4, 6, 8 and 10 MeV with a dose rate between 5 and 20 Gy/min and a pulse frequency between 5 and 20 Hz.

Figure 1.12: Liac® (from soiort.com).

The Liac® head has three degrees of freedom: it can be moved up and down for a maximum distance of 100 cm, it has a roll angle of ±60° and a pitch angle between +30° and -15°.

The output beam has a 3 mm diameter and is collimated by a 60 cm long applicator with different diameters and beveled angles. The dose homogeneity is generally guaranteed by a 100 μm brass foil scattering filter inserted in front of the titanium window. This technique keeps the level of stray radiation below the required limits.

1.4.2 Mobile devices for XIORT

There are two main systems used for IORT with low energy X-rays. The first is the Axxent® Electronic Brachytherapy System (Xoft Inc., Fremont, CA), a system of devices used for low-energy radiation at a high dose rate. The second, the Zeiss Intrabeam® (Carl Zeiss Surgical, Oberkochen, Germany), is a mobile photon radiosurgery system that procures a miniature electron beam-driven X-ray source [Park et al., 2010].

In this thesis the Intrabeam® system will be studied, so a detailed description of the device is given below.

1.4.2.1 Intrabeam®

The Intrabeam® system (Carl Zeiss Surgical, Oberkochen, Germany) is composed of a miniature, light-height (1.6 kg) X-ray source (XRS), settled in a stand with six degrees of freedom [Park et al., 2010, Kraus-Tiefenbacher et al., 2004, 2005]. Due to low-energy X-rays no special shielding is needed, and the treatment can be carried out in standard operating rooms [Eaton et al., 2011].

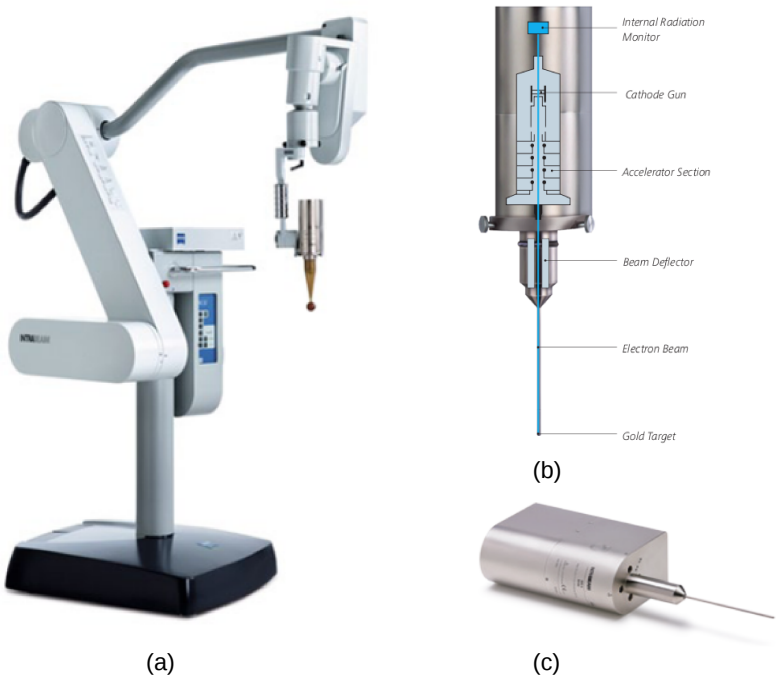

Figure 1.13: (a)The Intrabeam® system (Carl Zeiss Meditec AG, Jena) (b) The scheme of the miniature X-ray source. (c) The Intrabeam® source. *Courtesy of Zeiss* [Zeiss, 2012].

The electrons are generated and accelerated to a potential of 50 kV in the main unit and travel via the electron beam drift tube with 10 cm in length and 3.2 mm in diameter. At its end the accelerated electrons strike a gold target resulting in a nearly isotropic bremsstrahlung X-ray distribution around the tip [Yanch and Harte, 1996, Beatty et al., 1996, Dinsmore et al., 1996]. The scheme of the miniature X-ray source is shown in figure 1.13 (b).

The X-ray system produces low energy photons (up to 50 keV) with a steep dose falloff in soft tissue. This dose falloff in the tissue guarantees minimum exposure of the surrounding tissue.

Different cancer types can be treated with Intrabeam®, using different applicators, which can be attached to the XRS. These applicators are optimized in shape, size and physical dose distribution according to the cancer type, shape and location within the body. There are several applicators available, such as spherical, needle, cylindrical, flat and surface applicators (see figure 1.14).

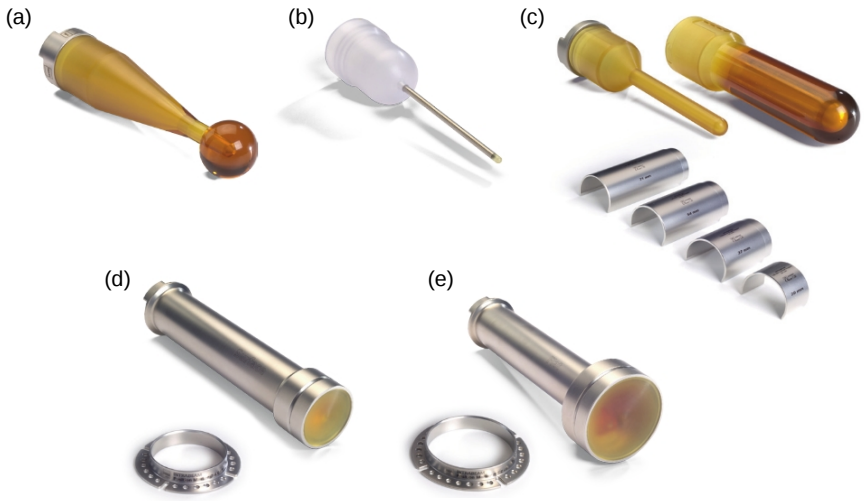

Figure 1.14: The Intrabeam® applicators. (a) Spherical applicator. (b) Needle applicator. (c) Cylindrical applicator. (d) Surface applicator. (e) Flat applicator [Zeiss, 2012].

a) Spherical applicators

The most used applicator for Intrabeam® is the Spherical, specially for irradiating the tumor

bed in breast-conserving surgery [Kraus-Tiefenbacher et al., 2005, Vaidya et al., 2001, 2010]. The applicator fills the tumor cavity created by the tumor excision. The probe tip is centered within the applicator and therefore the tumor cavity. A complete set of spherical applicators with diameters from 1.5 to 5.0 cm, in 0.5 cm increments, enables exact adaptation to the size of the tumor bed.

b) Needle applicator

The Needle Applicator can be used for the interstitial irradiation of tumors, e.g. in the treatment of spinal metastases. Spinal metastases are often accompanied by severed pain and the danger of a compression fracture. In Kypho-IORT with the needle applicator, vertebral metastases can be irradiated intraoperatively. After the IORT treatment, the affected vertebra is filled by the insertion of bone cement in a procedure known as kyphoplasty [Wenz et al., 2010, Schneider et al., 2011]. The Needle Applicator has a diameter of 4.4 mm.

c) Cylindrical applicator

The INTRABEAM Cylinder V Applicator is used for the irradiation of vaginal wall tumors and consists of a cylindrical applicator and a probe guard which may be inserted in the applicator. It enables manual stepping of the probe tip and the establishment of a homogeneous cylindrical dose distribution at a defined length [Schneider et al., 2009a]. The applicators are available in the diameters of 2, 2.5, 3 and 3.5 cm.

d) Surface applicators

The Surface Applicator is used to treat tumors on the surface of the body, for example, for the irradiation of non-melanoma skin cancers. It is particularly useful for patients with high surgical risk or for cosmetic purposes. The applicator generates an optimized flat radiation field (by means of a flattening filter) at the applicator surface [Schneider et al., 2014]. The surface applicators are available in the diameters of 1, 2, 3 and 4 cm.

e) Flat applicators

The Flat Applicator is used in the treatment of tumors on surgically exposed surfaces, such as gastrointestinal tract tumors [Schneider et al., 2014]. The Flat Applicator has an optimized flat radiation field (by means of a flattening filter) at 5 mm from the applicator surface. The applicators are available in the diameters of 1, 2, 3, 4, 5 and 6 cm.

1.5 Dosimetry in an IORT treatment

IORT treatments, as other modern radiotherapy techniques, have improved radiation delivery. But these techniques have also increased the complexity of the treatment planning and quality assurance needs to be done.

Dosimetry for IOERT treatments:

The most commonly used dosimeters for calibration of photon and electron beams are exposure-calibrated ionization chambers [Khan et al., 1991, Almond et al., 1999]. However, IORT dosimetry requires particular procedures for beam dosimetry and characterization, specially when using dedicated LINACs, which are sometimes different from those used in conventional external beam radiotherapy.

The main difference is related to the high dose per pulse of IOERT dedicated LINACs that does not allow the direct use of the ionization chamber as recommended in the IAEA 398 protocol for the absolute dose determination because of ion recombination effects [Marrale et al., 2015]. The direct use of ionization chambers could, in principle, lead to inaccurate measurements of output factors (OF) when applied to electron beams with these features of dose rate and energy and angular distribution. However, Björk et al. [Björk et al., 2004] have shown that ionization-chamber-based international dosimetry protocols could be applied in direct manner for output factor measurement in IORT beam, with an uncertainty less than 0.3%.

Furthermore, the high dose gradients used in IORT require high spatial resolution detectors. Other conventional measuring systems such as semiconductors do not provide enough spatial resolution. Thermoluminescent detectors are hard to setup and time consuming to read. Silver-halide radiographic film has large differences in sensitivity to photon energies in the 10-200 keV region, its properties of energy absorption and transfer do not match those of biological tissues, are sensitive to room light and require wet chemical processing [Niroomand-Rad et al., 1998, Fuss et al., 2007].

In contrast, radiochromic dosimeters provide high spatial resolution, have low spectral sensitivity variation and does not require post-processing, which make them one of the most reliable dosimetry methods.

Dosimetry for XIORT treatments:

Kilovoltage X-ray beam dosimetry provides a number of challenges which are not present for megavoltage X-ray beams [Hill et al., 2014, Ebert et al., 2002, Ebert and Carruthers, 2003].

Due to the low beam energy, the dose falls rapidly ($\sim 1/r^3$ in water, r being the distance to the center of the source [Armoogum et al., 2007]). Such a rapid falloff of the dose may complicate

dosimetry as dose can vary considerably across the volume of the detector when dose distributions are being measured. For example, the recommended ionization chamber is a parallel-plate chamber which has 1 mm width in the direction of the dose falloff (Type 23342, PTW, Freiburg, Germany), corresponding to a change in dose greater that 50% at 5 mm distance from the source at 50 kV [Ebert et al., 2002].

In addition, the energy spectrum is hardened quickly inside the water which can affect dosimetric parameters such as energy absorption coefficients and tissue equivalence materials.

Another issue is that the response of the dosimeter is sensitive to the materials used in its construction. For low energy X-ray beams, the photoelectric effect is a dominant interaction process and the photoelectric cross section has a strong dependence on the atomic number of the material.

The last challenge is that ionization chambers do not act as Bragg–Gray cavities in the kilovoltage X-ray energy range and so cavity theory cannot be used for reference dosimetry.

In contrast, some of the required dosimetric characteristics are found in radiochromic films [Avanzo et al., 2012, Ebert et al., 2009, Fletcher and Mills, 2008]:

- Intrabeam® dose reaches a maximum of about 20 Gy around the applicator surface and falls below 1 Gy at 3 cm depth in tissue. Gafchromic EBT3 (International Specialty Products, Wayne, NJ, USA) are recommended to be used in the range from 1 cGy to more than 40 Gy.
- Radiochromic films have a high spatial resolution, necessary for measuring the rapid Intrabeam® dose falloff.
- As described before, one of the concerns of kilovoltage X-rays is the energy response of the dosimeter. Gafchromic EBT3 are energy-independent.
- Regarding the dosimeter materials, these films are near tissue-equivalent.

In this thesis, experimental measurements have been performed with the Intrabeam® device. Two different dosimetric methods have been used: Ionization chambers and radiochromic film.

1.5.1 Ionization chambers

A ionization chamber is a gas filled detector. As radiation passes through a gas it can ionize the gas molecules. The charge pairs can be made to move in opposite directions by the application of an external electric field. The result is an electric pulse that can be measured by an associated measuring device. Based on the applied bias voltage, a detector can be operated in a number of modes, which differ from one to another by the amount of charges produced and their movement

inside the detector volume. In the ion chamber voltage region, all the charges that are being produced get collected.

Ionization chambers are widely used for absolute dose measurements in radiation therapy. By applying a certain detector specific calibration factor (e.g. Gy/C), the detector signal is related to a radiation dose value.

1.5.2 Radiochromic films

The radiochromic film consists of a radiation-sensitive dye embedded in an organic emulsion or an inert polymer. When an energetic photon or electron transfers its energy to the active layer, the active monomer components present in the film react to form a colored polymer [Niroomand-Rad et al., 1998, Schneider et al., 2009b, Fuss et al., 2007].

These films have very high spatial resolution and low energy dependence. Furthermore, they are insensitive to visible light, and the direct coloration does not require chemical, optical or thermal processing or amplification.

In this work Gafchromic EBT3 (International Specialty Products, Wayne, NJ, USA) have been used to perform absolute dosimetry. The film structure is made of an active layer (28 μm thick), between two polyester substrates (125 μm thick) [Gafchromic-EBT3]. The active layer contains the active component, a marker dye, stabilizers and other components giving the film its near energy-independent response.

1.5.2.1 Data analysis. The three channel technique

After irradiation, radiochromic films need to be scanned and converted to dose. The optical density has to be determined and, by using the dose-optical density response curve, the scanned image can be converted into dose (dose mapping). A multichannel flatbed scanner is the best option, as it offers the selection of the red color channel for greater sensitivity at lower doses and the blue and green color channel for higher doses.

Since the radiochromic film provides a different response to each of the channels, scanned films can be separated and analyzed in two parts: one part which is dose-dependent, and another dose-independent part which contains information about the differences in the film or the scanner (thickness inhomogeneities, noise, dust particles, scanner artifacts, etc) [Micke et al., 2011]. By separating the independent-dose part from the image, the remaining information is more reliable and therefore more useful for dosimetry.

After performing the calibration measurements [Devic et al., 2005, 2009, Lewis et al., 2012], films are scanned and data is obtained from the different channels at a resolution of 16 bits per channel. The images are defined by their optical density within a range between black (0: no observed signal) and white (I_0=65535; maximum signal). The optical density (OD) represents the capacity of the system to detect and reproduce the color range of the scanned images. The scanned optical density is defined as:

$$d_X = -\log_{10} X \tag{1.1}$$

where X [0,1] is the normalized color channel,

$$X = \frac{I}{I_0} \tag{1.2}$$

This X depends on scanner coordinates (i,j); X = X_{ij} reflects the optical density of the film at the coordinates (x_i,y_j).

The dose mapping is a nonlinear process and its conversion parameters are determined in the calibration, where a sufficient number of films exposed to a known dose are scanned to generate a calibration table {D_i,$d_x(D_i)$}. The calibration functions $\overline{d}_X$ (one for each color channel) are determined by correlating the calibration table, taking the form:

$$\overline{d}_X(D) = -\log\left(\frac{a+bD}{c+D}\right) \tag{1.3}$$

In the triple-channel film dosimetry method [Micke et al., 2011], the scanned optical density value can be separated into a dose-dependent part d_X^D and a dose-independent Δd.

$$d_X = d_X^D(D)\Delta d \tag{1.4}$$

And the dose value can be calculated for each color channel as

$$D_x = \overline{d}_X^{-1}(d_X \Delta d) \tag{1.5}$$

Since the dose cannot depend on the color channel X, a sequence of multiple channels can be selected and the differences in the dose results between the different color channels can be

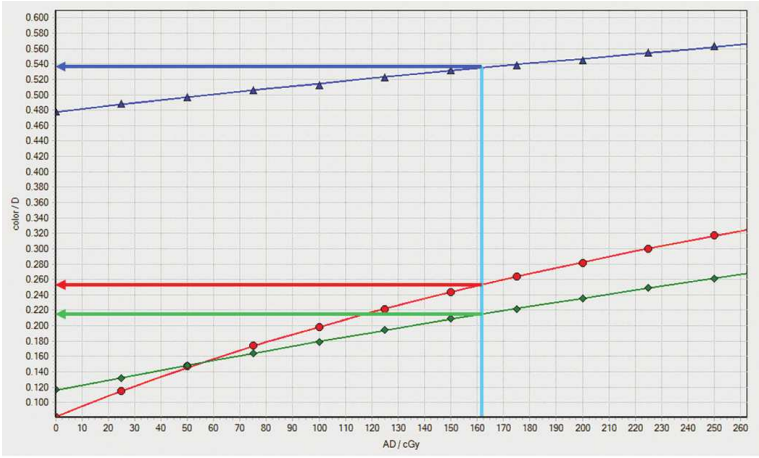

Figure 1.15: Multichannel calibration curves [Micke et al., 2011]

minimized (figure 1.15).

$$\Omega(\Delta d) = \sum_{i \neq j} (D_{X_i} - D_{X_j})^2 \rightarrow \min_{\Delta d} \tag{1.6}$$

This minimization is equivalent to finding the nearest color to the color path $\{\overline{d}_R(\mathrm{D}), \overline{d}_G(\mathrm{D}), \overline{d}_B(\mathrm{D})\}$. The distance of a point from his color path represents the disturbance value Δd, and the value of the path parameter is the best dose value.

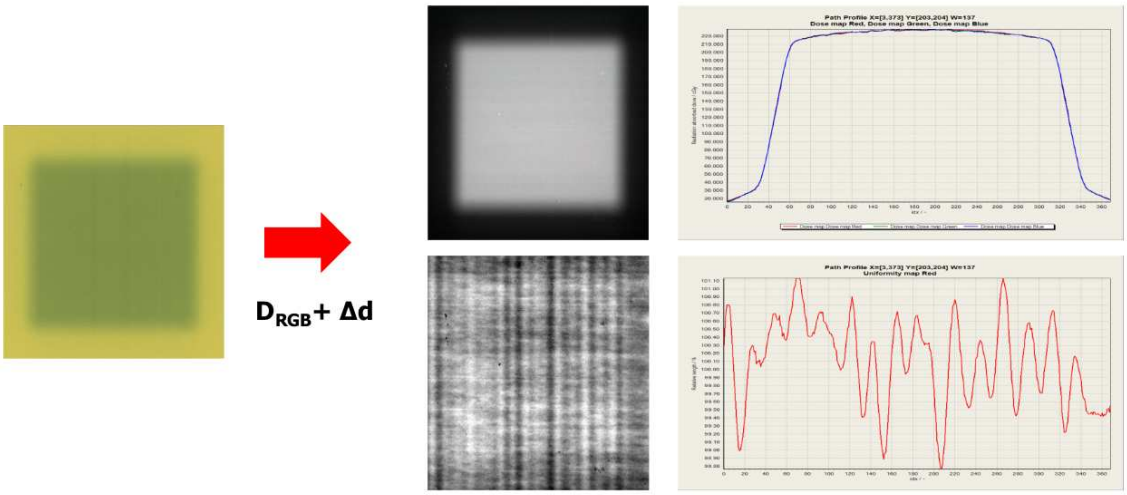

Figure 1.16: Dose map and disturbance map, and horizontal profiles [Micke et al., 2011]

Figure 1.16 shows the resulting dose and disturbance maps after performing a triple film dosimetry analysis to a radiochromic film. The horizontal profile in the dose map shows the improved flatness across the film. The corresponding profile along the disturbance map consists of a low frequency pattern dominated by thickness variations in the active layer.

1.6 Dosimetric characteristics of electron beams

When a clinical electron beam needs to be characterized, we are mainly interested in knowing how the dose is distributed inside the patient. In this section the main parameters that characterize the electron beam will be described.

1.6.1 Energy and angular distributions

One of the main characteristics of an electron beam is its energy distribution or energy spectrum. When a monoenergetic electron beam travels inside a scattering medium, its electrons are affected by the Coulomb interaction and its energy distribution is modified because of the elastic collisions with the atoms in the irradiated medium, broadening the spectrum. So, despite the initial monoenergetic electron beam when exiting the window, energy degradation of the beam produced by going through the different components located inside the accelerator head generates a broad energy spectrum at the end of the device, as shown in figure 1.17. In IOERT accelerators, because of the applicator need for further collimation, the energy broadening is bigger than in conventional radiotherapy. The path of electrons through IOERT applicators generates a greater amount of scattered electrons that can contribute to the final dose up to 40 %, while scattered electrons from conventional radiotherapy contribute up to 10% of the final dose [Björk et al., 2002]. This increase of scattered electrons results in a broadening of the energy spectrum when compared to conventional radiotherapy beams.

Moreover, the electron beam undergoes multiple collisions when traveling through the medium, what results in a whole beam scattering, and the scattering trajectories are characterized by the angular distribution of the beam. As a consequence, angular distributions in IOERT accelerators are broader than in conventional accelerators, as happens for energy spectrum.

The spectrum estimation is of great importance to make an accurate dose calculation, as it determines the initial energies and angles of the incident particles.

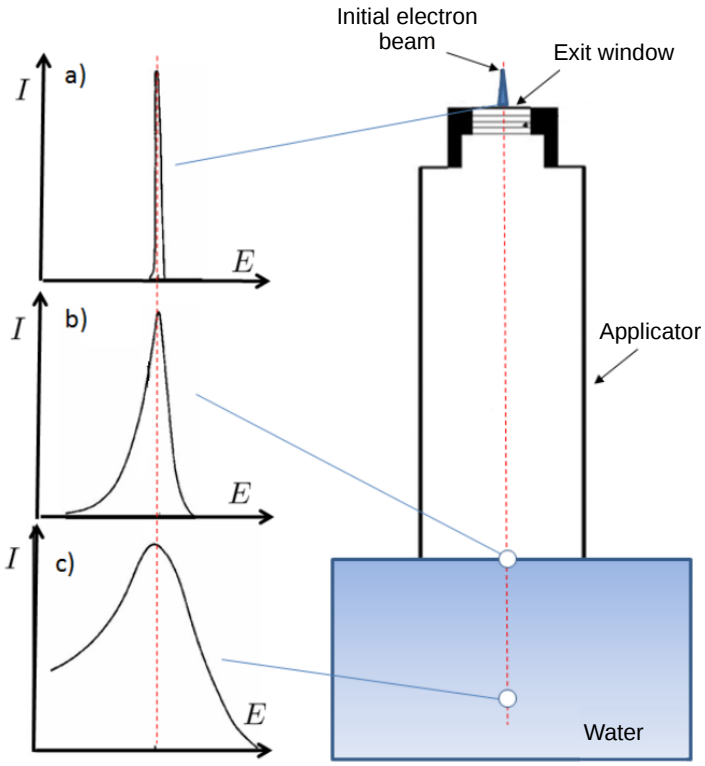

Figure 1.17: Energy distribution of an electron beam in a) the exit window, b) at the end of the applicator, c) at a certain depth inside the medium [Herranz, 2013]

1.6.2 Depth dose profiles

The graphic representation of dose deposition with depth is called depth dose profile (DDP), and it is related to the attenuation of the radiation inside a medium. This dose variation with depth along the central axis is one of the fundamental parameters for characterizing a radiation beam.

The depth dose curve of a beam depends on various factors such as beam energy, distance between the source and the irradiated surface, etc. To build these curves, the measured dose at different depths is usually normalized to the maximum dose measured. That is why these curves are usually known as **Percentage Depth Dose (PDD)**.

Figure 1.18 shows PDD curves for different clinical energies. High energy electrons deposit little energy between the surface and the point of maximum dose. From this point a great reduction of intensity takes place, until it reaches almost zero at a depth that depends on the initial beam

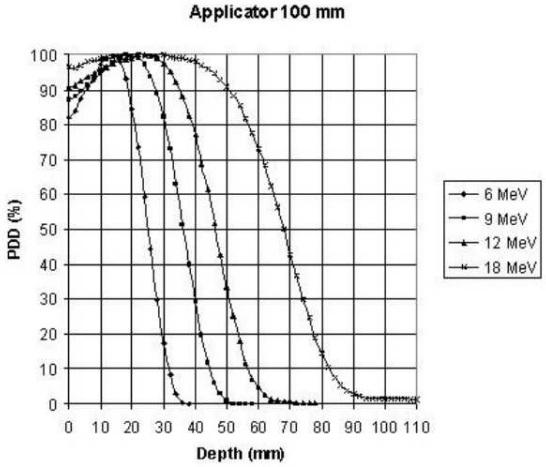

Figure 1.18: Percentage depth dose curves (PDD) for typical IOERT electron beams [Nevelsky et al., 2010].

energy. The rest of the dose contribution after this descending linear portion of the curve is caused by bremsstrahlung X-rays.

Different parameters can be defined looking at the PDD (see figure 1.19 (a)) [Delgado et al., 2013]:

- $\mathbf{R}_{max}$**:** Depth where absorbed dose in the central axis reaches the maximum.
- $\mathbf{R}_{90}$**:** Depth where dose reaches 90% of the maximum. The region between z=0 and R_{90} is called therapeutic range.
- $\mathbf{R}_{50}$**:** Depth where dose reaches 50% of the maximum.
- $\mathbf{R}_{p}$**:** Depth of the point where the tangent to the descending linear portion of the curve (at the point of inflection) intersects the extrapolated background. Also called Practical Range.
- **Bremsstrahlung tail:** X-ray contamination area. Dose measured in the central axis at d_{10} + 10 cm (d_{10} is the depth the dose reaches 10%) of the maximum.

1.6.3 Transverse dose profiles

Depth dose curves have not enough information to describe completely the deposited dose, and 3D dose distributions are necessary. To achieve this, dose measurements off-axis, also called transverse dose profiles, are performed. These curves take into account the beam spatial variation, and are used to know how dose is distributed perpendicularly to the beam. By combining depth dose profiles with off-axis data, 3D dose distribution can be reconstructed.

Information about symmetry and beam homogeneity can be obtained from lateral profiles. They have two distinguished regions: Central area and penumbra (as shown in figure 1.19 (b)).

The **central area** represents the radiation field central part, up to 10 to 15 mm from the geometrical edge of the field. In this area, the lateral profile depends mainly on the flattening filter and the geometry of the accelerator head.

The **penumbra region** of the lateral profile is characterized by a quick dose variation, which strongly depends on the collimation system, the radiation source focal size and the scattering properties of the charged particles.

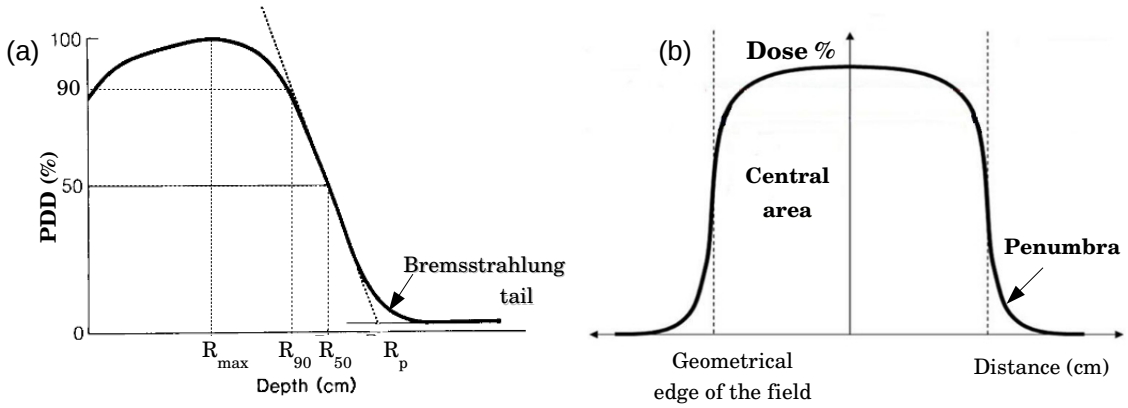

Figure 1.19: a) Depth dose curve illustrating the different parameters. (b) Typical shape of a transverse dose profile [Herranz, 2013].

1.6.4 Isodose contours

The combination of the two previously described curves provides a bidimensional modeling of the dose (Figure 1.20). Each curve represents an isodose level that includes spatial points that receive a dose equal or bigger than the one indicated by the curve. This kind of representation allows dose modeling inside a patient when he is irradiated.

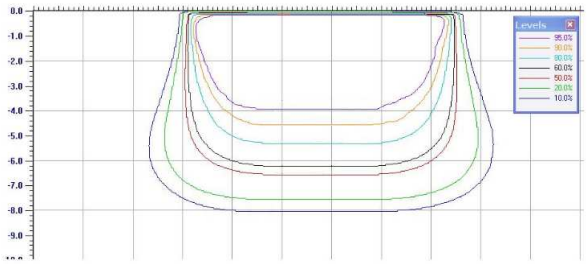

Figure 1.20: Isodose contours of a 18 MeV electron beam [Nevelsky et al., 2010]

1.7 Dosimetric characteristics of low energy X-rays

As previously done with electrons, in this section we are going to describe the main parameters that characterize the Intrabeam® photon beam.

1.7.1 Energy and angular distributions

The Intrabeam® source is a miniature X-ray source where electrons are accelerated up to 50 kV and hit a gold target. As a result, X-rays are emitted in all directions with a maximum energy of 50 keV. Therefore, the energy spectrum of the Intrabeam® source will be a classical X-ray spectrum with characteristic X-rays and a bremsstrahlung background.

The energy spectrum of the Intrabeam® X-ray source (XRS) can be seen in figure 1.21 (Left). The location of the prominent peaks correspond with the characteristic X-rays for gold and other materials of the source [Dinsmore et al., 1996, Beatty et al., 1996].

When an applicator is placed around the needle, the beam hardens as it passes through the different materials. As a result, there is a reduction of the characteristic X-rays and an increase of the bremsstrahlung tail. The energy spectrum of a spherical applicator is shown in figure 1.21 (Right).

Angular distribution of the Intrabeam® needle has been studied in previous works [Dinsmore et al., 1996]. It has been found (figure 1.22) that intensity is nearly isotropic, with an approximately 10 % decrease perpendicular to the probe axis (due to photon self-absorption in the gold) and a 7% dip in the forward direction (origin unknown).

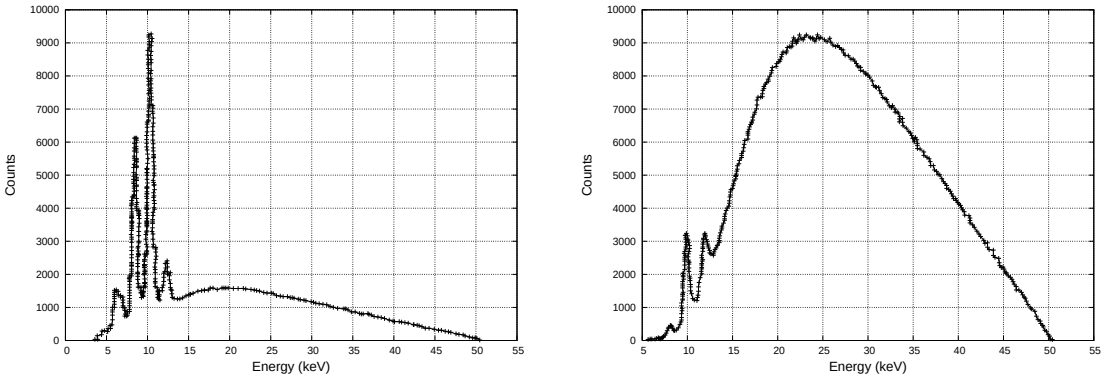

Figure 1.21: Left: Energy spectrum of the XRS. Right: Energy spectrum of the 1.75 cm radius spherical applicator [Schneider et al., 2010].

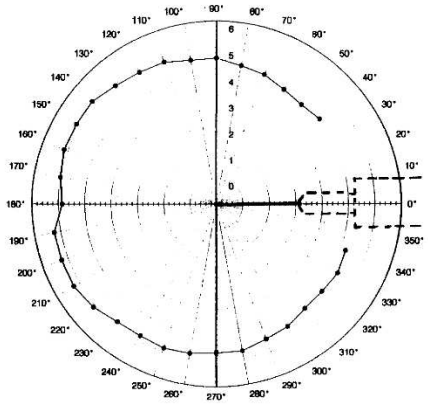

Figure 1.22: Polar representation of the angular photon flux in the plane of the probe axis [Dinsmore et al., 1996].

1.7.2 Depth dose profiles

Depth dose curves for low energy X-rays differ from the electron curves. The dose rate is the highest at the surface of the applicator and falls rapidly as the distance to the applicator increases.

These curves vary significantly with the applicator. For spherical applicators (figure 1.23 (a)), the applicator with the smallest diameter gets the highest dose at the surface. As the diameter of the applicator increases, the falling gradient of the dose slows down [Xiao et al., 2015]. For flat and surface applicators similar behavior is observed (figure 1.23 (b)): dose rate increases when

diameter decreases. Similarly, the falling dose gradient is slower when the applicator is bigger [Schneider et al., 2014, Goubert and Parent, 2015]. When comparing flat and surface applicators, flat applicators are about 1.5 times higher in dose rate value than the surface applicator of the same size [Lam et al., 2014].

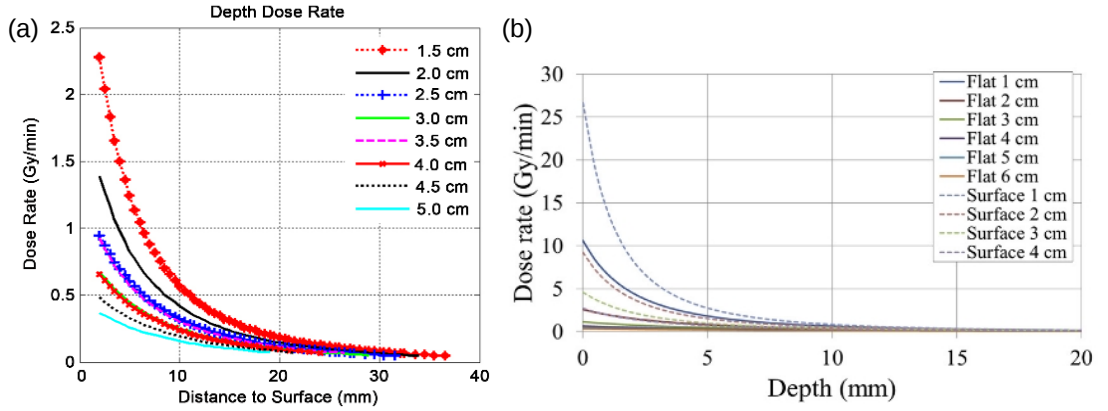

Figure 1.23: (a) Depth dose curve rate for each spherical applicator [Xiao et al., 2015]. (b) Depth dose curve rate for each flat and surface applicator [Goubert and Parent, 2015].

1.7.3 Transverse dose profiles

Off-axis measurements for Intrabeam® are significant when flat or surface applicators are used.

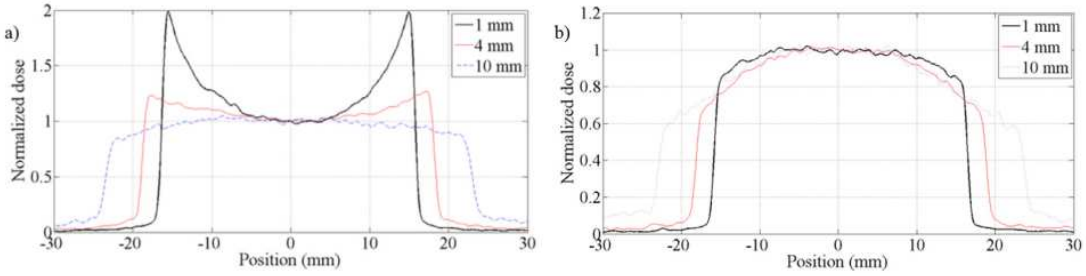

Figure 1.24: Transverse dose profiles at different depths for 3 cm (a) flat and (b) surface applicators, normalized to the dose along the central axis [Goubert and Parent, 2015].

In the case of surface applicators, transverse profiles give a uniform dose distribution at the applicator surface, and when depth increases, dose on the periphery becomes lower than dose at the center of the profile. In the case of flat applicators, dose uniformity is not reached until depth is 5 mm. Before this depth, dose on the periphery of the profile is higher than dose in the

center. For larger depths, dose on the periphery becomes lower than dose at the center [Goubert and Parent, 2015].

1.7.4 Isodose contours

Isodose contours are very useful to test the needle anisotropy. In previous studies, isodose contours of the needle have been proven to be similar to the angular distributions [Dinsmore et al., 1996]. According to vendor specifications, Intrabeam® construction yields an isotropic dose distribution with a maximal variation of 15% in all directions [Clausen et al., 2012].

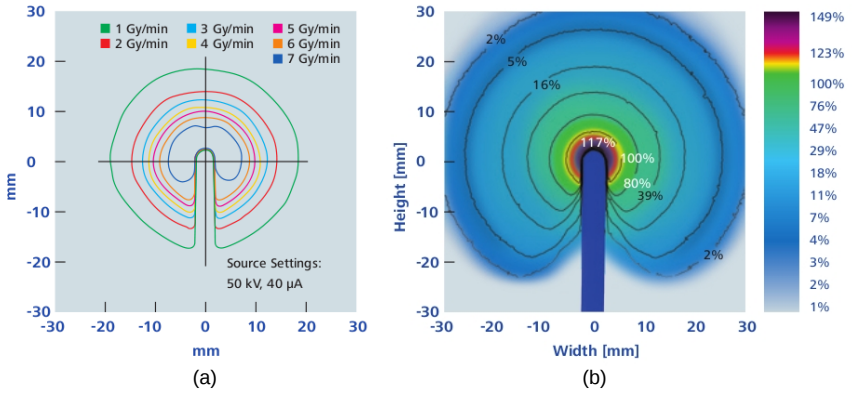

Figure 1.25: (a) Isodose contours of the Intrabeam® bare X-ray source. (b) Isodose contours of the Intrabeam® needle applicator (from Carl Zeiss Meditec AG)

1.8 Radiance®, a treatment planning system for IORT

A treatment planning system is an essential tool for oncologists, as it allows to perform an estimation of the dose distribution inside the patient before irradiation.

Although treatment planning is mandatory for external beam radiotherapy, the difficulties in an IORT treatment have not make it possible until recently. There are several reasons for this: most organs at risk are displaced or protected during surgery, the electron beam presents a very high dose gradient, and the treatment volume is directly visualized by the surgeon in the operating room.

radiance® is the first treatment planning system specially designed for intraoperative radiation therapy [Valdivieso-Casique et al., 2015, Pascau et al., 2012, GMV, 2015]. It is a planning system for IORT with electron beams and IORT with the Intrabeam®. It has been developed by the GMV company, and it is a result of a large collaboration between

private companies (Técnicas Radiofísicas), medical institutions (Hospital Universitario Gregorio Marañón, Consorcio Hospitalario Provincial de Castellón, Clínica La Luz, Hospital Ramón y Cajal) and universities (Universidad Politécnica de Madrid, Universidad Complutense de Madrid, Universidad Rey Juan Carlos, Universidad de Valencia, Universidad de Granada).

radiance® can be used in three different phases of the treatment:

- Pre-planning: Allows to try different positions of the applicator using CT images, and to select the optimum parameters for each treatment (applicator diameter, bevel angle and electron beam energy).
- Intra-planning: During surgery, previous planning studies can be checked and updates can be done if the situation requires it, checking the effects of these changes on the dose distribution inside the patient.
- Post-planning: After surgery, control CT studies combined with the simulation tool enable evaluation of the treatment.

Three dose calculation algorithms are implemented in ***radiance***®:

- A **pencil beam** (PB) algorithm [Hogstrom, 1985, López-Tarjuelo et al., 2010] for electrons. PB is very fast (running times up to 4 seconds). But this algorithm presents some limitations when heterogeneities are present (such as bad backscattering modeling). However, these deficiencies are covered by the Monte Carlo model.
- A **Monte Carlo** (MC) algorithm for electrons which has been optimized for computational efficiency.
- An **Hybrid Monte Carlo** algorithm capable of fast and accurate dose calculations with low energy photons for the Intrabeam® device.

Both Monte Carlo and Hybrid Monte Carlo implementations in the planning system have been possible thanks to the results presented in this thesis, that have been incorporated in ***radiance***®.

Two examples of treatment planning with ***radiance***® are shown in the figure 1.26.

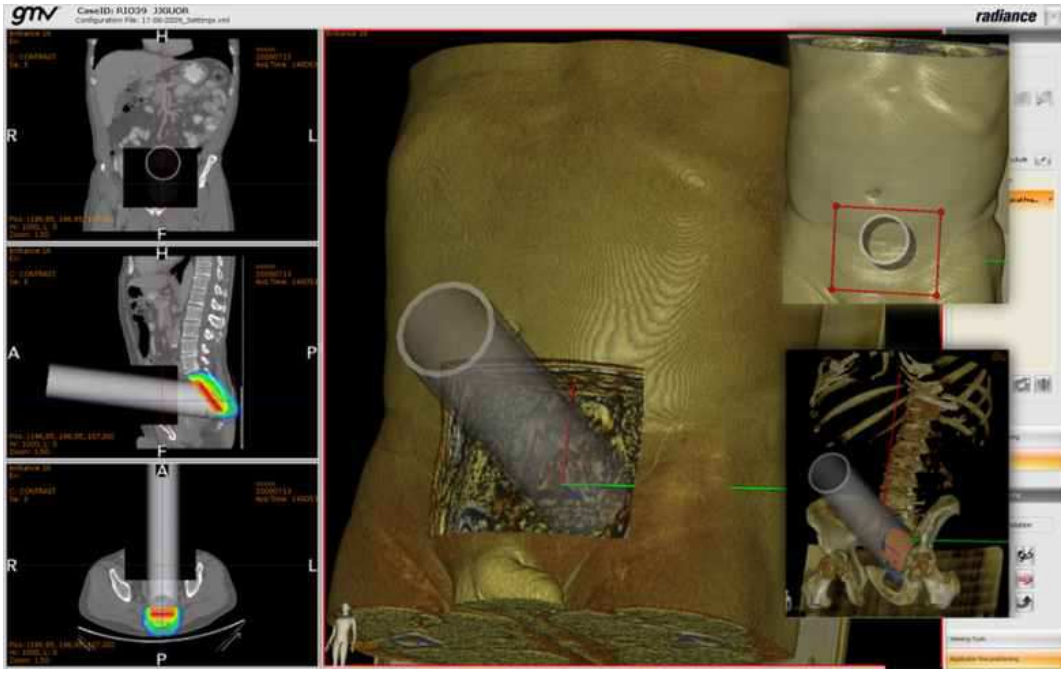

(a)

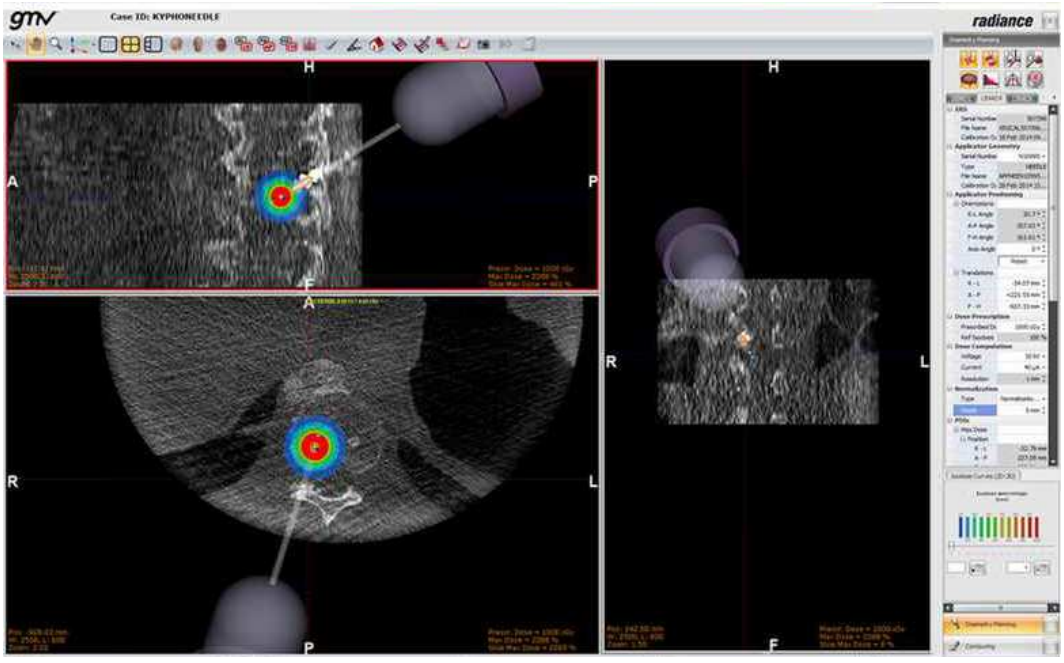

(b)

Figure 1.26: Dose distribution in ***radiance***® in a (a) IOERT treatment, and (b) in a XIORT treatment with a needle applicator [Valdivieso-Casique et al., 2015]

1.9 Gamma evaluation

To evaluate a radiotherapy planning system, comparisons of measured and calculated dose distributions are required, and quantitative evaluations need to be performed.

As a first approximation to define a quantitative evaluation method, *dose difference* was used as acceptance criterion. A distribution of dose differences can be represented to identify the regions where the calculated dose and the measurement differ. This criterion can be used in low gradient areas but is inadequate in high gradient regions, where a small spacial shift results in a large dose difference.

The sensitivity of the dose difference method to high dose gradients led to the development of a new tool called *Distance-to-agreement* (DTA) [Van Dyk et al., 1993]. The DTA is the evaluation of the distance between a measured data point and the nearest point in the calculated distribution that exhibits the same dose. However, in small dose gradient regions, small dose differences can lead to high DTA values.

Because of the complementary sensitivity of these methods, both evaluation images were merged to create a more complete evaluation criterion, the **gamma evaluation** [Low et al., 1998, Low and Dempsey, 2003, Depuydt et al., 2002].

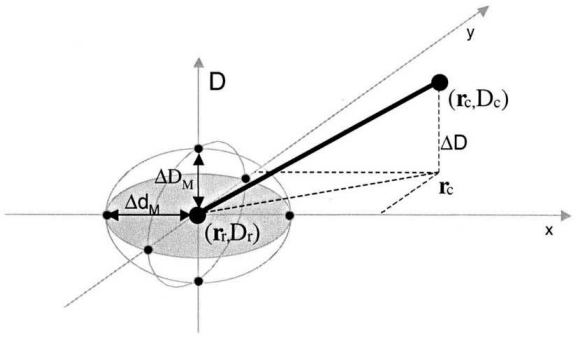

Figure 1.27: Schematic representation of the gamma evaluation method between the reference dose ($\mathbf{r}_r$,D_r) and the calculated dose ($\mathbf{r}_c$,D_c). The criteria is defined by an ellipsoid of acceptance determined by the dose difference tolerance $\Delta \mathrm{D}_M$ and the DTA tolerance $\Delta \mathrm{d}_M$ [Depuydt et al., 2002].

The gamma method, presented by Low *et al.* [Low et al., 1998], compares two dose distributions: The reference dose ($\mathrm{D}_r(\mathbf{r})$) and the calculated dose that needs to be evaluated ($\mathrm{D}_c(\mathbf{r})$). The acceptance criteria are denoted by $\Delta \mathrm{D}_M$ for the dose difference and $\Delta \mathrm{d}_M$ for the DTA. For a reference point at position $\mathbf{r}_r$ with a dose D_r, the surface representing these acceptance criteria

is an ellipsoid defined as:

$$1 = \sqrt{\frac{\Delta r^2}{\Delta d_M^2} + \frac{\Delta D^2}{\Delta D_M^2}} \tag{1.7}$$

Where Δr is the distance between the reference and the calculated point and ΔD is the dose difference at the position $\mathbf{r}_c$ relative to the reference dose D_r in $\mathbf{r}_r$.

$$\Delta r = \mid \mathbf{r}_r - \mathbf{r}_c \mid \tag{1.8}$$

$$\Delta D = D_c(\mathbf{r}_c) - D_r(\mathbf{r}_r) \tag{1.9}$$

The calculated dose will fit the gamma evaluation if at least one point ($\mathbf{r}_c$, D_c) of its dose distribution is contained inside the ellipsoid of acceptance showed in figure 1.27, ie. one point for which

$$\Gamma_r(\mathbf{r}_c, D_c) \equiv \sqrt{\frac{\Delta r^2}{\Delta d_M^2} + \frac{\Delta D^2}{\Delta D_M^2}} \leq 1 \tag{1.10}$$

The pass-fail criterion becomes:

- $\gamma(\mathbf{r}_r) \leq 1$, calculation passes.
- $\gamma(\mathbf{r}_r) > 1$, calculation fails.

For example, if a 3%-3 mm criterion is considered, points passing this criterion will be the ones located at 3 mm or less from a point in which dose difference with the reference is 3% or less.

Gamma evaluation limits depend on the type of radiotherapy and the location of the tumor. For a stereotactic brain treatment, with high precision systems and with organs at risk very close, it would be suitable a 1%-1 mm criterion. However, for IORT these precision requirements are not so restrictive, because the surgeon limits the treatment area and protects the organs at risk. Therefore, in IOERT it is reasonable to consider suitable a dosimetric study when 95% of the points pass the 3%-3 mm limit [Alber et al., 2008]. Nevertheless, this approximation can not be considered in a dose evaluation for the Intrabeam®, because of the rapid decrease of the dose. In this case, this limit can vary from 2%-1 mm [Nwankwo et al., 2013], to 2%-2 mm [Clausen et al., 2012] or even 10%-1 mm [Chiavassa et al., 2014]. In this thesis we have considered different limits, depending on the voxel size used.

Chapter 2

Monte Carlo methods in radiotherapy

2.1 Introduction

Determination of a dose distribution inside a patient or a phantom is of crucial importance to be able to determine the effectiveness of a radiotherapy treatment and to evaluate the effects of radiation in matter. Any dose measuring method will be only an estimation, because dose deposition will depend on the irradiated medium, and by introducing any dosimetry system the medium will be modified. This estimation of the dose can be measured with different dosimetry techniques (ionization chambers, radiochromic films, etc.), or calculated with numerical methods that implement different models of the interaction of radiation with matter.

The use of calculation algorithms in dosimetry allows the estimation of absorbed dose distributions inside irradiated volumes. These algorithms are based in radiation transport models that describe the mechanisms responsible for the transport and the interaction of radiation with matter. There are two main trends of dose calculation algorithms based in different mathematical models of energy deposition: one is a deterministic strategy based in Boltzmann equation and the other is based in Monte Carlo (MC) simulations.

In the deterministic approach, the model is built from a coupled set of equations (known as Boltzmann equation) that describe how a variety of different types of particles travel through a material. This technique works adequately in homogeneous media but has some problems with heterogeneities [Wang et al., 1996, Ding et al., 2005], which are specially important in radiotherapy dosimetry.

In the last years, Monte Carlo methods are becoming widely used. Monte Carlo simulation of radiation transport uses the probability distributions governing the individual interactions of electrons and photons in materials to simulate the random trajectories or histories of individual particles. These methods are more precise than the deterministic models, specially in complex media, but very time consuming.

In this chapter we will explain the basic concepts of MC methods and their application in radiotherapy. We will also describe the main MC codes used in radiation transport, specially the ones that have been used in this thesis.

2.2 Monte Carlo technique. Basic concepts

The name "Monte Carlo" references a group of mathematical procedures or numerical methods used to model complex systems by using the previously known probabilities of occurrence of the different events involved in the problem [Sobol, 1994, Kalos and Whitlock, 2008]. In these processes random variables are used, and by calculating their expected value we can reach the approximated solution of the problem. Therefore, a Monte Carlo simulation is a quantitative technique that uses statistics to mimic, by means of mathematic models, the behavior of a real system.

All processes involved in particle transport are stochastic, which means that we can not foresee what kind of interaction is going to happen next and where it is going to take place. We only can assign a probability to each possibility. However, the probability distributions associated at every event are well known, and, together with the use of a random number generator, they will be used to sample parameter values for calculating a possible solution to the problem for a single “history” or “event”. By simulating many histories, reliable average values can be obtained. Since the result is an average, it is associated with a standard deviation that expresses the uncertainty due to the fact that the simulated number of events is less than infinite [Reynaert et al., 2006].

In a Monte Carlo dose calculation, the track of each individual ionizing particle through the volume of interest is simulated. Along its way, the particle may interact with the matter through which it is passing. Using a random number generator and probability distributions for the different types of interaction, the program samples the distance to the next interaction for every particle at a given position and with a certain direction. The particle is propagated to the interaction location and next, the program chooses the type of interaction that will take place. After interaction, the same procedure is repeated with the remaining particle and secondary particles (if generated) [Reynaert et al., 2006]. Therefore, each history or trajectory of the particles can be seen as a sequence of free paths that end with an interaction event where the particle changes its direction, loses energy and can generate secondary particles.

All Monte Carlo codes have some components in common, regardless of its application field.

- **Probability distribution functions:** They contain all the information regarding the physical processes. All the physics or mathematical models must be described by these functions.
- **Random number generator:** A tool to generate aleatory numbers uniformly distributed between 0 and 1.
- **Sampling method:** A way to sample the variables of the probability distribution functions.
- **Scoring methods:** All results must be stored for each variable of interest.
- **Error estimation:** It is convenient to determine the error associated to the number of histories.

Furthermore, optimization tools can be found is most of the codes, such as:

- **Variance reduction techniques:** Methods introduced to increase the efficiency of MC calculations.
- **Parallelization techniques:** Algorithms that increase the efficiency by using the additive property of MC calculations. They require the use of advanced computer architectures.

2.2.1 Modeling of particle transport

The physics models are usually hard-coded in the Monte Carlo software. In radiation transport, photons are transported in a similar manner as in a real medium. For example, to determine the scattering angle and energy of a secondary electron in a Compton scattering event, we make use of the Klein-Nishina cross section for Compton scattering [Rogers, 2002]. However, this is not possible in the case of electrons because when an electron slows down in a material, it can undergo hundreds or thousands of scattering events in which it is deflected slightly but loses virtually no energy. Therefore, the simulation of each individual interaction is very time consuming and impractical for radiotherapy applications [Reynaert et al., 2006]. To accelerate the simulations, so-called condensed history techniques have been introduced. In section 2.2.5.2 further details of condensed histories can be found.

The physics modeling can be also modified via a number of transport parameters, such as cut-off energies or particles step length, that set thresholds when tracking a history. Depending on the values given to these parameters, the simulation can be accelerated, but they have to be handled with care because accuracy can be lost. These transport parameters are explained in section 2.2.5.1.

2.2.2 Random number generator

A sequence of random numbers is one where next number in the sequence can not be predicted. The random numbers used in MC are not really random, as they are generated with a computer algorithm, but pseudo-random, and they are the base of a Monte Carlo code. This pseudo-random nature of Monte Carlo simulations is what imitates the true stochastic or random nature of particle interactions. The pseudo-random number generators use an initial seed or number as a starting point for the sequence generation. The sequence will be sufficiently unpredictable and it will not be repeated in cycles. However, two sequences will be equal if the same initial seed is used.

These numbers must accomplish some characteristics:

- Good distribution. Generated random numbers must be uniformly distributed between [0,1].
- The sequence generated must be sufficiently large to ensure non repeatability.
- Reproducibility. If the simulation is repeated under the same circumstances, the result must be the same.

2.2.3 Probability distribution functions and sampling method

There are different kinds of sampling techniques. We will consider two of them.

2.2.3.1 Invertible cumulative distribution functions (direct method)

The direct method is the form used to calculate a particle's distance to an interaction in all Monte Carlo codes.

A probability distribution function, *p(x)* is a measure of the likelihood of observing x. For example, x could be the position at which a photon interacts via the Compton interaction.

In general, *p(x)* has some special properties that distinguishes it from other functions [Bielajew, 2001]:

- *p(x)*$\geq$0 since negative probabilities have no meaning.
- *p(x)* must be normalized to 1

$$\int_{x_{min}}^{x_{max}} p(x)dx = 1 \tag{2.1}$$

- x_{min} and x_{max} can be any real number as long as x_{min} is less than x_{max}.

Associated with each one-dimensional probability distribution function we find its cumulative probability distribution function [Bielajew, 2001].

$$c(x) = \int_{x_{min}}^{x} dx' p(x') \tag{2.2}$$

This cumulative function has the following properties:

- *p(x)* and *c(x)* are related by a derivative

$$p(x) = \frac{dc(x)}{dx} \tag{2.3}$$

- *c(x)* is zero at the beginning of the range and one at the end of the range: *c(x)* is contained within the range [0,1].

- *c(x)* is a monotonically increasing function of x as a result of *p(x)* always being positive.

Cumulative probability distribution functions can be related to uniform random numbers to provide a way for sampling these distributions. We can map the cumulative probability distribution function onto the range of random variables, r, where $0 \leq r \leq 1$ and r is distributed uniformly. That is, $r=c(x)$.

Having mapped the random numbers onto the cumulative probability distribution function, we may invert the equation (all cumulative probability distribution functions are invertible) to give:

$$x = c^{-1}(r) \tag{2.4}$$

Then, by choosing r's randomly over a uniform distribution and substituting them in the above equation, we generate x's according to the proper probability distribution function.

In the case of a particle interaction, the probability distribution function will be:

$$p(z)dz = \mu e^{-\mu z} dz \tag{2.5}$$

Where μ is the interaction coefficient needed to sample the distance to the next collision for a

given type of particle with a given energy in a given material [Reynaert et al., 2006]. Data tables with interaction probabilities of each type of interaction for each element are usually provided together with a Monte Carlo program.

The cumulative probability distribution will be:

$$r = c(z) = 1 - e^{-\mu z} \tag{2.6}$$

Inverting it:

$$z = -\frac{1}{\mu} log(1 - r) \tag{2.7}$$

If r is uniformly distributed over [0,1] then so is *1-r*.

The invertible cumulative probability distribution function method is always possible, but it is often impractical to calculate it because it may be exceedingly complicated mathematically or may contain a structure that is difficult to control. Another approach is to use the rejection method.

2.2.3.2 Rejection method

The procedure is the following:

- Scale the probability distribution function by its maximum value obtaining a new distribution function, *f(x)= p(x)/p(x_{max})*.
- Choose a random number, r_1, uniform in the range [0,1] and use it to obtain an x which is uniform in the probability distribution function's range [a,b] (by calculating x=*a+(b-a)*r_1).
- Choose a second random number r_2. If r_2 < *p(x)/p(x_{max})* then accept x, else, reject it and go back to the second point.

This method only works if the probability distribution function is not infinite anywhere and if it is not extremely difficult to determine the location of the maximum value. It is also restricted to finite values of a and b.

2.2.4 Error estimation

MC algorithms are statistical methods and, therefore, the results should be accompanied by the corresponding error. In general, the associated error of a result is inversely proportional to $\sqrt{N}$, where N is the number of simulated histories. Thus, if the uncertainty wants to the reduced by two, number of simulated histories must be increased by a factor four.

If we consider x_i as one of the calculated and stored parameters of the simulation for a history i, where $1 \leq i \leq N$, the mean value can be calculated as:

$$\bar{x} = \frac{1}{N} \sum_{i=1}^{N} x_i \tag{2.8}$$

The variance associated to de x_i distribution will be:

$$S_x^2 = \frac{1}{N-1} \sum_{i=1}^{N} (x_i - \bar{x})^2 \tag{2.9}$$

2.2.5 Monte Carlo optimization

The use in the clinic of the dose calculation systems requires a compromise between two main goals: Accuracy and precision in the results and a reasonable calculation time. The last condition is specially important in IORT, where the calculations must be done right after the surgery.

In MC methods the precision of the results can be improved by increasing the number of histories. However, by improving the precision there is an increasing in the simulation time. To solve this, some methods have been designed to reduce simulation time with different techniques.

In this section we will describe the most common optimization techniques. Some of them imply a certain loss in the results quality because the use simplifications in the physics model, in the input data or incorporate some strategies inside the MC algorithm to reduce the amount of needed histories regardless the consequences in the dose results.

Other techniques reduce computation time without losing quality in the data. Normally, they keep the physics of the model unaltered and change the calculation algorithm. These strategies are the most used and can be found in the configuration input of most codes.

2.2.5.1 Cut-off energies and step length

The mean free path of the particles (ie. the distance traveled between interactions) depends on their energy. Furthermore, the particle transfers energy to the medium in each interaction, until its energy is so low that the particle is absorbed. Some programs introduce these two facts in their code to accelerate simulation time.

The cut-off energy value is a threshold in energy. When the energy of a history goes below the cut-off energy value, the program stops following that particle. The particle is considered to be absorbed at that point. There are different cut-off values for the energy depending on the type of particle and the type of interaction.

The step length parameter defines the distance between interactions. The bigger the value is, the quicker the simulation.

The user may modify both of the mentioned parameters. They had to be handled carefully, as such parameters may significantly influence a simulation and accuracy might be lost.

Some of the available programs that use these techniques are: PENELOPE [Salvat et al., 2006], EGS4 [Kawrakow and Rogers, 2000, Kawrakow et al., 2014] and VMC [Kawrakow et al., 1996].

2.2.5.2 Condensed histories

Another optimization technique of the MC simulations is the use of condensed histories [Berger et al., 1963, Kawrakow and Bielajew, 1998]. It consists of replacing the calculation of a certain number of interactions (several thousands) by a single interaction whose effect will be the sum of all replaced particle effects.

A typical fast electron slowing down inside a medium undergoes of the order of 10^5-10^6 collisions with surrounding matter, causing in most interactions only minor changes in the particle's energy and direction of flight. This large number of interactions makes very difficult to track every electron individually, and the computation time of doing this is very high. To circumvent this difficulty, Berger [Berger et al., 1963] developed the condensed history technique. In this method, large numbers of transport and collision processes are condensed to a single electron step. The cumulative effect of the individual interactions is taken into account by the appropriate change of the particles energy and direction of motion at the end of the step.

This approximation has a limitation. In multiple dispersion theories, it is assumed that particles move in heterogeneous media and the distance they travel is bigger than their main free path. As

a result, condensed history approximation can lead to artifacts in areas next to interfaces and, in general, in any object with a comparable size to the mean free path of the particles. Another limitation of the condensed simulation is that this approximation cannot take into account the catastrophic effects (ie. individual interactions that significantly modify the energy or direction of the particles). To solve these limitations a mixed model can be implemented. In this model, condensed histories simulations are used to reproduce the soft interactions where the energy or direction of the particles do not exceed an user-defined threshold, and the rest of the simulations are calculated in detail (known as hard interactions) [Berger et al., 1963].

2.2.5.3 Variance reduction techniques

The variance reduction techniques may be used to make calculations more efficient. In some cases, these techniques require that no further approximations must be made to the transport physics. In other cases, the gains in computing speed come at the cost of computing results that may be less accurate since approximations are introduced [Bielajew, 2001].

Lets introduce the most used variance reduction techniques.

The **interaction forcing technique** takes advantage of the fact that, usually, a high variance comes from a low interaction rate. This is specially significant for photons, where efficiency may be lost because photons leave the geometry of the simulation without interacting and time is spent tracking photons through a geometry that do not contribute to the score. This technique forces photons to interact within the geometry of interest. These photons will then be weighted by the probability that the photon would have had of interacting before leaving the geometry of the simulation.

The **particle splitting** technique is used in situations where interest is focused on a particular volume inside the geometry. To increase interaction statistics within that area, a splitting technique can be used. It divides the particles with weight ω into a N smaller ones each with a new weight, $\omega' = \omega/N$.

Another technique is used when particle weights become very small. If this happens and the photon is headed away from the region of interest it can be used the **russian roulette** technique. It selects a random number. If this random number lies above a threshold α, the photon is discarded without scoring any quantity of interest. If the random number turns out to be below α the photon survives but with a new weight, $\omega' = \omega/\alpha$.

All these techniques distort the simulation results because they modify the probability distribution functions of the involved interactions. In order to minimize the alteration, parameters involved in these techniques must be chosen carefully.

Now, we will describe a technique that accelerate the simulation without modifying the quality of the results.

2.2.5.4 Pre-calculation of the source. Phase Space files

When a MC simulation of a treatment planning needs to be done, we need to simulate the detailed geometry of the accelerator. But if in each treatment planning the simulation is performed by starting the electrons at the beginning of the accelerator head, we will need a very long simulation to achieve a dose distribution with low variance.

This is because the particles, before entering the medium, go though a serial of materials, such as collimators, flattening filters, etc., as seen in Chapter 1. Most particles will interact in the accelerator head, being absorbed or generating secondary particles, and following their tracks will slow down considerably the simulation, even though these interactions are not directly contributing to the dose. But these elements, responsible of beam modification, are usually fixed to the accelerator head and used in all treatments. By taking advantage of this property, some codes have developed a strategy that consist of saving the information of the particles in a file at a certain point, usually at the end of the collimation system. With this, a full simulation of each accelerator head can be done once, and the information of the particles coming out the accelerator is recorded. Next time a simulation of that accelerator is required, instead of generating again the detailed geometry of all the components of the accelerator, all the beam information coming out of the accelerator can be read from the stored file.

This file is known as **Phase Space file**. It contains all the information needed to characterize the beam. This information includes type of particle, energy, position and direction of the particles, among other properties particular of each code.

2.3 Main Monte Carlo codes in radiotherapy

ETRAN (Electron TRANsport): First MC code designed for electrons and photons transport through simple geometries [Seltzer, 1991]. Its energy range is 1 keV-100 GeV.

EGS (Electron Gamma Shower): The actual version is called EGSnrc [Kawrakow and Rogers, 2000, Kawrakow et al., 2014]. It is a code that simulates photon, electron and positron transport considering only electromagnetic interactions, with energies from 1 keV to 10 GeV. The geometry can be built with a code called BEAMnrc [Rogers et al., 1995] that incorporates specific modules designed for medical physics. It has been widely validated, as it is one of the most used MC codes in medical physics. It is not an open code and may require that the user develops part of the code in MORTRAN language to define complex geometries.

FLUKA (FLUktuierendeKAskade): It is a code that reproduces the propagation in matter for up to 60 different particles, including electrons and photons (from 1 keV to 1000 TeV), hadrons (up to 20 TeV), neutrons and heavy ions [Ferrari et al., 2005]. It allows to reproduce complex geometries. Its main code is written in FORTRAN77.

GEANT4 (Geometry ANd Tracking): It is a code that simulates the transport of all kind of particles inside an energy range between 250 eV and 10 TeV [Agostinelli et al., 2003]. It is very powerful regarding the construction of complex geometries and can be used for a wide spectrum of applications: from high energy physics to medical physics. Part of the code must be developed by the user in C++ language. Its code is open source.

MCNP (Monte Carlo N-Particle): It is a code that simulates the transport of neutrons, photons and electrons. Because its wide validation, it is considered the most reliable MC code for neutron transport [Brown et al., 2002]. It is necessary a payment registration to use it.

MCNPX (Monte Carlo N-ParticleeXtended): It extends the application of the MCNP4C3 code to almost all kind of particles in a wide energy range. The source code, written in FORTRAN90, is only available by a previous agreement with the developers.

PENELOPE (PENetration and EnergyLOss of Positrons and Electrons): It is an open source code to simulate electrons, photons and positrons transport, in an energy range between 50 eV and 1 GeV [Salvat et al., 2006]. Its main application field is medical physics. Most of the calculations done in this thesis are based in this code, so further description of PENELOPE can be found in the next section.

2.4 PENELOPE

PENELOPE (PENetration and EnergyLOss of Positrons and Electrons) [Baro et al., 1995, Salvat et al., 1996, 2006, Sempau et al., 1997, 2003] is a Monte Carlo code of general purpose that simulates the transport of electrons, photons and positrons within an energy range from 50 eV to 1 GeV. It is formed by a package of subroutines written in FORTRAN77. It is an open source code developed by the Universitat Politècnica de Catalunya (UPC) and distributed by the Nuclear Energy Agency (NEA).

The main features of PENELOPE are the accurate description of particle transport through interfaces and the low-energy particles transport. It simulates with detail the transport of photons and applies a mixed-scheme for electron and positron transport.

The mechanisms responsible for particle transport are controlled by some user defined parameters. Elastic interactions are controlled by the parameters C_1 and C_2:

- C_1 defines the average angular deflection produced by multiple elastic scattering through the mean free path between consecutive elastic events.
- C_2 sets an upper bound for the average fractional energy loss between consecutive elastic events.

To ensure precision in the simulation, C_1 and C_2 must have small values. For both parameters, 0.05 is recommended and the maximum recommended value would be 0.2. Beyond this point, the simulation will be quicker but precision will decrease.

User can also define two parameters related to the energy values that delimit the distinction between hard and soft interactions:

- W_{CC}: Cutoff energy value (in eV) for hard inelastic collisions.
- W_{CR}: Cutoff energy value (in eV) for bremsstrahlung emissions.

Therefore, electron collisions whose energy loss is below W_{CC} and inelastic radiative interactions with energy loss below W_{CR} are considered soft interactions and treated as condensed histories. The step length parameter for these soft interactions can also be controlled externally with the s_{max} parameter.

W_{CC} and W_{CR} cutoff energies will affect the simulated energy distribution. If big values are used, the simulation time is reduced but energy distribution will be distorted. In real practice, energy distributions will not vary for different W_{CC} and W_{CR} values as long as these numbers are below the increment of energy used for energy distribution. Therefore, the desired energy resolution will determine the maximum value of these cutoff energy values.

PENELOPE code is formed by a set of FORTRAN 77 subroutines which are invoked from a main program. The main codes included in PENELOPE are the following:

- **penelope.f**: Block of subprograms with the coupled electron-photon transport.

- **material.f**: Program which extracts atomic interaction data from the database and creates the files with the physical information about each material.

- **pengeom.f**: Code that contains the geometry package. Any geometry is built from homogeneous bodies limited by quadric surfaces.

- **penvared.f**: Program that allows users to employ variance reduction techniques.

PENELOPE also includes other programs:

- GVIEW: Program used for displaying two- and three-dimensional images of the geometry.

- SHOWER: Program used to visualize particle tracks.
- EMFIELDS: Block of subroutines to simulate particle transport in static electromagnetic fields.
- TABLES: Program to generate tables with the physical data of radiation transport.

2.5 PenEasy

PenEasy [Sempau et al., 2011, Badal Soler et al., 2008] is a modular, general-purpose main program for PENELOPE that includes various source models and tallies. The goal of developing this program was to provide a tool suitable for a wide spectrum of problems so that users would not need to develop a specific code for each new application.

PenEasy is free and open software, and the source code is mostly written in FORTRAN77.

The code is structured in an initialization phase followed by three nested loops and the reporting of results. The skeleton of the main program is shown in figure 2.1. Uppercase names denote routines from PENELOPE, whereas lowercase subroutines are provided with the penEasy package.

```
call init; n=0                        ! Initialisation
history: do                           ! One history
  n = n+1                             ! Update history counter
  call CLEANS                         ! Clear stack
  call source                         ! Create primary particle
  particle: do                        ! One particle
    call SECPAR(left)                 ! Retrieve particle from stack
    if (left.eq.0) exit particle      ! Stack was empty
    call START                        ! Reset transport mechanics
    interact: do                      ! One interaction/intersection
      call JUMP(dsmax(mat),ds)        ! Distance to interaction
      call STEP(ds,dsef,ncross)       ! Geometry check
      if (ncross.ne.0) then           ! Interface crossed
        if (mat.eq.0) exit interact   ! Particle is gone
        call START                    ! Reset transport mechanics
        cycle interact                ! Start over
      endif
      call KNOCK(de,icol)             ! Simulate an interaction
      if (e.lt.eabs(kpar,mat)) exit interact   ! Absorbed
    enddo interact
  enddo particle
  if (endsim(n)) exit history         ! Check end-of-simulation
enddo history
call report
```

Figure 2.1: Basic structure of the FORTRAN version of the main program of penEasy. Calls to tallying and other auxiliary subroutines have been removed for clarity [Badal Soler et al., 2008].

The main cycles are: **history**, **particle** and **interaction**. Each cycle of the loop named *history* performs the simulation of one primary particle and all its descendants. Inside the cycle history

there is the loop *particle* that simulates a single photon, electron or positron. Finally, inside this loop we can find the cycle of *interact* that reproduces a single interaction, or the crossing of an interface if the distance to the intersection is shorter than the distance to the next interaction. For calculating these interactions, inside this final loop we find an algorithm that essentially consists of repeating the sequence of calls to subroutines JUMP, STEP and KNOCK: JUMP computes the distance to the next interaction event, returned through the variable *ds*; STEP determines if an interface is crossed before completing the step *ds* and displaces the particle; and KNOCK simulates the effect of the interaction and returns the energy lost by the particle. If an interface is crossed (*ncross* not zero) the trajectory is truncated at the boundary, no interaction takes place and a new "interact" cycle begins. The simulation of a particle ends when it leaves the material system (*mat* is zero), or when its kinetic energy (e) falls below some user-defined absorption energy (*eabs*), which may depend on the material and particle type.

PenEasy allows the use of quadric geometry (by invoking subroutines from PENELOPE's standard geometry package PENGEOM), voxelized geometry and a superposition of quadric objects and voxelized regions (with the package penVOX).

2.5.1 Source models

PenEasy includes two types of source models [Sempau et al., 2011, Badal Soler et al., 2008]. Their configuration parameters are set by the user through a global input file. Only one source can be active in any given simulation.

The source called **BIGS** (Box Isotropic Gauss Spectrum) allows the definition of volumetric sources limited by quadric surfaces. The type of particle can be either a photon, electron or positron with an arbitrary energy spectrum of emission or, alternatively, with the spectrum defined by means of a Gaussian function.

The source called **PSF** (Phase-Space File) reads the initial state of the particles from an external file. Usually, this file is created by penEasy in a previous simulation with the PSF tally. As explained in section 2.2.5.4, the phase space file contains information to identify all particles, either primary or secondary, belonging to the same history (i.e., descendants of the same primary particle).

2.5.2 Tallies

PenEasy includes subroutines to score the most common quantities of interest. The tallies available are listed below.

- Section Tally Spatial Dose Distrib: Calculates absorbed dose per history scored in parallelepiped bins.
- Section Tally Cylindrical Dose Distrib: Calculates absorbed dose per history in cylindrical shells.
- Section Tally Spherical Dose Distrib: Calculates absorbed dose per history in spherical shells.
- Section Tally Voxel Dose: Calculates absorbed dose when voxelized geometries are used.
- Section Tally Energy Deposition Pulse Spectrum: Determines the total deposited energy in the detection material per simulated history.
- Section Tally Fluence Track Length: Calculates the fluence spectrum per simulated history in the detection material.
- Section Tally Phase Space File: Stores the phase space file in the detection material.
- Section Tally Particle Current Spectrum: Determines energy spectra and total number of particles of each type entering a certain material.
- Section Tally Particle Track Structure: Allows the 3D representation of the particle tracks.

2.6 DPM

DPM (Dose Planning Method) [Sempau et al., 2000] is a MC code that share some of the PENELOPE characteristics and allows the simulation of the dose deposited by electron–photon showers under radiotherapy conditions in a fraction time of a regular MC calculation, such as penEasy. It can be used as an alternative to the analytical algorithms for treatment planning, as it gives an accurate dose in a very short time.

DPM employs the condensed history model for electron transport, and uses a mixed scheme for the treatment of energy losses, treating large energy transfer collisions with a simplified model and using the continuous slowing down approximation (CSDA) to model small-loss collisions.

The gain in performance time derives from a series of enhancements done to the algorithm [Sempau et al., 2000]:

- Employment and refinement of a new step size independent multiple-scattering theory.
- Use of new transport mechanics. DPM has adopted the 'random hinge' scheme employed in PENELOPE.
- Use of large electron transport steps, in which many voxels may be traversed before sampling a multiple scattering angle.
- DPM exploits the small dynamic range (in energy and material) of radiotherapy class problems. Energies are limited to those between 100 keV and 20 MeV, and cross sections and distribution functions are determined by scaling them appropriately to computed data in water.

DPM is formed by four main programs:

- **material.f**: Extracts from PENELOPE library the physical data of the materials.
- **predpm.f**: Program that allows the pre-calculation of cross sections and other calculations that DPM will use.
- **genvoxel.f**: Geometry program. The user can create a voxelized geometry or read a CT image.
- **dpm.f**: Program that performs the MC simulation, considering the previously calculated data from predpm.f

2.6.1 Source model

DPM generates the primary particles in the subroutine 'source'. In the original code, this routine generates unidirectional and monoenergetic electrons or photons that impact in a phantom. The source is centered in x=y=0 and its size can be defined in the configuration files.

However, DPM allows the user to write his own 'source' subroutine. In any case, the final result of this subroutine is to assign the particles the following variables:

- Kinetic energy of the particle in eV.
- Unit direction vectors {vx,xy,vz}
- Position coordinates of the particle in cm.
- Particle type.

In this work the 'source' subroutine has been modified to read the initial particle state from a phase space file.

2.6.2 Tallies

Subroutine 'report' scores the deposited dose inside the region of interest defined in the configuration files. This dose is written in an ASCII file, but the subroutine has been modified to include also a binary file.

Chapter 3

Detailed simulations of IORT systems

3.1 Introduction

Monte Carlo (MC) simulations are considered to be the most accurate methods for radiotherapy dose calculations in homogeneous and heterogeneous geometries [Rogers et al., 1995, Rogers, 2006, Ma and Jiang, 1999, Siebers et al., 2000, McDermott et al., 2003], since all the relevant effects, such as material inhomogeneities, back-scatter and beam hardening can be modeled with reasonable accuracy. While MC methods are computationally demanding, the development of a few accelerated MC codes, such as DPM [Sempau et al., 2000], makes them more practical in clinical settings.

MC dosimetry requires a realistic and reliable description of the electron and/or photon beams employed in the radiotherapy procedure [Chetty et al., 2007]. A phase space (PHSP) file containing the information of energy, angular and spatial distributions of the particles coming from the electron or photon beam, has to be fed into the MC algorithm. A common approach to build these PHSP files consists of carrying out realistic simulations of the accelerator head and other elements involved in the radiotherapy procedure such as applicators and collimators [Ma and Jiang, 1999, Capote et al., 2006, Faddegon et al., 1998].

Detailed MC modeling of IOERT accelerators and Intrabeam® devices has been widely reported [Ma and Jiang, 1999, Hogstrom and Almond, 2006, Janssen et al., 2008, Bush et al., 2008, Clausen et al., 2012, Nwankwo et al., 2013, Verhaegen et al., 1999, Yanch and Harte, 1996] and good results have been obtained with this method.

In this chapter we have simulated the most relevant dedicated accelerators employed in IOERT treatments (ie. NOVAC®, LIAC® and MOBETRON®) with their corresponding applicators, and Intrabeam® needle, spherical, surface and flat applicators. In most cases, the different components of the devices have been extracted from literature, in other cases, such as for flat and surface Intrabeam® applicators, the geometry details have been provided by the vendor. These simulations will represent a reference accelerator or applicator, and will be used to create a database that will be employed to generate a PHSP file tuned to each user machine in a dose treatment planning procedure explained in the following chapter.

From these simulations we will be interested especially in reproducing the shape of the experimental transverse dose profiles from the different machines. Our optimization procedure will only tune the depth dose profile (DDP) to the experimental data, so having the characterization of the off-axis profiles will be essential for an accurate dose distribution at the end of the procedure.

3.2 Intrabeam® applicators

3.2.1 MC characterization of Intrabeam® X-ray source

The Intrabeam® X-ray source (XRS) has been described in several works [Dinsmore et al., 1996, Beatty et al., 1996, Yanch and Harte, 1996, Clausen et al., 2012].

In the Intrabeam® system X-rays are generated by a 50 keV electron beam that travels through an evacuated tube (9 cm length and 3.2 mm diameter) and hits a 0.5 μm thick gold target at the end of the tube [Yanch and Harte, 1996]. The most distal 1.6 cm of the tube consists of beryllium. To make the XRS biocompatible, the target tube is coated on their outer surface with a nickel film and a titanium nitrite (TiN) layer [Dinsmore et al., 1996]. This construction yields an isotropic dose distribution with a maximal variation of 15% in all directions [Yanch and Harte, 1996].

In this thesis we have performed a detailed simulation of the XRS of the Intrabeam® with penEasy [Sempau et al., 2011, Badal Soler et al., 2008]. The objective was to test the accuracy of the penEasy code for kilo-voltage energies and to fix the shape of the energy spectrum. An experimental spectrum of the XRS [Schneider et al., 2010] was used to compare and adjust the simulation to the experiment.

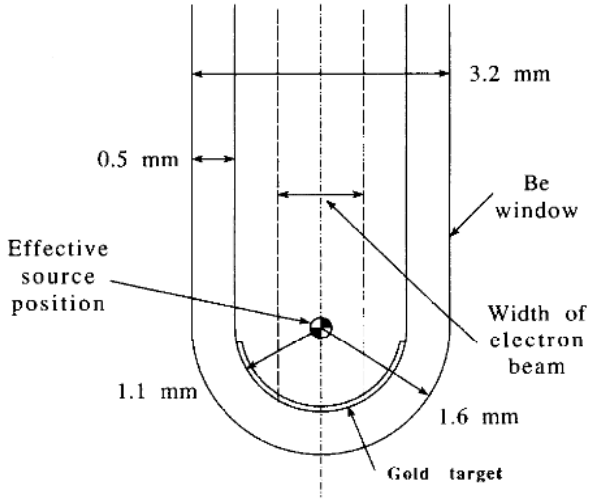

Figure 3.1: Cross section through the beryllium window of the INTRABEAM X-ray source (XRS) with the gold target [Beatty et al., 1996].

The geometry of the XRS was generated to fit the experimental measurements of the spectrum. It is shown in figure 3.2. It was defined as:

1. A 1.6 cm length beryllium needle with 1.1 mm inner radius and thickness of 0.5 mm.
2. A 0.5 μm layer of gold at the end of the probe.
3. A 5 μm layer of nickel surrounding the beryllium needle.
4. A 10 μm layer of TiN surrounding the nickel.
5. PHSP plane surrounding all the structure.

Regarding the electron source impinging on the gold target, it was characterized with a Gaussian energy distribution with a mean energy of 50 keV and a full width at half maximum (FWHM) of 5 keV. The source was located 1.6 cm above the gold target. Concerning the spatial distribution of the source, it was defined as a circular foil of 0.1 mm diameter with a Gaussian distribution centered at zero and a FWHM of 0.01 mm. The electron beam does not impact in all the target surface, but in a annular area between 0.6 and 0.8 mm radii [Clausen et al., 2012].

The dose was scored at the exit of the probe surface with $4{\cdot}10^{10}$ initial particles in order to accumulate more than 200 millions particles in the scoring plane and to fulfill good statistics and reduce statistical uncertainty of the simulation to around 2%. The voxel size employed in the simulation was 0.25 mm. This calculation was split up into 200 simulations running in parallel for around 12 hours in a high capacity cluster.

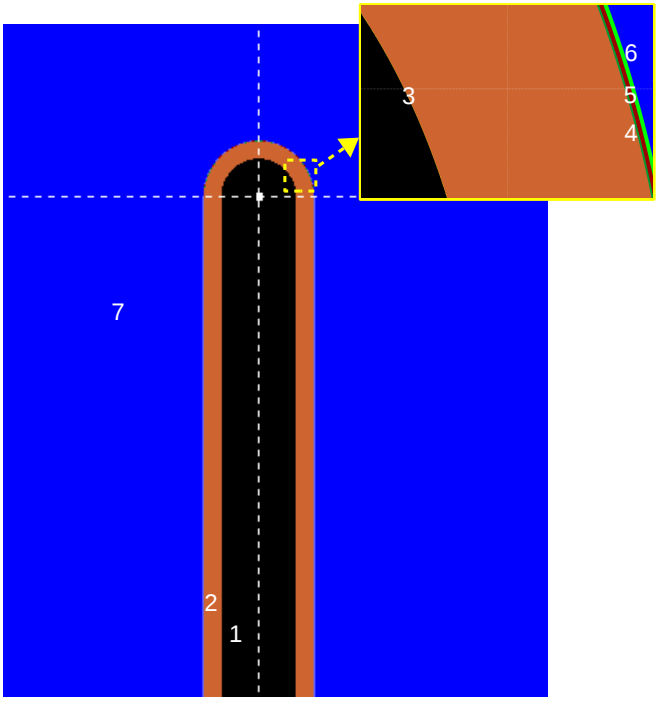

Figure 3.2: Geometry of the simulated Intrabeam® X-ray source visualized with the gview2d package from PENELOPE and a inset with a zoom of the target. The numeration corresponds to: 1. Vacuum inside the needle. 2. Beryllium. 3. Gold target. 4. Layer of nickel. 5. Layer of TiN. 6. PHSP plane definition. 7. Water phantom.

A comparison of the simulated and experimental energy spectra is shown in figure 3.3, and the classification of the characteristic X-rays peaks is detailed in table 3.1. Both energy spectra are very similar, although some differences can be seen in the characteristic X-rays peaks, mostly at low energies, where the lowest energy peak (4.41 keV), corresponding to the Ti characteristic X-rays is only seen in the simulation, and the second peak (7.54 keV), matching the Ni transitions, presents a higher intensity in the simulation than in the experiment. However, the most intense peaks, corresponding to the Au lines (9.54, 11.53 and 13.240 keV), present almost the same intensity as the experiment. In the case of the 4.41 keV line, the characteristic X-rays present such a small energy that is probably too low to be measured experimentally. In the case of the second peak at 7.54 keV, the difference can be either explained by the limited efficiency of the detector at measuring X-rays of such small energy or by a slight difference in the thickness of the Ni layer. Nevertheless, the differences that appear in these X-rays will not be reflected in the dose, as such low energetic X-rays are absorbed within the first micrometers in the tissue.

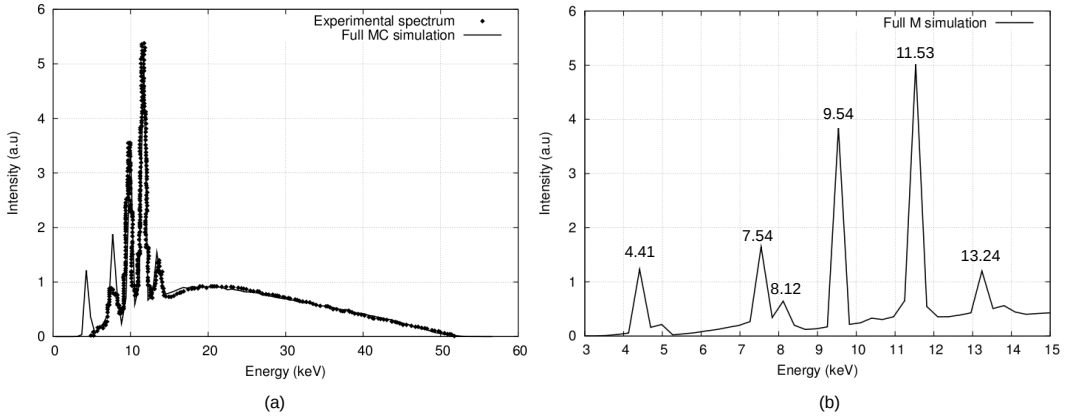

Figure 3.3: (a) Energy spectra obtained experimentally [Schneider et al., 2009b] and with the detailed simulation for the XRS. (b) An expanded view of the line-radiation region of (a).

Energy (keV)	Transition
4.41	L_2-K and L_3-K in Ti
7.54	L_2-K and L_3-K in Ni
8.12	<M>-K in Ni
9.54	<M>-L_3 in Au
11.53	<M>-L_2 in Au
13.24	<N>-L_2 in Au

Table 3.1: Classification of the characteristic X-rays present in the XRS energy spectrum.

Figure 3.4 shows the resulting 2D dose distribution for the XRS and the isodose lines at 40%, 20%, 10% and 5% of the maximum dose. Slight anisotropy in the backward direction of the dose can be been. This result agrees with previous studies [Dinsmore et al., 1996, Beatty et al., 1996], where was observed that there was an increase along the probe in the backward direction, consistent with the escaping photons through beryllium.

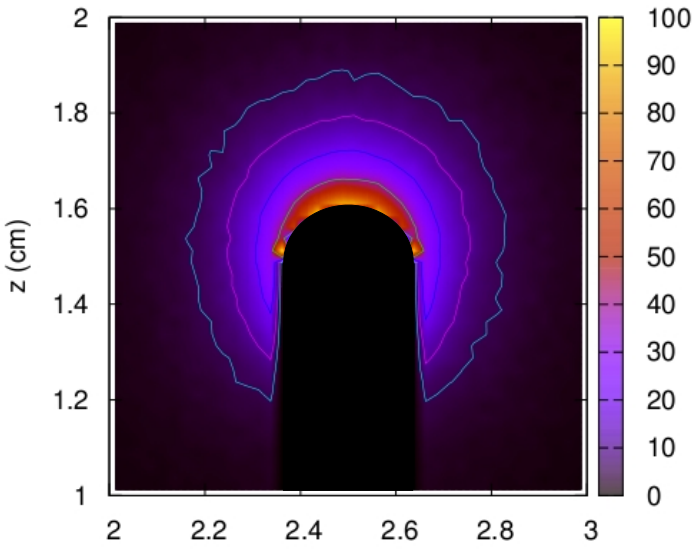

Figure 3.4: 2D dose distribution for the simulated XRS with isodose lines at 40%, 20%, 10% and 5% of the maximum dose.

3.2.2 MC characterization of Intrabeam® Spherical applicators

The spherical applicators are made of a polyether imide (PEI) material [Xiao et al., 2015], and can be classified into two groups according to the inner structure: the interior wall of the probe is embedded with a thin metal sheath for the applicators with diameter ≤ 3 cm whereas no metal sheath is included in those with diameter > 3 cm, as shown in figure 3.5 [Eaton and Duck, 2010, Xiao et al., 2015].

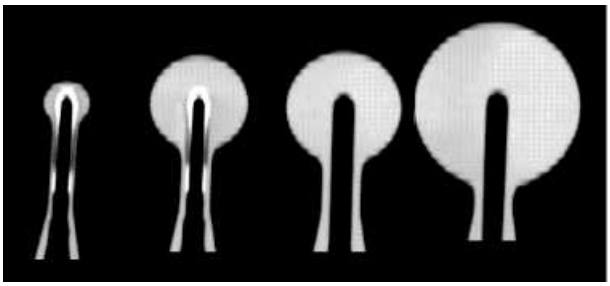

Figure 3.5: Computed tomography image showing the cross-section of 1.5 cm, 3.0 cm, 3.5 cm and 5.0 cm diameter applicator [Eaton and Duck, 2010].

In the case of spherical applicators, two different sets of applicators were designed: one set for diameters ≤ 3 cm, including the metal sheath, and another one for diameters > 3 cm, without it. The PEI material was defined with the ***material.f*** code from PENELOPE [Salvat et al.,

1996] and used to generate all spherical applicators.

Instead of generating the complete geometry including the probe surrounded by the spherical applicators, the PHSP file obtained from the simulation of the previous section was employed to substitute the simulation of the XRS.

A solid sphere and a cylinder of PEI were defined with penEasy surrounding an air cylinder and semi-sphere designed for the location of the needle. For the smaller applicators, an aluminum layer was set between the needle and the applicator. An example of both geometries can be seen in figure 3.6. In order to obtain dose distributions with enough statistics, each applicator was simulated during 24 hours in parallel in 200 different cores in a high capacity cluster.

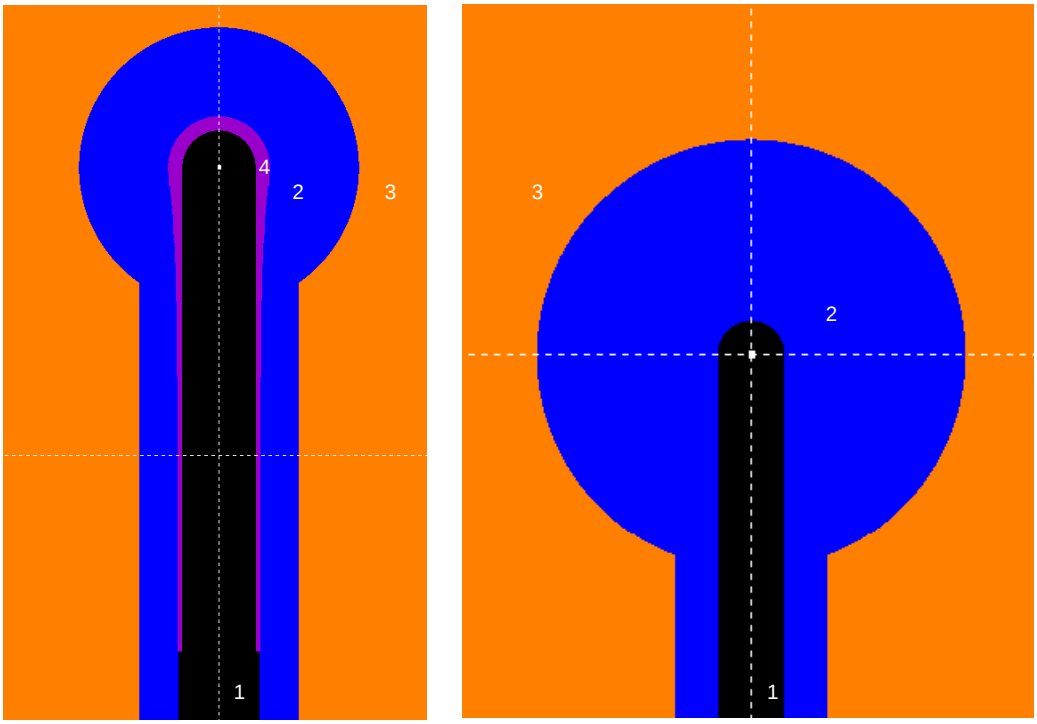

Figure 3.6: Geometries employed in the simulation for the two different set of applicators. Left: 1.5 cm diameter spherical applicator. Right: 3.5 cm diameter spherical applicator. The numeration corresponds to: 1. Air inside the applicator were the XRS is located. 2. Applicator walls made of PEI. 3. Water. 4. Aluminum layer for the $\leq$ 3 cm diameter applicators.

For the 1.75 cm radius spherical applicator, we could compare the energy spectrum and the depth dose profile obtained from the simulation with experimental data, and a good agreement was reached, as shown in Figure 3.7. For the other spherical applicators the obtained energy spectra are similar to the energy spectrum of the 1.75 cm radius spherical applicator, and have a reasonable shape with a bremsstrahlung background and characteristic rays located at the same

energies.

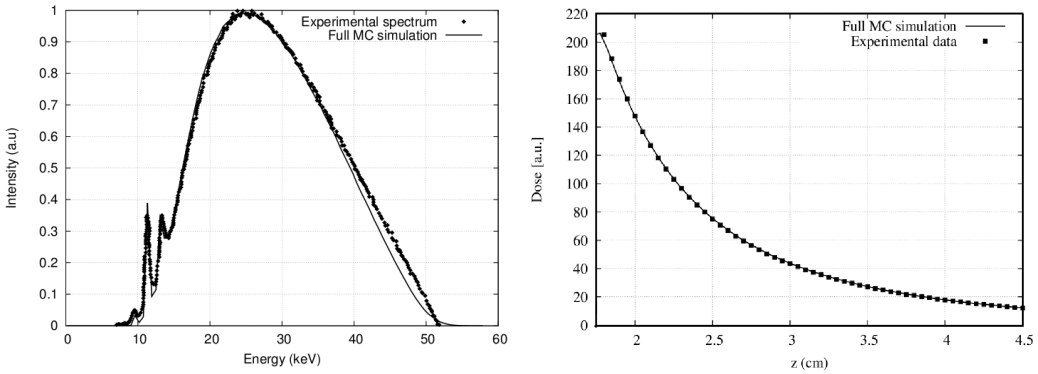

Figure 3.7: Left: Energy spectra obtained experimentally [Schneider et al., 2010] and with the detailed simulation for the 1.75 cm radius applicator. Right: Depth dose curves obtained experimentally [Schneider et al., 2010] and with the detailed simulation for the 1.75 radius applicator.

Two examples of the 2D dose distributions obtained with the detailed simulations for a 1.5 cm diameter applicator and a 4.0 cm diameter applicator against measurements are shown in figures 3.8 and 3.9, respectively.

The experimental 2D dose distributions of the detailed spherical applicators present a small anisotropy in the backward direction. This anisotropy was reproduced in the detailed simulations by displacing the PHSP file that replaces the XRS around 2 mm from the geometrical center of the applicator. This would correspond to leaving a 2 mm extra space in the hole inside the applicator to guarantee the protection of the XRS against the applicator walls when inserting it.

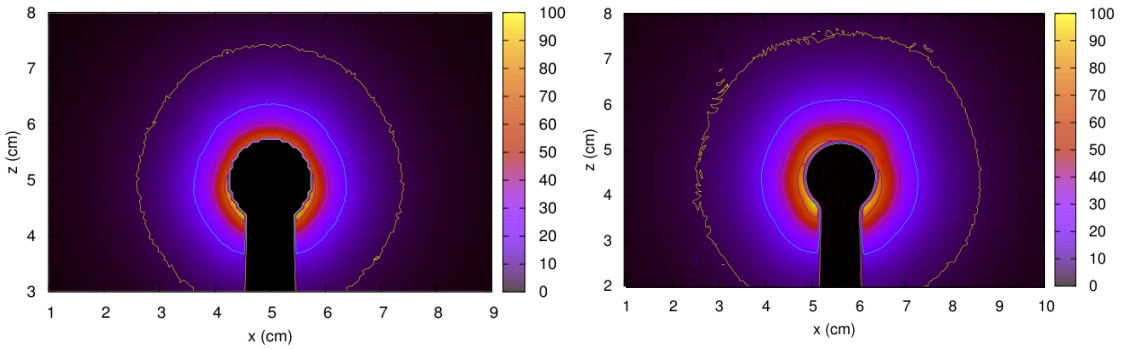

Figure 3.8: 2D dose distribution obtained with penEasy (Left) and with a radiochromic film (Right) for a 1.5 cm diameter applicator with isodose lines at 90%, 70%, 40%, 20% and 5%.

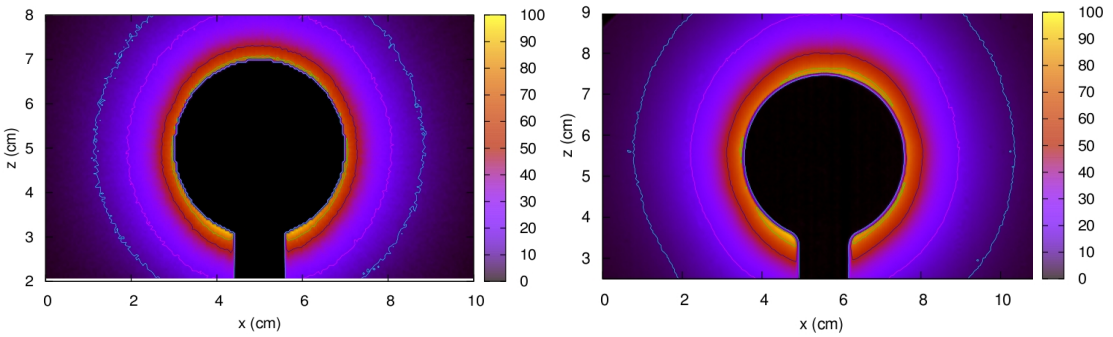

Figure 3.9: 2D dose distribution obtained with penEasy (Left) and with a radiochromic film (Right) for a 4.0 cm diameter applicator with isodose lines at 90%, 70%, 40%, 20% and 10% of the maximum dose.

3.2.2.1 Approximation for Intrabeam® needle and spherical applicators

In the previous section we have simulated in detail the spherical applicators, reaching a good agreement with the experimental measurements. However, these detailed simulations required a very high resource usage to do the calculations, as each applicator needed to run over 24 hours in parallel in a high capacity cluster in 200 different cores to obtain a dose distribution with enough statistics. If only one CPU had been used, the simulation of each applicator would have run for about 7 months to achieve good enough statistics.

Consequently, for this work we have used a simplified version of the spherical and needle applicators. We have considered a photon source emitting isotropically in a vacuum sphere with the radius of the real applicator. This way the simulation time needed to obtain a good dose distribution is reduced up to several hours.

This approach may introduce some changes in the energy deposition distribution in depth. However, these differences will be absorbed afterwards during the fitting procedure explained in the following chapter.

Regarding the anisotropy of the experimental measurements, it will not be reproduced with this approximation. Nevertheless, the area where the anisotropy is presented has not clinical interest, as it is behind the applicator, and we will take it into consideration in future works.

3.2.3 Simulation of Intrabeam® flat and surface applicators

For flat and surface applicators characterization, the vendor provided the information of the geometry, and therefore, the details are protected and can not be described in this work. Both

types of applicators have a lead casing with a filter made of PEI inside. The main difference between flat and surface applicators lies in the shape of the filter inside each applicator. A schematic geometry of these applicators is show in figure 3.10.

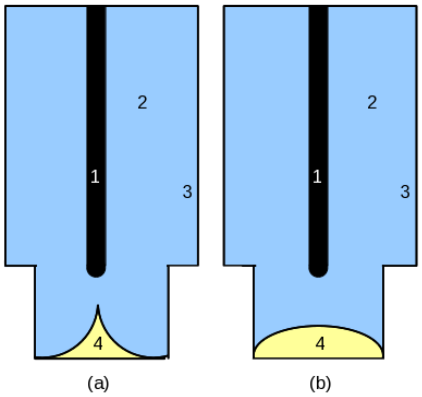

Figure 3.10: Schematic geometry for the (a) Flat applicators and (b) Surface applicators. The numbering represents 1. XRS, 2. Air inside the applicator, 3. Lead walls, 4. PEI filter.

The photon beam was generated as a punctual source of 1 mm width with a spatial FWHM of 0.01 mm. The energy distribution employed in the simulations corresponded to the energy spectrum obtained in the XRS characterization, with a FWHM of 1 keV. The position of the source inside the filter was provided by the vendors and the angular aperture of the beam was determined to cover the interior of the applicator.

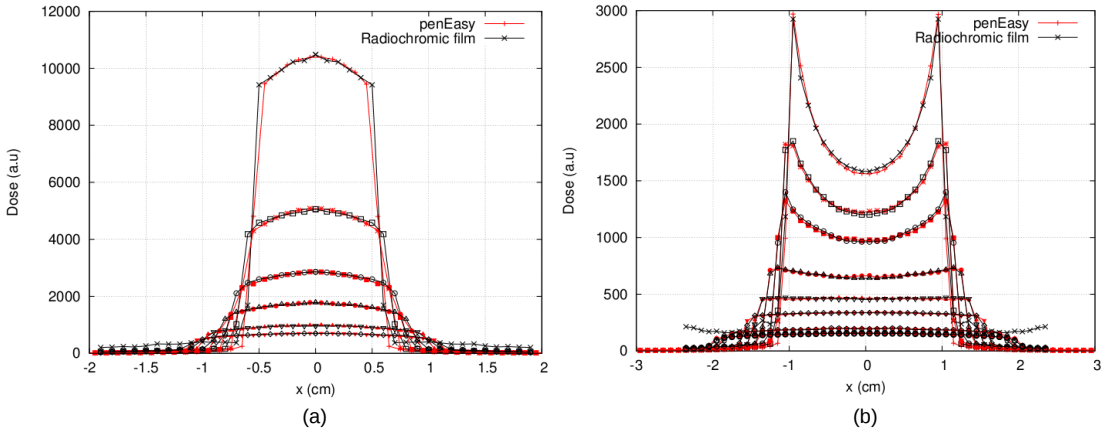

Figure 3.11: Experimental and simulated transverse dose profiles for (a) 1 cm surface applicator and (b) 2 cm flat applicator.

Some results can be seen in figure 3.11, where a comparison between measurements and simulated dose are shown for a 1 cm surface applicator and a 2 cm flat applicator. To perform these simulations, 10^9 histories were used.

3.3 Dedicated electron accelerators

In the case of the dedicated electron accelerators we did not have access to the vendor specifications. Some of the characteristics of the accelerator head and applicators have been extracted from the literature, and the unknown information has been obtained by comparing the simulations to the experimental measurements in water.

3.3.1 LIAC®

For the detailed simulation of the LIAC® (SORDINA, Italy), the available information about the geometry of the accelerator head and the beam characteristics was extracted from previous investigations [Iaccarino et al., 2011].

The different components of the geometry of the simulated accelerator are the following:

1. Titanium exit window of 55 μm.
2. Aluminum scattering foil with an 820 μm thickness.
3. PEEK™ cylindric primary collimator with two sections: The first section has an inner radius of 0.87 cm, outer radius of 2.13 cm and 2 cm length. The second section has an inner radius of 2 cm, outer radius of 3 cm and 6.5 cm length.
4. Mylar window with 0.1 mm thickness.
5. PMMA applicator with a length of 60 cm.
6. PHSP plane definition.
7. Water phantom.

The simulated geometry can be seen in figure 3.12. Simulations of each LIAC® applicator, from 4 to 10 cm diameter, were done. In all of them the accelerator head remained the same and the only change in the geometry was the diameter of the applicator.

Simulations were performed using 10^8 primary particles. The source was defined as a circular foil of 4 mm diameter with an angle of semi-aperture of 3° located 5 mm above the titanium exit window. Regarding the energy distribution, the source was characterized as a Gaussian distribution with FWHM of 0.1 MeV.

We also made a detailed study to see the impact of the air gap on patients dose distributions [García-Marcos et al., 2014]. Results showed that it may have an impact on dose distributions at the 3-4% level of the maximum dose, especially on the edge of the shallowest transverse dose profiles and we decided to include a 5 mm air gap, as it is the simulation that best describes the measured profiles.

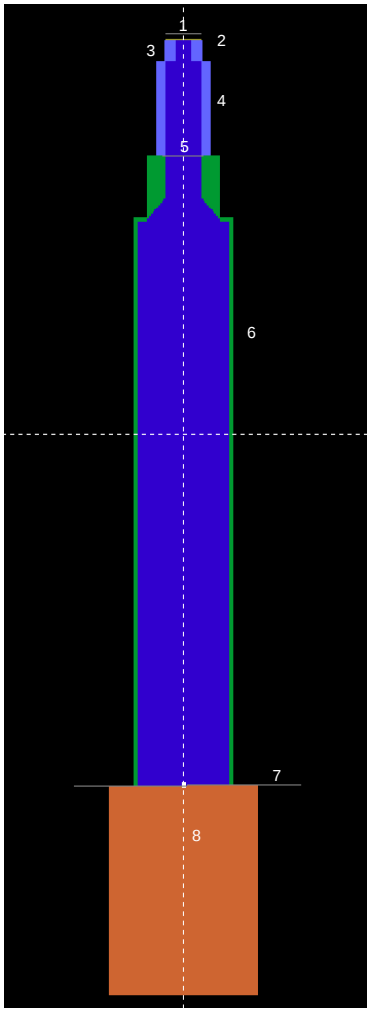

Figure 3.12: Geometry of the simulated LIAC®. The numeration, materials and dimensions correspond to the numbers shown in the description.

To validate the simulation and assure an accurate description of the accelerator, we compared the results of our simulation against transverse profiles measured in water at the Hospital Universitario Gregorio Marañón for energies of 6, 8, 10 and 12 MeV and the the different applicators. A comparison of transverse dose profiles is shown in figure 3.13.

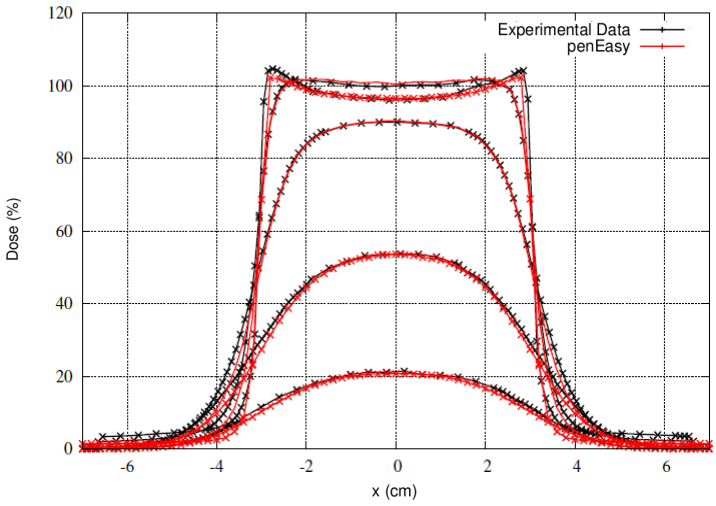

Figure 3.13: Transverse dose profiles in water for a 12 MeV LIAC®, 6 cm diameter applicator.

3.3.2 NOVAC®

For the NOVAC® simulation, information about the accelerator was obtained from previous works [Russo et al., 2012, Righi et al., 2013, Mihailescu et al., 2006]. The geometry is very similar to LIAC®'s, except for the absence of the scattering foil.

The different components of the geometry of the simulated accelerator are the following:

1. Titanium exit window of 60 μm.
2. A primary collimator made of brass and PVC.
3. PMMA applicator with thickness 0.5 cm and with different lengths depending on the applicator diameter. For the inner applicator diameters of 4, 6, 8 and 10 cm, the lengths are 69, 67, 67 and 87 cm, respectively [Mihailescu et al., 2006].
4. PHSP plane definition.
5. Water phantom.

The geometry of the accelerator can be seen in figure 3.14. Simulations of each NOVAC® applicator, from 4 to 10 cm diameter, were done. In all of them the accelerator head remained the same.

Simulations were performed using 10^8 primary particles. According to Russo *et al.* [Russo et al., 2012], the source was defined as a circular foil of 1 mm diameter with an angle of semi-aperture of 3° located 5 mm above the titanium exit window. Regarding the energy distribution, the source was characterized as a Gaussian distribution with FWHM of 0.1 MeV.

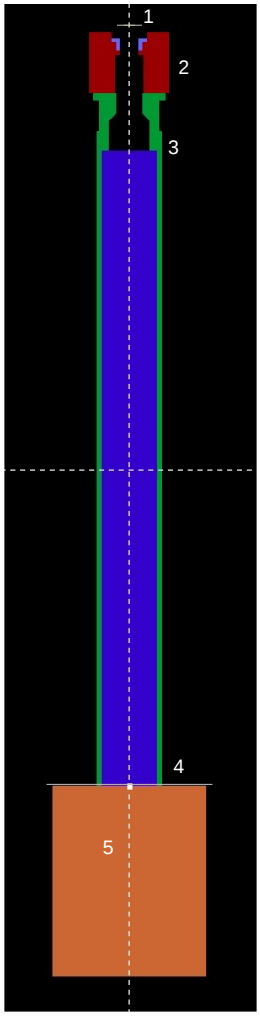

Figure 3.14: Geometry of the simulated NOVAC®. The numeration, materials and dimensions correspond to the numbers shown in the description.

Transverse dose profiles in water were measured in Düsseldorf and in Cefalu to validate the simulations. A comparison of the transverse dose distributions for a 10 MeV NOVAC® accelerator, 6 cm diameter applicator can be seen in figure 3.15.

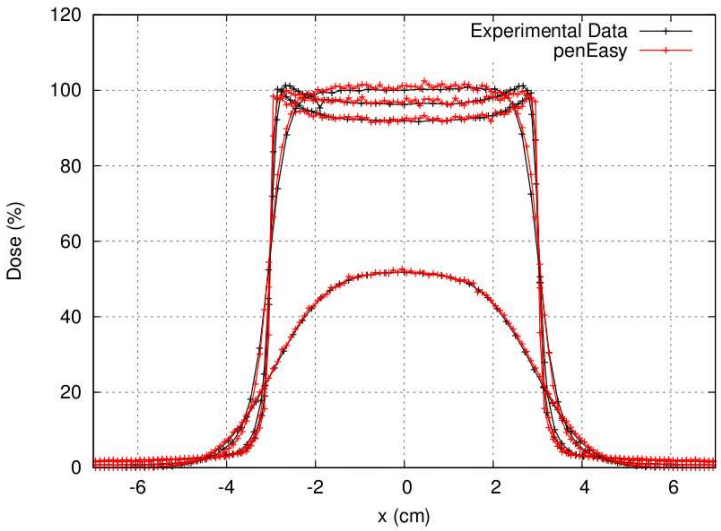

Figure 3.15: Transverse dose profiles in water for a 10 MeV NOVAC®, 6 cm diameter applicator.

3.3.3 MOBETRON®

MOBETRON® geometry has been extracted from different works [Janssen et al., 2008, Beddar, 2005, Beddar et al., 2006, Mills et al., 2001]. The main difference of this accelerator is the soft-docking system used for placing the applicators, so they are not fixed to the accelerator head.

The different elements of the accelerator's geometry are listed below:

1. Beryllium exit window of 1 mm.
2. Primary scattering foil made of tantalum with thickness 0.1 mm.
3. Secondary scattering foil made of aluminum with thickness 1 mm.
4. Primary collimator made of tungsten with two conical parts. These two parts are 5 cm long and are separated by 2 cm of air.
5. Stainless steel applicator with a thickness of 0.5 cm and with a length of 30 cm. Due to the soft-docking system, the applicator is detached from the accelerator head.
6. PHSP plane definition.
7. Water phantom.

The geometry of the simulated accelerator can be seen in figure 3.16.

The electron beam has been defined as a 3 mm diameter point source with an angle of aperture of 5°, spatial FWHM of 1 mm and a Gaussian energy distribution with FWHM of 0.1 MeV [Janssen et al., 2008]. The source-to-surface distance (SSD) is fixed to 547 mm.

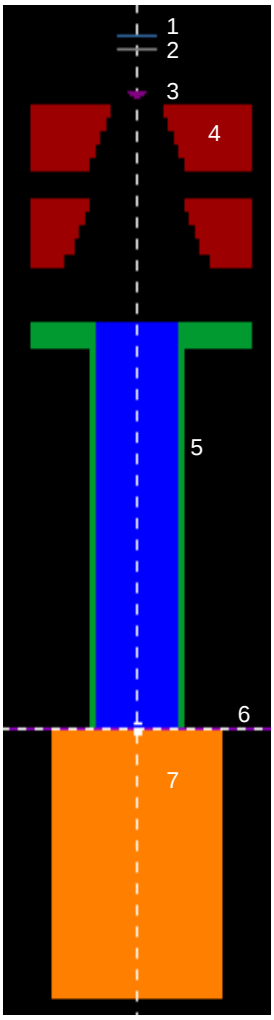

Figure 3.16: Geometry of the simulated MOBETRON®. The numeration, materials and dimensions correspond to the numbers shown in the description.

Simulations have been performed with 10^8 particles for all the accelerator working energies (6, 9 and 12 MeV) and applicators (ranging from 3 cm to 10 cm). Because of the soft-docking system, the behavior of the transverse dose profiles changes slightly with every applicator, so the geometries had to be re-adjusted for each case. Comparisons against experimental transverse profiles measured in Cuneo (Italy) have been done to assure the accuracy of the simulation. An example of these comparisons is shown in figure 3.17.

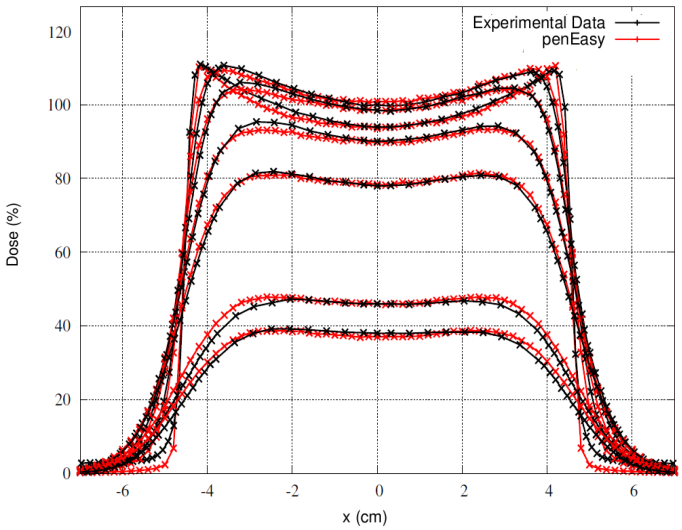

Figure 3.17: Transverse dose profiles in water for a 12 MeV MOBETRON®, 10 cm diameter applicator.

3.4 Phase Space parameterization

Since PHSP can be very heavy files and difficult to use, a simplification method was developed in order to reduce files sizes and to improve the flexibility while manipulating data, benefiting from the symmetry of the different applicators.

The huge amount of information contained in those files was parameterized and stored in bins. Each bin represents an elemental primary source and will have a fixed value of all the degrees of freedom relevant in our problem [Herranz et al., 2014]. The number of bins (up to two millions in the biggest PHSP file) of these parameterized PHSP files makes them easy to handle in a modern personal computer. Regarding the bin size, a trade-off between accuracy of the representation and number of requested bins was made.

We have performed three different kinds of PHSP files parameterization, depending on each geometry and its possible symmetries. Lets see all of them in detail.

3.4.1 Parameterization of PHSP files in the IOERT accelerators

For the parameterization of PHSP files in electron accelerators, the approach explained by Herranz *et al.* [Herranz et al., 2014] was followed.

Without loss of generality, it has been assumed that the PHSP file exiting a cylindrical applicator presents cylindrical symmetry. This assumption has been done considering that all the electron applicators studied in this project present a cylindrical shape. This hypothesis also requires that the bevel of the applicator must be equal to 0°. For those cases where a bevel of a certain angle is needed, which is a frequent situation in IOERT treatments, the PHSP plane is located at the point where the applicator looses its cylindrical symmetry (see figure 3.18), and the bevel is included as an additional piece that is simulated together with the phantom.

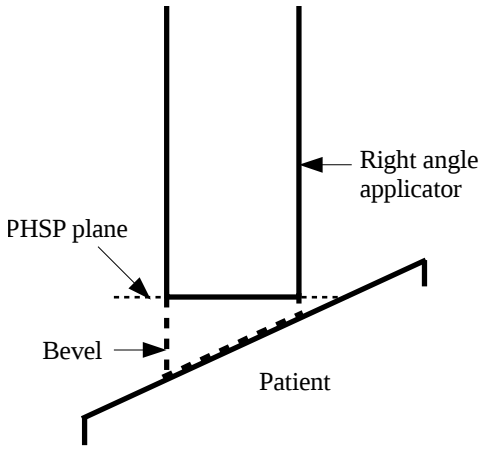

Figure 3.18: Schematic view of the PHSP plane at the exit of the right angle applicator showing the small piece of beveled applicator included in the simulation to compute the dose for non-right applicators [Herranz et al., 2014].

Exploiting the cylindrical symmetry mentioned, the PHSP is fully defined by the distribution of particles in energy *(E)*, distance to the applicator axis ρ, and two angles for the emission direction: θ, defined as the angle of the particle trajectory with the z axis, and ϕ, the azimuthal angle that forms the plane containing the trajectory and the z axis. We assume azimuthal symmetry around the applicator axis. In figure 3.19 the definition of these angles is shown.

This 4-dimensional representation was used to build a discretized finite set of up to a maximum of around 2.000.000 elementary sources or bins. Each bin represents a source with fixed values of energy, radial distance to the applicator axis and trajectory angles.

The following ranges and binning widths (BW) were considered for the definition of the elementary sources:

- Type of particle (electron, photon).
- Energy, ranging from 0 to 14 MeV (BW = 0.25 MeV).
- Axial angle θ, ranging from 0° to 29° (BW = 0.64°).
- Azimuthal angle ϕ, ranging from 0° to 180° (BW = 20°).
- Radial position ρ ranging from 0 to 10 cm (BW = 0.2 cm).

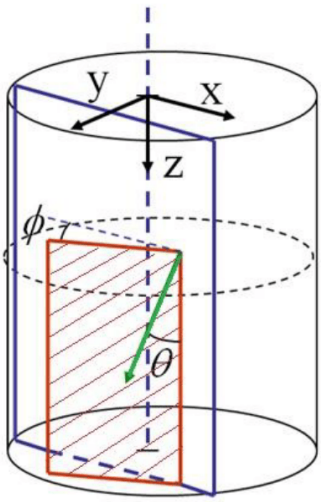

Figure 3.19: Angular variables employed to define the direction of a particle with the parameterization of the PHSP file. The green arrow represents the trajectory of the particle, contained in the red plane (striped plane). The angle with the z axis and the angle of the striped plane with the reference plane (xz plane) fully define the direction of the particle [Herranz et al., 2014].

To calculate dose from these binned PHSP files, we need to generate again the particle trajectories from these parameterized PHSP files. A uniformly distributed angle has to be produced which, in combination with the distance ρ to the applicator axis, defines the actual point in the xy plane where the particle originates. The value of the z position (along the applicator axis) of the point of origin of all the particles is assumed to be constant and it corresponds to the end of the non-beveled applicator. Particles generated by the PHSP code are represented in standard format [Capote et al., 2006] by n-tuples which include particle type, energy, (x,y,z) position and angles of emission (θ, ϕ) with respect to the axis of the applicator. The decoded PHSP files can be fed into MC dose-computation packages.

With regards to bin sizes, a trade-off between accuracy of the representation and number of requested bins was made. Starting from a reference PHSP file made up by 200 million electron particles, it was binned in successively coarser bins. The dose produced by the coarser bins was compared to the one of the unbinned PHSP file. With the bin sizes employed in this work, the doses from binned and unbinned PHSP files agree well within the 2%-2 mm gamma criterion [Low et al., 1998].

In figure 3.20, the distributions with respect to the individual variables for a standard PHSP file of an IOERT accelerator are shown. The distributions in energy, ρ and θ for PHSP files suitable to IOERT have been studied previously [Iaccarino et al., 2011, Björk et al., 2002], as well as the distribution in ϕ [Herranz et al., 2014]. From symmetry considerations, the distribution of ϕ verifies f(ϕ)=f(360° - ϕ) and thus, it is symmetrical around ϕ=180°. As a general rule, ϕ distributions peaked at values smaller than 90° would correspond to diverging

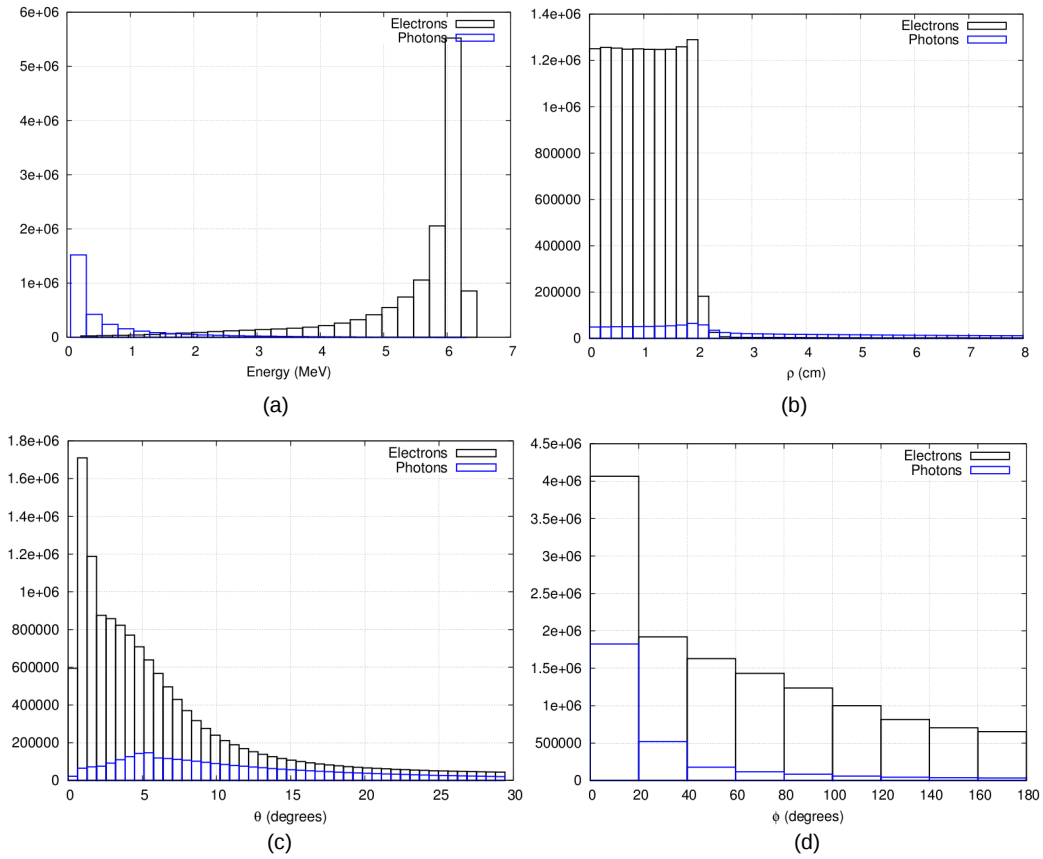

Figure 3.20: Histograms for a 6 MeV NOVAC® PHSP file with an applicator diameter of 60 mm, showing both electron and photon distributions. The ordinate axis shows the number of particles in each bin. The radial distribution shows number of particles crossing the unit of surface against ρ, the distance to the axis of the applicator.

beams while distributions peaked at values larger than 90° would represent convergent or focused beam. Radiotherapy beams in IOERT would be mostly diverging ones, with some non-dominant converging component coming from secondary particles generated in the walls of the applicators [Herranz et al., 2014].

3.4.2 Parameterization of PHSP files in the Intrabeam® spherical applicators

Exploiting the cylindrical geometry of the needle and spherical applicators, the PHSP file was fully defined by the distribution of particles in Energy *(E)* and two angles α and β, the first to position the particle in the sphere surface, and the second to determine the direction of emission of the particle with respect to the direction of the radius of the sphere at the point of emission.

We assumed that the particles were emitted from the spherical applicator surface. In the case of XIORT applicators, no electrons are considered, therefore there is no need to include the particle type parameterization. The definition of the angles is presented in Figure 3.21.

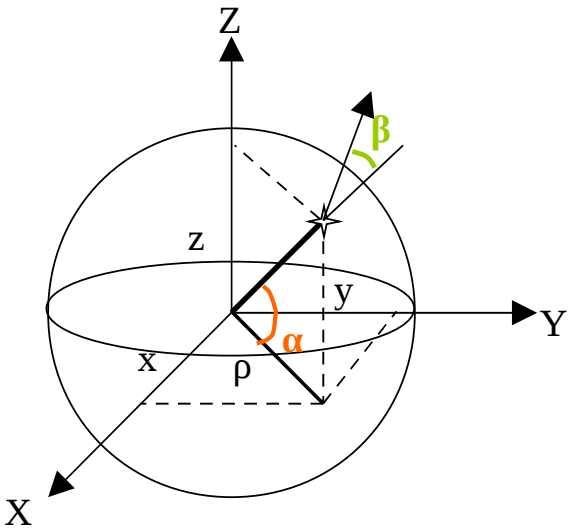

Figure 3.21: Schematic view of the parameterization of the PHSP files for spherical applicators in terms of the angles α and β.

In our parameterization we allow a dependency in the fluence of the particles on their forward or backward position along the surface of the sphere. We assume azimuthal symmetry around the axis of the applicator, and azimuthal symmetry of the emission direction of the particles with respect to the direction of the radius of the sphere at the point of emission of the particle. With this parameterization the PHSP file is fully described with a maximum of 2.000.000 bins or elementary sources.

To compute the actual dose, the condensed information contained in this compact PHSP file has to be "debinned" to produce histories combining the information in the PHSP file with two azimuthal angles with random values uniformly picked in between 0° and 360°. One of them combined with α fixes the location of the emission point for the particle in the surface of the sphere. The second one, combined with β, determines the direction of emission of the particle.

To determine the bin sizes, the reference PHSP file was binned in successively coarser bins in the variables previously described. The dose produced by the PHSP file from coarser bins, once debinned, was compared to the one of the unbinned PHSP file. With the bin sizes employed in this work, the doses from binned and unbinned PHSP files agree well within the 1%-1 mm gamma criteria (more than 99 % of the voxels passed the test). Finally, the following ranges and binning widths (BW) were considered for the definition of the elementary sources:

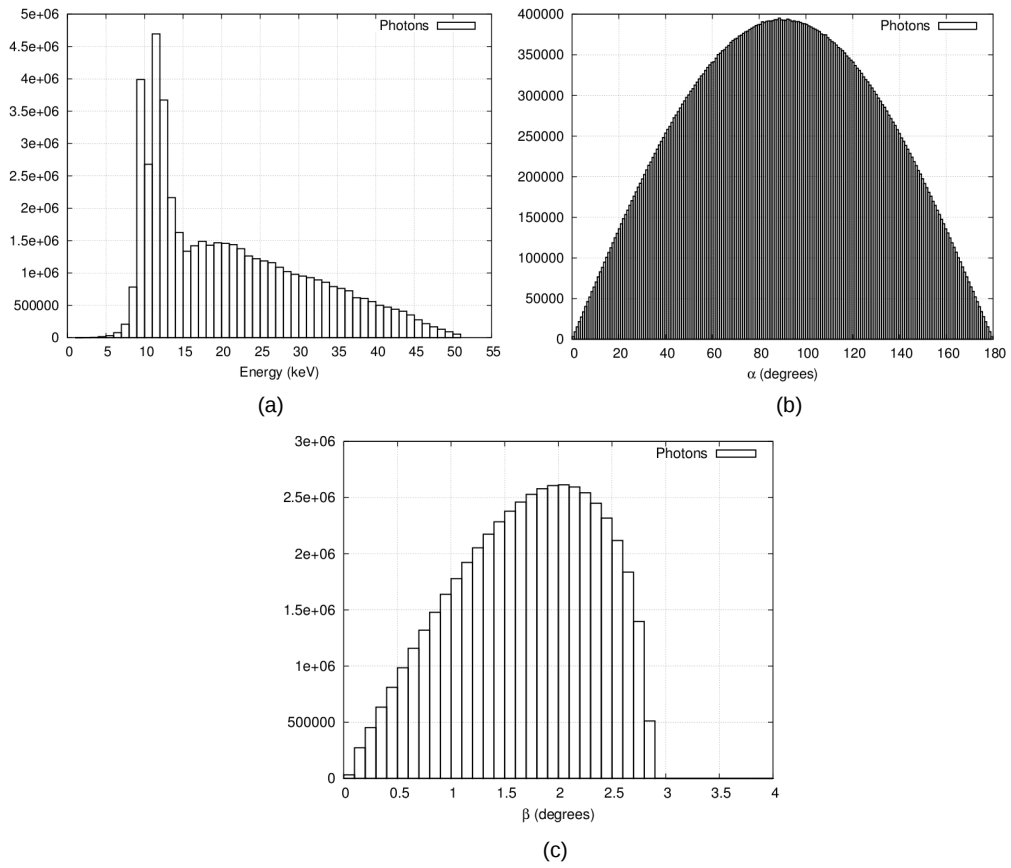

Figure 3.22: Histograms for a 20 mm diameter spherical applicator PHSP file in terms of the relevant variables (Energy, α and β), showing photon contributions. The ordinate axis shows the number of particles in each bin.

- Energy, ranging from 0 to 50 keV (BW = 1 keV).
- α angle to position the particle in the sphere surface, ranging from 0° to 180° (BW = 0.9°).
- Emission angle β, ranging from 0° to 20° (BW = 0.1°).

In figure 3.22 the histograms of a parameterized spherical PHSP file in terms of the relevant variables can be seen.

3.4.3 Parameterization of PHSP file in the Intrabeam® flat and surface applicators

For the case of Intrabeam® flat and surface applicators, the cylindrical approach used for electron's PHSP parameterization can be also used, because we can assume the same symmetries. However, a modification regarding the binning parameters definition has been introduced.

Instead of parameterizing the different degrees of freedom according to the z axis (applicator axis), the PHSP file is going to be binned according to the original particle trajectory. To do this approach the distance between the source location and the PHSP plane (SSD) must be known and introduced in the calculations.

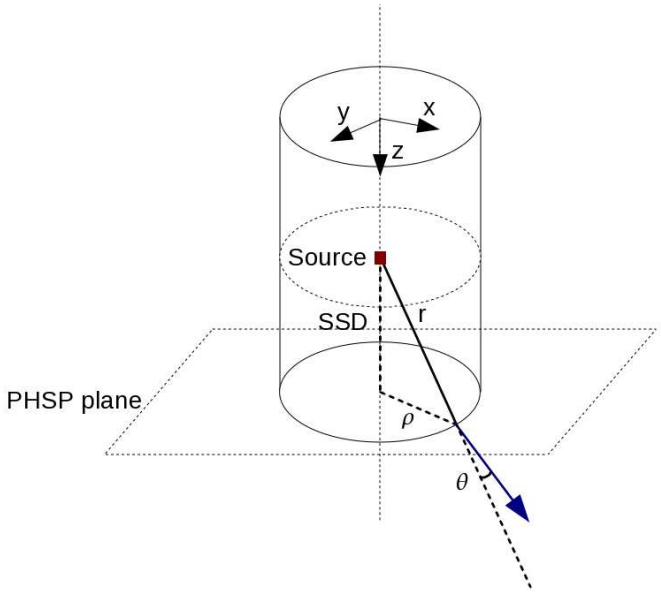

Figure 3.23: Schematic view of the parameterization of the PHSP files for flat and surface applicators in terms of the distance to the applicator ρ and the angle θ.

With this new binning, the angle ϕ turns to be almost isotropically distributed and can be eliminated from the parameterized file, and the angle θ, now representing the deviation angle of the particle trajectory when traveling through the interior of the applicator, will be decreased up to a few degrees. Eliminating ϕ from the binning entails a great decrease in the number of bins needed to characterize the PHSP file and allows a more detailed binning in the radial distance to the applicator axis, needed to reproduce accurately the shape of the lateral profiles that these applicators present. With this parameterization the PHSP file is fully described with a maximum of 630.000 bins or elementary sources.

Therefore, the PHSP file is fully defined by the distribution of particles in Energy *(E)*, the radial distance to the applicator axis ρ and the angle θ, the deviation angle of the particle with respect

to the primary angle of the trajectory.

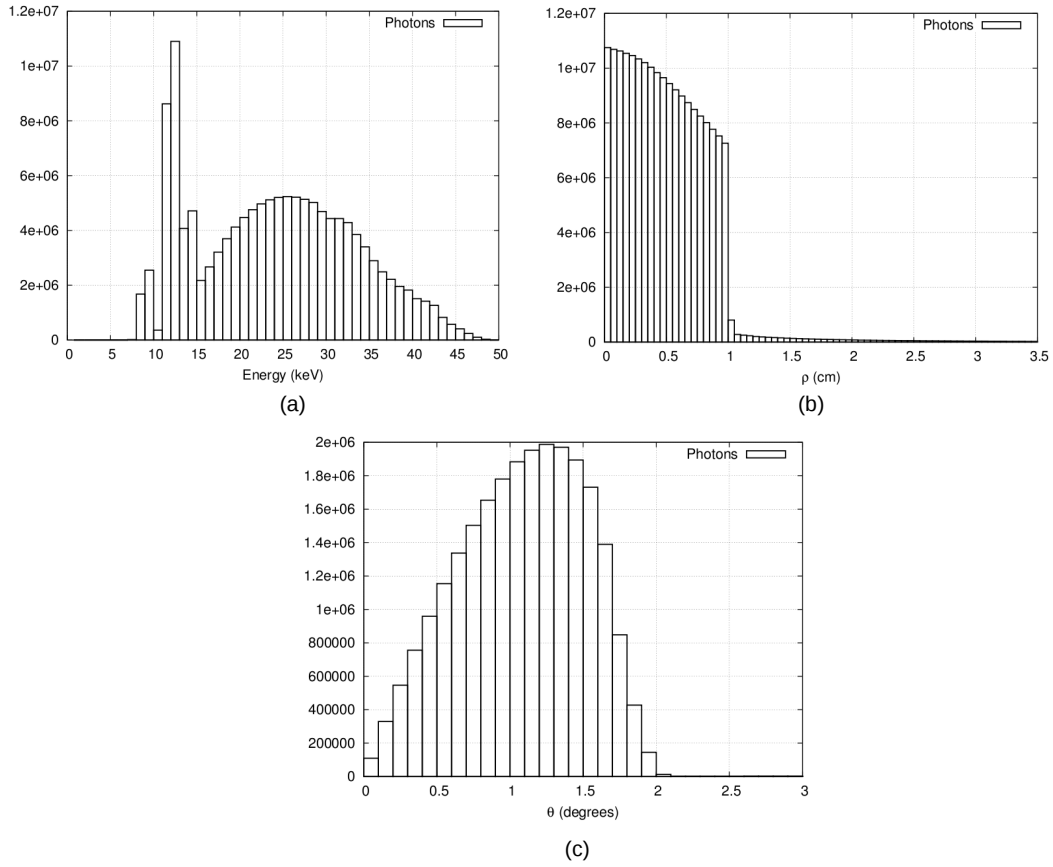

Figure 3.24: Histograms for a 20 mm diameter surface applicator PHSP file in terms of the relevant variables (Energy, ρ and θ), showing photon contributions. The ordinate axis shows the number of particles in each bin.

To select the optimal binning steps, the previously described approach of comparing dose from binned and unbinned PHSP files was done. With the bin sizes employed in this work, more than 99% of the dose voxels calculated from binned and debinned PHSP files passed the 1%-1 mm gamma evaluations. The following ranges and binning widths (BW) were considered for the definition of the elementary sources:

- Energy, ranging from 0 to 50 keV (BW = 1 keV).
- Deviation θ angle of the particle trajectory, ranging from 0° to 18° (BW = 0.1°).
- Radial position ρ, ranging from 0 cm to 3.5 cm (BW = 0.05 cm).

As in the other cases, to compute dose the PHSP file needs to be "debinned". The debinning process works the same was as for electrons, where a uniformly distributed angle is produced

which defines the position of the particle (x,y,z), in combination with the distance ρ to the applicator axis.

In figure 3.24 are represented the histograms in terms of the variables used for the parameterization of the PHSP file.

3.5 Conclusion

In this chapter we have simulated in detail a large group of IOERT accelerators and Intrabeam® applicators that represent accurately the experimental dose distributions.

Furthermore, with the parameterization of the PHSP files we have turned these huge files containing all the information of the particle beam into an easy-to-manipulate file without loss of information. These binned PHSP files can be stored and used without storage issues. And finally, with the debinning tool we can transform the simplified version of the PHSP file into the unbinned file.

The results from this chapter will be essential for the objectives of this thesis, because the simulation results will be used as a pre-computed database that will be needed in the PHSP optimization procedure explained in the following chapter. The binning and debinning tools will make possible to handle and work with a large set of PHSP files.

Chapter 4

Phase space optimization process

4.1 Introduction

Accurate calculation of dose distribution in an inhomogeneous medium such as a human body is a complicated task. To date, the Monte Carlo (MC) method is considered to be the most accurate algorithm for dose calculation but it requires the greatest processing time. Apart from the MC method, all other methods make different degrees of approximation and simplification which lead to much faster calculations but also result in less accurate dose distributions when comparing to the MC simulation [Chen et al., 2014]. The ideal planning system would be a calculation tool that can provide accurate dose distributions in minutes by means of a MC algorithm.

As we explained in chapter 3, MC codes for dosimetry require a realistic and accurate description of the electron and/or photon beam employed in the radiotherapy procedure [Chetty et al., 2007], and this information is included in the phase space (PHSP) file. The most common approach to generate these PHSP files is by simulating in a realistic way the accelerator. To do this, we require a detailed knowledge of the device and other elements, such as applicators. However, sometimes this information is protected by the manufacturers, and even if the geometry is available, dose distributions may vary slightly in different devices of the same model, so each specific accelerator should be tuned.

In the case of intraoperative electron radiotherapy, the development of new tools for MC simulation of clinical linear accelerators, such a PRIMO [Rodriguez et al., 2013], can simplify the simulation task as they include the geometry of some accelerators, but they still require a few hours of simulation for each applicator diameter, LINAC model and energy configuration, and the tuning of each specific accelerator is not contemplated.

A previous procedure [Herranz et al., 2014, Herranz, 2013, Ibáñez, 2012, Ibáñez et al., 2014, Pérez-

Liva, 2012] developed in our group was done to characterize beams of medical linear accelerators for intraoperative radiotherapy with electrons. This method relied on fitting with an iterative procedure the relevant variables of a PHSP file (such as energy spectrum, spatial and angular distributions of the particles) until it reproduced experimental dose measurements in water and in air. Despite this method could perform the machine-specific tuning within minutes, the user was required to introduce several input data of water and air dose profiles in the algorithm and the accuracy of the fitting depended strongly on the quality of the measurements.

The aim of this part of the thesis was to develop a fast and accurate phase space tuning tool which can be fitted to the user's device with only an experimental depth dose profile (DDP) in water [Ibáñez et al., 2015, Vidal et al., 2015, Udías et al., 2017a], and which has been implemented into a commercial treatment planning system for intraoperative electron radiotherapy (IOERT) and low energy X-rays radiotherapy (XIORT). The proposed process uses a parameterized phase space model of the source defined at the surface of the treatment applicator and optimizes it to the user's source characteristics, by means of an optimization procedure that relies on a simple set of experimental measurements.

In chapter 3 we have characterized all mobile IOERT accelerators as well as the spherical, needle, flat and surface Intrabeam® applicators. We now will use these geometries to calculate a set of monoenergetic (also called monochromatic) PHSP files and DDPs in water and store them, in order to create a database to feed the PHSP optimization tool. After that, the optimization method proposed in this thesis can be separated in two consecutive phases:

- In phase one, the set of monochromatic DDPs will be weighted and combined until the sum of all the contributions reproduces the experimental DDP. This will be done with a genetic algorithm and as a result of the fitting process we will obtain an optimized energy spectrum created from the relative contribution of each DDP to the experimental dose.

- In phase two, we will use the energy spectrum from phase one to weight the monochromatic PHSP files stored in the database and generate an optimized PHSP file that will reproduce the experimental data.

These two phases have to be performed for each energy and applicator of every accelerator or Intrabeam® that is going to be tuned, but the whole process takes only a few minutes, and once the PHSP file is obtained it can be stored and used any time is needed. A scheme of the process is shown in figure 4.1.

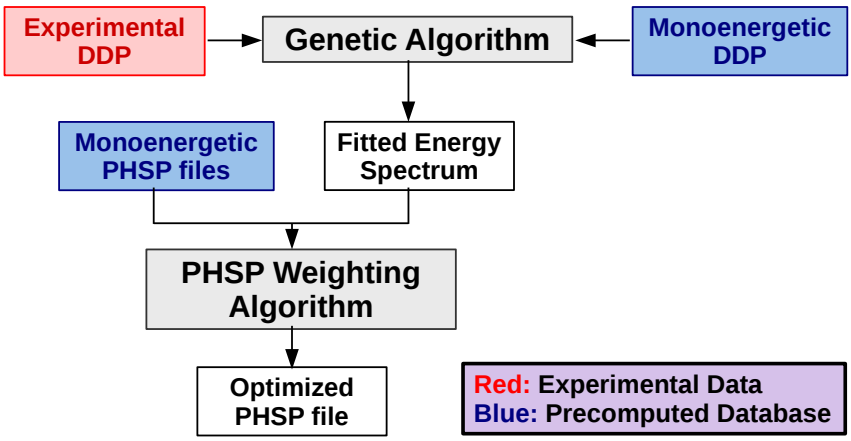

Figure 4.1: Scheme of the phase space optimization process.

4.2 Database generation

First of all we need to generate the database that is going to be used in the rest of the process, and to do this we will use the detailed simulations from chapter 3.

This part of the process requires a long simulation time, as we need to calculate enough monoenergetic simulations of each device to cover its energy range. However, in a high capacity cluster, a whole accelerator including its applicators can be characterized in several days.

Lets see the characteristics of the monochromatic simulations for the IOERT and XIORT devices.

4.2.1 Intrabeam® applicators

As explained in chapter 3, for spherical and needle applicators we did not simulate the full description of the system but a simplified geometry which consists of a quasi-punctual source of photons interacting with a standard geometry per applicator size. However, for flat and surface applicators this approximation could not be done and the detailed geometry of the applicators was considered.

The photon beam exiting the source was characterized with a Gaussian energy distribution with 1 keV full width-half maximum (FWHM). The source had a spatial distribution defined as a circular foil of 0.01 cm radius and a spatial FWHM of 0.001 cm in order to approximate a point source. 50 MC simulations, from 1 keV to 50 keV, were performed with 10^8 initial particles for each applicator and the resulting PHSP files were collected at the external surface of the

applicator.

Since PHSP are huge files and therefore difficult to use, each one was parameterized in terms of the relevant variables to make them easy to manipulate, following the considerations described in section 3.4 of the previous chapter. All parameterized PHSP files were finally stored in a binary format to reduce even more their size.

Regarding the monochromatic depth dose profiles (DDPs), they were either calculated with penEasy at the same time as the PHSP files, or afterwards using a hybrid MC code specifically developed to accelerate dose calculations for the Intrabeam® photon beams. The code description is detailed in chapter 6.

4.2.2 IOERT accelerators

Geometries of the MOBETRON®, LIAC® and NOVAC® described in chapter 3 were used to generate the IOERT database.

The source was defined as circular, with a diameter of several millimeters (3-4 mm depending on the accelerator) and with a Gaussian distribution centered at zero with 0.1 mm FWHM. 140 simulations were performed for each applicator and each accelerator, from 1 MeV to 14 MeV with 0.1 MeV FWHM. 10^8 histories were calculated, and the PHSP files were parameterized in the type of particle, energy, axial angle and radial position each 10^7 histories to save computer memory. This part of the simulation took several days computation time (from 48 hours to 5 days depending on the accelerator geometry on a 8 cores high capacity cluster).

Depth dose profiles in water were obtained from these parameterized PHSP files with DPM [Sempau et al., 2000] and stored as well (1 hour computation time on a 8 cores high capacity cluster).

4.3 Optimization of energy spectrum

In the first phase of the phase space optimization process, the monochromatic DDPs are going to be adjusted to the experimental dose by means of a genetic algorithm [Fernandez-Ramirez et al., 2008].

A genetic algorithm is an optimization tool inspired by the process of natural selection. The algorithm creates a randomly generated population of possible solutions with a set of properties that can be mutated. The evolution of this population follows an iterative process, where each iteration is called a generation. In each generation, the more fit individuals are selected, and

their properties are mutated to form another generation, which is used in the next iteration of the algorithm. The optimization ends when either a maximum number of generations have been produced or a certain fitness level has been reached.

The genetic algorithm requires a fitting function, and in this case this function will be a generic energy spectrum. This way, the genetic algorithm will generate an optimized energy spectrum which weights the relative contributions of the monochromatic DDPs that reproduces the experimental dose data.

The fitting procedure will be the same for XIORT and for IOERT, but the shape of the initial energy spectrum will differ. Both energy spectra are going to de defined by simple mathematical functions describing the expected shape of the beam at the beginning of the accelerator head or at the exit of the Intrabeam® X-ray source.

4.3.1 Energy spectrum for Intrabeam® applicators

The energy spectrum of the Intrabeam® X-ray source is defined as a function that describes the Bremsstrahlung behavior of the energy spectrum and the characteristic rays. Based on Kramers theory of the photons emitted when they hit a target (without taking into account the characteristic lines) [Kramers, 1923], equation 4.1 describes the bremsstrahlung background of the energy spectrum $S_{background}$ in function of energy E:

$$S_{background}(E) = (E - E_1)^a \left(\frac{E_0}{E} - 1\right)^b \tag{4.1}$$

Where E_0 is the maximal energy of the photon beam and E_1 the cut-off energy. a and b are the filtration parameter and the Kramers law adjustment parameter respectively.

The gold characteristic X-rays have been added to the background at energies of 9, 12 and 14 keV, as measured by Schneider *et al.* at the probe surface [Schneider et al., 2010].

$$S_{spectrum}(E) = S_{background}(E) + c \cdot I_p \tag{4.2}$$

Where c is the mix parameter, fixing the amplitude of the characteristic lines relative to the spectrum background intensity and I_p the intensity of the characteristic line with energy E relative to the other two lines.

For each experimental DDP provided by the user, the parameters E_1, E_0, a, b and c are varied and the energy spectrum optimization results in a specific energy spectrum shape (with different

bremsstrahlung backgrounds and characteristic lines intensities) reproducing each experimental DDP.

4.3.2 Energy spectrum for IOERT accelerators

In the case of electrons, the initial electron beam entering the accelerator head is simulated as a combination of a Gaussian distribution with Kramers functions. For each central energy E_0 of the Gaussian distribution, a Kramers function is generated. The sum of all combinations will generate the energy spectrum.

A set of Gaussian distributions from E_0-3.5σ to E_0+3.5σ will be generated, being E_0 the central energy of the Gaussian distribution and σ its standard deviation:

$$\omega(E) = \frac{1}{\sqrt{2\pi\sigma^2}} e^{-\frac{(E-E_0)^2}{2\sigma^2}} \tag{4.3}$$

These Gaussian distributions will be used to weight the 140 Kramers functions associated to each monochromatic energy (E_c):

$$f_{Kramers} = \left(\frac{E}{(E - E_c) + \Delta} \right)^{\alpha} \tag{4.4}$$

Being Δ a blurring parameter inserted to avoid differences in the denominator between different energies because of the energy binning that it is being used.

The energy spectrum will be the sum of all normalized Kramers functions weighted by the Gaussian distributions:

$$S_{spectrum}(E) = \omega(E) \frac{\sum_{i=1}^{140} f_{Kramers}(E, i)}{normalization} \tag{4.5}$$

For each experimental DDP provided by the user, the parameters E_0, σ, α and Δ will be varied and, as in the case of XIORT, the optimization will result in a specific energy spectrum shape reproducing each experimental DDP.

4.3.3 Treatment of the experimental data

To perform this fitting, usually a previous treatment of the experimental DDP needs to be performed. Specially in the case of electron doses, sometimes the experimental profiles do not have a soft shape and present some irregularities. This may affect the fitting process as these errors are introduced in the algorithm. To avoid it and to guaranteer an accurate adjustment, a previous treatment is done to the DDP by approximating it to a general function with the form:

$$f(x) = A\left[e^{-Bx} - Ce^{-Dx}\right] e^{-\frac{Ex^4+Fx^2}{G}} + H \tag{4.6}$$

Figure 4.2 shows the treatment done to an experimental DDP from a NOVAC® accelerator with 9 MeV.

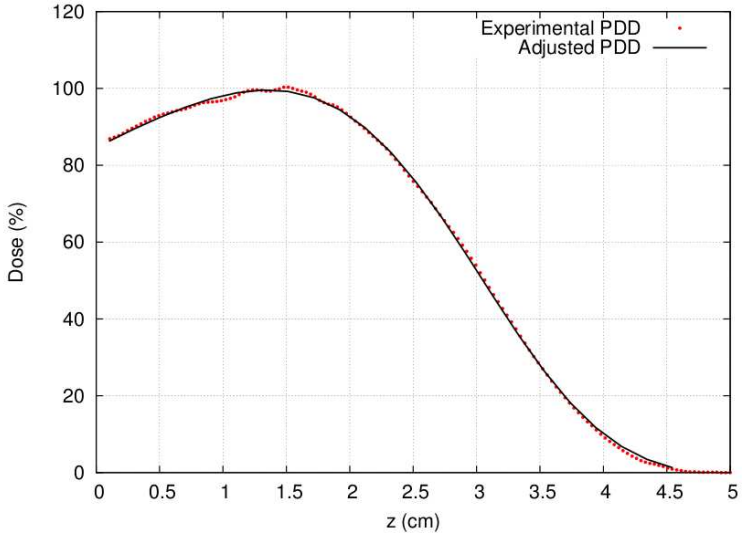

Figure 4.2: Experimental DDP and adjusted DDP for a 9 MeV NOVAC® with 4 cm diameter.

4.4 PHSP weighting algorithm

Once the energy spectrum is optimized, we need to generate the tuned phase space file. To do this, the monochromatic PHSP files are weighted with the optimized energy spectrum from the genetic algorithm and merged to obtain the final PHSP file. This file also needs to include a scale factor that is going to be applied to the final dose so that it is scaled to the input experimental DDP.

The genetic algorithm supplies a scale factor needed to scale the adjusted DDP to the experimental one, and applies a normalization of the spectrum that will have to be considered in the final scale of the weighting procedure. However, this factor will not be sufficient to scale the problem, and we will need to introduce an extra scale factor derived from the number of particles used to calculate the monochromatic DDPs.

The final scale factor will be a contribution of both factors:

$$f = f_{genetic} \cdot f_{weighting} \tag{4.7}$$

The weighting procedure will depend on the way the monochromatic DDPs are generated. Dose distributions obtained with any MC algorithm are always defined as dose per primary history. When the primary beam travels through the different elements of the accelerator head or the applicators, some of the original particles are absorbed or scattered and do not reach the PHSP recollection plane. The number of lost particles increases as the energy decreases, so the monochromatic PHSP files will not have information of the same number of particles for all the energies. However, if the monochromatic DDPs are calculated in the same simulation as the PHSP files, these dose distributions will be all divided by the same number of histories, ie. the initial primary histories of the simulations. But if these curves are obtained with other code, such as DPM or the hybrid MC algorithm described in chapter 6, they are going to be calculated from the monochromatic PHSP files, and every curve will be divided by a different number of primary histories.

Therefore, two different approaches must be taken into consideration, depending on the procedure used for generating the monochromatic DDPs.

4.4.1 Weighting approach for DDPs with the same number of histories

If the monochromatic DDPs have been generated at the same time as the PHSP files, and therefore they are all divided by the same number of primary histories, the optimized spectrum will be used to directly weight the monochromatic PHSP files. The dose distribution obtained with the optimized PHSP file will be divided by the number of its primary histories, which in this case will be sum of the number of histories of each monochromatic PHSP file multiplied by the corresponding value of the energy spectrum:

$$[\sum_{i=1}^{E_{max}} PHSP(i) \cdot spectrum(i)] \rightarrow \frac{dose}{\sum_{i=1}^{E_{max}} [weight_{PHSP}(i) \cdot spectrum(i)]} \tag{4.8}$$

Where $weight_{PHSP}(i)$ is the number of histories of the monochromatic PHSP file with energy i. As mentioned before, there is also a normalization factor coming from the genetic fitting that needs to be included, the spectrum normalization. With this information, the extra scale factor needed to reproduce the experimental dose will then be:

$$f_{weighting} = \frac{\sum_{i=1}^{E_{max}} [weight_{PHSP}(i) \cdot spectrum(i)]}{\sum_{i=1}^{E_{max}} spectrum(i)} \tag{4.9}$$

4.4.2 Weighting approach for DDPs with different number of histories

If the monochromatic DDPs have been calculated from the monoenergetic PHSP files, each one will be divided by a different number of primary particles. Therefore, in this case, the merging procedure needs to be corrected by the number of histories of each monochromatic PHSP file, the $weight_{PHSP}(i)$. So the merging we have to consider is:

$$\sum_{i=1}^{E_{max}} \left[\frac{PHSP(i) \cdot spectrum(i)}{weight_{PHSP}(i)} \right] \tag{4.10}$$

The dose per history we will obtain from the merged PHSP will then be:

$$\sum_{i=1}^{E_{max}} \left[\frac{PHSP(i) \cdot spectrum(i)}{weight_{PHSP}(i)} \right] \rightarrow \frac{dose}{\sum_{i=1}^{E_{max}} \left[\frac{weight_{PHSP}(i) \cdot spectrum(i))}{weight_{PHSP}(i)} \right]} \tag{4.11}$$

And if we finally incorporate the normalization factor of the energy spectrum from the genetic fitting:

$$f_{weighting} = \sum_{i=1}^{E_{max}} \left[\frac{weight_{PHSP}(i) \cdot spectrum(i))}{weight_{PHSP}(i)} \right] \frac{1}{\sum_{i=1}^{E_{max}} spectrum(i)} = 1 \tag{4.12}$$

We can see that, in this case, the scale factor will only be given by the genetic algorithm.

4.5 Results

In this section we will focus on some of the results obtained from the fitting procedure. A full validation of the procedure can be found in next chapter, where comparisons against experimental measurements and detailed simulations in different heterogeneous phantoms have been performed.

Some examples of the fitted DDP obtained with the genetic algorithm, as well as the optimized energy spectra, can be seen for the different approaches in figures 4.3 (spherical applicator), 4.4 (flat applicator) and 4.5 (IOERT accelerator).

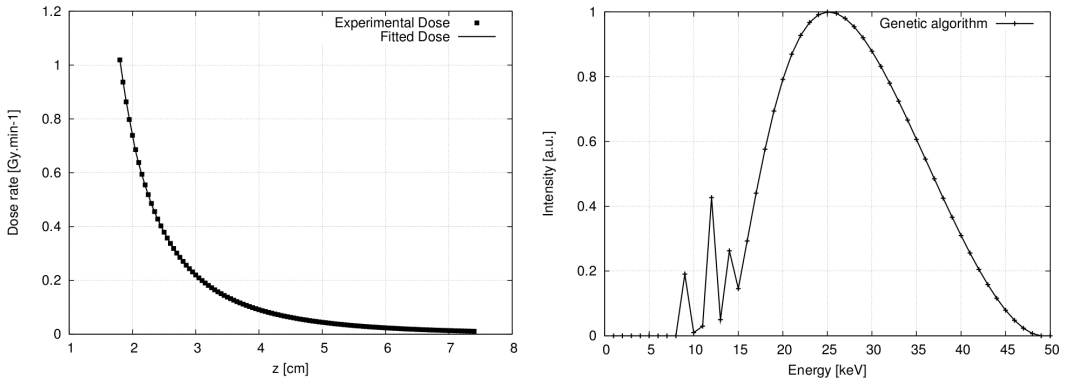

Figure 4.3: Left: Comparison of experimental DDP and optimized DDP for the 1.75 cm radius spherical applicator. Right: Optimized energy spectrum.

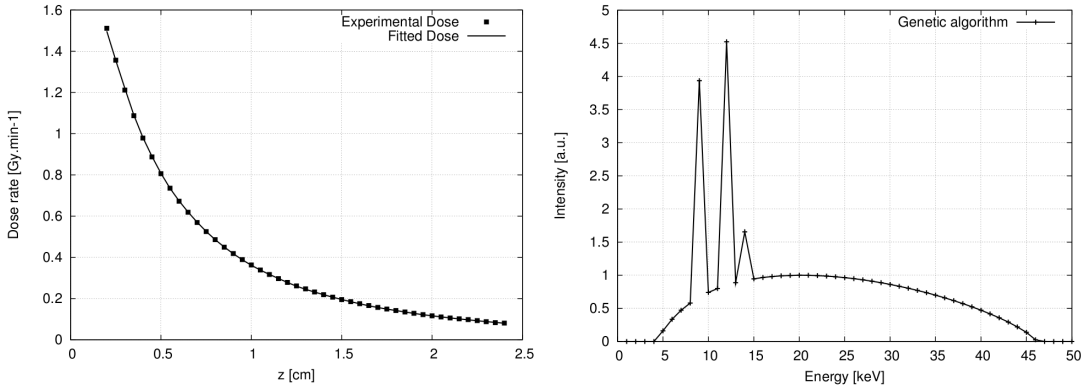

Figure 4.4: Left: Comparison of experimental DDP and optimized DDP for the 2 cm flat applicator. Right: Optimized energy spectrum.

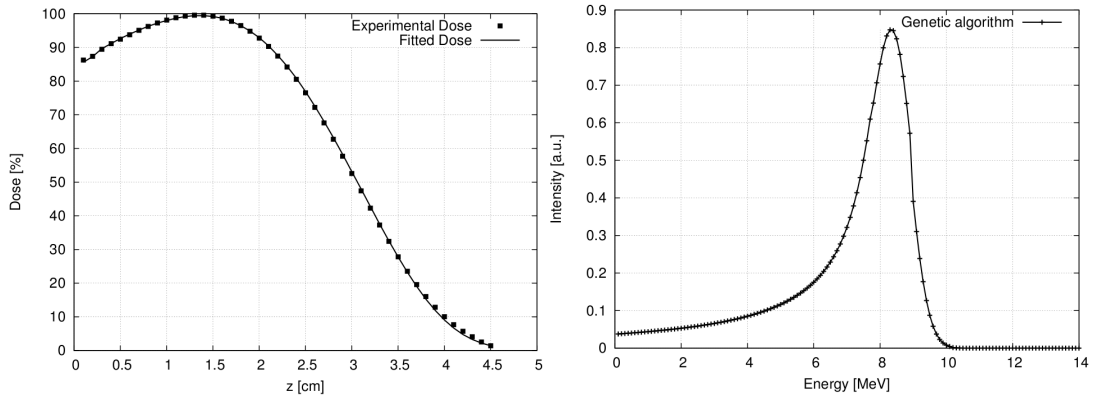

Figure 4.5: Left: Comparison of experimental DDP and optimized DDP for the 9 MeV NOVAC® with a 4 cm applicator. Right: Optimized energy spectrum.

As it can be seen from the different figures, the fitting procedure works accurately, reproducing the provided DDPs while maintaining the physical shape of the spectra. Although the optimization process only fits the DDPs, by having extracted the monochromatic data from detailed simulations of the different accelerators we guarantee that the transverse profiles are also going to behave correctly.

Computation time of the whole fitting process (genetic + weighting algorithms) varies on each case. The genetic algorithm is the most time consuming procedure. The number of dose values of the experimental profile and the voxel size employed in the simulation of the monochromatic DDPs are a contributing factor in the running time of the code. However, its computation time goes from less than a minute up to 6-7 minutes. The weighting algorithm is faster. In this part of the procedure, the computation time is highly dependent on the number of bins in which each PHSP file has been discretized. The computation time of this part of the fitting progress goes from 3-5 seconds (for the flat and surface applicators) to about 40 seconds for the spherical applicators. Nevertheless, in all cases the overall time needed to generate an optimized PHSP file that reproduces any given experimental DDP is below 10 minutes.

4.6 Conclusion

In this chapter we have developed a fitting procedure that allows to obtain a PHSP file that reproduces the DDP of any device within minutes.

For this optimization, the user does not need to perform specific measurements to feed the algorithm, because the only required input is the DDP in water, which is a measurement that

has been previously done for each energy and applicator of the accelerator as it is mandatory for the commissioning of the device.

By combining PHSP files and DDPs from realistic simulations and by using a realistic shape of the energy spectra we guarantee an accurate behavior of the dose distributions, not only of the DDP but also of the transverse profiles.

In the next chapter we will validate this procedure by comparing dose distributions calculated from optimized PHSP files to measurements in different scenarios, proving that the phase space tuning process can be a powerful dosimetric tool.

Chapter 5

Validation of the phase space optimization process with experimental data

5.1 Introduction

In this chapter we present the validation and application of the phase space optimization process described in the previous chapter using experimental measurements from clinical intraoperative electron radiotherapy (IOERT) accelerators and Intrabeam® applicators used in low energy X-rays intraoperative radiotherapy (XIORT) [Ibáñez et al., 2015, 2016, Vidal et al., 2015].

For the validation of XIORT applicators, a set of measurements based on clinical situations has been used, such as air gaps or bone inhomogeneities, and in the case of IOERT validation, the set of measurements were based on the ECWG (Electron Collaborative Working Group, AAPP) report [Shiu et al., 1992] and on the quality control protocol [Rodríguez et al., 2005] for treatment planning systems from the SEFM (Sociedad Española de Física Médica) [Ibáñez, 2012, Herranz, 2013, Leoz Munté, 2015].

The set of measurements includes homogeneous and heterogeneous phantoms. Usually, the required measurements for the characterization of any clinical machine include air and water dose distributions. But when a patient is treated, the radiation beam travels through heterogeneous media, depositing its energy in a different way than in water or air. Therefore, dose distributions in heterogeneous phantoms are also very valuable to verify any radiotherapy device.

Gafchromic EBT3 films were used for performing all the dose measurements. This choice of

radiochromic films is due to the high spatial resolution they present, as well as their low energy dependence, which make them suitable for measuring dose distribution for both electron and low-energy X-rays radiotherapy [Avanzo et al., 2012, Ebert et al., 2009, Fletcher and Mills, 2008].

5.2 Validation for XIORT applicators

Before every session of measurements, the isotropy and dose rate of the source were checked. For this purpose, accessories of the Intrabeam® were used: the photodiode array (PDA), which contains five diodes at orthogonal positions in the front and side of the probe tip, to measure and adjust isotropy; the PAICH unit, which contains a light source to verify straightness of the probe and a holder for a type 23342 chamber, to measure stability of the dose rate [Avanzo et al., 2012].

Films were marked for orientation, numbered, and were handled and stored in order to minimize exposure to light. An Epson Expression 10000XL (US Epson, Long Beach, CA) flatbed scanner was used for scanning the films. A scanning protocol was adopted that follows the modification of Devic *et al.* protocol [Devic et al., 2005] described by Avanzo *et al.* where, instead of reading all the films before and after exposure, only one piece of unirradiated film was scanned and used for all films [Avanzo et al., 2012].

The scanning was performed at least 24 hours after irradiation. For proper warming up of the scanner, five preview scans were done before scanning the films. The films were scanned in transmission mode, in 48 bit RGB format, at a scanning resolution of 72 dpi (0.0847 mm=pixel) with the Epson Scan software, with all the filters and image corrections turned off. All films were scanned in portrait orientation, one at a time, with the film placed in the central area of the scanner. No inhomogeneity correction in scanner response was applied. Every film was scanned two times consecutively [Aranda Escolástico, 2013].

Images were saved in uncompressed tagged image file format (TIFF). Film images were analyzed using an in-house image manipulation routine written with MATLAB 7.6.0.324 (MathWorks, Natick, MA, USA) based in the three channel technique explained in chapter 1 [Lewis et al., 2012].

5.2.1 Experimental measurements for Spherical applicators

Measurements for all spherical applicators were done at the Universitätsklinikum Mannheim, Germany. The set of measurements includes depth dose profiles (DDPs) in a water equivalent phantom and 2D dose distributions, dose measurements in an air-water step phantom and

calibration.

5.2.1.1 Calibration

The calibration phantom is a Gammex® solid water phantom with two blocks joined with screws to form a single block. One of the blocks is a (14×14×0.25) cm^3 layer and the other is thicker, a (14×14×1) cm^3 block with a hole to insert the ionization chamber. On top of the chamber the film is located, in order to acquire a simultaneous measure from both the chamber and the film.

Films were cut into pieces of 5×5 cm^2 for calibration, and were marked to keep the original orientation of the film. A "PTW Soft X-Ray Chamber" (Volume: 0.02cm^3, type: 23342, Physikalisch-Technische Werkstaetten, Freiburg, Germany) with a sensitive window radius of 1.5 mm and 1 mm thick was used. A PTW UNIDOS (Type: 10001-010582, Physikalisch-Technische Werkstaetten, Freiburg, Germany) electrometer was used to read the dose lectures, and the necessary corrections were included (pressure, temperature, etc) for an absolute dose reading.

For the calibration measurements, a 4 cm diameter spherical applicator was used. A stand was designed to fix the distance between the Intrabeam® XRS and the calibration phantom at a known depth. This stand is a special construction built at the hospital intended to be used for dosimetry measurements of the INTRABEAM XRS with or without attaching an applicator. Instead of varying the distance between the source and the phantom at a fixed irradiation time, we decided to vary the irradiation time at a fixed depth. Therefore, the distance between the applicator and the ionization chamber was set at 0.75 cm, and the dose rate was fixed to 0.716 Gy/min. 7 measurements (plus the unirradiated) were taken to cover the energy range of the Intrabeam®. The values of this calibration are shown in table 5.1.

Exposure time (s)	Absolute dose (Gy)
0	0.00
300	1.37
600	2.78
900	4.16
1800	8.49
2700	12.50
3600	16.63
4500	20.73

Table 5.1: Measured dose values during the calibration procedure obtained with the ionization chamber.

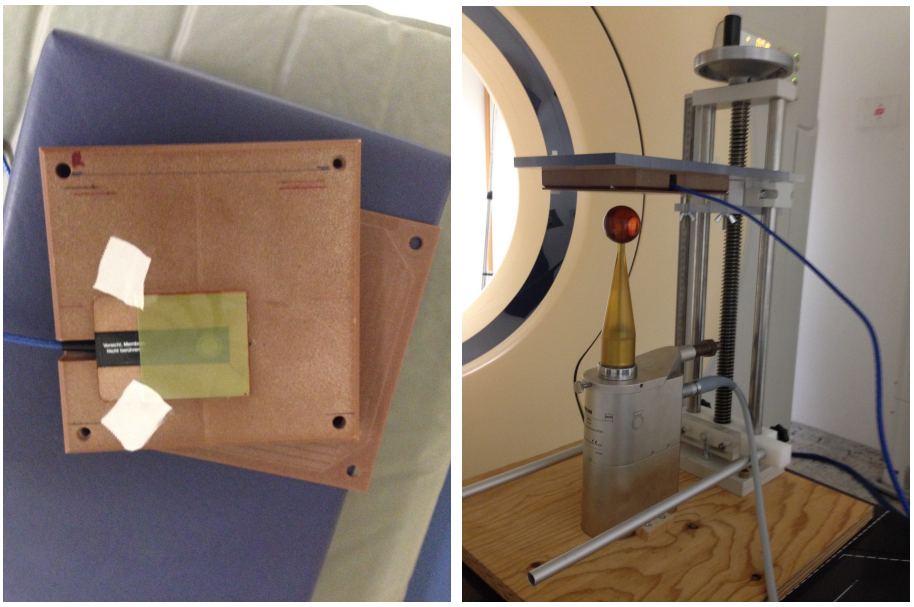

Figure 5.1: Left: Gammex® solid water phantom employed in calibration measurements with the ionization chamber and a EBT3 film. Right: Experimental setup for the calibration measurements.

5.2.1.2 Experimental setup and phantom description

2D dose distributions in water

A Gammex® phantom, specifically created to measure 2D dose distributions along the applicator axis, was employed. It consists of two blocks made of solid water with an applicator-shaped hole. The film is located between the two blocks and the applicator is placed in the phantom hole. This way, dose surrounding the applicator can be measured.

There are different types of solid water plates used in radiotherapy dosimetry, but not all materials are water-equivalent at kilovoltage energies due to increased number of photoelectric interactions, which depends on the atomic number [Eaton and Duck, 2010]. Several authors have investigated the suitability of different materials in the kV energy range [Hermann et al., 1985, Meigooni et al., 1988, Hill et al., 2005, 2010]. In this study "Gammex" solid water was used because it seems to be the best suitable material for Intrabeam® X-rays working energy.

Prescribed dose was set to 20 Gy at the surface, corresponding to the dose rate employed in a breast cancer treatment.

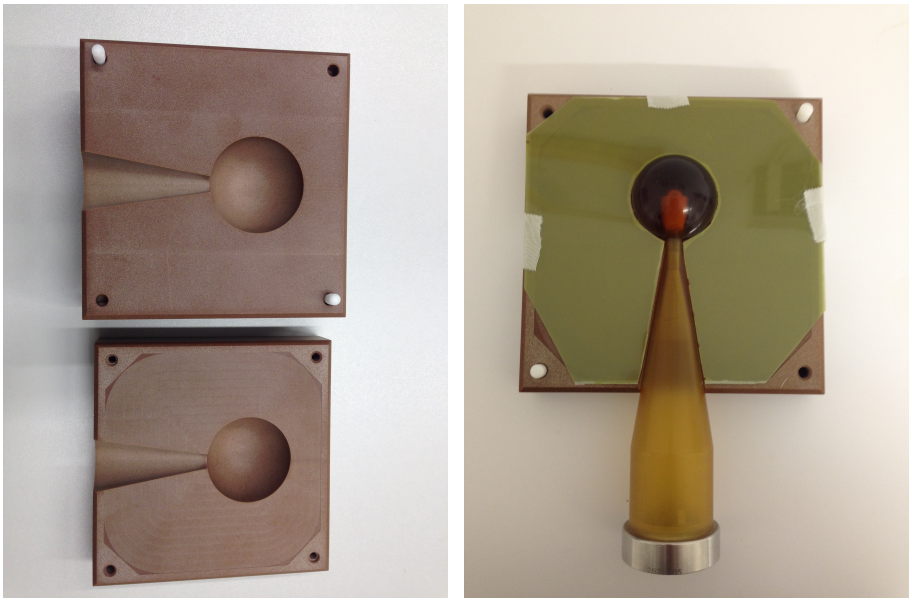

Figure 5.2: Gammex solid water phantoms employed in 2D dose distribution measurements.

Depth dose curves in water

Although Gammex is believed to be the best water-equivalent material for kV X-rays, in the clinic there were only a few Gammex phantoms for specific measurements. Therefore, in order to perform different measurements, we were forced to use a CIRS Plastic Water® solid water phantom (Norfolk, VA).

To absorb possible differences in dose due to the material type, DDPs were measured for all applicators with this solid water material and were used as the input experimental DDP needed for the fitting process.

Ten films were placed at different depths to reproduce the fall of the dose with distance. Measurements at 1, 2, 4, 6, 8, 10, 15, 20, 30 and 40 mm were taken. In figure 5.3 a view of the setup with the location of the radiochromic films is shown.

A comparison between the measured DDPs and the DDPs provided by Zeiss in water was done to check the differences of using the plastic water as reference. Figure 5.4 shows the comparison for all the spherical applicators of the measured DDPs described above (dots) and the DDPs provided by Zeiss (solid lines). It can be seen that the behavior of the measured curves is very similar to the ones the provided by Zeiss.

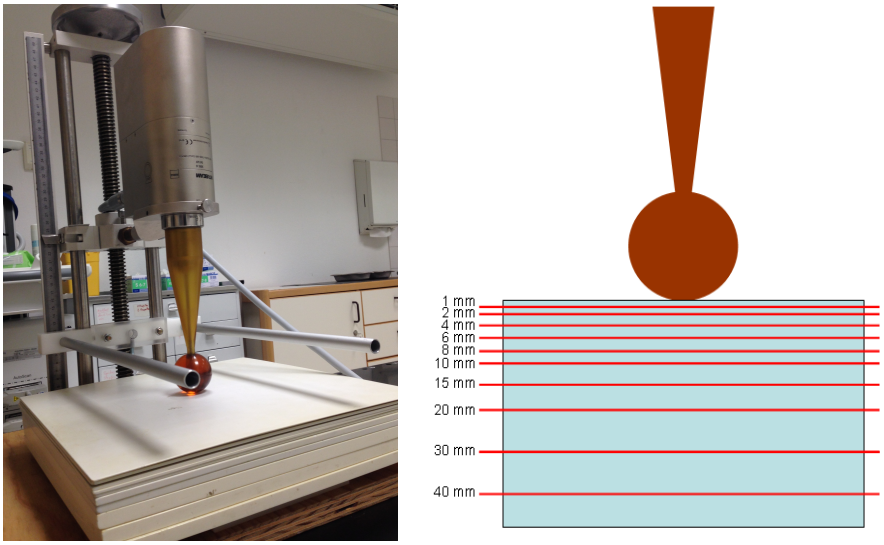

Figure 5.3: Experimental setup (left) and schematic view of the position where the radiochromic films were placed (right).

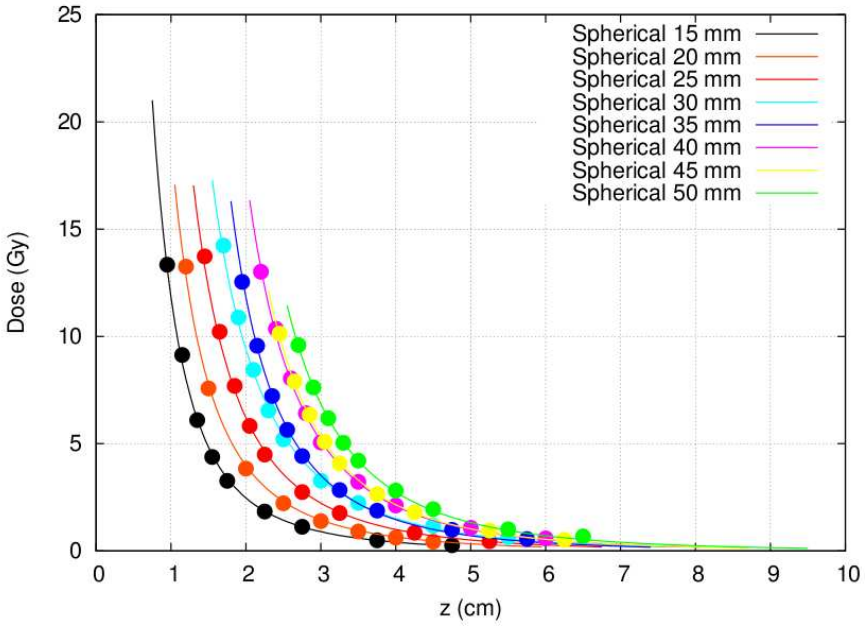

Figure 5.4: DDPs for all the spherical applicators. Dotted curves correspond to our experimental measurements, and the solid lines correspond to the DDPs provided by Zeiss.

Air step heterogeneous phantom

The same Plastic Water blocks presented from the DDP measurements were used to build a 5 mm air step. Three radiochromic films were placed at different depths, 5, 10 and 15 mm. In figure 5.5 the experimental setup and a schematic representation of the heterogeneity with the location of the EBT3 films can be seen.

Dose distributions were measured for all spherical applicators with a prescribed dose of 20 Gy at the surface.

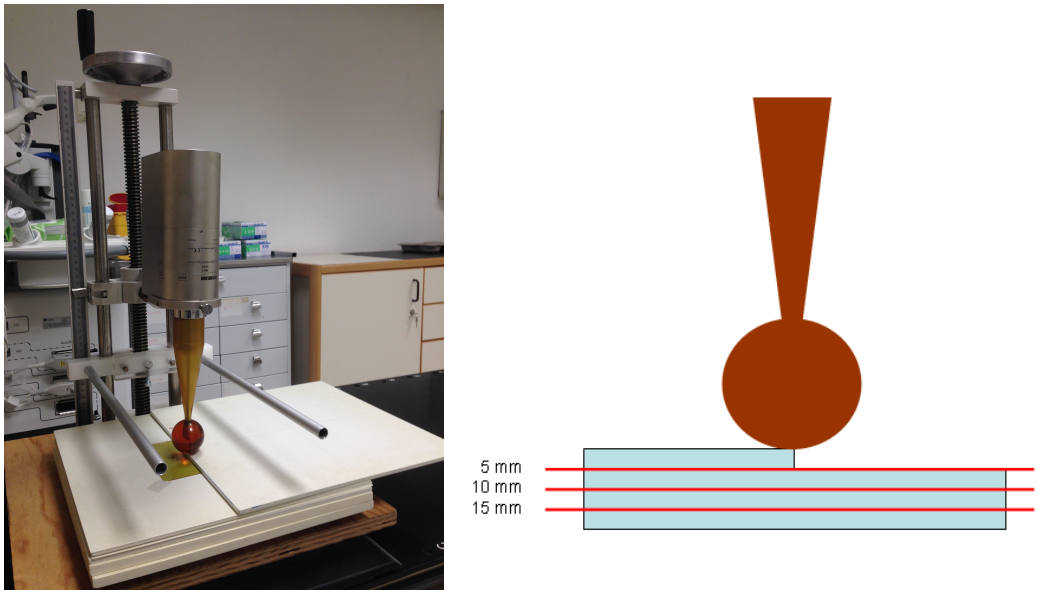

Figure 5.5: Experimental setup (left) of the Air-water step and schematic view of the position where the radiochromic films were placed (right).

5.2.2 Experimental measurements for Flat and surface applicators

Measurements for flat and surface applicators were done at the IUCT Oncopole (Toulouse, France). The set of measurements includes calibration, DDPs and 2D dose distributions in water, dose measurements in an air-water equivalent step phantom and in a bone-water equivalent phantom.

5.2.2.1 Calibration

To perform the calibration measurements, the Intrabeam® water tank was used. This tank has a positioning unit where the XRS is mounted that permits to move the XRS inside the tank. It also contains a waterproof holder made of solid water to accommodate the soft X-ray ionization chamber (manufactured by PTW Freiburg, Germany, type 23342) [Zeiss, 2011]. The films were placed on top of the holder.

Films were irradiated with the 4 cm diameter flat applicator at a fixed depth of 6 mm, and films were irradiated with 0, 1, 2, 3, 4, 5, 6 and 7 Gy. To do this, Zeiss provides the user with conversion tables to extract, from each needed dose value at the film depth, the corresponding dose prescription at a fixed depth of 21.5 mm. Table 5.2 shows the values of the calibration curve.

Exposure time (s)	Absolute dose (Gy) at 21.5 mm	Absolute dose (Gy) at 6 mm
0	0.00	0.00
22	0.15	1.00
43	0.30	2.00
65	0.45	3.00
87	0.60	4.00
108	0.75	5.00
130	0.90	6.00
152	1.05	7.00

Table 5.2: Measured dose values during the calibration procedure obtained with the ionization chamber.

5.2.2.2 Experimental setup and phantom description

Dose distributions with depth for all applicators were measured with Gafchromic EBT3 by locating a single film parallel to the beam between solid water plaques. Two heterogeneous situations were studied as well: An air step and a bone phantom.

Air step heterogeneous phantom

Several PMMA blocks were used to build a 5 mm air step. Three radiochromic films were placed at 5, 10 and 15 mm depth. Figure 5.6 shows the schematic representation with the location of the films.

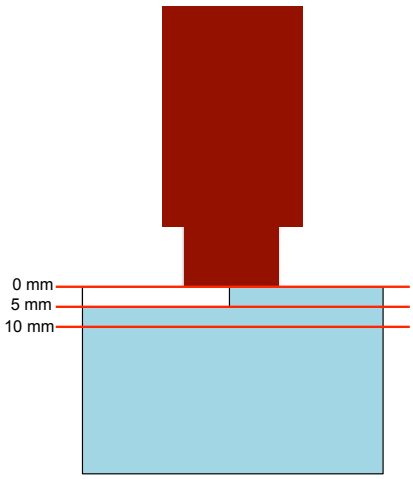

Figure 5.6: Schematic view of the air step setup with the position where the radiochromic films were placed.

Bone heterogeneous phantom

The same PMMA blocks were used to build a bone-equivalent heterogeneous phantom. To do this, a Teflon block with 4 mm thickness was inserted between the PMMA blocks at a depth of 5 mm. Figure 5.7 shows a picture of the experimental setup and its schematic representation with the location of the films.

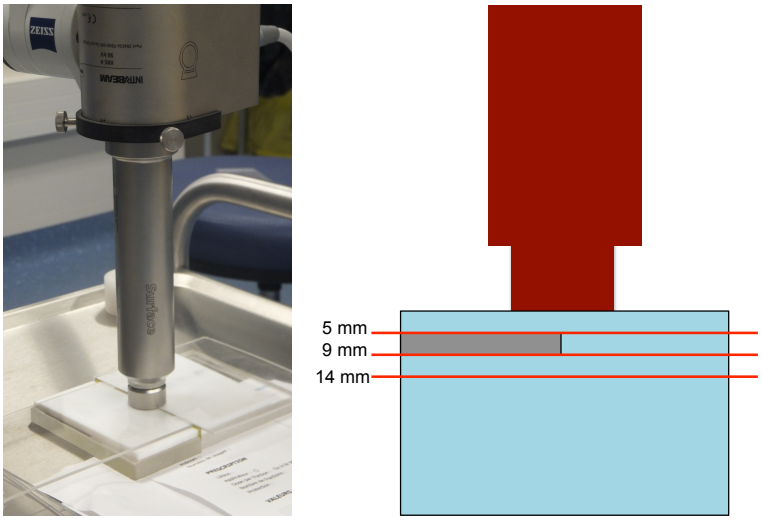

Figure 5.7: Experimental setup (left) of the bone heterogeneity and schematic view of the position where the radiochromic films were placed (right).

5.2.3 Dose comparison for spherical applicators

The measured DDPs were used to fit the monochromatic DDPs and phase space (PHSP) files by means of our optimization algorithm, and the resulting PHSP files were used to compute dose with penEasy in water and in the air step phantom. Results were then compared with the radiochromic film measurements qualitatively and quantitatively (ie. gamma evaluation).

5.2.3.1 Dose distributions in water

We have compared 2D dose distributions for the 40 mm diameter spherical applicator and the 25 mm diameter applicator. The reference DDPs were extracted from the radiochromic films and used to fit the monochromatic PHSP files and DDPs in order to generate the optimized PHSP file.

For the calculation of both the 40 mm and 25 mm diameter spherical applicator, 10^9 histories were simulated in (120×120×120) voxels phantoms, with 1 mm voxel size.

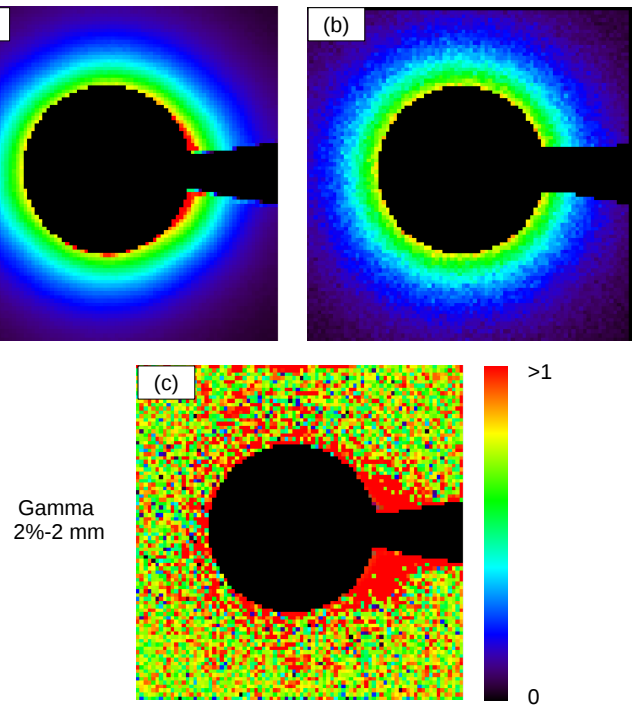

Figure 5.8: 2D dose distributions in water for a 40 mm diameter spherical applicator obtained from (a) radiochromic films, (b) penEasy calculation with the reconstructed PHSP file and (c), the gamma evaluation distribution for a 2%-2 mm criterion with 5% threshold. 83.82% voxels passed the test.

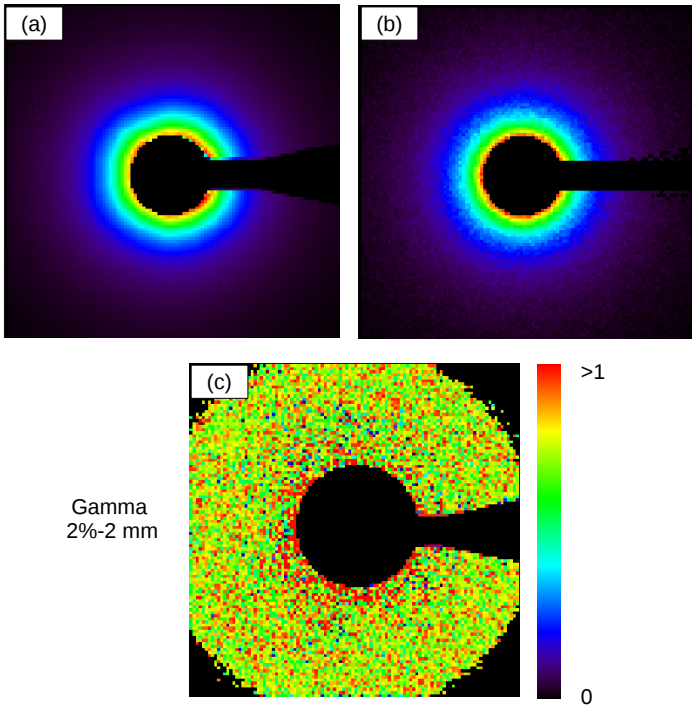

Figure 5.9: 2D dose distributions in water for a 25 mm diameter spherical applicator obtained from (a) radiochromic films, (b) penEasy calculation with the reconstructed PHSP file and (c), the gamma evaluation distribution for a 2%-2 mm criterion with 5% threshold. 94.43% voxels passed the test.

We have compared the experimental and computed dose distributions in terms of gamma evaluation. For this section, we chose a 2%-2 mm criterion and considered a threshold of 5%. The 2 mm distance criterion was chosen because of the voxel size we used. In this work the different distance-to-agreement criteria used in the gamma evaluations have been chosen to be at least twice the voxel size, to allow the code to look for gamma values in the nearest neighbors of the evaluated voxel.

The experimental and simulated dose distributions for the 40 mm applicator can be seen in figure 5.8, as well as the gamma distribution for the 2%-2 mm criterion (5% threshold). The same distributions for the 25 mm applicator are showed in figure 5.9. The main differences between experimental and simulated images are due to the anisotropy presented in the films in the backward direction. Our spherical approximation considers isotropy in the particle emission, and therefore the real behavior of the dose can not be exactly reproduced. This dose difference in the backward direction is reflected in the gamma evaluation, specially for the 40 mm diameter applicator, where a large concentration of voxels failing the criterion can be seen in the backward area. As a result, only 83.82% of the voxels passed the test. In the case of the 25 mm diameter applicator, the film presented a less pronounced anisotropy in the dose distribution, and therefore the number of voxels in the MC simulation of this applicator passing the evaluation increased

up to 94.43%.

5.2.3.2 Dose distributions in heterogeneous phantoms

The phantoms were defined by a volume of (100×100×126) voxels, with a voxel size of 1 mm. The number of histories of each simulation varied from 10^9 histories to $3{\cdot}10^9$, depending on the noise of the resulting dose distribution.

Due to the difficulty in assuring geometrical positioning of the experimental setup within 1 mm or less, the simulation had to be slightly modified for every case, moving the interface air-water from the center when necessary.

Figure 5.10 shows an example of the results we obtained. It includes the 2D dose distributions at the depths where the films were located from the radiochromic films (a) and from penEasy (b) for the 40 mm diameter spherical applicator.

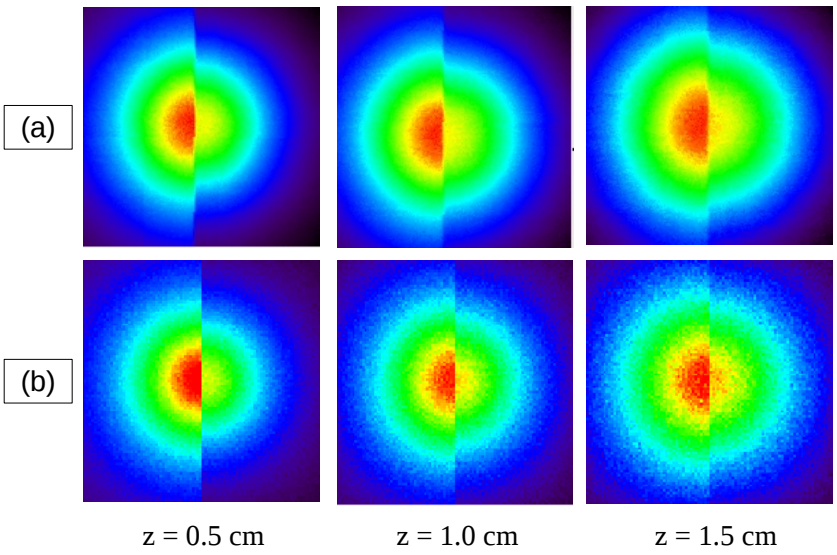

Figure 5.10: 2D dose distributions in the air step at the different measured depths for a 40 mm diameter spherical applicator obtained from (a) radiochromic films, (b) penEasy calculation with the reconstructed PHSP file.

We also performed a gamma evaluations of the results. As the voxel size was set at 1 mm, we chose a 2%-2 mm criterion with a 5% threshold. The results are presented in table 5.3.

Gamma evaluation with 2% - 2 mm	
	Air step
Spherical ϕ 15 mm	96.77%
Spherical ϕ 20 mm	99.40%
Spherical ϕ 25 mm	99.30%
Spherical ϕ 30 mm	95.69%
Spherical ϕ 35 mm	99.49%
Spherical ϕ 40 mm	99.61%
Spherical ϕ 45 mm	99.11%
Spherical ϕ 50 mm	99.29%

Table 5.3: Results of gamma evaluation between MC simulations and measurements in the air step phantom (5% threshold).

For all the cases, more than 95% voxels passed the 2% - 2 mm gamma index, which indicates that there is a good agreement between simulations and measurements.

5.2.4 Dose comparison for flat and surface applicators

5.2.4.1 Dose distributions in water

Dose in water was calculated from the optimized PHSP file and compared with measurements from radiochromic films for two cases: a 3 cm diameter flat applicator and a 3 cm surface applicator. Dose was calculated in volumes of (120×120×120) voxels with a voxel size of 1 mm. The results of these comparisons are displayed in figures 5.11 and 5.12.

In terms of gamma evaluation, there is a good agreement with the measurements, with more than 99% voxels passing the 2%-2 mm criterion (with a 5% threshold) for the 3 cm flat applicator and more than 95% voxels passing it in the case of the 3 cm surface applicator.

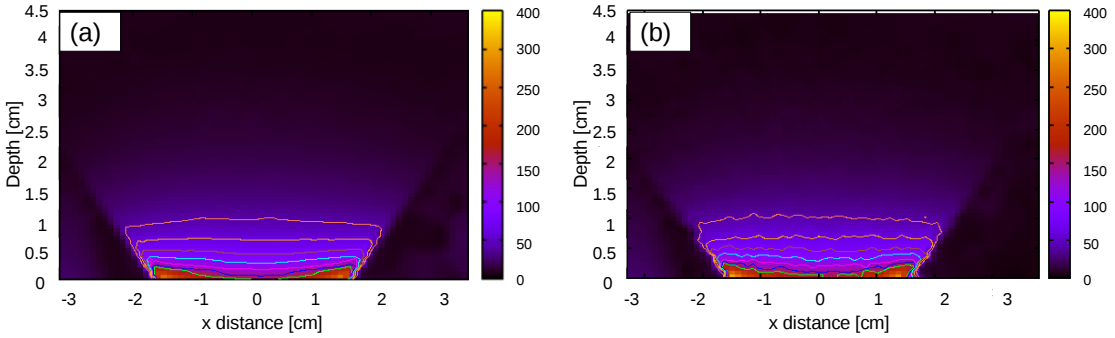

Figure 5.11: Dose distribution comparison for a 30 mm diameter flat applicator obtained with (a) a radiochromic film and (b) penEasy calculation from the reconstructed PHSP file.

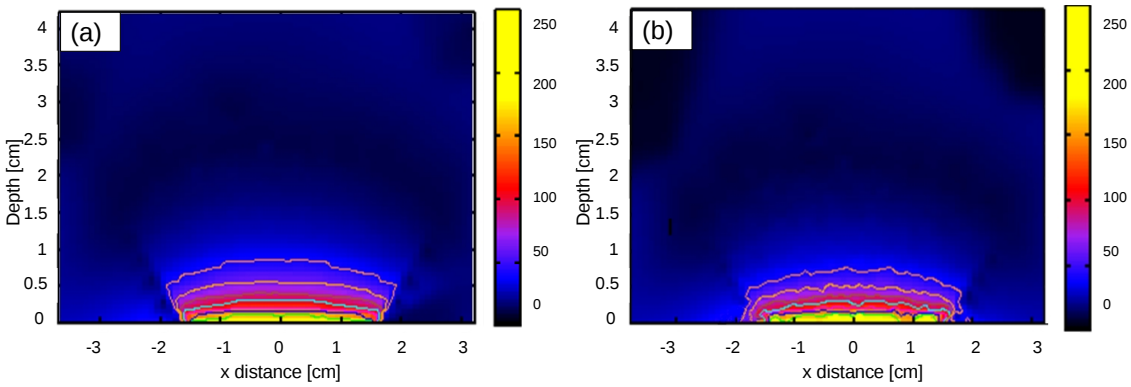

Figure 5.12: Dose distribution comparison for a 30 mm diameter surface applicator obtained with (a) a radiochromic film and (b) penEasy calculation from the reconstructed PHSP file.

5.2.4.2 Dose distributions in heterogeneous phantoms

The experimental DDPs measured at Toulouse were introduced into the fitting algorithm to generate the optimized PHSP files for each applicator, and they were used to calculate dose distributions in the different heterogeneous phantoms.

The phantoms were defined by a (200×200×100) voxels volume, with 1 mm voxel size. As for the spherical validation, the number of histories varied with the applicator, depending on the noise of the dose distribution, from $5{\cdot}10^8$ to 10^9 histories.

Two examples of the results that we have obtained can be seen in the following figures. Figure 5.13 includes 2D views of the dose distribution in the bone phantom for a 3 cm flat applicator at the depths where the films were placed obtained with (a) the radiochromic films and (b)

penEasy. The same comparison is showed in figure 5.14 with a 3 cm surface applicator in the air step phantom.

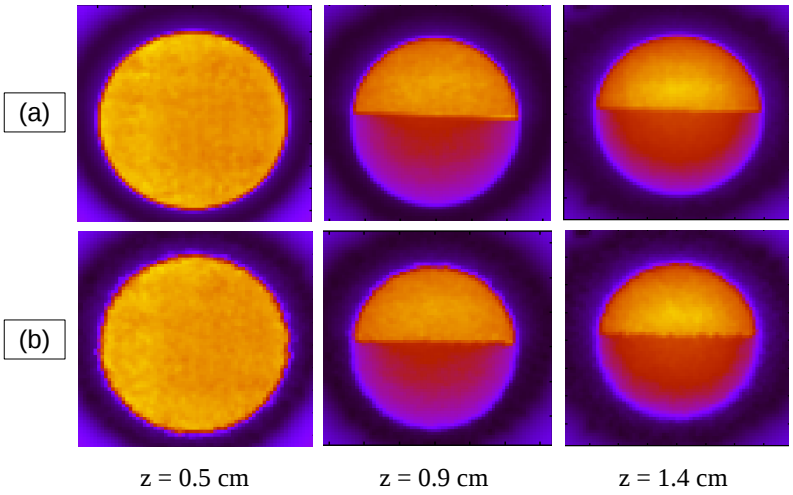

Figure 5.13: 2D dose distributions in the bone phantom at the different measured depths for a 30 mm diameter flat applicator obtained from (a) radiochromic films, (b) penEasy calculation from the reconstructed PHSP file.

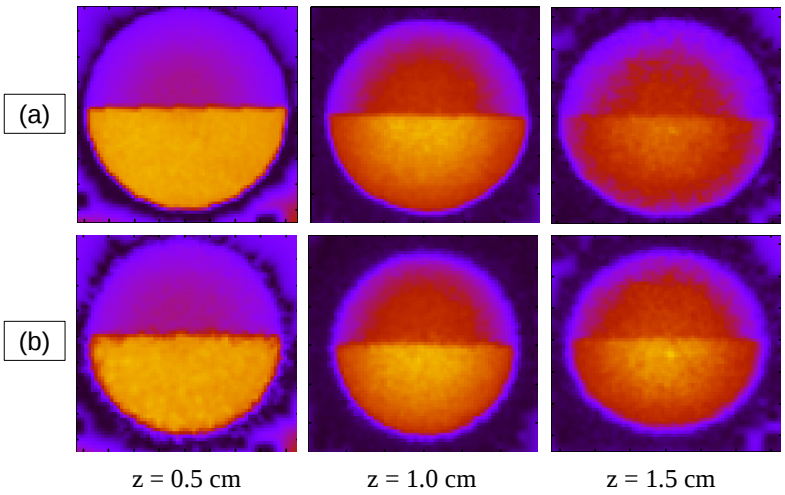

Figure 5.14: 2D dose distributions in the air step at the different measured depths for a 30 mm diameter surface applicator obtained from (a) radiochromic films, (b) penEasy calculation from the reconstructed PHSP file.

Finally, dose distributions were also compared in terms of gamma evaluation with a 2%-2 mm criterion (5% threshold). The results of the evaluation are presented in table 5.4. In the bone phantom, more than 95% voxels passed the evaluation in all the applicators. In the case of the air step, these percentages dropped a little, but even though a good percentage of voxels passed. We can conclude that a reasonable agreement was reached between simulations and measurements.

Gamma evaluation with 2% - 2 mm		
	Air step	Bone
Flat ϕ 10 mm	93.91%	98.79%
Flat ϕ 20 mm	96.67%	99.17%
Flat ϕ 30 mm	96.85%	99.23%
Flat ϕ 40 mm	93.61%	97.80%
Flat ϕ 50 mm	93.37%	97.30%
Surface ϕ 10 mm	94.88%	96.94%
Surface ϕ 20 mm	96.66%	99.38%
Surface ϕ 30 mm	97.54%	99.28%

Table 5.4: Results of gamma evaluation between MC simulations and measurements in the air step phantom and in the bone heterogeneity (5% threshold).

5.3 Validation for IOERT accelerators

5.3.1 Experimental measurements for IOERT accelerators

In the case of IOERT accelerators we had access to fewer experimental data.

Transverse dose profiles and DDPs in water were provided for all the dedicated accelerators, but in the case of heterogeneities, only one set of data from a NOVAC® was provided. These measurements were performed at the Universitätsklinikum Düsseldorf, Germany.

5.3.1.1 Experimental setup and phantom description

As previously said, the set of measurements were based on quality control reports designed for electron beams, such as ECWG report [Shiu et al., 1992] or SEFM report [Rodríguez et al., 2005]. Four different setups were considered:

Solid water step

Several solid water blocks were used to create an air-water step. First, a 10 mm layer was placed in order to create the step. Then there was a 2 mm layer, under which the first film was located, and then other 5 mm layer with the second film. Finally, an appropriate thickness of solid water layers were placed to avoid retro-diffusion (60 mm). In figure 5.15 the schematic location of the films are represented.

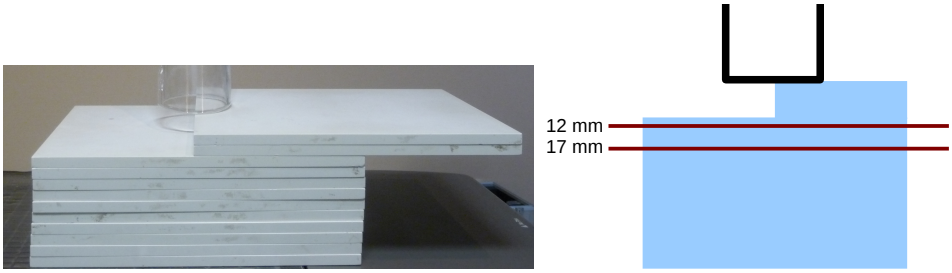

Figure 5.15: Experimental setup (left) of a solid water step measurement and its schematic view with the location of the films (right).

Lung heterogeneity, costal wall type

The first solid water layer was 10 mm thick with a film underneath. Then, another 1 mm thick solid water layer was placed with a film in the interface with the cork. Following this film, two 5 mm-cork layers with films were placed and finally several cork layers were placed for retro-diffusion (30 mm). The schematic view with the film locations is showed in figure 5.16.

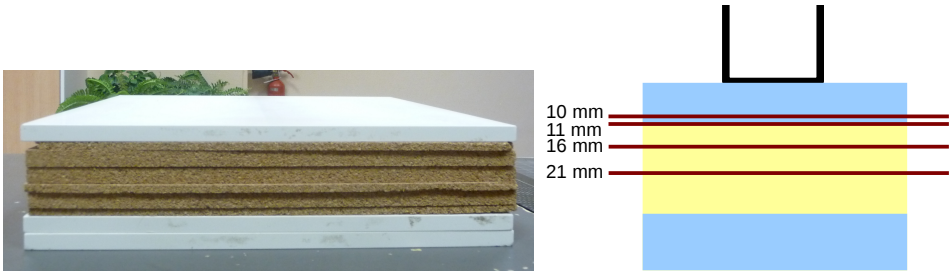

Figure 5.16: Experimental setup (left) of a lung heterogeneity measurement and its schematic view with the location of the films (right).

Heterogeneity mediastinum-lung type

The first solid water layer was 10 mm thick with a film underneath. Then, there was a 5 mm cork and solid water layer with a film, followed by a 10 mm layer with the corresponding film and finally we had a 1 mm solid water layer to see the rebuild-up in the cork part with two films, one before and the other after the layer. After that, some solid water layers were placed for retro-diffusion (60 mm). Details about the location of the films can be seen in figure 5.17.

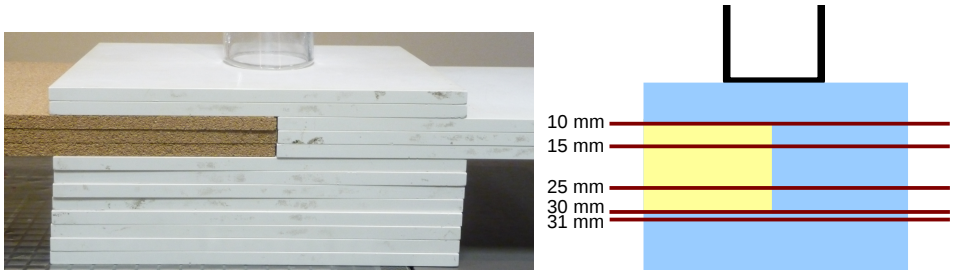

Figure 5.17: Experimental setup (left) of a mediastinum-lung type measurement and its schematic view with the location of the films (right).

3D internal heterogeneity water/bone type

A Teflon block was used to simulate bone. Here only one film was used, just under the Teflon. First, a 10 mm thick solid water layer was placed followed by a $(30\times160\times10)$ mm^3 Teflon block surrounded by solid water layers and the film. Finally, some solid water layers were placed for retro-diffusion (60 mm). The schematic view is shown in figure 5.18.

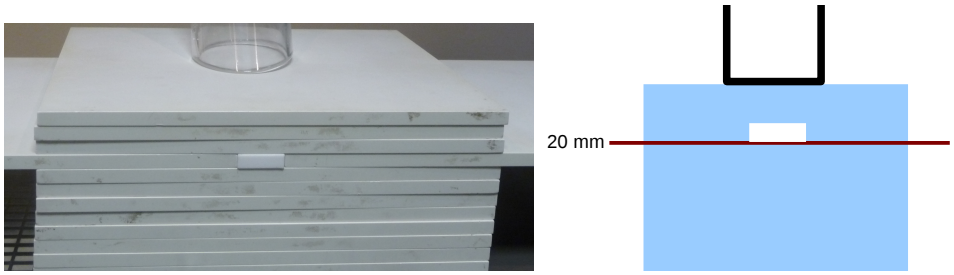

Figure 5.18: Experimental setup (left) of a water/bone type measurement and its schematic view with the location of the films (right).

5.3.2 Dose comparison for IOERT accelerators

Radiophysicists from Universitätsklinikum Düsseldorf provided us with DDPs and transverse profiles in water for all NOVAC® energies and applicators, and regarding the heterogeneous phantoms, they supplied the central transverse profiles extracted from the radiochromic films for a 4 cm diameter applicator and a 9 MeV working energy. Therefore, we will focus the IOERT validation in these heterogeneities.

Furthermore, we extended the validation to include the LIAC® and MOBETRON® accelerators, where dose distributions in heterogeneous phantoms were compared against simulations from detailed accelerators.

5.3.2.1 Dose distributions against measurements

The PHSP file was reconstructed from the experimental DDP for the 9 MeV, 4 cm diameter NOVAC®, following the procedure explained in the previous chapter. This PHSP file was then used to calculate dose distributions in the different heterogeneities with DPM [Sempau et al., 2000]. The volumes were defined by (161×161×200) voxels with 1 mm voxel size, and 200 million histories were simulated.

The results of these simulations can be seen in the following figures, where the transverse profiles from the reconstructed PHSP file are represented against the profiles extracted from the radiochromic films for the different setups. Figure 5.19 shows the results in the solid water step calculation, figure 5.20 corresponds to the costal wall phantom, figure 5.21 to the mediastinum-lung heterogeneity and figure 5.22 to the water/bone phantom.

As it can be seen from the figures, in all the cases a reasonable agreement was reached. A gamma evaluation with 2%-2 mm criterion (5% threshold) was also performed and the results are presented in table 5.5. Despite the low number of dose values to compare, more than 95% of voxels fulfilled the evaluation in most cases. It can be seen from the experimental profiles that some of the measurements present positioning errors, so the accuracy of the comparison was mostly limited by the difficulty of reproducing these misplacements in the simulations.

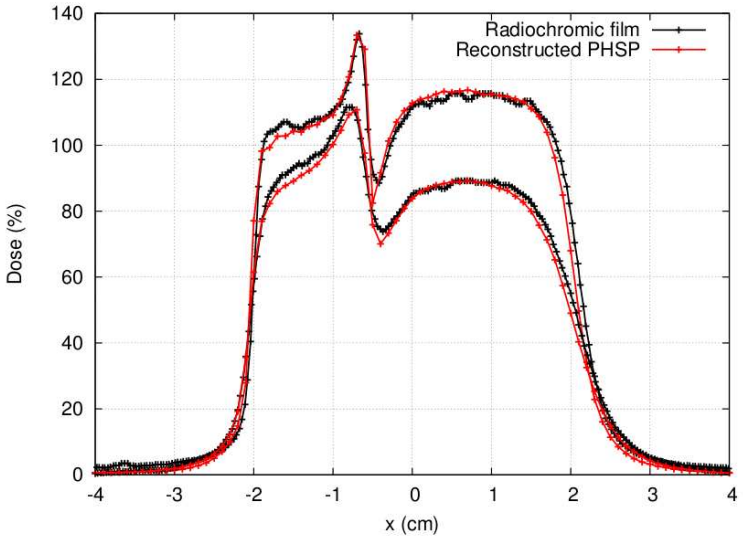

Figure 5.19: Transverse dose profiles at 1.2 (shifted up by 20%) and 1.7 cm depth in the solid water step phantom obtained from the radiochromic films and from the reconstructed PHSP file (NOVAC®, 9MeV, 4 cm ϕ applicator).

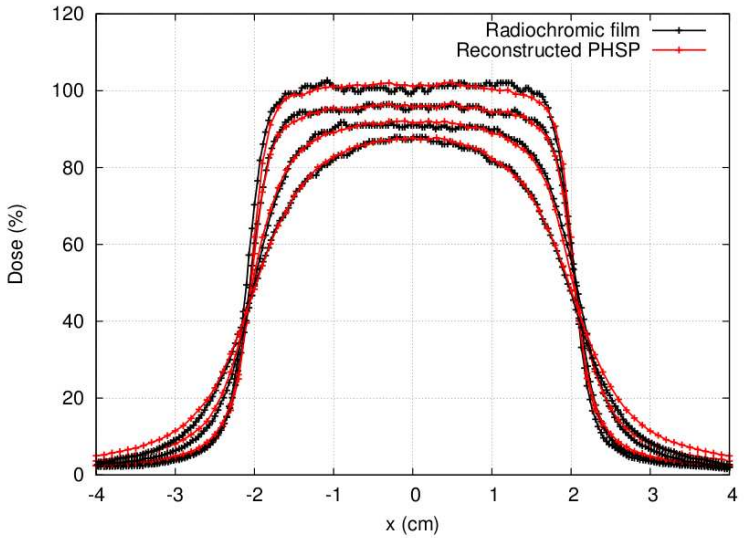

Figure 5.20: Transverse dose profiles at 1.0 (shifted up by 5%), 1.1, 1.6 and 2.1 cm depth in the lung heterogeneity, costal wall type phantom obtained from the radiochromic films and from the reconstructed PHSP file (NOVAC®, 9MeV, 4 cm ϕ applicator).

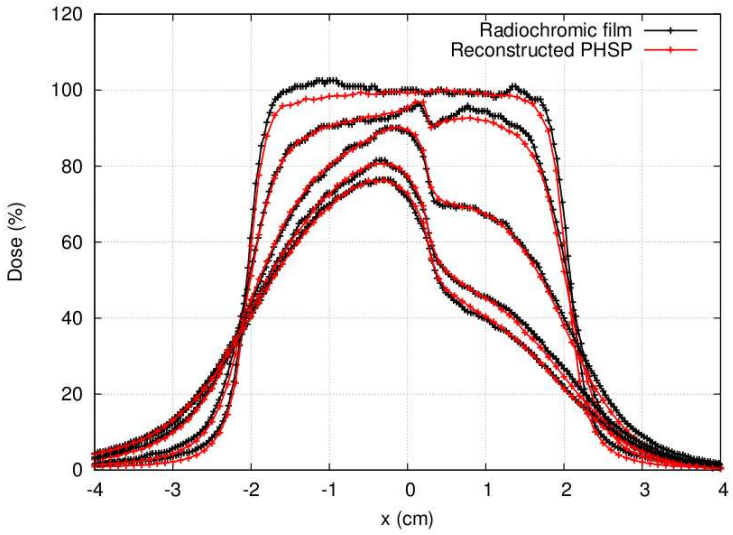

Figure 5.21: Transverse dose profiles at 1.0 (shifted up by 10%), 1.5, 2.5, 3.0 and 3.1 cm depth in the mediastinum-lung type phantom obtained from the radiochromic films and from the reconstructed PHSP file (NOVAC®, 9MeV, 4 cm ϕ applicator).

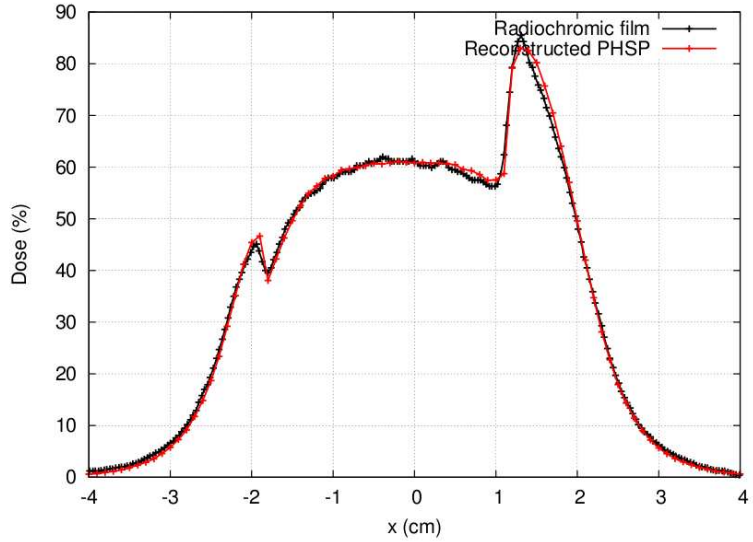

Figure 5.22: Transverse dose profiles at 2.0 cm depth in the water/bone type phantom obtained from the radiochromic films and from the reconstructed PHSP file (NOVAC®, 9MeV, 4 cm ϕ applicator).

Gamma evaluation with 2% - 2 mm	
	NOVAC®, 9 MeV, 4 cm ϕ
Step	96.19%
Costal wall	93.21%
Mediastinum	95.91%
Water/bone	96.92%

Table 5.5: Results of gamma evaluation between MC simulations and measurements in the different phantoms (5% threshold).

5.3.2.2 Dose distributions against simulations

We decided to include in the validation the LIAC® and MOBETRON® accelerators, but as we did not have access to experimental data of these accelerators in heterogeneous phantoms, we compared against simulations.

We used the detailed simulations from chapter 3 of the 6 cm diameter applicator LIAC® and the MOBETRON® with 9 cm diameter applicator and calculated dose distributions with a realistic energy spectrum of 12 MeV (for the LIAC®) and 9 MeV (for the NOVAC®). We used the DDPs from these simulations as the input dose that feeds the genetic algorithm and the monochromatic

DDPs and PHSP files were optimized to generate the fitted PHSP file that was used afterwards in four different heterogeneous phantoms.

The setups used for the validation are shown in figure 5.23. They are very similar to the ones used in the validation with radiochromic films, with the exception of using a phantom with a lead protection disk instead of the costal wall type phantom.

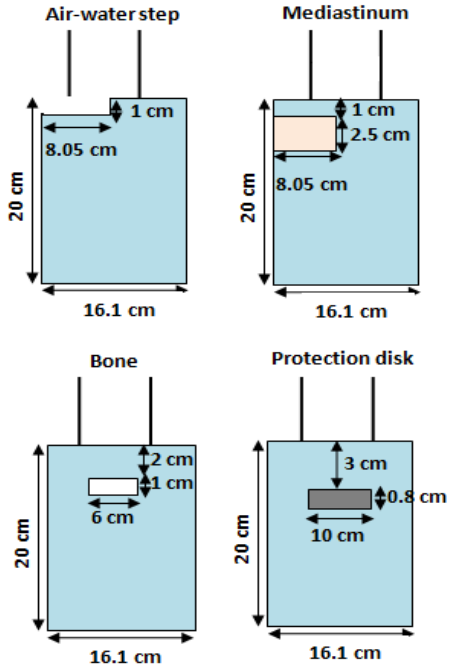

Figure 5.23: Setups where the dose produced by the solution PHSP file and the full MC simulation were compared.

Two sets of simulations were performed for each phantom: One with the optimized PHSP file and the other directly with the PHSP file obtained from the detailed simulation of the accelerators. Dose was calculated in volumes with (161×161×200) voxels (voxel size: 1 mm) and 200 million histories were employed. Figure 5.24 shows two of the results of these comparisons. In figure 5.24 (Left) it is represented the dose comparison in the air-step phantom with the 12 MeV LIAC®, and 5.24 (Right) compared the profiles for the 9 MeV MOBETRON® in the bone phantom.

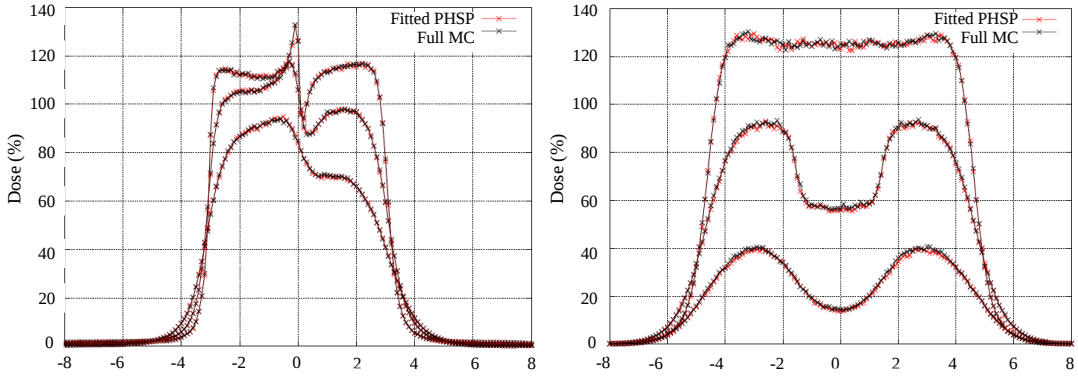

Figure 5.24: (Left) Dose profiles at 1.5 (shifted up by 20%), 2.5 (shifted up by 10%) and 3.5 cm depth in the air-water step phantom for the 12 MeV LIAC®. (Right) Dose profiles at 1.95 (shifted up by 20%), 3.0 (shifted up by 10%) and 4.0 cm depth in the bone phantom for the 9 MeV MOBETRON®

A gamma evaluation was performed, again with the 2%-2 mm criterion (5% threshold). Table 5.6 includes the results of this evaluation. Almost 100% the voxels accomplish the gamma index, because in this case we have eliminated possible inaccuracies in the geometrical positioning of the reference dose.

Gamma evaluation with 2% - 2 mm		
	LIAC® (12 MeV, ϕ=6 cm)	MOBETRON® (9 MeV, ϕ=9 cm)
Step	99.95%	99.81%
Mediastinum	100.00%	100.00%
Bone	100.00%	99.99%
Disk	100.00%	100.00%

Table 5.6: Results of gamma evaluation in the different phantoms (5% threshold).

5.4 Conclusion

In this chapter we have tested the proposed phase space optimization process against experimental data for the different Intrabeam® applicators and the mobile IOERT accelerators. To do this, we have compared dose distributions in water and in heterogeneous phantoms measured at different European hospitals.

For the validation of dose distributions in water with Intrabeam® spherical applicators, we found some discrepancies between simulations and measurements due to the anisotropy of the dose in

the backward direction. The isotropic approach we considered for our spherical dose definition does not reproduce completely the experiment. However, the area presenting the anisotropy is next to the cone of applicator, which is an area without clinical interest, and in any case it should be corrected by introducing an angular-dependent function in the X-rays beam fluence, which is the next approach we want to introduce in future work.

Regarding the dose distributions in water with Intrabeam® flat and surface applicators, we found a good agreement for the two cases studied, with more than 95% of the voxels fulfilling the gamma criterion at the 2%-2 mm level.

In the dose comparisons inside heterogeneous phantoms, either with Intrabeam® applicators or IOERT accelerators, we reached a reasonable agreement at the 2%-2 mm level, specially considering that a non-negligible contribution to the dose differences is attributed to uncertainties in the measurements, such as asymmetries or displacements of the films. When these uncertainties disappear, the agreement increases substantially, something that has been seen in the validation of IOERT accelerators against simulations, where almost a 100% of the voxels passed the 2%-2 mm level in all the phantoms.

Therefore, in view of the results of this chapter, we can conclude that the proposed optimization method works accurately reproducing dose distributions in clinical situations. In fact, it has already been implemented for the tuning of the different IOERT and Intrabeam® devices in ***radiance***® [Valdivieso-Casique et al., 2015, Pascau et al., 2012], the first treatment planning system for intraoperative radiotherapy.

Chapter 6

Hybrid Monte Carlo for dose calculation

6.1 Introduction

The use of intraoperative radiotherapy with low energy X-rays is increasing rapidly in the clinical field, as has been previously explained in this thesis.

However, this technique is currently limited by the inherent difficulties associated with the planning process and until recently there was no commercial tool for 3D planning of the Intrabeam® system (Carl Zeiss Surgical Gmbh, Oberkochen, Germany) that allowed a fast an accurate dose deposition inside the patient. The commercial planning tool that users got with the device was based in isodose curves in water. Even if this procedure works correctly in homogeneous tissues, inaccuracies appear when heterogeneous media are treated. In October 2016 the companies Carl Zeiss and GMV signed a commercial collaboration agreement, and ever since every Intrabeam® machine is being sold with the ***radiance***® treatment planning system (TPS), thus incorporating the TPS codes described in this thesis, fully taking into account patient's anatomy.

Detailed Monte Carlo simulations of miniature 50 keV accelerators have been performed in the past. Simulations of a radiosurgery X-ray tube used to treat brain tumors were done [Yanch and Harte, 1996] with ITS 3.0 code. A Geant4/GATE code suitable to Intrabeam® treatment issues [Bouzid et al., 2015] was also developed, and the Intrabeam® source was modeled with the EGSnrc code [Ebert and Carruthers, 2003].

A high level of accuracy is reached with full Monte Carlo simulations, however it is still a time-

consuming technique and it is not suitable to real-time planning in operating room.

The use of phase space (PHSP) files, as we have discussed previously, reduces the overall computation time because the radiotherapy device and applicators do not need to be simulated for every treatment. Therefore, in order to speed up dose calculation, Clausen *et al.* developed a Geant4-based source model using PHSP files and decreased computation time to 12 minutes for a full gynecological treatment [Clausen et al., 2012]. However, the proposed technique was tested only for water dose calculations and simulation time would increase when applied to more complex geometries with heterogeneities. Moreover, PHSP files could have some disadvantages like lack of flexibility in manipulating the data, huge storage requirement and resources for reading-in the stored data during simulation.

Alternatively, Nwankwo et al. approximated PHSP files by a virtual source model to generate photons for a specific Intrabeam® source defined in Geant4 and a reasonable calculation uncertainty was achieved within 2 hours of simulation [Nwankwo et al., 2013]. Nevertheless, dose computation time is still too long for operating room irradiations or to be implemented in a commercial treatment planning system, and the proposed methods are not prepared for tuning easily every actual X-ray source.

In chapter 4 the procedure to generate an optimized PHSP file tuned to a given Intrabeam® device, using as input just experimental DDP in water has been described. The accuracy of this method has been validated in chapter 5. In the case of IOERT, the DPM code [Sempau et al., 2000] gives an accurate deposited dose in a short time. However, we found that DPM would not be an efficient and fast solution to describe photon interactions in the energy range from 1 to 50 keV.

We thus decided to develop from scratch a new algorithm, named **hybrid Monte Carlo (HMC)**, to calculate dose deposited by the Intrabeam® device within minutes, fully taking into account the different tissues and structures in the region of patient, i.e. as derived from a CT image.

HMC computes an accurate dose for both homogeneous and heterogeneous media [Vidal et al., 2014b,a, Udías et al., 2017b], as it incorporates all the relevant physics processes at Intrabeam® working energies. The savings in calculation time are possible thanks to taking to the extreme some variance reduction techniques. The HMC algorithm has been complemented with PHSP files generated for the needle, spherical, flat and surface applicators.

To face the problem of fast dose calculation, lets first analyze the specifics of the radiotherapy situation we are dealing with, and of the MC simulations in general.

6.2 MC simulations

MC packages assume a stochastic approach to generate particles and to decide the fate of these radiation particles. Probability distributions of the different processes are taken from computations, tables, etc. The particles are generated in random positions and emitted at random directions (following the known distributions) from the primary source in the simulated device. They are tracked by the code, and interaction and evolution of the particles are computed, stochastically, based upon assumed probabilities for different processes (Compton interactions, Rayleigh interactions, photoelectric effect, etc.) to happen.

The random nature of the variables defining every particle we generate introduces a statistical noise, due to the limited amount of particles (histories) we deal with in any actual simulation. In figure 6.1 it is showed a representation of a pure random sampling in a XY plane. If the number of points is very big, the sampling becomes homogeneous, but is the number of points is not big enough, areas with high concentration of points are visible, as well as empty spaces in between, introducing statistical noise.

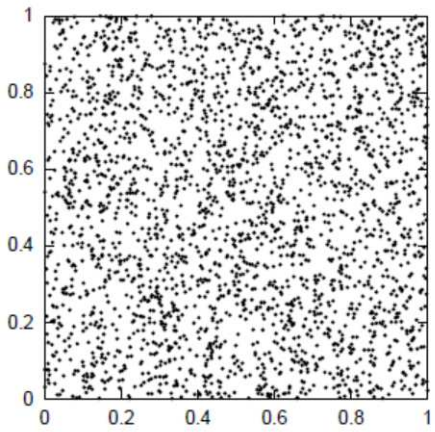

Figure 6.1: Randomly generated coordinates populating a XY plane.

The statistical noise of MC simulations bears no interest in radiotherapy (it is, however, very important to keep it close to the actual statistical level of the real images, when simulating medical imaging devices), as the actual number of particles involved in any radiotherapy treatment, even in regions of low dose (say 5% of the dose at the maximum) is well in excess of 10^{12}, for any realistic treatment. With this in mind, we have taken the idea of condensation of histories to compute the dose not from the number of histories reaching a region, but rather from the relative change of weights of these histories when traveling through this region. We will describe the algorithm in detail in what follows.

6.3 Code description

In the energy region, and with the geometry of the Intrabeam® device, particle interactions are not distributed very uniformly. Particularly for small applicators (the needle case being the extreme), depth dose profiles show a very fast reduction of dose with the distance to the source, in part due to the solid angle effects, but also due to absorption of photons via photoelectric effect. Indeed, after traveling a couple of cm in water, in a typical MC calculation, most of the histories we have produced at the source, and that are being tracked so expensively, will have disappeared and will not contribute to statistical accuracy.

In a traditional MC, to keep a large number of histories in regions away from the source, we would have to produce a very large number of histories at the source. The result would be an oversampling closer to the source, that is, we will have the best precision where we do not need it, and we would spend a lot of time in those regions that already have good precision, in order to improve precision away from the source. The same happens when we include shieldings in the simulation, if we want to obtain accurate readings of the dose after the protection, we must send many histories to the shield, most of which will die without contributing to the result in the region we are interested.

Of course, there are several ways to improve the efficiency of MC simulations under these circumstances, such as factorizing the problem in different regions, using particle splitting when the particles reach the region of interest or stop tracking the particles when the fluence is below a certain threshold. In our tool, we generalized this idea, without the need to adapt it to different tissues or to enable a different detail of simulation when fluences fall below a certain threshold.

Summarizing what we have just said, a regular Monte Carlo will calculate millions of histories, even if they would barely interact or leave energy in the medium, increasing significantly the simulation time. Furthermore, small size, low energy photon sources present very high fluence gradients, which implies high statistics next to the applicator, but very low statistics when the distance to the source increases. Therefore, obtaining an accurate dose distribution with small statistical noise will require very long simulations. We want to improve this situation.

The algorithm we have developed, called **Hybrid MC algorithm, or HMC algorithm**, will include all the relevant physics of a Monte Carlo algorithm minimizing the contribution of statistical noise. The HMC algorithm takes into consideration photoelectric and Compton interactions. Rayleigh interactions are not included because they are not a relevant mechanism for energy deposition at the energies considered here.

Condensed histories and particle splitting approximations will be generalized in this algorithm. We will use meta-histories (m-histories for short) to represent particles, each one of them representing the fate of an arbitrary high number of photons N. Every m-history carries a

weight when it is generated at the source, proportional to the number of photons that should be generated with the given characteristics (energy, position, emission angle). The probability of interaction of this m-history, either by photoelectric (P_{PE}) or Compton effect (P_{CE}), will be computed in a continuum way as 1-e$^{-\mu dx}$, where dx is the spatial displacement in the direction of the m-history since the last update and μ is the attenuation coefficient for the photoelectric or the Compton effects, taken from the material tables of PENELOPE [Salvat et al., 1996], at the spatial point where the updates of m-history position is being done. More information about the material tables generation can be found in the appendix A.

In other words, instead of studying microscopically each interaction, which has a high computational cost, we will condensate many possible interactions into a single one with an accumulated probability which will be the sum of all individual interactions. We will score the accumulated probability of interaction after moving a given step size. After each step, the new weights for the m-history will be computed, taking into account the lost weight by photoelectric and Compton interactions. Moreover, new m-histories, corresponding to secondary photons coming from Compton interactions, can be generated with the corresponding weight, and stacked in the pile for calculating them in the same way as primary photons.

Thus, condensed histories (m-histories) of the photons at the source are generated from the information stored in the PHSP files, and transported throughout the volume in steps of fixed length dx, whose value is typically smaller than half the voxel size. At each step, a fraction of the m-history will interact, being absorbed by photoelectric effect or being scattered by Compton effect. Each condensed history updates its weight as it travels through matter, according to the weight lost until the moment.

This way, the number of m-histories remains constant along the volume, being only its weight reduced at each interaction, so that the number of m-histories does not decrease far from the source due to photon absorption. Dose is computed not from the number of interactions or the number of photons who are absorbed in a region, but rather from the accumulated reduction of the weight of the m-histories as they travel through the region. Therefore, problems associated with low statistics are reduced, as we have always the same number of primary virtual histories, no matter how much attenuation the material offers. Due to the fact that we follow in a detailed way the trajectory of all m-histories and that we produce also secondary m-histories, our simulation will be able to reproduce all the relevant phenomena related to interaction of radiation in media such as backscatter, build-up or diffraction.

Consequently, the following aspects are included in the simulation:

- The m-histories approximation. Every primary m-history represents the fate of many photons. The m-history can scatter or undergo photoelectric effect, with a given probability, and the weight of the m-history is shared among the different secondary particles that this m-history can produce. Weights are updated after each spatial time progression.
- Photoelectric forced interaction. After each simulation step, a fraction of the energy of

the primary m-history is deposited in the voxel and the new weight w of the m-history is $w(1\text{-}P_{PE})$.

- Compton scattering is implemented by creating N secondary m-histories, each of them with a fraction w/N of the initial weight w of the particle and weighted by the associated probability of the primary m-history of experiencing a Compton interaction, from the previous computed position.
- A fluence normalization has been implemented to reduce dose artifacts due to poor statistics or suboptimal sampling of the region of interest.

6.3.1 Photoelectric effect

In a photoelectric interaction, the photon is absorbed and an electron is emitted. At each step of the simulation, a fraction of each m-history will suffer a photoelectric interaction, decreasing the weight of the m-history. The energy of the emitted electron is very low, as well as it is its range, so we assume that it is absorbed in the same voxel where the interaction is being assigned.

Therefore, the deposited energy will be the product of the weight of the m-history, the energy of these m-histories, and the probability of a photoelectric absorption after a distance dx has been traveled in the material.

$$dW = N \cdot E \cdot (1 - e^{-\mu_{ph} dx}) \tag{6.1}$$

The beam intensity (weight) after the m-history has traveled a distance dx will be decreased by a factor $e^{-\mu_{ph} dx}$:

$$N' = N \cdot e^{-\mu_{ph} dx} \tag{6.2}$$

6.3.2 Compton effect

In a Compton interaction, part of the energy of the incident photon is transferred to an emitted electron. As it was the case for the photoelectric effect, the energy of the released electron is very low and thus we assume that it is immediately absorbed at the voxel where the interaction took place. The weight associated to the scattered photons disappears from the weight of the primary m-history, and secondary m-histories will be produced with their corresponding weight and energy. These photons will have even less energy than the primary beam and thus they will interact almost exclusively by photoelectric effect, relatively near to the place where they were

created. The primary m-history keeps traveling through the volume with the same direction, but with an updated weight and the same initial energy.

Similarly to the photoelectric effect, the deposited energy will be the product of the weight of the primary m-history, the average energy lost in the Compton interaction (into the electron that is locally absorbed) and the Compton interaction probability when a distance dx is traveled in the material:

$$dW = N < E_{ave}(Compton) > (1 - e^{-\mu_c dx}) \tag{6.3}$$

And the weight of the primary m-history after traveling a distance dx will be decreased by a factor $e^{-\mu_c dx}$:

$$N' = N \cdot e^{-\mu_c dx} \tag{6.4}$$

Regarding secondary photons created during Compton interactions, they are also treated as m-histories. The weight corresponding to each secondary m-history is split into $N_{Compton}$ different m-histories, each one of then with a fraction of the original weight $w/N_{Compton}$. They would be emitted in different angles and with different energies, according to the energy-angle relationship for the Compton effect on bound electrons. However, at these low energies, the angular distribution is essentially isotropic and thus secondary photons are emitted along uniformly distributed random directions.

The energy deposited by the secondary particles is calculated analogously to the one of the primary particles, after photoelectric or Compton interactions. Now, as said before, these secondary particles have lower energy. If for the primary particles, the most likely energy is of the order of 30 keV, and the maximum photon energy is 50 keV, for the secondary particles, the large majority of photons are below 30 keV and thus they decay mostly via photoelectric absorption. For speed reasons, the code has been limited to *first and a half order Compton interactions*, meaning that Compton interactions of the secondary photons would not produce traceable tertiary photons, but rather null-range tertiary photons that, as it is case for secondary or tertiary electrons, are assumed to deposit all their energy in the same voxel than they were generated.

We have compared the results of this first and a half order Compton interaction with a second and a half Compton interaction version of the code, and indeed we have verified that the changes in the computed dose are very small, while the increase in simulation time can be noticeable. Figure 6.2 shows the comparison of two depth dose profiles (DDPs) for a 1.5 cm diameter spherical applicator. The first dose distribution (solid line curve) was calculated with the first and a half Compton interaction, and for the second one (dotted line) two and a half Compton interactions

were considered. It can be seen that including in the simulation a whole second Compton vertex does not affect significantly the dose distributions, with differences between both curves well below 1%. Thus, it is the first and a half Compton interactions version of the code the one that has been implemented in ***radiance***® and, unless otherwise indicated, the one we would use in the remainder of this work.

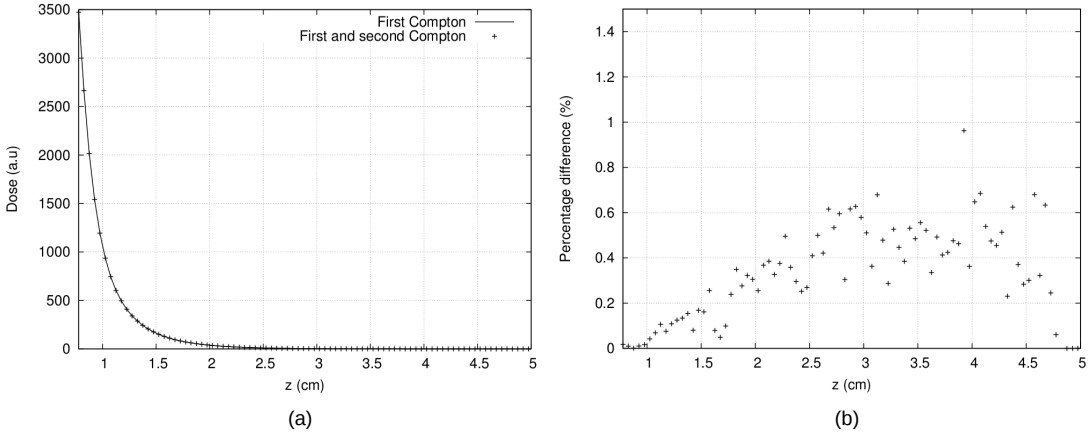

Figure 6.2: (a) Comparison of DDPs of a 1.5 cm diameter spherical applicator with a single full Compton interaction (solid line) and with two full Compton interactions (dots). (b) Statistical difference between the two profiles in (a).

6.3.3 Study of the zero range approximation for electrons

A MC study has been performed to evaluate the range of electrons with energies up to 50 keV in different media. For all the energies, more than 99% of electrons are absorbed before 0.25 mm. Therefore, in the case of the electrons emitted by photoelectric or Compton interactions, it is reasonable to consider that they are absorbed in the same voxel as they are generated, provided voxel sizes are not much smaller than 0.25 mm.

6.3.4 Flow chart of the code

A simplified flow chart of the HMC can be seen in figure 6.3. After each update of the position along the trajectory of the m-history, given by dx, the probabilities of photoelectric and Compton interactions are calculated for every condensed history. The absorbed energy due to the photoelectric interaction and to the secondary electron from the Compton interaction are stored within the interaction voxel. Compton secondary photons are generated randomly and at each dx step, photoelectric and Compton probabilities are calculated, and the energy due to photoelectric absorption and secondary Compton electrons is stored in a similar way as

for the primary photon m-histories. Finally, deposited dose is calculated and fluences (weights) are updated from the weights of the previous step, minus the weight that has decayed due to photoelectric and Compton interactions.

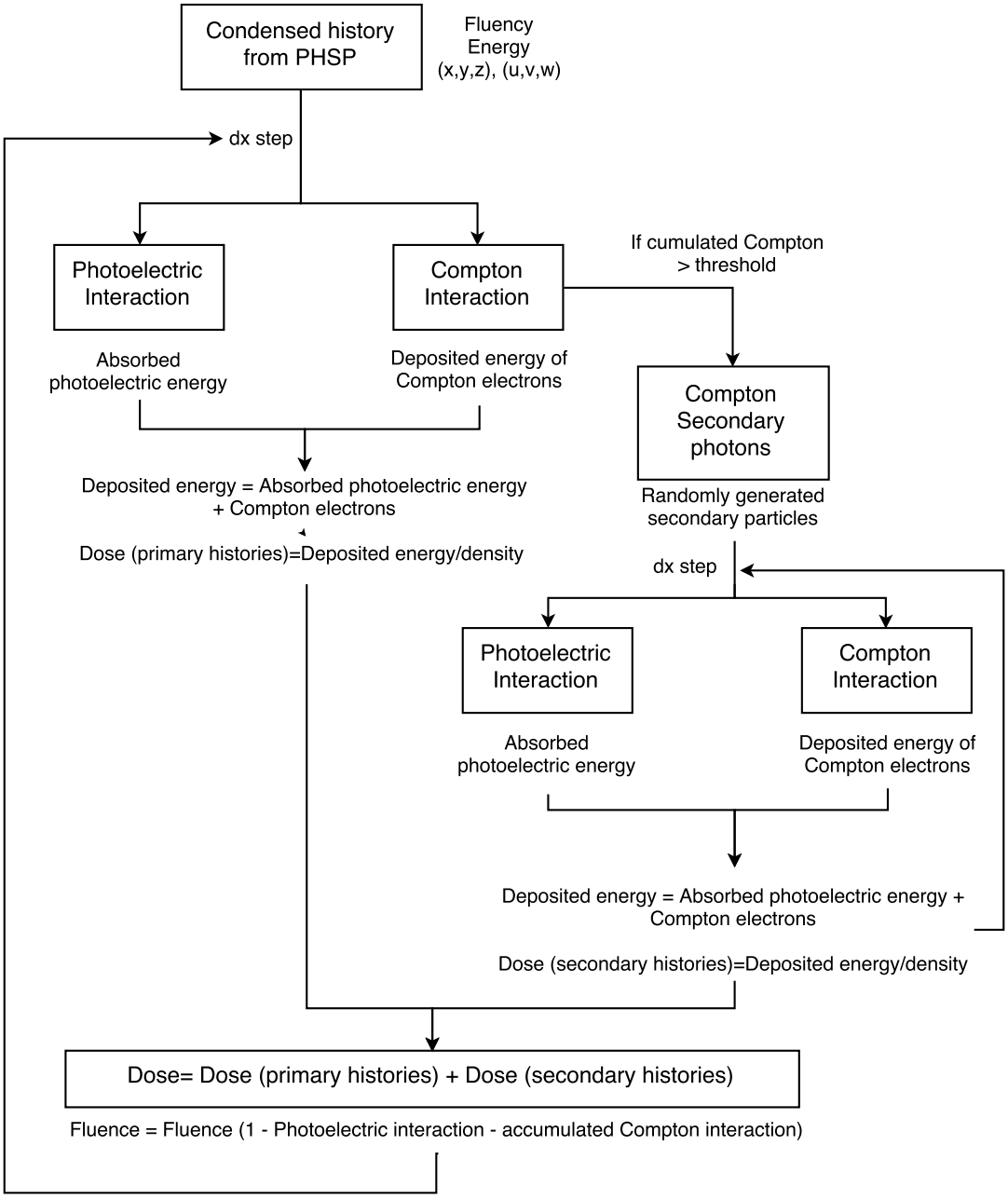

Figure 6.3: Flow chart of the HMC.

6.4 Dose normalization

The use of m-histories, each one of them representing a high number of photons, and the fact that these primary histories never die away, only their weight gets reduced, makes possible a large reduction of the statistic noise, for the same number of primary particles, when comparing to a pure MC calculation. Statistical noise comes now almost exclusively from the fact that the number of secondary photons is finite and that the emission angles are random.

If the number of primary m-histories is not big enough, ray patterns may appear in the dose image. This is due to, on the one hand, the stochastical procedure that is used to pick histories inside the PHSP file. If only few histories are chosen, the initial angular distribution may not be just homogeneous enough. And as typically seen in pure random sampling (see figure 6.1 with the XY points where one can see clusters and empty spaces), it is likely that two m-histories are produced very close to each other, thus producing a high-intensity ray-like artifact, while there are angular ranges left without any m-history, producing a low-intensity ray-like artifact. On the other hand, artifacts in dose computation may also appear due to the use of voxelized geometries and the subsequent subsampling leading to aliasing artifacts, more apparent if a very low number of m-histories is used. The trajectories of the m-histories have different inclinations within a finite number of angles in the PHSP file. The angle of the history with respect to the orientation of the Cartesian grid has an impact in the path length of the history inside a given voxel. This makes that different voxels present an apparent higher number of interactions than others, even if they are at the same distance to the source.

In standard MC codes these patters are not appreciated, because the step taken to update particle position, their emission angles, and the resulting angles after interactions are purely stochastic. Statistical noise is clearly present in standard MC, and thus no ray-like patterns are visible.

Figure 6.4 shows a comparison of dose distributions for a 40 mm spherical applicator with penEasy and HMC using different number of (m-)histories. When using HMC, we can see that the streak or radial artifact decreases with the number of histories. When using penEasy, no patterns are appreciated, but the dose is very noisy, even when 5 million histories are used (Figure 6.4 (b)).

In order to solve this problem, a fluence normalization for the primary histories has been incorporated in the code. As m-histories never die inside the region considered, it is possible to know the number of m-histories that have traveled through every voxel of the volume, and how many interactions have taken place in each voxel. And this is independent on the materials the region is made of. Different materials, thus different absorptions, would only affect the weights, but not the fluence of the number of m-histories. Therefore, for a given source, the number of m-histories in a region is identical if the region is made out of water or if it has heterogeneities. This means that this number of m-histories, and moreover, the number of interactions of these

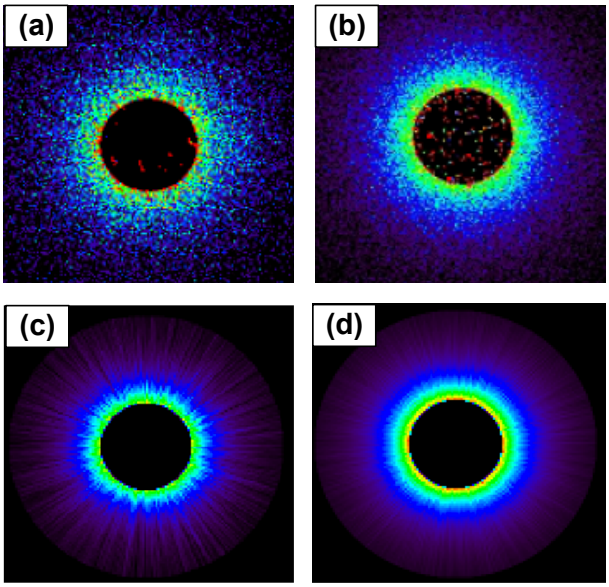

Figure 6.4: Comparison of dose distributions calculated with penEasy and the HMC algorithm for different number of histories or m-histories. (a) penEasy simulation with 0.5 million histories, (b) penEasy simulation with 5 million histories, (c) HMC simulation with 0.5 million m-histories, (d) HMC simulation with 5 million m-histories.

m-histories at every voxel, is known beforehand with the information of the PHSP file, and it is independent of the composition of the region where dose is being computed. Thus, we can calculate *a priori* the number of m-histories and interactions that should correspond to each voxel from the known source fluence (say, for example, in a spherical source for which the flux of histories decreases following an inverse-square law). These two facts make possible to apply a normalization to the dose that will remove the artifacts described before and will generate an accurate, artifact-free dose using a much smaller number of primary m-histories. The only requisite is that, of course, in every voxel where we want to compute the dose, interactions must have been recorded.

The normalization will be done by comparing the number of interactions inside each voxel for the HMC calculation, with the estimated value based on the known fluence. As explained before, this comparison is meaningful only if the primary m-histories in the HMC do not disappear, no matter how small is their associated weight.

Thus, a *normalization* volume will be generated, *norm(x,y,z)*, and the value for each voxel will be incremented by an unit each time a m-history interacts inside the voxel, *irrespectively of its weight*. This matrix volume contains the actual fluence (how many rays travel through a given voxel for a particular source, effects of anisotropy and homogeneity) in the HMC calculation, and it is influenced by effects of sampling imperfections due to aliasing, statistical fluctuations, irregularities in the PHSP file sampling, subsampling or others, in exactly the same way as the

deposited dose is. The difference is that the dose accumulates interactions weighted by the weight of the m-histories and the interaction probabilities.

As it has been already said, in the HMC the fluence of primary m-histories in dose calculation will only depend on the fluence at the source, not on medium heterogeneities. The dose effect due to heterogeneities will be reflected in the associated weights, that will be updated after each interaction and that are adjusted dynamically as the particle travels in the medium.

In the normalized implementation of the algorithm, the dose accumulated in each voxel is divided by the voxel normalization, removing to a high extent sampling error and aliasing effects. But taking this ratio also removes the dependence on the fluence of m-histories from the accumulated dose. To recover it, the normalized accumulated dose has to be multiplied by the ideal fluence for the given source and a homogeneous material.

To clarify more the method, we will apply it for the case of isotropically emitting sources, representing ideal spherical applicators, and for flat and surface applicators. As we have just said, the normalized dose will be computed as:

$$normalized\ dose(x,y,z) = \frac{dose(x,y,z)}{norm(x,y,z)} fluence(x,y,z) \tag{6.5}$$

Where *fluence(x,y,z)* is the fluence of an identical source as the one considered here, traveling through an homogeneous, non attenuating medium, let's say in vacuum.

6.4.1 Calculation of the expected fluence for spherical applicators

In spherical applicators there is a localized source in space emitting particles with fluence $f(\theta,\phi)$ per surface unit. We assume that fluence does not depend on the azimuthal angle ϕ, that is, we are assuming that the spherical sources exhibit, at least, rotational symmetry. This assumption can be removed if needed, but we will keep it here for the purpose of simplicity in the explanation of the normalization procedure.

The number of primary m-histories passing through a differential area dS is $f(\theta)dS$, being $dS=r^2 sin(\theta)d\theta d\phi$. $f(\theta)$ can be obtained by making a histogram in θ of the PHSP file. If we consider the source isotropic, there is no dependence on θ. This way, the expected fluence can be obtained with a simple analytical expression.

Let us consider a spherical shell covering all the angles. If N rays are generated, the number of

rays per surface unit will be

$$\frac{N}{4\pi R^2} \tag{6.6}$$

On the other hand, if every ray is sampled longitudinally every *dl*, in a spherical shell with radius *dR* there will be *dR/dl* samples per each ray traversing it. Therefore, in total there will be *N(dR/dl)* samples within the spherical shell with radius *dR*.

The volume of the spherical shell is:

$$dV = 4\pi R^2 dR \tag{6.7}$$

Then, the density of sampling points within the spherical shell will be:

$$density = \frac{Number\ samples\ shell}{Shell\ volume} = \frac{N\frac{dR}{dl}}{4\pi R^2 dR} = \frac{N}{4\pi R^2 dl} \tag{6.8}$$

Therefore, the number of samples corresponding to a voxel with volume f^3 will be the density described in equation 6.8 multiplied by the voxel volume, or:

$$fluence = \frac{N \cdot f^3}{4\pi R^2 dl} \tag{6.9}$$

The dose per m-history will be:

$$\left[\frac{dose(x,y,z)}{norm(x,y,z)}\right]\left[\frac{1}{N}\right]\left[\frac{Nf^3}{4\pi R^2 dl}\right] \tag{6.10}$$

Finally, the normalized dose can be written as:

$$normalized\ dose(x,y,z) = \frac{dose(x,y,z)}{norm(x,y,z)}\frac{f^3}{4\pi R^2 dl} \tag{6.11}$$

Image 6.5 shows the effect of the normalization of the dose for a 3 cm diameter spherical applicator and 5 million m-histories. When the normalization is applied, the dose distribution shows the expected angular uniformity and no artifacts are visible.

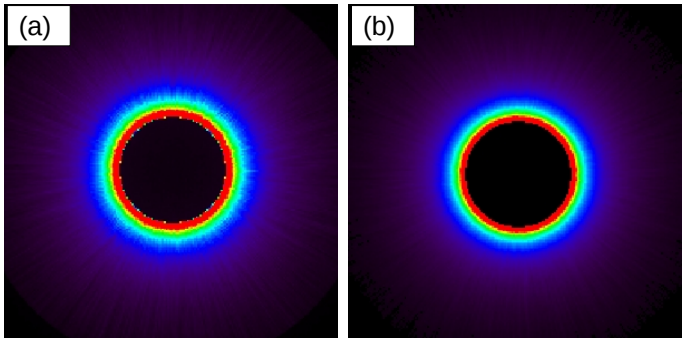

Figure 6.5: Effect of normalization on a 3 cm diameter spherical applicator dose distribution calculated with the HMC algorithm and 5 million m-histories. (a) Unnormalized dose, (b) normalized dose.

6.4.2 Calculation of the expected fluence for flat and surface applicators

In flat and surface applicators, the source is located at a known position inside the applicator and the beam goes through different filters before reaching the surface of the applicator. Therefore, in this case there are no simple analytical expressions to obtain the expected fluence.

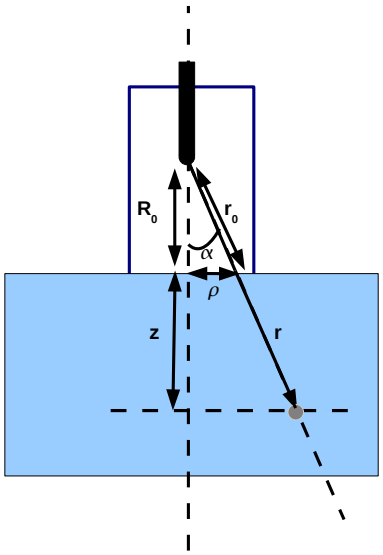

Figure 6.6: Schematic representation of the parameters that characterize the fluence in flat and surface applicators.

The number of particles reaching a voxel is going to be determined (see figure 6.6) by the emission

angle α, that defines each particle's position with respect to the origin. Therefore, normalization is going to depend on α and is going to decrease as $1/r^2$.

$$f(\alpha)\frac{r_0^2}{r^2} \tag{6.12}$$

With:

$$r_0 = \frac{R_0}{cos(\alpha)} \;\; and \;\; r = \frac{R_0 + z}{cos(\alpha)} \tag{6.13}$$

The angle α needs to be corrected to remove the dependency of the number of particles with ρ. The normalization will have the following aspect:

$$\frac{f(\alpha)}{\rho}\frac{R_0^2}{(R_0 + z)^2} \tag{6.14}$$

The angular fluence factor is extracted from the PHSP file. Taking advantage of the symmetry of the reference dose, two normalization histograms are computed: One stores the volume of the number of interactions in Cartesian coordinates (*norm(x,y,z)*) that will be used to correct the reference dose, and the other stores the 2D-surface containing the fluence normalization in cylindrical coordinates (*norm(ρ,z)*) that will be used to reintroduce the fluence in the dose after normalizing by the 3D-normalization volume.

The normalization in cylindrical coordinates contains the ideal fluence of the photons emitted from the source, after going through the flat and surface filters, and therefore we expect if to be a rather smooth function with the angle, so we can filter the *(ρ,z)* 2D-histogram to avoid possible patterns that may still remain in it due to finite size of bins in ρ and z.

Finally we need to consider the number of interactions per unit of volume, which will be the voxel volume (f^3) for the Cartesian normalization, and the volume of the ring between ρ and ρ+$d\rho$ with a width dz for cylindrical normalization ($\pi[(\rho+d\rho)^2$-$\rho^2]dz$).

With all this, the normalized dose will be obtained from the following expression:

$$normalized\ dose(x,y,z) = \left[\frac{dose(x,y,z)}{\frac{norm(x,y,z)}{f^3}}\right]\left[\frac{norm(\rho,z)}{\pi[(\rho+d\rho)^2 - \rho^2]dz}\right] \tag{6.15}$$

Image 6.7 shows the effect of the normalization of the dose for a 2 cm diameter surface applicator and 5 million m-histories. As in spherical applicators, the dose distribution after normalization is as smooth as expected, and the streak and aliasing artifacts disappear.

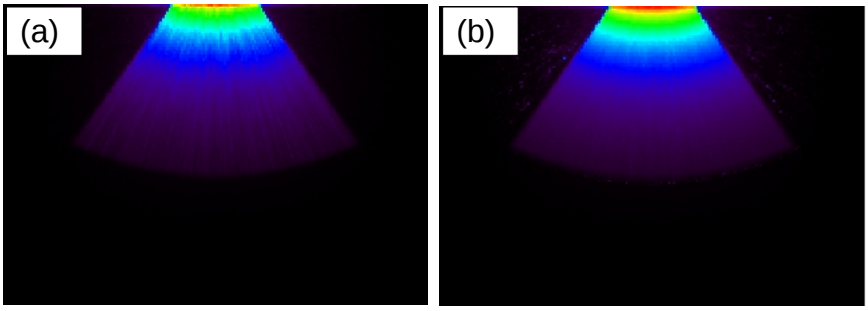

Figure 6.7: Effect of normalization on a 2 cm diameter surface applicator dose distribution calculated with the HMC algorithm an 5 million m-histories. (a) Unnormalized dose, (b) normalized dose.

6.5 Validation of the Hybrid Monte Carlo against MC simulations

Several tests have been performed in order to validate the HMC for every applicator. For each validation case, the same PHSP file has been used to calculate dose with penEasy and with HMC. These reference phase space files have been obtained with penEasy [Sempau et al., 2011, Badal Soler et al., 2008] from realistic simulations of the different Intrabeam® applicators, and have been then used to compare dose distributions from both codes in homogeneous and heterogeneous phantoms.

6.5.1 Hybrid Monte Carlo for spherical applicators

First of all, we calculated the PHSP files for all spherical and needle applicators, in order to use them afterwards for the comparison between penEasy and HMC. These PHSP files were obtained considering the spherical approximation explained in section 3.2.2.1, and the X-ray source was characterized by the energy spectrum extracted from the detailed XRS simulation of section 3.2.1.

With these PHSP files we calculated our reference dose distributions with penEasy in the different validation phantoms. For all penEasy calculations, 500 million histories were used and phantoms of (5×5×5) cm^3 were generated (volumes of (200×200×200) voxels, with a voxel size of 0.5 mm).

The PHSP files were also used to obtain dose distributions with the HMC. These calculations were done simulating 5 million histories in (5×5×5) cm^3 phantoms, also with a voxel size of 0.5 mm.

We also included a quantitative evaluation of the dose. For all validation cases, a gamma index calculation was computed to compare 3D dose distributions with different dose distance criteria: 1%-1 mm, 2%-1 mm and 5%-1 mm.

6.5.1.1 Homogeneous phantoms

Dose was computed in water, lung and bone phantoms, as shown in figure 6.8. The dose distributions from full MC simulations were compared to the dose distributions obtained by the HMC in the same conditions for all spherical applicators, including the needle applicator.

Figure 6.8: Schema of the homogeneous phantoms surrounding the spherical or the needle applicators.

Some results of DDPs and 2D dose maps can be seen below. Figure 6.9 shows the transverse view of the dose and the DDPs in water for a 15 mm diameter spherical applicator using penEasy and the HMC. The same information can be seen in figure 6.10 for a dose calculation in lung with a 40 mm diameter applicator, and in figure 6.11 for a dose calculation in bone with a 30 mm diameter applicator.

We can see that, in all the cases presented, dose distributions with the HMC show a good agreement with the reference penEasy distributions, reproducing appropriately the dose falloff in the different materials.

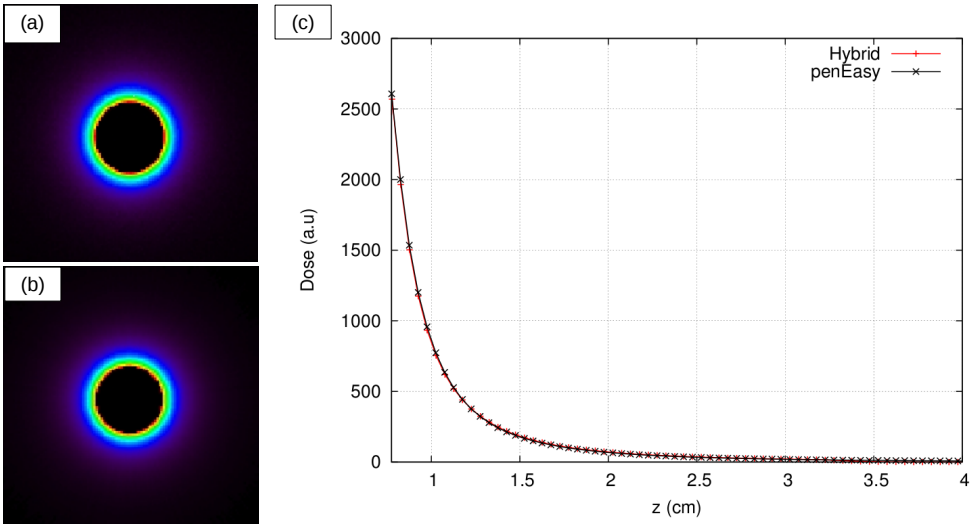

Figure 6.9: 2D dose distributions in water for a 15 mm diameter spherical applicator using (a) penEasy and (b) the HMC and their DDPs (c).

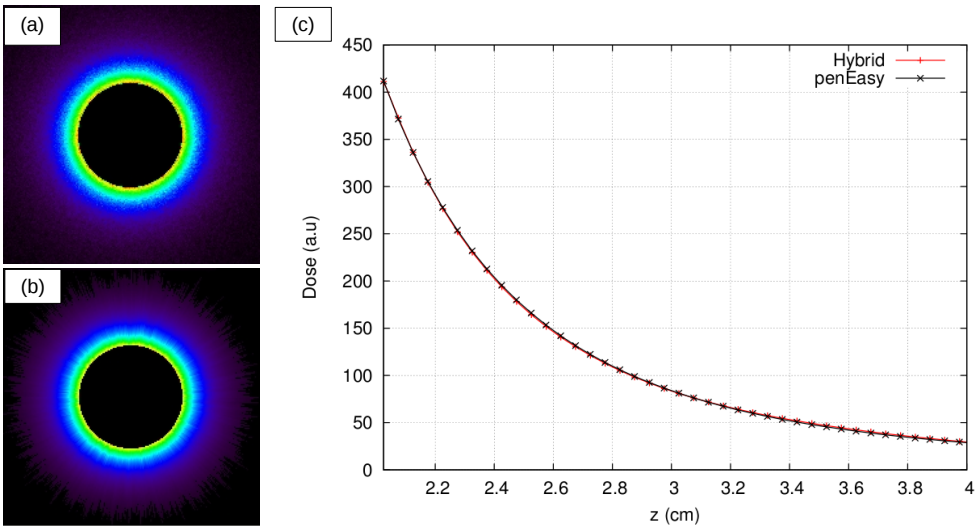

Figure 6.10: 2D dose distributions in lung for a 40 mm diameter spherical applicator using (a) penEasy and (b) the HMC and their DDPs (c).

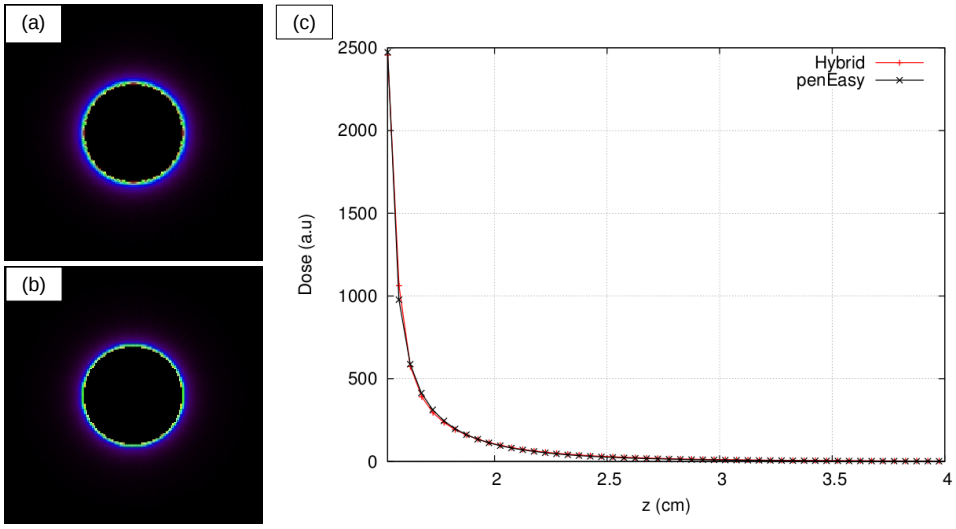

Figure 6.11: 2D dose distributions in bone for a 30 mm diameter spherical applicator using (a) penEasy and (b) the HMC and their DDPs (c).

Gamma evaluations have been performed for all cases with 1%-1 mm, 2%-1 mm and 5%-1 mm criteria. The results are presented in the following tables.

Gamma evaluation in water

	1% - 1 mm	2% - 1 mm	5% - 1 mm
Needle	96.13%	98.50%	99.51%
Spherical ϕ 15 mm	95.81%	98.11%	99.40%
Spherical ϕ 20 mm	96.22%	98.84%	99.77%
Spherical ϕ 25 mm	96.47%	98.86%	99.75%
Spherical ϕ 30 mm	96.38%	99.25%	99.91%
Spherical ϕ 35 mm	95.69%	99.21%	99.97%
Spherical ϕ 40 mm	95.84%	99.04%	99.99%
Spherical ϕ 45 mm	97.02%	99.47%	99.98%
Spherical ϕ 50 mm	95.78%	99.23%	99.98%

Table 6.1: Results of gamma evaluation between MC simulations and HMC calculations in water (5% threshold).

Gamma evaluation in lung			
	1% - 1 mm	2% - 1 mm	5% - 1 mm
Needle	95.84%	98.59%	99.59%
Spherical ϕ 15 mm	98.05%	99.44%	99.90%
Spherical ϕ 20 mm	98.52%	99.73%	99.96%
Spherical ϕ 25 mm	98.52%	99.80%	99.97%
Spherical ϕ 30 mm	98.40%	99.80%	99.97%
Spherical ϕ 35 mm	97.95%	99.70%	99.99%
Spherical ϕ 40 mm	96.59%	99.24%	99.96%
Spherical ϕ 45 mm	97.91%	99.71%	99.98%
Spherical ϕ 50 mm	97.19%	99.52%	99.91%

Table 6.2: Results of gamma evaluation between MC simulations and HMC calculations in lung (10% threshold).

Gamma evaluation in bone			
	1% - 1 mm	2% - 1 mm	5% - 1 mm
Needle	86.03%	91.59%	95.57%
Spherical ϕ 15 mm	87.31%	92.38%	96.99%
Spherical ϕ 20 mm	86.49%	92.58%	97.46%
Spherical ϕ 25 mm	85.51%	92.62%	97.81%
Spherical ϕ 30 mm	85.86%	92.38%	97.91%
Spherical ϕ 35 mm	86.58%	92.23%	98.35%
Spherical ϕ 40 mm	87.02%	92.46%	97.88%
Spherical ϕ 45 mm	87.63%	92.97%	98.38%
Spherical ϕ 50 mm	88.37%	93.67%	98.75%

Table 6.3: Results of gamma evaluation between MC simulations and HMC calculations in bone (5% threshold).

The best results of the gamma evaluation correspond to the water and lung measurements. In these phantoms, all applicators fulfill the most restrictive criterion (1%-1 mm) with more than 95% voxels with $\gamma < 1$. The worst evaluation is obtained with the bone phantom, where only around 90% voxels pass the 2%-1 mm criterion for the spherical applicators. We have to go to the 5%-1 mm criterion to obtain results above 95%.

The bone phantom presents the highest dose gradients of all the materials studied in this section. Actually, if we look at the DDPs in figure 6.11, we can see an 80% drop of the dose only in the first 3 mm. This can produce high dose differences in the gamma evaluation, even if the behavior of the dose distributions seems to be very similar, because we can find dose differences of about 10% in the distance between the beginning and the end of a 0.5 mm voxel. Furthermore, if the falloff of the dose is quicker than in other cases, it means that the dose threshold imposed in the gamma evaluation is reached sooner in depth, and therefore the number of voxels contemplated in the gamma evaluation is lower.

6.5.1.2 Heterogeneous phantoms

Dose was computed in heterogeneous phantoms representing possible clinical situations. In the first situation, the applicator was simulated surrounded by water, a layer of bone 1.5 mm thick, and then water, representing a surface cancer. The second situation represented a spinal metastasis with the applicator surrounded by lung, then a layer of bone 1.5 mm thick, and then lung. And the last phantom represents a breast cancer treatment with the applicator surrounded by water, then a layer of bone 1.5 mm thick, and then lung. The scheme of the three phantoms is presented in figure 6.12.

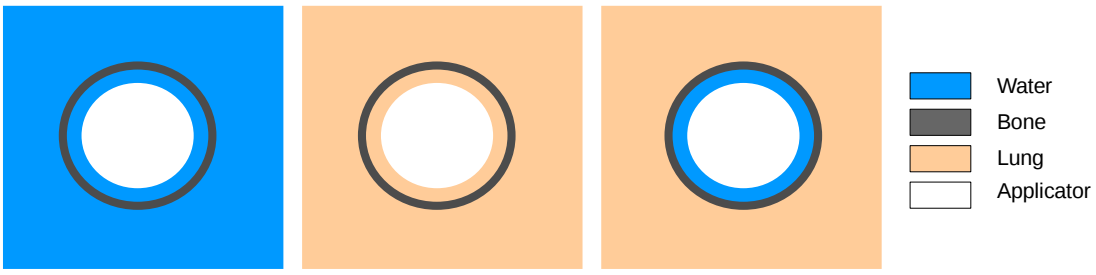

Figure 6.12: Schema of the heterogeneous phantoms surrounding the spherical or the needle applicators.

As in the previous section, we show some of the obtained results of DDPs and 2D dose maps. In figure 6.13 the comparison of the transverse dose view calculated with penEasy and with the HMC for the needle applicator in the water/bone phantom is shown, as well as the DDPs. The same comparisons are shown in figure 6.14 in the case of a 50 mm diameter spherical applicator in a lung/bone phantom, and in figure 6.15 for a 20 mm diameter spherical applicator in a water/bone/lung phantom.

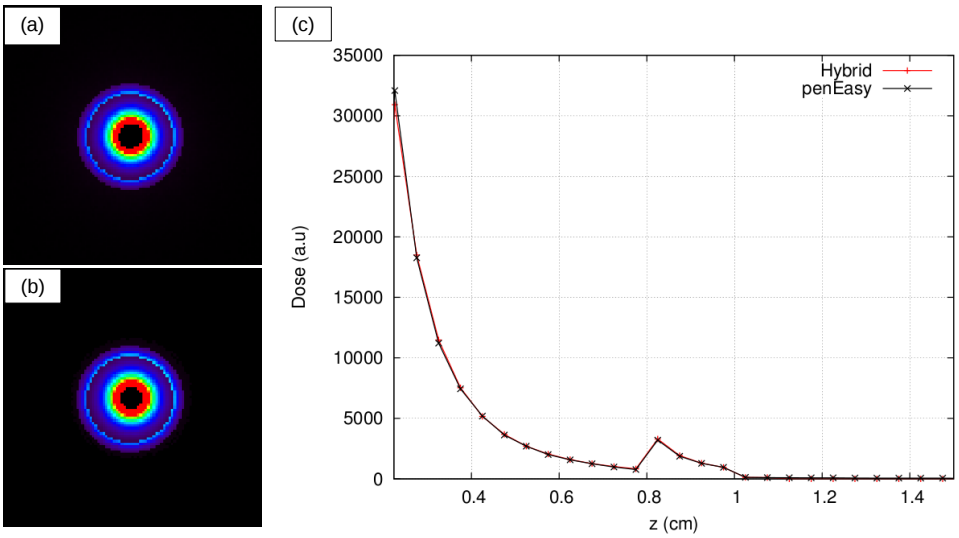

Figure 6.13: 2D dose distributions in a water/bone phantom for the needle applicator using (a) penEasy and (b) the HMC and their DDPs (c).

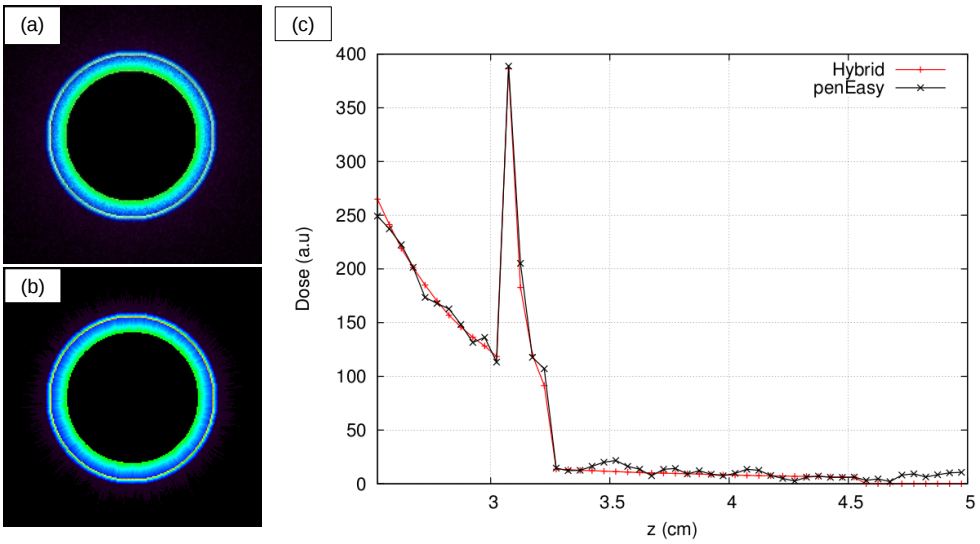

Figure 6.14: 2D dose distributions in a lung/bone phantom for the 50 mm spherical applicator using (a) penEasy and (b) the HMC algorithm and their DDPs (c).

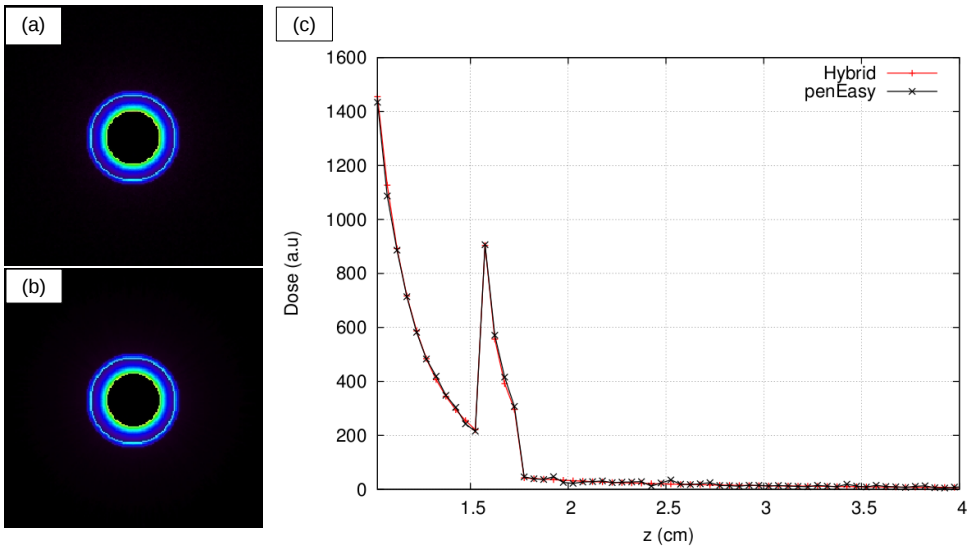

Figure 6.15: 2D dose distributions in a water/bone/lung phantom for the 20 mm spherical applicator using (a) penEasy and (b) the HMC algorithm and their DDPs (c).

Looking at the examples, the HMC seems to behave accurately when heterogeneities are present. The HMC DDPs for all cases agree with the reference ones obtained with penEasy.

Gamma evaluations have also been performed for all cases with 1%-1 mm, 2%-1 mm and 5%-1 mm criteria. The results are exposed in the following tables.

Gamma evaluation in the water/bone phantom

	1% - 1 mm	2% - 1 mm	5% - 1 mm
Needle	95.15%	97.82%	99.29%
Spherical ϕ 15 mm	90.33%	96.22%	99.23%
Spherical ϕ 20 mm	89.40%	96.18%	99.45%
Spherical ϕ 25 mm	88.44%	95.75%	99.36%
Spherical ϕ 30 mm	83.31%	93.70%	99.45%
Spherical ϕ 35 mm	82.48%	93.29%	99.40%
Spherical ϕ 40 mm	81.32%	92.63%	99.26%
Spherical ϕ 45 mm	85.78%	95.75%	99.74%
Spherical ϕ 50 mm	86.02%	95.53%	99.60%

Table 6.4: Results of gamma evaluation between MC simulations and HMC calculations in the water/bone phantom (5% threshold).

Gamma evaluation in the lung/bone phantom			
	1% - 1 mm	2% - 1 mm	5% - 1 mm
Needle	97.72%	99.17%	99.59%
Spherical ϕ 15 mm	89.30%	96.34%	99.64%
Spherical ϕ 20 mm	85.76%	95.03%	99.26%
Spherical ϕ 25 mm	88.64%	96.33%	99.99%
Spherical ϕ 30 mm	89.30%	96.31%	99.52%
Spherical ϕ 35 mm	89.86%	96.66%	100.00%
Spherical ϕ 40 mm	89.80%	96.65%	99.63%
Spherical ϕ 45 mm	89.89%	96.68%	99.63%
Spherical ϕ 50 mm	89.92%	96.64%	99.66%

Table 6.5: Results of gamma evaluation between MC simulations and HMC calculations in the lung/bone phantom (5% threshold).

Gamma evaluation in the water/bone/lung phantom			
	1% - 1 mm	2% - 1 mm	5% - 1 mm
Needle	95.08%	97.77%	99.26%
Spherical ϕ 15 mm	89.98%	96.25%	99.29%
Spherical ϕ 20 mm	89.76%	96.25%	99.45%
Spherical ϕ 25 mm	88.14%	95.75%	99.44%
Spherical ϕ 30 mm	86.64%	95.26%	99.56%
Spherical ϕ 35 mm	85.30%	94.84%	99.57%
Spherical ϕ 40 mm	83.37%	93.96%	99.43%
Spherical ϕ 45 mm	85.56%	95.43%	99.68%
Spherical ϕ 50 mm	85.65%	95.50%	99.69%

Table 6.6: Results of gamma evaluation between MC simulations and HMC calculations in the water/bone/lung phantom (5% threshold).

The results from the gamma evaluation in heterogeneities show that, if we consider the most strict limit of 1%-1 mm, the number of voxels passing the test is below 90% average for all scenarios, which is not good enough. For the 2%-1 mm this number increases to values around 95%, although some applicators still remain a little underneath. And if we extend the limit to 5%-1 mm, all cases obtain values close to 100%.

6.5.2 Hybrid Monte Carlo for flat and surface applicators

The same validation procedure was applied to flat and surface applicators. Different setups were considered, including homogeneous and heterogeneous phantoms representing different clinical situations.

6.5.2.1 Homogeneous phantoms

As in the spherical applicators validation, dose was computed in water, lung and bone. The dose distributions from full MC simulation were compared to the dose distributions obtained by the HMC in the same conditions for all flat and surface applicators.

The same PHSP file was employed to compute dose with penEasy and with the HMC. Phantoms of (200×200×200) voxels were used, with a voxel size of 0.5 mm. In the case of the HMC simulations, 5 million meta-histories were calculated, while 500 million were used when calculating with penEasy.

For all the cases studied, a good agreement was reached between penEasy and our HMC. Some of the obtained results are shown below. In figure 6.16 it is represented the transverse view of the 2D dose distribution for a 3 cm flat applicator in water for both penEasy and HMC algorithms, as well as their transverse profiles at different depths. The same comparison is shown in figure 6.17 for a 2 cm surface applicator in a lung phantom and in figure 6.18 for a 6 cm flat applicator in a bone phantom.

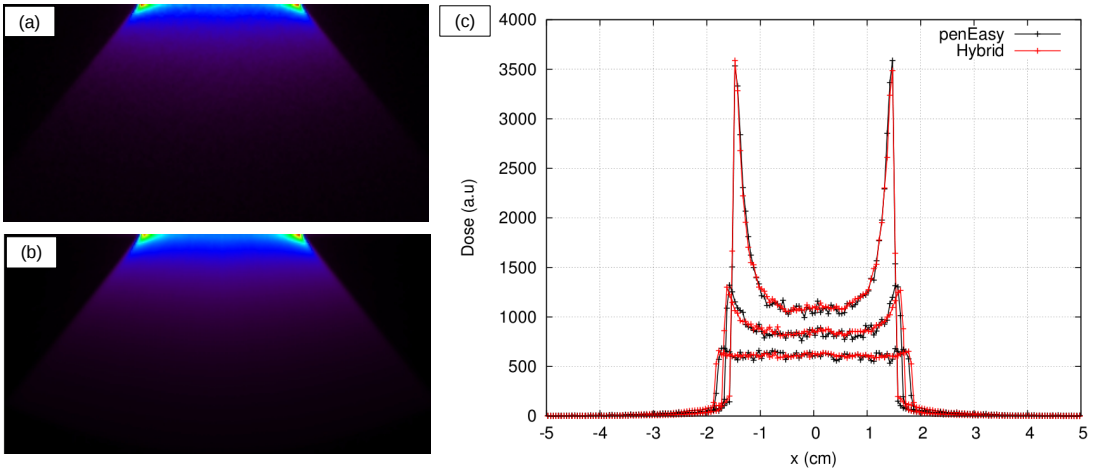

Figure 6.16: 2D dose distribution in a water phantom for the 30 mm flat applicator using (a) penEasy and (b) the HMC algorithm and (c) their transverse profiles at 0, 2 and 5 mm depth.

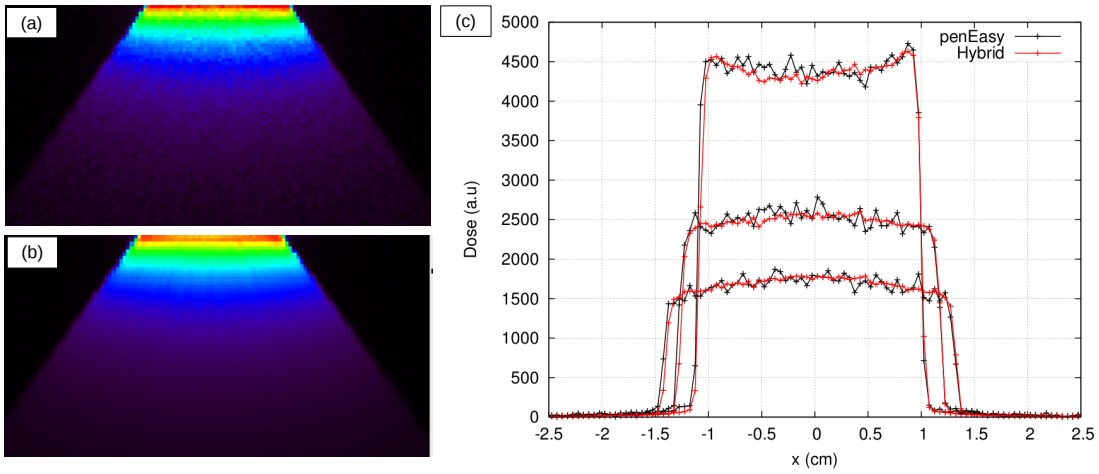

Figure 6.17: 2D dose distribution in a lung phantom for the 20 mm surface applicator using (a) penEasy and (b) the HMC algorithm and (c) their transverse profiles at 0, 2 and 5 mm depth.

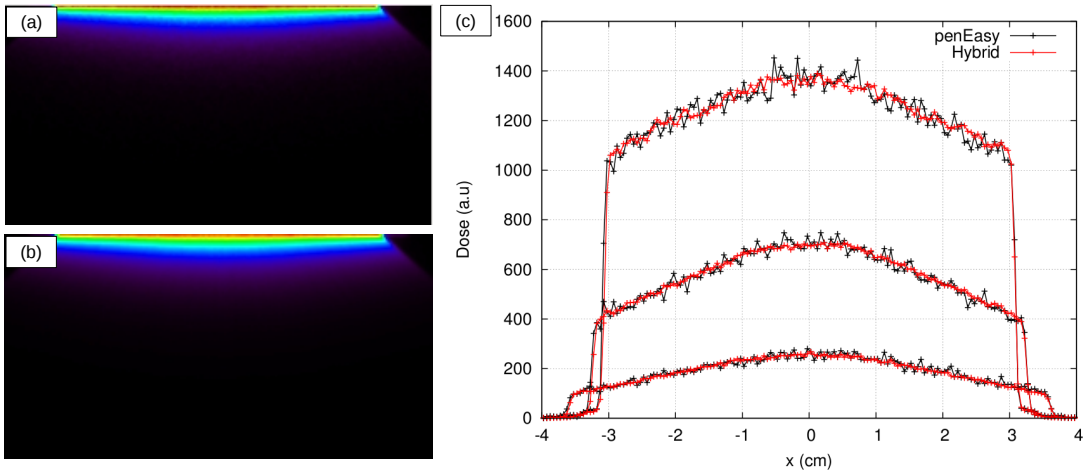

Figure 6.18: 2D dose distribution in a bone phantom for the 60 mm flat applicator using (a) penEasy and (b) the HMC algorithm and (c) their transverse profiles at 0.5, 2 and 5 mm depth.

Figure 6.19 also shows a dose comparison between penEasy and HMC, where the DDPs obtained in the different media for a 1 cm flat applicator are represented. Solid lines correspond to the curves computed with the HMC, and the dash lines to the ones calculated with penEasy.

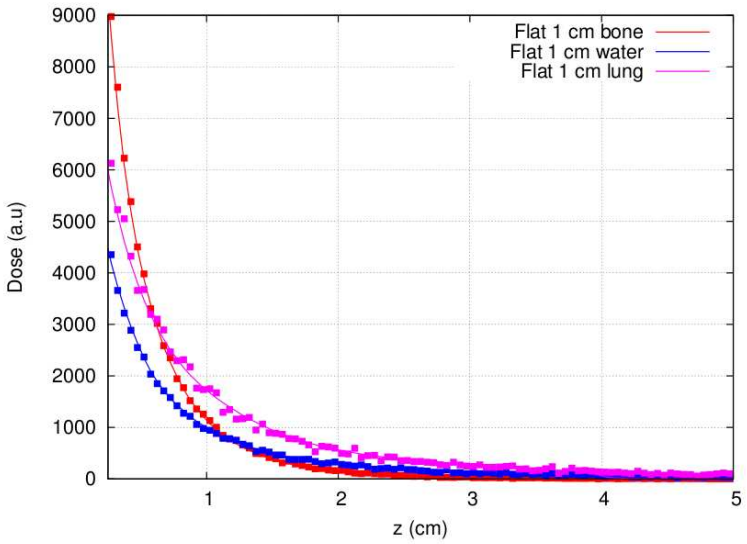

Figure 6.19: Depth dose curves obtained with the HMC (solid lines) and penEasy (dashed lines) in the 3 different phantoms.

Furthermore, quantitative evaluations were also performed in terms of gamma index. As in spherical applicators, three criteria were calculated; 1%-1 mm, 2%-1 mm and 5%-1 mm (5% threshold). The results are shown in the following tables.

Gamma evaluation in the water phantom

	1% - 1 mm	2% - 1 mm	5% - 1 mm
Flat 10 mm	96.33%	98.84%	99.56%
Flat 20 mm	96.29%	98.34%	99.62%
Flat 30 mm	96.79%	98.77%	99.76%
Flat 40 mm	96.52%	98.84%	99.79%
Flat 50 mm	96.36%	99.13%	99.93%
Flat 60 mm	96.78%	99.10%	99.91%
Surface 10 mm	97.39%	98.21%	98.44%
Surface 20 mm	97.18%	98.38%	98.81%
Surface 30 mm	97.42%	98.93%	99.65%
Surface 40 mm	97.63%	99.27%	99.88%

Table 6.7: Results of gamma evaluation between MC simulations and HMC calculations in the water phantom (5% threshold).

Gamma evaluation in the lung phantom			
	1% - 1 mm	2% - 1 mm	5% - 1 mm
Flat 10 mm	97.62%	99.42%	99.95%
Flat 20 mm	96.89%	98.68%	99.72%
Flat 30 mm	96.75%	98.84%	99.74%
Flat 40 mm	95.03%	98.60%	99.72%
Flat 50 mm	92.83%	98.66%	99.77%
Flat 60 mm	90.82%	98.28%	99.53%
Surface 10 mm	98.45%	99.03%	99.19%
Surface 20 mm	98.09%	99.31%	99.86%
Surface 30 mm	98.33%	99.57%	99.97%
Surface 40 mm	98.32%	99.66%	99.98%

Table 6.8: Results of gamma evaluation between MC simulations and HMC calculations in the lung phantom (5% threshold).

Gamma evaluation in the bone phantom			
	1% - 1 mm	2% - 1 mm	5% - 1 mm
Flat 10 mm	94.89%	96.44%	98.12%
Flat 20 mm	93.23%	96.01%	98.84%
Flat 30 mm	88.91%	94.50%	99.14%
Flat 40 mm	90.14%	94.69%	99.32%
Flat 50 mm	88.83%	94.38%	99.30%
Flat 60 mm	90.87%	95.95%	99.50%
Surface 10 mm	95.41%	96.37%	97.56%
Surface 20 mm	94.85%	96.29%	97.98%
Surface 30 mm	94.25%	95.74%	98.58%
Surface 40 mm	93.76%	96.65%	99.21%

Table 6.9: Results of gamma evaluation between MC simulations and HMC calculations in the bone phantom (5% threshold).

In the water phantom, it can be seen that the 1%-1 mm criterion present good results, with all applicators having more than 95% voxels passing the gamma. For the lung phantom the values for this limit are a bit lower, presenting some cases below this percentage. However, for the

2%-1 mm criterion the number of voxels with $\gamma < 1$ are above 98% for all applicators. Once again, the worst results are obtained with the bone phantom where the dose gradients are higher. Nevertheless, around 95% average voxels pass the 2%-1 mm criterion and more than 97% voxels pass the test in the 5%-1 mm limit for all cases.

6.5.2.2 Heterogeneous phantoms

3 case studies were analyzed including heterogeneous situations:

- **Bone layer**: A 2 mm thick layer of bone located at 5 mm from the water surface.
- **Air gap**: An air disk with diameter $\phi/2$, being ϕ the applicator diameter, located at the surface of the water phantom and with a thickness of 2 mm.
- **Lead protection disk**: A lead disk with diameter ϕ, being ϕ the applicator diameter, located at 5 mm from the water and with a thickness of 2 mm.

The scheme of these case studies is shown in figure 6.20.

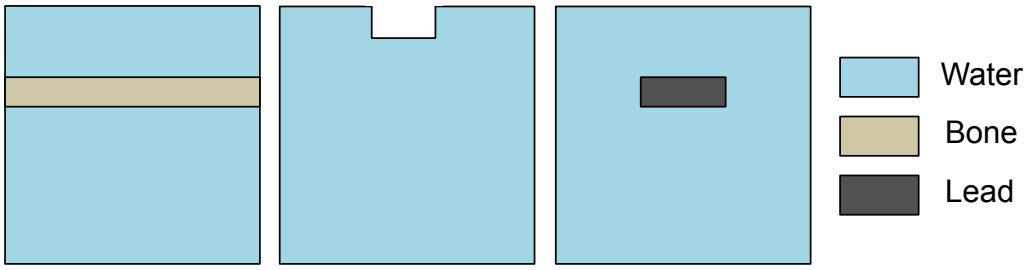

Figure 6.20: Schemes of the heterogeneous phantoms used for the validation of the flat and surface applicators.

As in the homogeneous phantoms, the same PHSP file was employed to compute dose with penEasy and with the HMC. Phantoms of (200×200×200) voxels were used, with a voxel size of 0.5 mm. 5 million meta-histories were calculated when using the HMC, while 500 million were used when calculating with penEasy.

A good agreement was also reached between penEasy and our HMC. Some of the obtained results are shown below. In figure 6.21 both algorithms were compared for a 4 cm flat applicator in the bone layer phantom. 2D transverse dose distributions are showed for both algorithms, as well as the corresponding DDPs and transverse profiles. The same results are showed in figure 6.22 for the air gap phantom with a 2 cm flat applicator, and in figure 6.23 for the dose in the phantom with a lead protection disk with the 3 cm surface applicator.

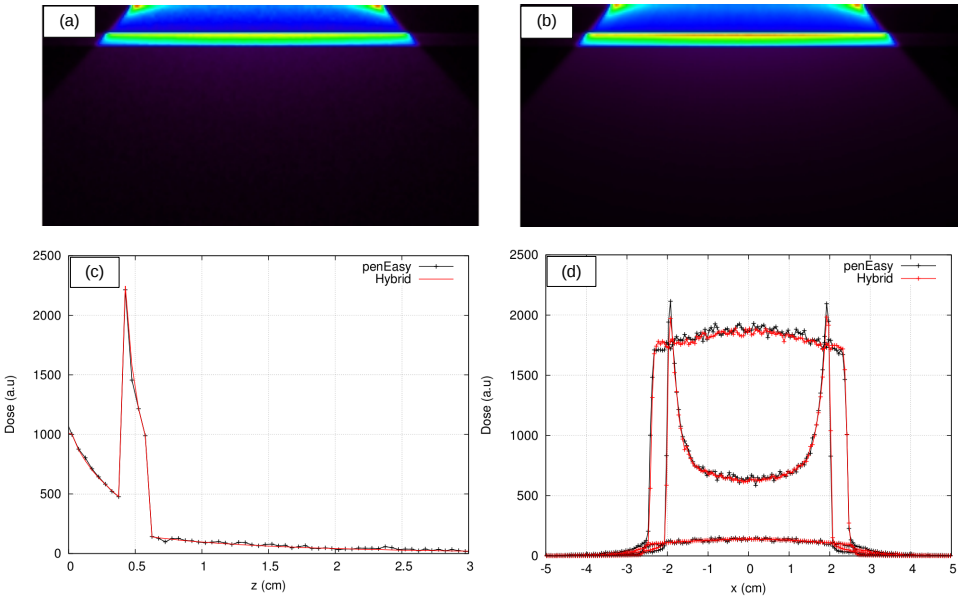

Figure 6.21: 2D dose distribution in the bone layer phantom for the 40 mm flat applicator using (a) penEasy and (b) the HMC algorithm. (c) Depth dose profiles obtained with both codes and (d), their transverse profiles at the water surface, at the bone surface and right after the bone layer.

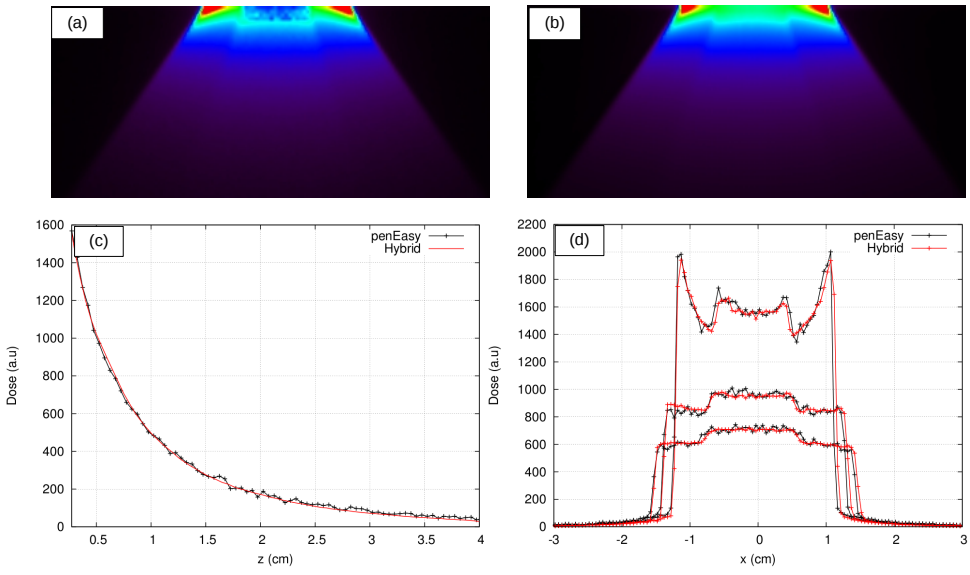

Figure 6.22: 2D dose distribution in the air gap phantom for the 20 mm flat applicator using (a) penEasy and (b) the HMC algorithm. (c) Depth dose profiles obtained with both codes starting after the air gap and (d), their transverse profiles at 2 mm, 4 mm and 6 mm depth.

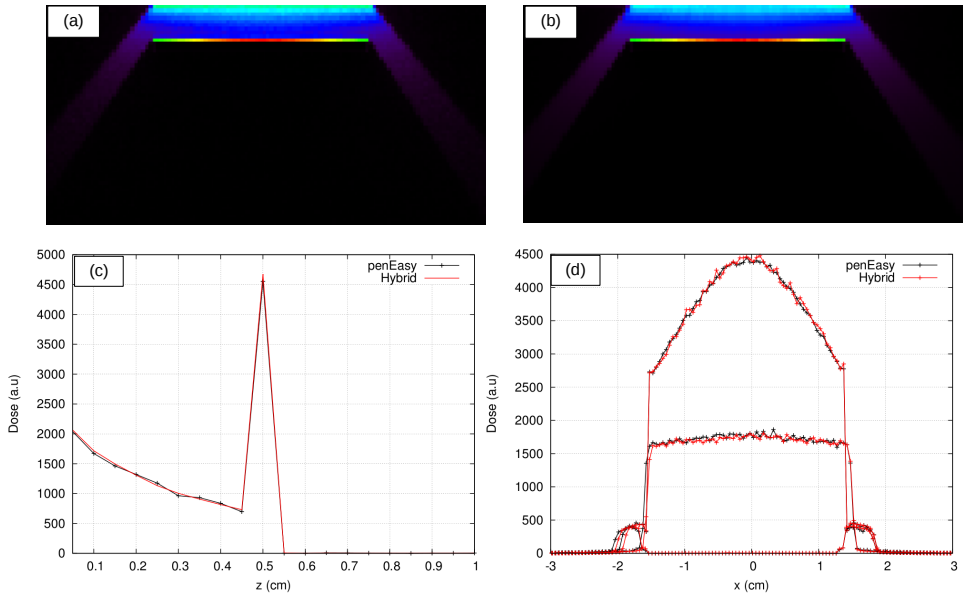

Figure 6.23: 2D dose distribution in the lead protection disk phantom for the 30 mm surface applicator using (a) penEasy and (b) the HMC algorithm. (c) Depth dose profiles obtained with both codes and (d), their transverse profiles at the water surface, at the lead interface and right after the disk.

In the case of the dose comparison for the air gap phantom (figure 6.22), the dose distributions seem to differ in the air material. This is due to the low interaction that the photons present in air. In the penEasy dose distribution, despite the high number of initial histories, the statistics in air are very low, while this does not happen in the HMC, as we have previously explained. However, right after the air gap both distributions behave similarly, which proves that the HMC reproduces accurately the physical interactions in the different media. If the number of histories employed in the penEasy simulation would have been much higher, the resulting dose distribution would behave as the one of the HMC. Therefore, once again it seems that the HMC reproduces the reference dose distributions in heterogeneous phantoms.

Gamma evaluations have been done as well. The next tables contain the percentage of voxels with $\gamma < 1$ with different criteria: 1% - 1 mm, 2% - 1 mm and 5% - 1 mm (5% threshold).

Gamma evaluation in the bone layer phantom			
	1% - 1 mm	2% - 1 mm	5% - 1 mm
Flat 10 mm	90.18%	95.57%	98.97%
Flat 20 mm	90.18%	95.57%	98.97%
Flat 30 mm	90.60%	95.31%	98.64%
Flat 40 mm	91.45%	96.23%	99.21%
Flat 50 mm	91.19%	95.28%	98.25%
Flat 60 mm	92.65%	96.99%	99.41%
Surface 10 mm	89.77%	95.97%	98.35%
Surface 20 mm	90.36%	95.79%	98.25%
Surface 30 mm	90.41%	95.79%	98.43%
Surface 40 mm	90.73%	96.43%	99.32%

Table 6.10: Results of gamma evaluation between MC simulations and HMC calculations in the bone layer phantom (5% threshold).

Gamma evaluation in the air gap phantom			
	1% - 1 mm	2% - 1 mm	5% - 1 mm
Flat 10 mm	93.37%	96.47%	98.84%
Flat 20 mm	95.06%	97.30%	99.02%
Flat 30 mm	95.52%	97.79%	99.19%
Flat 40 mm	94.90%	97.60%	99.08%
Flat 50 mm	94.31%	97.56%	99.08%
Flat 60 mm	94.72%	98.12%	99.21%
Surface 10 mm	93.52%	96.87%	98.85%
Surface 20 mm	94.87%	97.51%	98.96%
Surface 30 mm	95.43%	97.92%	99.36%
Surface 40 mm	96.01%	98.27%	99.39%

Table 6.11: Results of gamma evaluation between MC simulations and HMC calculations in the air gap phantom (5% threshold).

Gamma evaluation in the protection lead disk phantom

	1% - 1 mm	2% - 1 mm	5% - 1 mm
Flat 10 mm	87.17%	93.82%	96.17%
Flat 20 mm	87.48%	92.44%	96.41%
Flat 30 mm	87.71%	92.55%	96.05%
Flat 40 mm	86.50%	92.08%	95.78%
Flat 50 mm	87.63%	93.13%	96.35%
Flat 60 mm	88.10%	93.12%	96.55%
Surface 10 mm	88.97%	93.24%	94.50%
Surface 20 mm	87.10%	91.08%	93.24%
Surface 30 mm	86.08%	90.48%	94.32%
Surface 40 mm	85.97%	91.36%	95.61%

Table 6.12: Results of gamma evaluation between MC simulations and HMC calculations in the protection lead disk phantom (5% threshold).

We obtain a good gamma evaluation with a 2%-1 mm criterion for all applicators in the bone layer and in the air gap phantoms, where more than 95% voxels pass the evaluation. In the protection disk phantom the number of voxels with $\gamma < 1$ is lower, and even with the 5%-1 mm limits we still have some applicators with less than 95% voxels passing. Again, this case presents very high dose differences in the interface water-lead, and, besides, after 5 mm the dose falls abruptly to 0, decreasing considerably the number of voxels involved in the evaluation.

6.5.3 Validation in clinical situations

Finally, to conclude the validation of the HMC, two simulations have been performed in a patient CT. We will focus on two of the most common treatments with Intrabeam® nowadays: A partial breast irradiation and a Kypho-IORT.

6.5.3.1 Simulation of a partial breast irradiation treatment planning

The aim of partial breast irradiation is to reduce the risk of local recurrence in the tumor bed after the surgery. In this case, the surgery is immediately followed by an irradiation of the surrounding tissue, requiring approximately 2-3 hours for the entire process, reducing overall treatment time and cost [Bouzid et al., 2015]. The main difficulty is to obtain reliable data of

the dose distribution inside the patient, because, as it is been previously explained in this thesis, at the Intrabeam® working energies the dose gradients are so high that measuring them is a very difficult task. Furthermore, at 50 kV the assumption of considering the patient as water may not be appropriate, particularly in regions where tissue densities and heterogeneities may be present. In order to overcome these limitations, some MC dose calculations platforms have been developed [Bouzid et al., 2015]. However, the time limitation in the clinic requires the look for other alternatives, such as the HMC. To test the viability of our algorithm in a real CT planning, a comparison against penEasy has been done.

We used a thorax CT from a female patient to calculate dose distributions in breast with penEasy and the HMC. The region of interest of our CT had (340×340×400) voxels with a voxel size of 0.5 mm. For the HMC calculations, $5{\cdot}10^6$ histories were enough to achieve good statistics, taking less than 5 minutes simulation time, while 10^9 histories were needed in penEasy (several days of computation time). The results of the simulation are shown in figure 6.24, where dose distributions in the transverse, coronal and sagittal views are represented for (a) penEasy calculation and (b) HMC calculation.

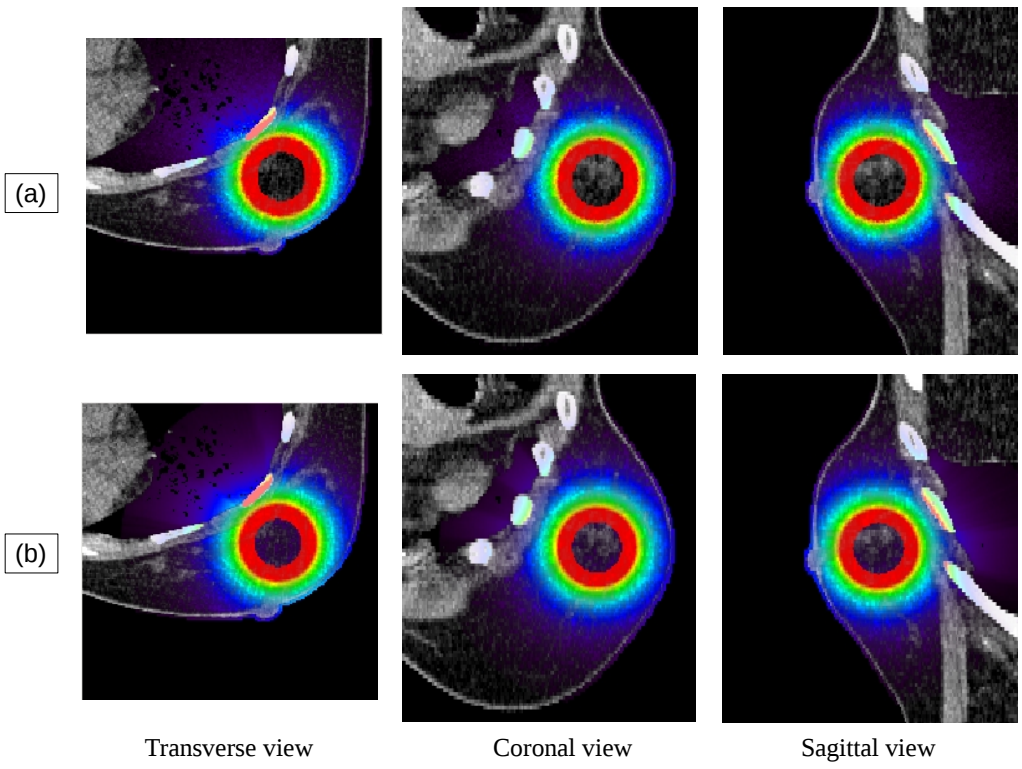

Figure 6.24: Dose distribution on a CT representing a breast conserving treatment with (a) penEasy, (b) HMC

Dose distributions were evaluated by means of a gamma index. We used the 2%-1 mm criterion and 5% threshold. 95.51% of the voxels passed these values, as can be seen in figure 6.25, where the gamma distribution is represented. The black voxels correspond to the point which failed the gamma evaluation.

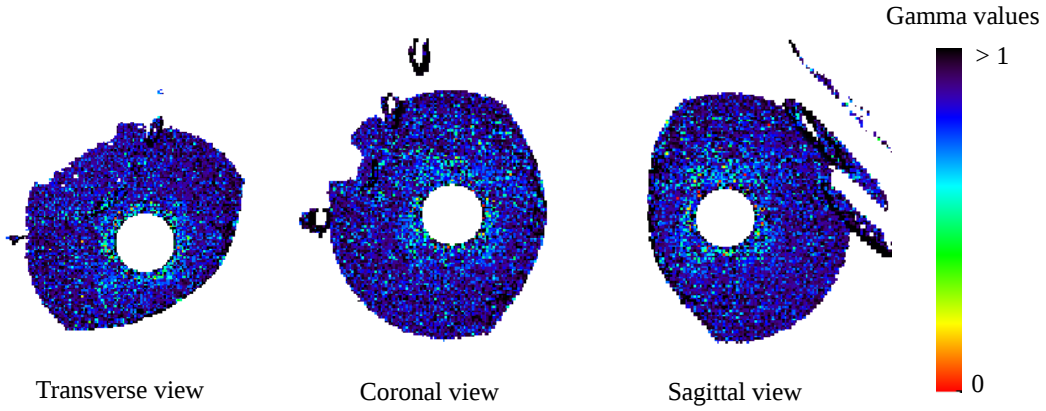

Figure 6.25: Gamma distribution on the partial breast irradiation treatment simulation with a 2%-1 mm criterion and 5% threshold. 95.51% of the voxels passed the evaluation.

6.5.3.2 Simulation of a Kypho-IORT treatment planning

The skeletal system is one of the most common places that develop metastases. Up to 85% of the patients with breast, prostate and lung cancer suffer from bone metastases, of which approximately 50% are in the spinal cord [Schneider et al., 2011]. Cancer treatments in the spine are usually treated with a combination of radiotherapy (for tumor treatment) and surgery (for pain relief). Kypho-IORT is a novel treatment that combines both treatments in a single procedure, shortening overall treatment time up to 90 minutes [Wenz et al., 2010]. The needle applicator is placed in the center of the metastases, irradiating the tissue with 8 Gy at 5 mm distance during 90 seconds. Then, Intrabeam® source is removed and the surgeon proceeds to perform the kyphoplasty.

As in the breast study, it is very difficult to obtain the dose deposited during the IORT treatment inside the patient, and the water approximation is particularly not accurate in this case, as very different density tissues are involved (vertebral bone, tissue, lung). Therefore, our HMC seems to be a good candidate for dose calculation. We have calculated the dose delivered with the Intrabeam® needle applicator in a patient CT and we have compared the results with penEasy.

A patient CT scan of the spine was used to compute dose distributions with penEasy and the

HMC. The image had (150×150×150) voxels with a voxel size of 0.5 mm. As in the breast study, $5{\cdot}10^6$ histories were enough to achieve good statistics in the HMC dose calculation, taking less than 5 minutes simulation time, while in penEasy we needed 10^9 histories. The results of the simulation are shown in figure 6.26, where dose distributions in the transverse, coronal and sagital views are represented for (a) penEasy calculation and (b) HMC calculation.

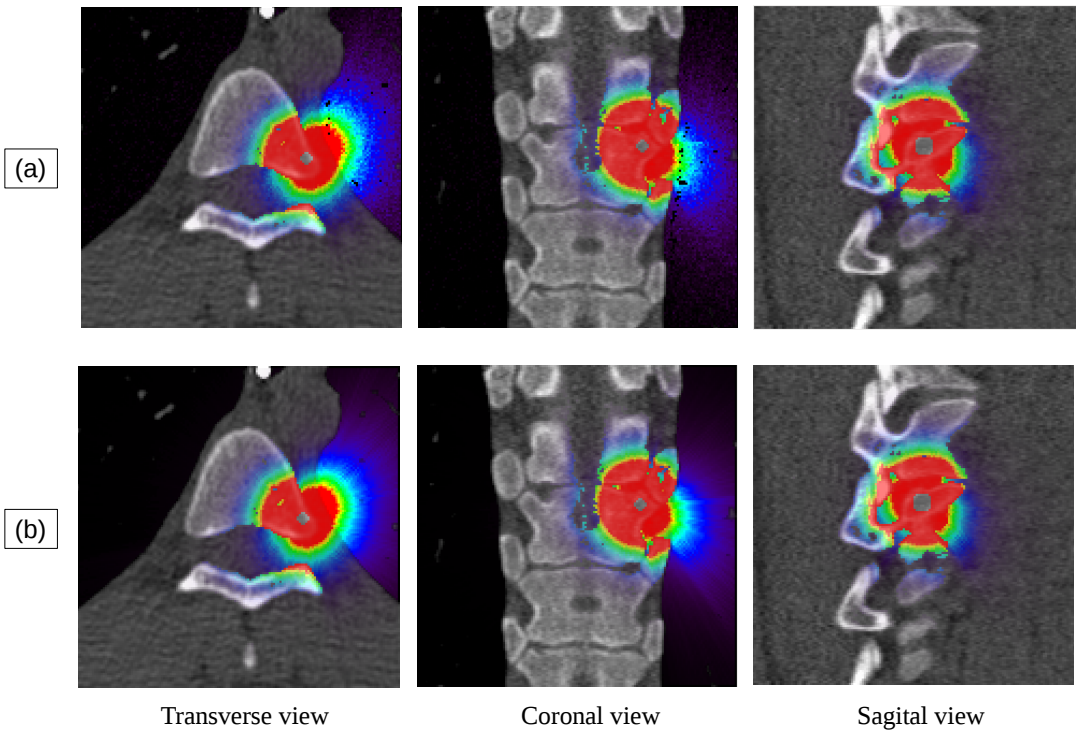

Figure 6.26: Dose distribution on a CT representing a Kypho-IORT treatment with (a) penEasy, (b) HMC

A gamma evaluation was performed for the 2%-1mm criterion and 5% threshold. 95.11% of the voxels passed these values, as can be seen in figure 6.27, where the gamma distribution is represented. The black voxels correspond to the points which failed the gamma evaluation.

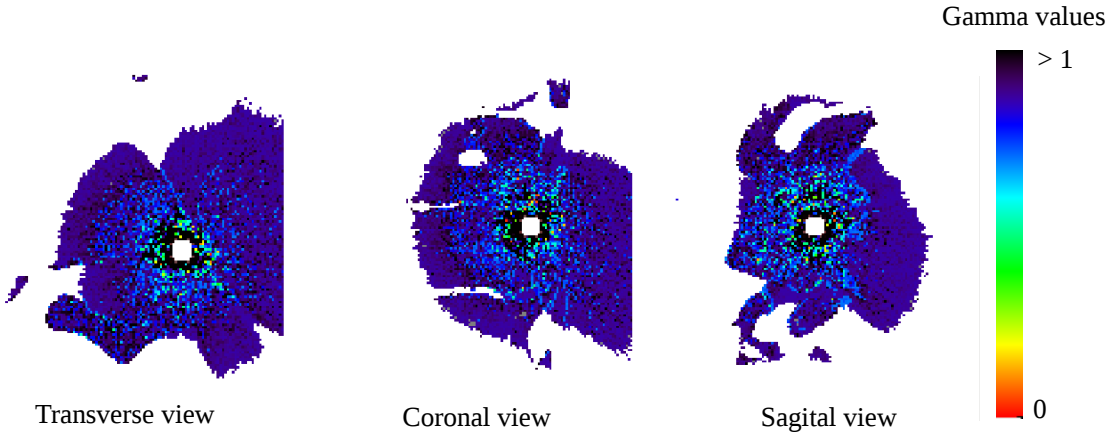

Figure 6.27: Gamma distribution on the Kypho-IORT treatment simulation with a 2%-1 mm criterion and 5% threshold. 95.11% of the voxels passed the evaluation.

6.6 Conclusion

In this chapter we present an in-house developed dose calculation algorithm suitable for XIORT with the Intrabeam® device, called **Hybrid Monte Carlo (HMC)**. This algorithm includes all the physics of a MC calculation and generates dose distributions suitable for dose planning within minutes. It takes into consideration photoelectric and Compton interactions, and brings to the extreme some variance reduction techniques to accelerate the calculations. As a result, instead of the regular histories used in any standard MC, the HMC employs meta-histories. Each m-history represents the fate of many photons and has a special property, different from the common MC: the m-histories never die, only their weights are decreased after each interaction.

This characteristic allows us to know how many times has each m-history interacted inside each voxels, and which voxels has the ray crossed. By knowing this, we can perform a normalization of the dose, eliminating the dependence on how many histories have deposited dose into each voxel (which introduces artifacts if the number of m-histories is not high enough), and introducing an ideal fluence that only depends on the trajectory of the m-history.

By doing this, we are able to obtain very soft dose distributions (free of statistical noise) using only few m-histories, shortening considerably the simulation time. The normalization does not affect to the physics of the radiation, as all the possible interactions are contemplated in the weight of the m-history, not in its fluence.

We have validated the HMC against penEasy in different phantoms, including homogeneous and heterogeneous media. We have also compared dose distributions in two clinical situations, a

partial breast irradiation and a Kypho-IORT. In general, good results were obtained with the gamma evaluation, for some situations even with the 1%-1 mm criterion. In a few cases we had to go to a 5%-1 mm criterion to achieve a good agreement. However, the gamma limits for the Intrabeam® has not been stipulated, and values of previous studies can go from 2%-1 mm [Nwankwo et al., 2013], 2%-2 mm [Clausen et al., 2012] to even 10%-1 mm [Chiavassa et al., 2014].

Therefore, we can conclude that the HMC is a powerful tool that provides soft dose distributions accurately and within minutes. It can be used as a dose calculation tool in the operating room (OR), as its high speed allows an on-the-fly dose calculation which includes the realistic effects of the beam in the different tissues within the patient's body.

The HMC, in combination with the phase space optimization process described in chapter 4, provides dose distributions that reproduce the experimental data of any given Intrabeam®'s applicator in minutes, and both codes have been integrated into ***radiance***®.

Conclusions of this thesis

The main contributions and conclusions of the thesis are summarized in this chapter.

Detailed simulation of IORT systems

We have simulated the most relevant dedicated accelerators employed in IOERT treatments (ie. NOVAC®, LIAC® and MOBETRON®) with their corresponding applicators, and Intrabeam® needle, spherical, surface and flat applicators. In most cases, the different components of the devices have been extracted from literature, in other cases, such as for flat and surface Intrabeam® applicators, the geometry details have been provided by the vendor. These simulations will represent a reference accelerator or applicator, and will be used to create a database that will be employed to generate a PHSP file tuned to each user machine in a dose treatment planning procedure.

After characterizing each device, we used the geometries to calculate monoenergetic simulations and store the PHSP files and DDPs. The PHSP files were parameterized in order to reduce the size of the files. The monoenergetic simulations covered the energy range of the devices. For the IOERT accelerators, 140 simulations, from 1 MeV to 14 MeV were done. In the case of Intrabeam® applicators we calculated 50 simulations, from 1 to 50 keV.

The conclusions of this part are:

- Regarding the X-ray source study, a slight anisotropy in the backward direction of the dose can be seen, which is consistent with previous studies [Dinsmore et al., 1996, Beatty et al., 1996], where an increase along the probe in the backward direction was observed from the escaping photons through beryllium.

- For the spherical applicators characterization, the backwards anisotropy seen in the experimental measurements was reproduced by displacing the PHSP file that replaces the XRS around 2 mm from the geometrical center of the applicator, corresponding to leaving

a 2 mm extra space in the hole inside the applicator to guarantee the protection of the XRS against the applicator walls when inserting it.

- In the simplified approach for the spherical applicators, while the possible differences in the energy deposition distribution with depth will be absorbed afterwards in the optimization process, the anisotropy will not be reproduced.

- For the flat and surface Intrabeam® applicators, the detailed geometries provided by the vendor led to accurate dose distributions for all diameters.

- Regarding the electron beam dedicated accelerators, we were able to reproduce the dose distributions by extracting the information from the literature and tuning the geometries.

- While for the LIAC® and the NOVAC® the same geometries were used to simulate all the applicators and energies, for the MOBETRON® we had to re-adjust slightly the geometries for each case, due to changes in the transverse profiles with every applicator. This is possibly a consequence of its soft-docking system.

- The parameterization performed to the PHSP files reduce the number of lines of each file up to a maximum of 2 million. Regarding the bin size, a trade-off between accuracy of the representation and number of requested bins was made.

Phase space optimization process and validation

We have developed a fast and accurate accelerator's tuning tool which can be optimized to the user's device with only an experimental DDP in water [Ibáñez et al., 2015, Vidal et al., 2015, Udías et al., 2017a] for IOERT accelerators and Intrabeam® applicators. This optimization process will be possible thanks to the database of monochromatic PHSP files and DDPs in water that has been obtained and stored from the detailed simulations that we have previously done.

A complete validation has been carried out against experimental measurements.

We have seen that:

- The procedure works accurately, reproducing the provided DDPs while maintaining the physical shape of the spectra.

- Computation time of the whole optimization is below 10 minutes for all cases.

- The optimization process only fits the DDPs, which is why it is essential that the rest of the dose distribution behaves correctly.

- By combining PHSP files and DDPs from realistic simulations and by using a realistic shape of the energy spectra we guarantee an accurate behavior of the dose distributions, not only of the DDP but also of the transverse profiles.

- For the validation of dose distributions in water with spherical applicators, we found some discrepancies between simulations and measurements due to the anisotropy of the dose in the backward direction.

- The next step in the future work should be correcting these discrepancies due to the anisotropy by introducing an angular-dependent function in the X-rays beam fluence.

- Regarding the dose distributions in water with flat and surface applicators, we found a good agreement for the two cases studied, with more than 95% of the voxels fulfilling the gamma criterion at the 2%-2 mm level.

- In the dose comparisons inside heterogeneous phantoms, either with Intrabeam® applicators or IOERT accelerators, we reached a reasonable agreement at the 2%-2 mm level, specially considering that a non-negligible contribution to the dose differences is attributed to uncertainties in the measurements, such as asymmetries or displacements of the films.

- When these uncertainties disappear, the agreement increases substantially, something that has been seen in the validation of IOERT accelerators against simulations, where almost a 100% of the voxels passed the 2%-2 mm level in all the phantoms.

Hybrid Monte Carlo

We have developed a new dose computation algorithm for the Intrabeam® applicators, named **hybrid Monte Carlo (HMC)** [Vidal et al., 2014b,a, Udías et al., 2017b]. The HMC calculates dose deposited by the Intrabeam® device within minutes, fully taking into account the different tissues and structures in the region of patient, i.e. as derived from a CT image.

The HMC algorithm has been complemented with PHSP files generated for the needle, spherical, flat and surface applicators and has been validated in different phantoms including clinical situations.

We can conclude:

- HMC computes an accurate dose for both homogeneous and heterogeneous media, as it incorporates all the relevant physics processes at Intrabeam® working energies.

- The savings in calculation time are possible thanks to taking to the extreme some variance reduction techniques.

- By not letting the meta-histories die inside the volume, we can normalize the dose, decreasing substantially the statistical noise of the distribution, and therefore, decreasing the number of needed initial particles and consequently, the simulation time.

- The limitation of the number of Compton scatterings to one does not affect the final dose, and the reduction of the simulation time is considerable.

- It can be considered that the electrons produced by the X-rays interactions inside the media are absorbed in the same voxel as they are generated, provided voxel sizes not much smaller than 0.25 mm.

- Regarding the validation of the HMC, good results were obtained, in general, with the gamma evaluation, for some situations even with the 1%-1 mm criterion. In a few cases we had to go to a 5%-1 mm criterion to achieve a good agreement. However, the gamma criteria for the Intrabeam® has not been stipulated, and values of previous studies can go from 2%-1 mm [Nwankwo et al., 2013], 2%-2 mm [Clausen et al., 2012] to even 10%-1 mm [Chiavassa et al., 2014].

- For all the validations performed, we see that the worst results in terms of gamma evaluation appear when the dose gradients are higher, corresponding also to the cases were the number of evaluated voxels is lower.

The final conclusions of this thesis are:

- The proposed phase space optimization process works accurately reproducing dose distributions in clinical situations for both electrons or X-rays beams. It has proven to be fast, flexible and accurately enough for IORT planning.

- The HMC provides soft dose distributions accurately and within minutes. It can be used as a dose calculation tool in the operating room (OR), as its high speed allows an on-the-fly dose calculation which includes the realistic effects of the beam in the different tissues within the patient's body.

- The HMC, in combination with the phase space optimization process, provides dose distributions that reproduce the experimental data of any given Intrabeam® in minutes, and both codes have been integrated into ***radiance***® [Valdivieso-Casique et al., 2015,

Pascau et al., 2012].

Appendix A

Generation of the material list for the Hybrid Monte Carlo

The Hybrid Monte Carlo extracts the photon's attenuation coefficients for the different materials from PENELOPE. One of the programs included in the distribution package is **tables**, which generates tables with the physical information (physical properties, interaction cross sections, attenuation coefficients, etc) from an input material data file. These material data files are created by means of the **material** program which extracts atomic interaction data from the PENELOPE database [Salvat et al., 2006].

Of all the physical information provided by the **tables** program for the different materials, we will be interested in the photon mass attenuation coefficients. This table includes the photoelectric, Compton, Rayleigh and pair production attenuation coefficients for the selected material and for different energies. The attenuation table has to be interpolated to cover the energy range of the Intrabeam®, from 1 keV to 50 keV (50 values for each material).

We have implemented 20 materials in the HMC code, covering different densities and materials (biologic and non-biologic):

- Air [Reference density (g/cm^3): $1.21 \cdot 10^{-3}$]
- Water [Reference density (g/cm^3): 1.00]
- Solid Water [Reference density (g/cm^3): 1.02]
- Methacrylate [Reference density (g/cm^3): 1.10]
- Aluminum [Reference density (g/cm^3): 2.70]
- Brass [Reference density (g/cm^3): 8.60]
- Lead [Reference density (g/cm^3): 11.35]
- Copper [Reference density (g/cm^3): 8.96]
- Cork [Reference density (g/cm^3): $2.40 \cdot 10^{-1}$]

- Teflon [Reference density (g/cm^3): 2.20]
- PVC [Reference density (g/cm^3): 1.40]
- Dry Air [Reference density (g/cm^3): $1.21 \cdot 10^{-3}$]
- Lung [Reference density (g/cm^3): $3.00 \cdot 10^{-1}$]
- Adipose Tissue [Reference density (g/cm^3): $9.20 \cdot 10^{-1}$]
- Muscle Striated [Reference density (g/cm^3): 1.04]
- Muscle [Reference density (g/cm^3): 1.11]
- Sacrum [Reference density (g/cm^3): 1.29]
- Rib [Reference density (g/cm^3): 1.41]
- B100 [Reference density (g/cm^3): 1.45]
- Cortical Bone [Reference density (g/cm^3): 1.85]

Main contributions of this thesis

While this PhD. thesis was being carried out, partial results have been presented in publications in international journals and relevant conferences in the field. The contributions of this thesis are presented in the following list.

Published articles in indexed international journals

1. E. Herranz, J. Herraiz, **P. Ibáñez**, M. Pérez-Liva, R. Puebla, J. Cal-González, P. Guerra, R. Rodríguez, C. Illana, and J.M. Udías. Phase space determination from measured dose data for intraoperative electron radiation therapy. *Physics in Medicine and Biology*, 60(1):375-401, 2014

2. M. F. Valdivieso-Casique, R. Rodríguez, S. Rodríguez-Bescós, D. Lardíes, P. Guerra, M. J. Ledesma, A. Santos, **P. Ibáñez**, M. Vidal, J. M. Udías, et al. Radiance - a planning software for intra-operative radiation therapy. *Translational Cancer Research*,4(2):196-209, 2015

3. R. Lica , H. Mach, L. Fraile, A. Gargano, M. Borge, N. Marginean, C. Sotty, V. Vedia, A. Andreyev, G. Benzoni, P. Bomans, R. Borcea, L. Coraggio, C. Costache, F. De Witte, H. Flavigny, H. Fynbo, P. Gaffney, P. Greenlees, L. Harkness-Brennan, M. Huyse, **P. Ibáñez**, S. Judson, J. Konki, A. Korgul, T. Kroll, et al. Fast-timing study of the l-forbidden $1/2^+ \rightarrow 3/2^+$ M 1 transition in Sn 129. *Physical Review C*, 93(4):044303 1-7, 2016

Articles submitted to indexed international journals

4. M. Vidal, **P. Ibáñez**, P. Guerra, M.F. Valdivieso-Casique, R. Rodríguez, C. Illana and J.M. Udías. Fast optimized Monte Carlo phase-space based dose prediction for low energy

X-rays Intra Operative Radiation Therapy. *Physics in Medicine and Biology*. Submitted.

Conference proceedings published in indexed international journals

1. M. Vidal, **P. Ibáñez**, P. Guerra, E. Herranz, and J.M. Udías. Realistic on-the-fly dose calculation for low energy x-rays intra-operative radiation therapy. *Radiotherapy and Oncology*, 110:S103-S104, 2014.

2. E. Herranz, J.M. Udías, **P. Ibañez**, J. Herraiz, M. Pérez-Liva, M. Vidal, and P. Guerra. Iterative reconstruction of clinical electron beam phase space for intra-operative radiation therapy. *Radiotherapy and Oncology*, 110:S42, 2014

3. **P. Ibáñez**, M. Vidal, R. García Marcos, E. Herranz Muelas, P. Guerra Gutiérrez, C. Santiago, J. Agustín, M. Infante, M. Lavado, and J. M. Udías. Validation of a phase space determination algorithm for intraoperative radiation therapy. *Radiotherapy and Oncology*, 111(S1):331-331, 2014

4. R. G. Marcos, M. Vidal, **P. Ibáñez**, R. Ayala, R. Sendón, R. Polo, and J.M. Udías. Impact of patient-applicator air-gap in dedicated mobile accelerator for intra-operative radiation therapy. *Radiotherapy and Oncology*, 111:S161-S162, 2014.

5. J.M. Udías, **P. Ibáñez**, M. Vidal, R. García-Marcos, G. Russo, C. Casarino, G. Candiano, G. Borasi, C. Messa, and M. Gilardi. A fast monte carlo-based calculation algorithm for a intra-operative radiation therapy TPS: A validation study. *Radiotherapy and Oncology*, 111: S181-S182, 2014

6. M. Vidal, **P. Ibáñez**, J. Cal González, P. Guerra Gutiérrez, and J. M. Udías. Hybrid monte carlo dose algorithm for low energy x-rays intraoperative radiation therapy. *Radiotherapy and Oncology*, 111(S1):117-118, 2014

7. **P. Ibáñez**, M. Vidal, R. García-Marcos, P. Guerra and J.M. Udías. New genetic algorithm-based procedure to determine phase space for intraoperative radiation therapy. *Radiotherapy and Oncology*, 115:S278-S279, 2015.

8. M. Perez-Liva, J. Herraiz, L. Medina-Valdés, J. Camacho, C. Fritsch, **P. Ibáñez**, and J.M. Udías. Ultrasound computed tomography for early breast cancer detection. *Radiotherapy and Oncology*, 115:S65, 2015

9. M. Vidal, **P. Ibáñez**, L. Parent, M. Goubert, R. Ferrand, P. Guerra, and J.M. Udias.

Optimized monte-carlo intra-operative radiotherapy dose prediction for flat and surface applicators. *Radiotherapy and Oncology*, (115):S277-S278, 2015

10. **P. Ibáñez**, M. Vidal, P. Guerra, and J.M. Udías. Validation of an optimized MC dose prediction for low energy x-rays intraoperative radiation therapy. *Radiotherapy and Oncology*, 119:S269-S270, 2016

Work presented in international or national conferences

Authors: E. Herranz, J. L. Herráiz, **P. Ibáñez**, M. Pérez-Liva, R. Puebla, J. Cal-González, P. Guerra, R. Rodríguez, C. Illana, J. M. Udías
Title: Phase space determination of electron beam for intraoperative radiation therapy from measured dose data
Type of presentation: Oral
Congress: Third European Workshop on Monte Carlo Treatment Planning (EW-MCTP)
Place and date: Sevilla, Spain, 15-18 May, 2012.

Authors: E.Herranz, J.L. Herraiz, P. Guerra, J. Cal-González, **P. Ibáñez**, R. Rodríguez, C. Illana, M. J. Ledesma-Carbayo, M. A. Infante, M. E. Lavado, J. M. Udías
Title:Iterative reconstruction of clinical electron beam phase space for intraoperative radiation therapy from measured beam dose data.
Type of presentation: Poster
Congress: 7th International Conference of the International Society of Intraoperative Radiation Therapy (ISIORT)
Place and date: Baveno, Italy, 22-24 June, 2012.

Authors: E. Herranz, J. L. Herráiz, **P. Ibáñez**, M. Pérez-Liva, R. Puebla, P. Guerra, J. M. Udías.
Title:terative reconstruction of clinical electron beam phase space for intraoperative radiation therapy from measured dose data.
Type of presentation: Poster
Congress: XXXIV Reunión Bienal de la Sociedad Española de Física
Place and date: Valencia, Spain, 15-18 July, 2013.

Authors: **P. Ibáñez***, E. Herranz, M. Pérez-Liva, R. Puebla, P. Guerra, C. Illana, R. Rodríguez, J.Calama, M. A. Infante, M. E. Lavado, J. M. Udías.
Title: Verificación del algoritmo de determinación de espacios de fase para Radioterapia Intraoperatoria (RIO) a partir de medidas experimentales.
Type of presentation: Oral

*presenting author

Congress: XXXIV Reunión Bienal de la Sociedad Española de Física
Place and date: Valencia, Spain, 15-18 July, 2013.

Authors: M.Vidal, **P. Ibáñez**, E. Herranz, P. Guerra, J.M. Udías
Title: Realistic on-the-fly dose calculation for low energy X-rays Intra-Operative Radiation Therapy
Type of presentation: Oral
Congress: ICTR-PHE
Place and date: Geneva, Switzerland, 10-14 February, 2014.

Authors: E. Herranz, **P. Ibáñez***, J.L. Herraiz, M. Pérez Liva, M. Vidal, P. Guerra, J.M. Udías
Title: Iterative Reconstruction of Clinical Electron Beam Phase Space for Intra-Operative Radiation Therapy
Type of presentation: Poster
Congress: ICTR-PHE
Place and date: Geneva, Switzerland, 10-14 February, 2014.

Authors: M. Vidal, **P. Ibáñez**, J. Cal-González, P. Guerra, J.M. Udías
Title: Algorithme Monte Carlo hybride pour le calcul de dose de l'Intrabeam dans le système de simulation Radiance de GMV
Type of presentation: Oral
Congress: Zeiss Symposium, SFPM 53 conference
Place and date: Deauville, France, 4-6 June, 2014.

Authors: **P. Ibáñez***, M. Vidal, R. García-Marcos, E. Herranz, P. Guerra, J.A. Calama, M.A. Infante, M.E. Lavado, J.M. Udías
Title: Validation of a phase space determination algorithm for intra-operative radiation therapy
Type of presentation: Poster
Congress: ESTRO 33
Place and date: Vienna, Austria, 4-8 April, 2014.

Authors: M. Vidal, **P. Ibáñez**, J. Cal González, P. Guerra, J.M. Udías
Title: Hybrid Monte Carlo dose algorithm for low energy X-rays intra-operative radiation therapy
Type of presentation: Oral
Congress: ESTRO 33
Place and date: Vienna, Austria, 4-8 April, 2014.

Authors: J.M. Udías, **P. Ibáñez***, M. Vidal, R. García-Marcos, G. Russo, C. Casarino, G.C.

*presenting author

Candiano, G. Borasi, C. Messa, M.C. Gilardi
Title: A fast Monte Carlo-based calculation algorithm for a Intra-Operative Radiation Therapy TPS : A validation study
Type of presentation: Poster
Congress: ESTRO 33
Place and date: Vienna, Austria, 4-8 April, 2014.

Authors: R. García Marcos, M. Vidal, **P. Ibáñez**, R. Ayala, R. Sendón, R. Polo, J.M. Udías
Title: Impact of patient-applicator air-gap in dedicated mobile accelerator for Intra-Operative Radiation Therapy
Type of presentation: Poster
Congress: ESTRO 33
Place and date: Vienna, Austria, 4-8 April, 2014.

Authors: J. López, **P. Ibáñez**, J.M. Udías, E. Herranz, V. Morillo, A. Bouché, J. Bonaque, C. Ferrer, A. Santos
Title: Dosimetría con Monte Carlo de algunos casos prácticos en radioterapia intraoperatoria.
Type of presentation: Poster
Congress: 4° Congreso conjunto SEFM/SEPR
Place and date: Valencia, Spain, 23-26 June, 2015.

Authors: P. Mur, **P. Ibáñez**, J.M. Udías
Title: Development of a brachytherapy sources library for treatment planning with Monte Carlo Methods
Type of presentation: Poster
Congress: 4° Congreso conjunto SEFM/SEPR
Place and date: Valencia, Spain, 23-26 June, 2015.

Authors: **P. Ibáñez*** , M. Vidal , R. García-Marcos, P. Guerra, J.M. Udías
Title: Phase space determination for intraoperative electron radiation therapy with a genetic algorithm-based procedure
Type of presentation: Oral
Congress: 4° Congreso conjunto SEFM/SEPR
Place and date: Valencia, Spain, 23-26 June, 2015.

Authors: A. Sethi, B. Chinsky, M. Vidal, **P. Ibáñez**, J.M Udías, C. Illana
Title: Monte Carlo Modeling of IORT Dose Distributions in a Commercial Treatment Planning System
Type of presentation: Poster
Congress: 9th Intrabeam User Meeting

*presenting author

Place and date: Mannheim, Germany, 9-10 July, 2015.

Authors: M. Vidal, **P. Ibáñez**, P. Guerra, J. M. Udías
Title: Optimized Monte-Carlo based dose computation for low energy X-rays IORT implemented in Radiance TPS.
Type of presentation: Oral
Congress: 9th Intrabeam User Meeting
Place and date: Mannheim, Germany, 9-10 July, 2015.
Note: This work was awarded with the ***best scientific contribution*** *mention.*

Authors: **P. Ibáñez***, M. Vidal, R. García-Marcos, P. Guerra, J.M. Udías
Title: New genetic algorithm-based procedure to determine phase space for intraoperative radiation therapy
Type of presentation: Poster
Congress: 3rd ESTRO Forum
Place and date: Barcelona, Spain, 24-28 April, 2015.

Authors: M. Vidal, **P. Ibáñez**, L .Parent, M. Goubert, R. Ferrand, P.Guerra, J.M. Udías.
Title: Optimized Monte-Carlo intra-operative radiotherapy dose prediction for superficial skin cancers treatment
Type of presentation: Oral
Congress: 3rd ESTRO Forum
Place and date: Barcelona, Spain, 24-28 April, 2015.

Authors: M. Perez-Liva, J.L. Herraiz, L. Medina-Valdés, J. Camacho, C. Fritsch, **P. Ibáñez**, J.M. Udías.
Title: Ultrasound Computed tomography for early breast cancer detection
Type of presentation: Poster
Congress: 3rd ESTRO Forum
Place and date: Barcelona, Spain, 24-28 April, 2015.

Authors: **P. Ibáñez***, M. Vidal, L. Parent, M. Goubert, P. Guerra and J.M. Udías,
Title: Optimized Monte Carlo dose calculation for superficial low energy X-rays intraoperative radiation therapy
Type of presentation: Oral
Congress: XXXV Reunión Bienal de la Real Sociedad Española de Física
Place and date: Gijón, Spain, 13-17 July, 2015.

Authors: **P. Ibáñez***, M. Vidal, P. Guerra and J.M. Udías
Title: Optimized Monte-Carlo based dose calculation for low energy X-rays intraoperative radiation therapy

*presenting author

Type of presentation: Oral
Congress: I Jornadas RSEF / IFIMED de Física Médica
Place and date: Valencia, Spain, 10-11 March, 2016.

Authors: **P. Ibáñez***, M. Vidal, P. Guerra and J.M. Udías
Title:Validation of an optimized MC dose prediction for low energy X-rays intraoperative radiation therapy
Type of presentation: Poster
Congress: ESTRO 35
Place and date: Turin, Italy, 29 April - 03 May, 2016.

Authors: J.M. Udías, **P. Ibáñez**, M. Vidal, J. Cal-González, P. Guerra, MJ Ledesma, A. Santos, JE Ortuño, C. Illana
Title: Cálculo acelerado de espacios de fases y dosis HMC en radioterapia intraoperatoria con el sistema Intrabeam
Type of presentation: Oral
Congress: VIII CPAN DAYS
Place and date: Zaragoza, Spain, 28-30 November, 2016.

List of Figures

1.1 Basic interactions of photons with matter [Salvat et al., 2006]. 4
1.2 The three major types of photon interaction [Evans and Noyau, 1955]. 5
1.3 Basic interactions of electrons with matter [Salvat et al., 2006]. 6
1.4 Percent Depth Dose (PDD) as a function of depth in water. The photon behavior is compared to the electron delivered dose. [Lamanna et al., 2012] 9
1.5 Components of the treatment head of A: X-ray therapy mode and B: Electron therapy mode [Khan, 1994]. 11
1.6 Main components of an ELEKTA PRECISE device [Nevelsky et al., 2010] 12
1.7 IOERT procedure with a stationary linear accelerator. The treatment room changes temporarily into an operating room with all the needed equipment for monitoring the anesthetized patient [Calvo et al., 2013] 13
1.8 Mobetron® linear accelerator (extracted from www.md51.com). 14
1.9 The soft-docking system used by the Mobetron®. (a) The electron applicator, in contact with the tumor bed, is rigidly clamped to the surgical bed [Beddar et al., 2006].(b) The gantry being moved for soft docking to the applicator [Beddar et al., 2006]. (c) Schematic diagram of the soft-docking system [Björk et al., 2000]. . . 15
1.10 On the left, the mobile accelerator Novac7® in the operating room [Russo et al., 2012]. On the right, scheme of the accelerator head [Pimpinella et al., 2007]. . . 16
1.11 Hard-docking system employed in Novac7®. (a) The collimation system fixed to the accelerator and the electron applicator before docking. (b) The hard-docking mechanism. (c) The unit ready for treatment with the applicator in contact with the tumor [Beddar et al., 2006]. 16
1.12 Liac® (from soiort.com). 17
1.13 (a)The Intrabeam® system (Carl Zeiss Meditec AG, Jena) (b) The scheme of the miniature X-ray source. (c) The Intrabeam® source. *Courtesy of Zeiss* [Zeiss, 2012]. 18
1.14 The Intrabeam® applicators. (a) Spherical applicator. (b) Needle applicator. (c) Cylindrical applicator. (d) Surface applicator. (e) Flat applicator [Zeiss, 2012]. . 19
1.15 Multichannel calibration curves [Micke et al., 2011] 25
1.16 Dose map and disturbance map, and horizontal profiles [Micke et al., 2011] 25
1.17 Energy distribution of an electron beam in a) the exit window, b) at the end of the applicator, c) at a certain depth inside the medium [Herranz, 2013] 27

1.18 Percentage depth dose curves (PDD) for typical IOERT electron beams [Nevelsky et al., 2010]. . . . 28
1.19 a) Depth dose curve illustrating the different parameters. (b) Typical shape of a transverse dose profile [Herranz, 2013]. . . . 29
1.20 Isodose contours of a 18 MeV electron beam [Nevelsky et al., 2010] . . . 30
1.21 Left: Energy spectrum of the XRS. Right: Energy spectrum of the 1.75 cm radius spherical applicator [Schneider et al., 2010]. . . . 31
1.22 Polar representation of the angular photon flux in the plane of the probe axis [Dinsmore et al., 1996]. . . . 31
1.23 (a) Depth dose curve rate for each spherical applicator [Xiao et al., 2015]. (b) Depth dose curve rate for each flat and surface applicator [Goubert and Parent, 2015]. . . . 32
1.24 Transverse dose profiles at different depths for 3 cm (a) flat and (b) surface applicators, normalized to the dose along the central axis [Goubert and Parent, 2015]. . . . 32
1.25 (a) Isodose contours of the Intrabeam® bare X-ray source. (b) Isodose contours of the Intrabeam® needle applicator (from Carl Zeiss Meditec AG) . . . 33
1.26 Dose distribution in ***radiance***® in a (a) IOERT treatment, and (b) in a XIORT treatment with a needle applicator [Valdivieso-Casique et al., 2015] . . . 35
1.27 Schematic representation of the gamma evaluation method between the reference dose ($\mathbf{r}_r$,D_r) and the calculated dose ($\mathbf{r}_c$,D_c). The criteria is defined by an ellipsoid of acceptance determined by the dose difference tolerance $\Delta \mathrm{D}_M$ and the DTA tolerance $\Delta \mathrm{d}_M$ [Depuydt et al., 2002]. . . . 36

2.1 Basic structure of the FORTRAN version of the main program of penEasy. Calls to tallying and other auxiliary subroutines have been removed for clarity [Badal Soler et al., 2008]. . . . 51

3.1 Cross section through the beryllium window of the INTRABEAM X-ray source (XRS) with the gold target [Beatty et al., 1996]. . . . 57
3.2 Geometry of the simulated Intrabeam® X-ray source visualized with the gview2d package from PENELOPE and a inset with a zoom of the target. The numeration corresponds to: 1. Vacuum inside the needle. 2. Beryllium. 3. Gold target. 4. Layer of nickel. 5. Layer of TiN. 6. PHSP plane definition. 7. Water phantom. . 58
3.3 (a) Energy spectra obtained experimentally [Schneider et al., 2009b] and with the detailed simulation for the XRS. (b) An expanded view of the line-radiation region of (a). . . . 59
3.4 2D dose distribution for the simulated XRS with isodose lines at 40%, 20%, 10% and 5% of the maximum dose. . . . 60
3.5 Computed tomography image showing the cross-section of 1.5 cm, 3.0 cm, 3.5 cm and 5.0 cm diameter applicator [Eaton and Duck, 2010]. . . . 60

3.6 Geometries employed in the simulation for the two different set of applicators. Left: 1.5 cm diameter spherical applicator. Right: 3.5 cm diameter spherical applicator. The numeration corresponds to: 1. Air inside the applicator were the XRS is located. 2. Applicator walls made of PEI. 3. Water. 4. Aluminum layer for the ≤ 3 cm diameter applicators. 61
3.7 Left: Energy spectra obtained experimentally [Schneider et al., 2010] and with the detailed simulation for the 1.75 cm radius applicator. Right: Depth dose curves obtained experimentally [Schneider et al., 2010] and with the detailed simulation for the 1.75 radius applicator. 62
3.8 2D dose distribution obtained with penEasy (Left) and with a radiochromic film (Right) for a 1.5 cm diameter applicator with isodose lines at 90%, 70%, 40%, 20% and 5%. 62
3.9 2D dose distribution obtained with penEasy (Left) and with a radiochromic film (Right) for a 4.0 cm diameter applicator with isodose lines at 90%, 70%, 40%, 20% and 10% of the maximum dose. 63
3.10 Schematic geometry for the (a) Flat applicators and (b) Surface applicators. The numbering represents 1. XRS, 2. Air inside the applicator, 3. Lead walls, 4. PEI filter. 64
3.11 Experimental and simulated transverse dose profiles for (a) 1 cm surface applicator and (b) 2 cm flat applicator. 64
3.12 Geometry of the simulated LIAC®. The numeration, materials and dimensions correspond to the numbers shown in the description. 66
3.13 Transverse dose profiles in water for a 12 MeV LIAC®, 6 cm diameter applicator. 67
3.14 Geometry of the simulated NOVAC®. The numeration, materials and dimensions correspond to the numbers shown in the description. 68
3.15 Transverse dose profiles in water for a 10 MeV NOVAC®, 6 cm diameter applicator. 69
3.16 Geometry of the simulated MOBETRON®. The numeration, materials and dimensions correspond to the numbers shown in the description. 70
3.17 Transverse dose profiles in water for a 12 MeV MOBETRON®, 10 cm diameter applicator. 71
3.18 Schematic view of the PHSP plane at the exit of the right angle applicator showing the small piece of beveled applicator included in the simulation to compute the dose for non-right applicators [Herranz et al., 2014]. 72
3.19 Angular variables employed to define the direction of a particle with the parameterization of the PHSP file. The green arrow represents the trajectory of the particle, contained in the red plane (striped plane). The angle with the z axis and the angle of the striped plane with the reference plane (xz plane) fully define the direction of the particle [Herranz et al., 2014]. 73
3.20 Histograms for a 6 MeV NOVAC® PHSP file with an applicator diameter of 60 mm, showing both electron and photon distributions. The ordinate axis shows the number of particles in each bin. The radial distribution shows number of particles crossing the unit of surface against ρ, the distance to the axis of the applicator. . 74
3.21 Schematic view of the parameterization of the PHSP files for spherical applicators in terms of the angles α and β. 75

3.22 Histograms for a 20 mm diameter spherical applicator PHSP file in terms of the relevant variables (Energy, α and β), showing photon contributions. The ordinate axis shows the number of particles in each bin. 76
3.23 Schematic view of the parameterization of the PHSP files for flat and surface applicators in terms of the distance to the applicator ρ and the angle θ. 77
3.24 Histograms for a 20 mm diameter surface applicator PHSP file in terms of the relevant variables (Energy, ρ and θ), showing photon contributions. The ordinate axis shows the number of particles in each bin. 78

4.1 Scheme of the phase space optimization process. 83
4.2 Experimental DDP and adjusted DDP for a 9 MeV NOVAC® with 4 cm diameter. 87
4.3 Left: Comparison of experimental DDP and optimized DDP for the 1.75 cm radius spherical applicator. Right: Optimized energy spectrum. 90
4.4 Left: Comparison of experimental DDP and optimized DDP for the 2 cm flat applicator. Right: Optimized energy spectrum. 90
4.5 Left: Comparison of experimental DDP and optimized DDP for the 9 MeV NOVAC® with a 4 cm applicator. Right: Optimized energy spectrum. 91

5.1 Left: Gammex® solid water phantom employed in calibration measurements with the ionization chamber and a EBT3 film. Right: Experimental setup for the calibration measurements. 96
5.2 Gammex solid water phantoms employed in 2D dose distribution measurements. . 97
5.3 Experimental setup (left) and schematic view of the position where the radiochromic films were placed (right). 98
5.4 DDPs for all the spherical applicators. Dotted curves correspond to our experimental measurements, and the solid lines correspond to the DDPs provided by Zeiss. 98
5.5 Experimental setup (left) of the Air-water step and schematic view of the position where the radiochromic films were placed (right). 99
5.6 Schematic view of the air step setup with the position where the radiochromic films were placed. 101
5.7 Experimental setup (left) of the bone heterogeneity and schematic view of the position where the radiochromic films were placed (right). 101
5.8 2D dose distributions in water for a 40 mm diameter spherical applicator obtained from (a) radiochromic films, (b) penEasy calculation with the reconstructed PHSP file and (c), the gamma evaluation distribution for a 2%-2 mm criterion with 5% threshold. 83.82% voxels passed the test. 102
5.9 2D dose distributions in water for a 25 mm diameter spherical applicator obtained from (a) radiochromic films, (b) penEasy calculation with the reconstructed PHSP file and (c), the gamma evaluation distribution for a 2%-2 mm criterion with 5% threshold. 94.43% voxels passed the test. 103
5.10 2D dose distributions in the air step at the different measured depths for a 40 mm diameter spherical applicator obtained from (a) radiochromic films, (b) penEasy calculation with the reconstructed PHSP file. 104

5.11 Dose distribution comparison for a 30 mm diameter flat applicator obtained with (a) a radiochromic film and (b) penEasy calculation from the reconstructed PHSP file. . . . 106
5.12 Dose distribution comparison for a 30 mm diameter surface applicator obtained with (a) a radiochromic film and (b) penEasy calculation from the reconstructed PHSP file. . . . 106
5.13 2D dose distributions in the bone phantom at the different measured depths for a 30 mm diameter flat applicator obtained from (a) radiochromic films, (b) penEasy calculation from the reconstructed PHSP file. . . . 107
5.14 2D dose distributions in the air step at the different measured depths for a 30 mm diameter surface applicator obtained from (a) radiochromic films, (b) penEasy calculation from the reconstructed PHSP file. . . . 107
5.15 Experimental setup (left) of a solid water step measurement and its schematic view with the location of the films (right). . . . 109
5.16 Experimental setup (left) of a lung heterogeneity measurement and its schematic view with the location of the films (right). . . . 109
5.17 Experimental setup (left) of a mediastinum-lung type measurement and its schematic view with the location of the films (right). . . . 110
5.18 Experimental setup (left) of a water/bone type measurement and its schematic view with the location of the films (right). . . . 110
5.19 Transverse dose profiles at 1.2 (shifted up by 20%) and 1.7 cm depth in the solid water step phantom obtained from the radiochromic films and from the reconstructed PHSP file (NOVAC®, 9MeV, 4 cm ϕ applicator). . . . 111
5.20 Transverse dose profiles at 1.0 (shifted up by 5%), 1.1, 1.6 and 2.1 cm depth in the lung heterogeneity, costal wall type phantom obtained from the radiochromic films and from the reconstructed PHSP file (NOVAC®, 9MeV, 4 cm ϕ applicator). 112
5.21 Transverse dose profiles at 1.0 (shifted up by 10%), 1.5, 2.5, 3.0 and 3.1 cm depth in the mediastinum-lung type phantom obtained from the radiochromic films and from the reconstructed PHSP file (NOVAC®, 9MeV, 4 cm ϕ applicator). . . . 112
5.22 Transverse dose profiles at 2.0 cm depth in the water/bone type phantom obtained from the radiochromic films and from the reconstructed PHSP file (NOVAC®, 9MeV, 4 cm ϕ applicator). . . . 113
5.23 Setups where the dose produced by the solution PHSP file and the full MC simulation were compared. . . . 114
5.24 (Left) Dose profiles at 1.5 (shifted up by 20%), 2.5 (shifted up by 10%) and 3.5 cm depth in the air-water step phantom for the 12 MeV LIAC®. (Right) Dose profiles at 1.95 (shifted up by 20%), 3.0 (shifted up by 10%) and 4.0 cm depth in the bone phantom for the 9 MeV MOBETRON® . . . 115

6.1 Randomly generated coordinates populating a XY plane. . . . 119
6.2 (a) Comparison of DDPs of a 1.5 cm diameter spherical applicator with a single full Compton interaction (solid line) and with two full Compton interactions (dots). (b) Statistical difference between the two profiles in (a). . . . 124
6.3 Flow chart of the HMC. . . . 125

6.4 Comparison of dose distributions calculated with penEasy and the HMC algorithm for different number of histories or m-histories. (a) penEasy simulation with 0.5 million histories, (b) penEasy simulation with 5 million histories, (c) HMC simulation with 0.5 million m-histories, (d) HMC simulation with 5 million m-histories. . . . 127
6.5 Effect of normalization on a 3 cm diameter spherical applicator dose distribution calculated with the HMC algorithm and 5 million m-histories. (a) Unnormalized dose, (b) normalized dose. . . . 130
6.6 Schematic representation of the parameters that characterize the fluence in flat and surface applicators. . . . 130
6.7 Effect of normalization on a 2 cm diameter surface applicator dose distribution calculated with the HMC algorithm an 5 million m-histories. (a) Unnormalized dose, (b) normalized dose. . . . 132
6.8 Schema of the homogeneous phantoms surrounding the spherical or the needle applicators. . . . 133
6.9 2D dose distributions in water for a 15 mm diameter spherical applicator using (a) penEasy and (b) the HMC and their DDPs (c). . . . 134
6.10 2D dose distributions in lung for a 40 mm diameter spherical applicator using (a) penEasy and (b) the HMC and their DDPs (c). . . . 134
6.11 2D dose distributions in bone for a 30 mm diameter spherical applicator using (a) penEasy and (b) the HMC and their DDPs (c). . . . 135
6.12 Schema of the heterogeneous phantoms surrounding the spherical or the needle applicators. . . . 137
6.13 2D dose distributions in a water/bone phantom for the needle applicator using (a) penEasy and (b) the HMC and their DDPs (c). . . . 138
6.14 2D dose distributions in a lung/bone phantom for the 50 mm spherical applicator using (a) penEasy and (b) the HMC algorithm and their DDPs (c). . . . 138
6.15 2D dose distributions in a water/bone/lung phantom for the 20 mm spherical applicator using (a) penEasy and (b) the HMC algorithm and their DDPs (c). . . . 139
6.16 2D dose distribution in a water phantom for the 30 mm flat applicator using (a) penEasy and (b) the HMC algorithm and (c) their transverse profiles at 0, 2 and 5 mm depth. . . . 141
6.17 2D dose distribution in a lung phantom for the 20 mm surface applicator using (a) penEasy and (b) the HMC algorithm and (c) their transverse profiles at 0, 2 and 5 mm depth. . . . 142
6.18 2D dose distribution in a bone phantom for the 60 mm flat applicator using (a) penEasy and (b) the HMC algorithm and (c) their transverse profiles at 0.5, 2 and 5 mm depth. . . . 142
6.19 Depth dose curves obtained with the HMC (solid lines) and penEasy (dashed lines) in the 3 different phantoms. . . . 143
6.20 Schemes of the heterogeneous phantoms used for the validation of the flat and surface applicators. . . . 145

6.21 2D dose distribution in the bone layer phantom for the 40 mm flat applicator using (a) penEasy and (b) the HMC algorithm. (c) Depth dose profiles obtained with both codes and (d), their transverse profiles at the water surface, at the bone surface and right after the bone layer. 146
6.22 2D dose distribution in the air gap phantom for the 20 mm flat applicator using (a) penEasy and (b) the HMC algorithm. (c) Depth dose profiles obtained with both codes starting after the air gap and (d), their transverse profiles at 2 mm, 4 mm and 6 mm depth. 146
6.23 2D dose distribution in the lead protection disk phantom for the 30 mm surface applicator using (a) penEasy and (b) the HMC algorithm. (c) Depth dose profiles obtained with both codes and (d), their transverse profiles at the water surface, at the lead interface and right after the disk. 147
6.24 Dose distribution on a CT representing a breast conserving treatment with (a) penEasy, (b) HMC 150
6.25 Gamma distribution on the partial breast irradiation treatment simulation with a 2%-1 mm criterion and 5% threshold. 95.51% of the voxels passed the evaluation. 151
6.26 Dose distribution on a CT representing a Kypho-IORT treatment with (a) penEasy, (b) HMC 152
6.27 Gamma distribution on the Kypho-IORT treatment simulation with a 2%-1 mm criterion and 5% threshold. 95.11% of the voxels passed the evaluation. 153

List of Tables

3.1 Classification of the characteristic X-rays present in the XRS energy spectrum. . 59

5.1 Measured dose values during the calibration procedure obtained with the ionization chamber. 95
5.2 Measured dose values during the calibration procedure obtained with the ionization chamber. 100
5.3 Results of gamma evaluation between MC simulations and measurements in the air step phantom (5% threshold). 105
5.4 Results of gamma evaluation between MC simulations and measurements in the air step phantom and in the bone heterogeneity (5% threshold). 108
5.5 Results of gamma evaluation between MC simulations and measurements in the different phantoms (5% threshold). 113
5.6 Results of gamma evaluation in the different phantoms (5% threshold). 115

6.1 Results of gamma evaluation between MC simulations and HMC calculations in water (5% threshold). 135
6.2 Results of gamma evaluation between MC simulations and HMC calculations in lung (10% threshold). 136
6.3 Results of gamma evaluation between MC simulations and HMC calculations in bone (5% threshold). 136
6.4 Results of gamma evaluation between MC simulations and HMC calculations in the water/bone phantom (5% threshold). 139
6.5 Results of gamma evaluation between MC simulations and HMC calculations in the lung/bone phantom (5% threshold). 140
6.6 Results of gamma evaluation between MC simulations and HMC calculations in the water/bone/lung phantom (5% threshold). 140
6.7 Results of gamma evaluation between MC simulations and HMC calculations in the water phantom (5% threshold). 143
6.8 Results of gamma evaluation between MC simulations and HMC calculations in the lung phantom (5% threshold). 144
6.9 Results of gamma evaluation between MC simulations and HMC calculations in the bone phantom (5% threshold). 144

6.10 Results of gamma evaluation between MC simulations and HMC calculations in the bone layer phantom (5% threshold). 148
6.11 Results of gamma evaluation between MC simulations and HMC calculations in the air gap phantom (5% threshold). 148
6.12 Results of gamma evaluation between MC simulations and HMC calculations in the protection lead disk phantom (5% threshold). 149

Bibliography

M. Abe. Intraoperative radiotherapy—past, present and future. *International Journal of Radiation Oncology* Biology* Physics*, 10(10):1987–1990, 1984.

M. Abe and M. Takahashi. Intraoperative radiotherapy: the Japanese experience. *International Journal of Radiation Oncology* Biology* Physics*, 7(7):863–868, 1981.

M. Abe, M. Fukuda, K. Yamano, S. Matsuda, and H. Handa. Intra-operative irradiation in abdominal and cerebral tumours. *Acta radiologica: therapy, physics, biology*, 10(4):408–416, 1971.

S. Agostinelli et al. Geant4-a Simulation Toolkit, Nuclear Instruments and Methods in Physics Research Section A: Accelerators, Spectrometers. *Detectors and Associated Equipment*, 506 (3), 2003.

M. Alber, S. Broggi, C. De Wagter, I. Eichwurzel, P. Engström, C. Fiorino, D. Georg, G. Hartmann, T. Knöös, A. Leal, et al. Guidelines for the verification of IMRT. *ESTRO booklet*, 7, 2008.

P. R. Almond, P. J. Biggs, B. Coursey, W. Hanson, M. S. Huq, R. Nath, and D. Rogers. AAPM's TG-51 protocol for clinical reference dosimetry of high-energy photon and electron beams. *Medical physics*, 26(9):1847–1870, 1999.

E. Aranda Escolástico. Análisis de películas radiocrómicas para su utilización en dosimetría médica. *Final Degree Project*. Advisors: José Manuel Udías Moinelo y Marie Vidal.Universidad Complutense de Madrid, 2013.

K. S. Armoogum, J. M. Parry, S. K. Souliman, D. G. Sutton, and C. D. Mackay. Functional intercomparison of intraoperative radiotherapy equipment–Photon Radiosurgery System. *Radiation Oncology*, 2(1):1, 2007.

F. H. Attix. *Introduction to radiological physics and radiation dosimetry*. John Wiley & Sons, 2008.

M. Avanzo, A. Rink, A. Dassie, S. Massarut, M. Roncadin, E. Borsatti, and E. Capra. In vivo dosimetry with radiochromic films in low-voltage intraoperative radiotherapy of the breast. *Medical physics*, 39(5):2359–2368, 2012.

A. Badal Soler et al. Development of advanced geometric models and acceleration techniques for Monte Carlo simulation in Medical Physics. PhD. thesis, 2008.

J. Baro, J. Sempau, J. M. Fernández-Varea, and F. Salvat. PENELOPE: an algorithm for Monte Carlo simulation of the penetration and energy loss of electrons and positrons in matter. *Nuclear Instruments and Methods in Physics Research Section B: Beam Interactions with Materials and Atoms*, 100(1):31–46, 1995.

J. Beatty, P. Biggs, K. Gall, P. Okunieff, F. Pardo, K. Harte, M. Dalterio, and A. Sliski. A new miniature x-ray device for interstitial radiosurgery: Dosimetry. *Medical physics*, 23(1):53–62, 1996.

C. Beck. On external Roentgen treatment of internal structures (eventration treatment). *NY Med J*, 89:621–622, 1909.

A. S. Beddar. Stability of a mobile electron linear accelerator system for intraoperative radiation therapy. *Medical physics*, 32(10):3128–3131, 2005.

A. S. Beddar, P. J. Biggs, S. Chang, G. A. Ezzell, B. A. Faddegon, F. W. Hensley, and M. D. Mills. Intraoperative radiation therapy using mobile electron linear accelerators: Report of AAPM Radiation Therapy Committee Task Group No. 72. *Medical physics*, 33(5):1476–1489, 2006.

M. J. Berger et al. Monte Carlo calculation of the penetration and diffusion of fast charged particles. *Methods in computational physics*, 1:135–215, 1963.

A. F. Bielajew. Fundamentals of the Monte Carlo method for neutral and charged particle transport. *The University of Michigan*, 2001.

P. Björk, T. Knöös, P. Nilsson, and K. Larsson. Design and dosimetry characteristics of a soft-docking system for intraoperative radiation therapy. *International Journal of Radiation Oncology* Biology* Physics*, 47(2):527–533, 2000.

P. Björk, P. Nilsson, and T. Knöös. Dosimetry characteristics of degraded electron beams investigated by Monte Carlo calculations in a setup for intraoperative radiation therapy. *Physics in medicine and biology*, 47(2):239, 2002.

P. Björk, T. Knöös, and P. Nilsson. Measurements of output factors with different detector types

and Monte Carlo calculations of stopping-power ratios for degraded electron beams. *Physics in medicine and biology*, 49(19):4493, 2004.

W. R. Bodner, B. S. Hilaris, M. Alagheband, B. Safai, C. A. Mastoras, and S. Saraf. Use of Low-Energy X-Rays in the Treatment of Superficial Nonmelanomatous Skin Cancers. *Cancer investigation*, 21(3):355–362, 2003.

D. Bouzid, J. Bert, P.-F. Dupre, S. Benhalouche, O. Pradier, N. Boussion, and D. Visvikis. Monte-Carlo dosimetry for intraoperative radiotherapy using a low energy x-ray source. *Acta Oncologica*, 54(10):1788–1795, 2015.

F. B. Brown, R. F. Barrett, T. E. Booth, J. S. Bull, L. J. Cox, R. A. Forster, T. J. Goorley, R. D. Mosteller, S. E. Post, R. E. Prael, E. C. Selcow, A. Sood, and J. Sweezy. MCNP VERSION 5 Technical report LA-UR- 02-3935 Los Alamos National Laboratory. Technical report, 2002.

K. Bush, I. Popescu, and S. Zavgorodni. A technique for generating phase-space-based Monte Carlo beamlets in radiotherapy applications. *Physics in medicine and biology*, 53(18):N337, 2008.

F. Calvo, C. Sole, R. Herranz, M. Lopez-Bote, J. Pascau, A. Santos, A. Muñoz-Calero, C. Ferrer, and J. Garcia-Sabrido. Intraoperative radiotherapy with electrons: fundamentals, results, and innovation. *Ecancermedicalscience*, 7:339, 2013.

F. A. Calvo, B. Micaily, and L. W. Brady. Intraoperative radiotherapy: a positive view. *American journal of clinical oncology*, 16(5):418, 1993.

R. Capote, R. Jeraj, C. Ma, D. Rogers, F. Sánchez-Doblado, J. Sempau, J. Seuntjens, and J. Siebers. Phase-space database for external beam radiotherapy. *IAEA, Nucl. Data Sec. Report INDC (NDS)-0484, International Atomic Energy Agency, Vienna, Austria*, 2006.

W.-Z. Chen, Y. Xiao, and J. Li. Impact of dose calculation algorithm on radiation therapy. *World journal of radiology*, 6(11):874, 2014.

S. R. Cherry, J. A. Sorenson, and M. E. Phelps. *Physics in nuclear medicine*. Elsevier Health Sciences, 2012.

I. J. Chetty, B. Curran, J. E. Cygler, J. J. DeMarco, G. Ezzell, B. A. Faddegon, I. Kawrakow, P. J. Keall, H. Liu, C.-M. C. Ma, et al. Report of the AAPM Task Group No. 105: Issues associated with clinical implementation of Monte Carlo-based photon and electron external beam treatment planning. *Medical physics*, 34(12):4818–4853, 2007.

S. Chiavassa, C. Hervé, F. Buge, J. Rigaud, S. Supiot, A. Lisbona, and G. Delpon. Validation

of a MC-based dose calculation environment for feasibility of IORT in prostate cancer with INTRABEAM. *Radiotherapy and Oncology*, 111:S68, 2014.

S. Clausen, F. Schneider, L. Jahnke, J. Fleckenstein, J. Hesser, G. Glatting, and F. Wenz. A Monte Carlo based source model for dose calculation of endovaginal TARGIT brachytherapy with INTRABEAM and a cylindrical applicator. *Zeitschrift für Medizinische Physik*, 22(3): 197–204, 2012.

B. J. Debenham, K. S. Hu, and L. B. Harrison. Present status and future directions of intraoperative radiotherapy. *The Lancet Oncology*, 14(11):e457–e464, 2013.

G. Delaney, S. Jacob, C. Featherstone, and M. Barton. The role of radiotherapy in cancer treatment. *Cancer*, 104(6):1129–1137, 2005.

J. M. Delgado, A. García, F. García, and E. Millán. *Fundamentos de Física Médica, Volumen 4, Radioterapia externa II. Dosimetría clínica, algoritmos de cálculo, sistemas de planificación y control de calidad.* Sociedad Española de Física Médica ADI Servicios Editoriales, 2013.

T. Depuydt, A. Van Esch, and D. P. Huyskens. A quantitative evaluation of IMRT dose distributions: refinement and clinical assessment of the gamma evaluation. *Radiotherapy and Oncology*, 62(3):309–319, 2002.

M. Desco, J. López, F. A. Calvo, A. Santos, J. A. Santos, F. del Pozo, and P. García-Barreno. Simulated surgery on computed tomography and magnetic resonance images: an aid for intraoperative radiotherapy. *Computer Aided Surgery*, 2(6):333–339, 1997.

S. Devic, J. Seuntjens, E. Sham, E. B. Podgorsak, C. R. Schmidtlein, A. S. Kirov, and C. G. Soares. Precise radiochromic film dosimetry using a flat-bed document scanner. *Medical physics*, 32(7):2245–2253, 2005.

S. Devic, N. Tomic, C. G. Soares, and E. B. Podgorsak. Optimizing the dynamic range extension of a radiochromic film dosimetry system. *Medical physics*, 36(2):429–437, 2009.

G. X. Ding, J. E. Cygler, W. Y. Christine, N. I. Kalach, and G. Daskalov. A comparison of electron beam dose calculation accuracy between treatment planning systems using either a pencil beam or a Monte Carlo algorithm. *International Journal of Radiation Oncology* Biology* Physics*, 63(2):622–633, 2005.

M. Dinsmore, K. Harte, A. Sliski, D. Smith, P. Nomikos, M. Dalterio, A. Boom, W. Leonard, P. Oettinger, and J. Yanch. A new miniature x-ray source for interstitial radiosurgery: Device description. *Medical physics*, 23(1):45–52, 1996.

D. Eaton and S. Duck. Dosimetry measurements with an intra-operative x-ray device. *Physics in medicine and biology*, 55(12):N359, 2010.

D. Eaton, R. Gonzalez, S. Duck, and M. Keshtgar. Radiation protection for an intra-operative X-ray device. *The British journal of radiology*, 2011.

M. Ebert and B. Carruthers. Dosimetric characteristics of a low-kV intra-operative x-ray source: implications for use in a clinical trial for treatment of low-risk breast cancer. *Medical physics*, 30(9):2424–2431, 2003.

M. Ebert, B. Carruthers, P. Lanzon, A. Haworth, J. Clarke, N. Caswell, and S. Siddiqui. Dosimetry of a low-kV intra-operative X-ray source using basic analytical beam models. *Australasian Physics & Engineering Sciences in Medicine*, 25(3):119–123, 2002.

M. Ebert, A. H. Asad, and S. A. Siddiqui. Suitability of radiochromic films for dosimetry of very-low energy X-rays. *Journal of applied clinical medical physics*, 10(4), 2009.

R. D. Evans and A. Noyau. *The atomic nucleus*, volume 582. McGraw-Hill New York, 1955.

B. Faddegon, J. Balogh, R. Mackenzie, and D. Scora. Clinical considerations of Monte Carlo for electron radiotherapy treatment planning. *Radiation Physics and Chemistry*, 53(3):217–227, 1998.

C. Fernandez-Ramirez, E. M. de Guerra, A. Udias, and J. M. Udias. Properties of nucleon resonances by means of a genetic algorithm. *Physical Review C*, 77(6):065212, 2008.

A. Ferrari, P. R. Sala, A. Fasso, and J. Ranft. FLUKA: A multi-particle transport code (Program version 2005). Technical report, 2005.

C. L. Fletcher and J. A. Mills. An assessment of GafChromic film for measuring 50 kV and 100 kV percentage depth dose curves. *Physics in medicine and biology*, 53(11):N209, 2008.

M. Fuss, E. Sturtewagen, C. De Wagter, and D. Georg. Dosimetric characterization of GafChromic EBT film and its implication on film dosimetry quality assurance. *Physics in Medicine and Biology*, 52(14):4211, 2007.

Gafchromic-EBT3. Gafchromic EBT3 Technical Specifications. Technical report, Ashland.

R. García-Marcos, M. Vidal, P. Ibáñez, R. Ayala, R. Sendón, R. Polo, and J. M. Udías. Impact of patient-applicator air-gap in dedicated mobile accelerator for Intra-Operative Radiation Therapy. *Radiotherapy and Oncology*, 111:S161–S162, 2014.

GMV. *Radiation treatment simulation platform for IORT suitable devices, White Paper*, 2015.

M. Goubert and L. Parent. Dosimetric characterization of INTRABEAM® miniature accelerator flat and surface applicators for dermatologic applications. *Physica Medica*, 31(3):224–232, 2015.

P. Guerra, J. M. Udías, E. Herranz, J. A. Santos-Miranda, J. L. Herraiz, M. F. Valdivieso, R. Rodríguez, J. A. Calama, J. Pascau, F. A. Calvo, et al. Feasibility assessment of the interactive use of a Monte Carlo algorithm in treatment planning for intraoperative electron radiation therapy. *Physics in medicine and biology*, 59(23):7159, 2014.

P. Guerra Gutiérrez, J. M. Udías Moinelo, A. d. Santos Lleo, E. Herranz Muelas, M. Valdivieso, C. Santiago, J. Agustín, C. Illana Alejandro, and M. J. Ledesma Carbayo. Optimization of Monte Carlo code for clinical simulation of electron beams. *International Journal of Radiation Oncology, Biology, Physics*, 84:S870, 2012.

L. L. Gunderson, C. G. Willett, F. A. Calvo, and L. B. Harrison. *Intraoperative irradiation: techniques and results*. Springer Science & Business Media, 2011.

E. C. Halperin, C. A. Perez, and L. W. Brady. *Perez and Brady's principles and practice of radiation oncology*. Lippincott Williams & Wilkins, 2008.

M. G. Herman. Clinical use of electronic portal imaging. In *Seminars in radiation oncology*, volume 15, pages 157–167. Elsevier, 2005.

K.-P. Hermann, L. Geworski, M. Muth, and D. Harder. Polyethylene-based water-equivalent phantom material for x-ray dosimetry at tube voltages from 10 to 100 kV. *Physics in medicine and biology*, 30(11):1195, 1985.

E. Herranz. *Simulaciones Monte Carlo para radioterapia intraoperatoria con haces de electrones*. PhD thesis, Advisors: José Manuel Udías and Joaquín López. Universidad Complutense de Madrid, 2013.

E. Herranz, J. Herraiz, P. Ibáñez, M. Pérez-Liva, R. Puebla, J. Cal-González, P. Guerra, R. Rodríguez, C. Illana, and J. M. Udías. Phase space determination from measured dose data for intraoperative electron radiation therapy. *Physics in medicine and biology*, 60(1):375, 2014.

R. Hill, L. Holloway, and C. Baldock. A dosimetric evaluation of water equivalent phantoms for kilovoltage x-ray beams. *Physics in medicine and biology*, 50(21):N331, 2005.

R. Hill, Z. Kuncic, and C. Baldock. The water equivalence of solid phantoms for low energy photon beams. *Medical physics*, 37(8):4355–4363, 2010.

R. Hill, B. Healy, L. Holloway, Z. Kuncic, D. Thwaites, and C. Baldock. Advances in kilovoltage x-ray beam dosimetry. *Physics in medicine and biology*, 59(6):R183, 2014.

K. Hogstrom. Evaluation of electron pencil beam dose calculations. In *Medical physics*, volume 12, pages 554–554. Amer Inst Physics circulation fulfillment Div, 500 Sunnyside Blvd, Woodbury, NY, 11797-2999, 1985.

K. R. Hogstrom and P. R. Almond. Review of electron beam therapy physics. *Physics in medicine and biology*, 51(13):R455, 2006.

G. Iaccarino, L. Strigari, M. D'Andrea, L. Bellesi, G. Felici, A. Ciccotelli, M. Benassi, and A. Soriani. Monte Carlo simulation of electron beams generated by a 12 MeV dedicated mobile IORT accelerator. *Physics in medicine and biology*, 56(14):4579, 2011.

P. Ibáñez. Validación de modelos de aceleradores para radioterapia intraoperatoria. Master's thesis, Advisor: José Manuel Udías, Universidad Complutense de Madrid, 2012.

P. Ibáñez, M. Vidal, R. García Marcos, E. Herranz Muelas, P. Guerra Gutiérrez, C. Santiago, J. Agustín, M. Infante, M. Lavado, and J. M. Udías. Validation of a phase space determination algorithm for intraoperative radiation therapy. *Radiotherapy and Oncology*, 111(S1):331–331, 2014.

P. Ibáñez, M. Vidal, R. García-Marcos, P. Guerra, and J. M. Udías. New genetic algorithm-based procedure to determine phase space for intraoperative radiation therapy. *Radiotherapy and Oncology*, 115:S278–S279, 2015.

P. Ibáñez, M. Vidal, P. Guerra, and J. M. Udías. Validation of an optimized MC dose prediction for low energy x-rays intraoperative radiation therapy. *Radiotherapy and Oncology*, 119:S269–S270, 2016.

D. A. Jaffray. Emergent technologies for 3-dimensional image-guided radiation delivery. In *Seminars in radiation oncology*, volume 15, pages 208–216. Elsevier, 2005.

R. W. Janssen, B. A. Faddegon, and W. J. Dries. Prototyping a large field size IORT applicator for a mobile linear accelerator. *Physics in medicine and biology*, 53(8):2089, 2008.

R. Jones, B. Libby, S. L. Showalter, D. R. Brenin, D. D. Wilson, A. Schroen, M. Morris, K. A. Reardon, J. Morrison, and T. N. Showalter. Dosimetric comparison of 192 Ir high-dose-rate brachytherapy vs. 50 kV x-rays as techniques for breast intraoperative radiation therapy: Conceptual development of image-guided intraoperative brachytherapy using a multilumen balloon applicator and in-room CT imaging. *Brachytherapy*, 13(5):502–507, 2014.

M. H. Kalos and P. A. Whitlock. *Monte carlo methods*. John Wiley & Sons, 2008.

C. J. Karzmark and R. J. Morton. Primer on theory and operation of linear accelerators in radiation therapy. Technical report, Bureau of Radiological Health, 1981.

I. Kawrakow and A. F. Bielajew. On the condensed history technique for electron transport. *Nuclear Instruments and Methods in Physics Research Section B: Beam Interactions with Materials and Atoms*, 142(3):253–280, 1998.

I. Kawrakow and D. Rogers. The EGSnrc code system: Monte Carlo simulation of electron and photon transport. 2000.

I. Kawrakow, M. Fippel, and K. Friedrich. 3D electron dose calculation using a Voxel based Monte Carlo algorithm (VMC). *Medical physics*, 23(4):445–457, 1996.

I. Kawrakow, A. Rogers D.W.O, Kling, F. J. Barao, M. Nakagawa, L. Tavora, and P. Vaz. *The EGSnrc system, a status report In: Advanced Monte Carlo for Radiation Physics, Particle Transport Simulation and Applications: Proceedings of the Monte Carlo 2000 Conference, Lisbon, 23–26 October 2000*. Springer Science & Business Media, 2014.

F. Khan. *The Physics of Radiation Therapy 2nd edn (Baltimore, MD: Williams and Wilkins)*. 1994.

F. Khan. Handbook of the physics of radiation therapy. *Baltimore: Williams and Wilkins*, pages 36–53, 2009.

F. M. Khan, K. P. Doppke, K. R. Hogstrom, G. J. Kutcher, R. Nath, S. C. Prasad, J. A. Purdy, M. Rozenfeld, and B. L. Werner. Clinical electron-beam dosimetry: report of AAPM radiation therapy committee task group No. 25. *Medical physics*, 18(1):73–109, 1991.

G. F. Knoll. *Radiation detection and measurement*. John Wiley & Sons, 2010.

H. A. Kramers. XCIII. On the theory of X-ray absorption and of the continuous X-ray spectrum. *The London, Edinburgh, and Dublin Philosophical Magazine and Journal of Science*, 46(275): 836–871, 1923.

U. Kraus-Tiefenbacher, V. Steil, L. Bauer, F. Melchert, and F. Wenz. A novel mobile device for intraoperative radiotherapy (IORT). *Oncology Research and Treatment*, 26(6):596–598, 2004.

U. Kraus-Tiefenbacher, A. Scheda, V. Steil, B. Hermann, T. Kehrer, L. Bauer, F. Melchert, and F. Wenz. Intraoperative radiotherapy (IORT) for breast cancer using the IntraBeam TM system. *Tumori*, 91:339–345, 2005.

S. C. Lam, Y. Xu, G. Ingram, and L. Chong. Dosimetric characteristics of INTRABEAM® flat and surface applicators. *Translational Cancer Research*, 3(1):106–111, 2014.

E. Lamanna, A. Gallo, A. Soriani, F. Russo, L. Strigari, and R. Brancaccio. *Intra-operative radiotherapy with electron beam*. INTECH Open Access Publisher, 2012.

N. Leoz Munté. Verificación del código de simulación Monte Carlo para Radioterapia. Análisis y comparación de resultados teóricos y experimentales. Master's thesis, Advisors: José Manuel Udías Moinelo and Paula Ibáñez García. Universidad Complutense de Madrid, 2015.

D. Lewis, A. Micke, X. Yu, and M. F. Chan. An efficient protocol for radiochromic film dosimetry combining calibration and measurement in a single scan. *Medical physics*, 39(10):6339–6350, 2012.

D. Lindner, C. Trantakis, C. Renner, S. Arnold, A. Schmitgen, J. Schneider, and J. Meixensberger. Application of intraoperative 3D ultrasound during navigated tumor resection. *min-Minimally Invasive Neurosurgery*, 49(04):197–202, 2006.

J. López-Tarjuelo, M. Lardiés, A. García-Romero, J. R. Rodriguez, E. Lavado-Rodríguez, J. Calama-Santiago, M. Infante-Utrilla, C. Ferrer-Albiach, and E. Sanfeliu-Lucas. SU-GG-T-98: Pencil Beam for Electron Intraoperative Radiotherapy. Early Results from Profile and Percentage Depth Dose Modeling. *Medical Physics*, 37(6):3206–3207, 2010.

D. A. Low and J. F. Dempsey. Evaluation of the gamma dose distribution comparison method. *Medical physics*, 30(9):2455–2464, 2003.

D. A. Low, W. B. Harms, S. Mutic, and J. A. Purdy. A technique for the quantitative evaluation of dose distributions. *Medical physics*, 25(5):656–661, 1998.

C.-M. Ma and S. B. Jiang. Monte Carlo modelling of electron beams from medical accelerators. *Physics in medicine and biology*, 44(12):R157, 1999.

T. R. Mackie, J. Kapatoes, K. Ruchala, W. Lu, C. Wu, G. Olivera, L. Forrest, W. Tome, J. Welsh, R. Jeraj, et al. Image guidance for precise conformal radiotherapy. *International Journal of Radiation Oncology* Biology* Physics*, 56(1):89–105, 2003.

G. S. Mageras and E. Yorke. Deep inspiration breath hold and respiratory gating strategies for reducing organ motion in radiation treatment. In *Seminars in radiation oncology*, volume 14, pages 65–75. Elsevier, 2004.

M. Marrale, A. Longo, G. Russo, C. Casarino, G. Candiano, S. Gallo, A. Carlino, and M. Brai. Dosimetry for electron Intra-Operative RadioTherapy: Comparison of output factors obtained

through alanine/EPR pellets, ionization chamber and Monte Carlo-GEANT4 simulations for IORT mobile dedicate accelerator. *Nuclear Instruments and Methods in Physics Research Section B: Beam Interactions with Materials and Atoms*, 358:52–58, 2015.

A. Martignano, L. Menegotti, and A. Valentini. Monte Carlo investigation of breast intraoperative radiation therapy with metal attenuator plates. *Medical physics*, 34(12):4578–4584, 2007.

J. E. Martin. *Physics for radiation protection: a handbook*. John Wiley & Sons, 2006.

P. N. McDermott, T. He, and A. DeYoung. Dose calculation accuracy of lung planning with a commercial IMRT treatment planning system. *Journal of Applied Clinical Medical Physics*, 4 (4):341–351, 2003.

A. S. Meigooni, J. A. Meli, and R. Nath. A comparison of solid phantoms with water for dosimetry of 125I brachytherapy sources. *Medical physics*, 15(5):695–701, 1988.

A. Micke, D. F. Lewis, and X. Yu. Multichannel film dosimetry with nonuniformity correction. *Medical physics*, 38(5):2523–2534, 2011.

D. Mihailescu, M. Pimpinella, A. Guerra, and R. Laitano. Comparison of measured and Monte Carlo calculated dose distributions for the NOVAC7® linear accelerator. *Romanian Journal of Physics*, 51(7/8):729, 2006.

M. D. Mills, L. C. Fajardo, D. L. Wilson, J. L. Daves, and W. J. Spanos. Commissioning of a mobile electron accelerator for intraoperative radiotherapy. *Journal of Applied Clinical Medical Physics*, 2(3):121–130, 2001.

A. Nevelsky, Z. Bernstein, R. Bar-Deroma, A. Kuten, and I. Orion. Design and dosimetry characteristics of a commercial applicator system for intra-operative electron beam therapy utilizing ELEKTA Precise accelerator. *Journal of Applied Clinical Medical Physics*, 11(4), 2010.

A. Niroomand-Rad, C. R. Blackwell, B. M. Coursey, K. P. Gall, J. M. Galvin, W. L. McLaughlin, A. S. Meigooni, R. Nath, J. E. Rodgers, C. G. Soares, et al. Radiochromic film dosimetry: recommendations of AAPM radiation therapy committee task group 55. *Medical physics*, 25 (11):2093–2115, 1998.

O. Nwankwo, S. Clausen, F. Schneider, and F. Wenz. A virtual source model of a kilo-voltage radiotherapy device. *Physics in medicine and biology*, 58(7):2363, 2013.

R. Orecchia and U. Veronesi. Intraoperative electrons. In *Seminars in radiation oncology*,

volume 15, pages 76–83. Elsevier, 2005.

R. Orecchia, M. Ciocca, R. Lazzari, C. Garibaldi, M. Leonardi, A. Luini, M. Intra, G. Gatti, P. Veronesi, J. Petit, et al. Intraoperative radiation therapy with electrons (ELIOT) in early-stage breast cancer. *The Breast*, 12(6):483–490, 2003.

T. Oshima, Y. Aoyama, T. Shimozato, M. Sawaki, T. Imai, Y. Ito, Y. Obata, and K. Tabushi. An experimental attenuation plate to improve the dose distribution in intraoperative electron beam radiotherapy for breast cancer. *Physics in medicine and biology*, 54(11):3491, 2009.

J. R. Palta, P. J. Biggs, J. D. Hazle, M. S. Huq, R. A. Dahl, T. G. Ochran, J. Soen, R. R. Dobelbower, and E. C. McCullough. Intraoperative electron beam radiation therapy: technique, dosimetry, and dose specification: report of task force 48 of the Radiation Therapy Committee, American Association of Physicists in Medicine. *International Journal of Radiation Oncology* Biology* Physics*, 33(3):725–746, 1995.

C. C. Park, S. S. Yom, M. B. Podgorsak, E. Harris, R. A. Price, A. Bevan, J. Pouliot, A. A. Konski, P. E. Wallner, E. B. W. Group, et al. American Society for Therapeutic Radiology and Oncology (ASTRO) emerging technology committee report on electronic brachytherapy. *International Journal of Radiation Oncology* Biology* Physics*, 76(4):963–972, 2010.

J. Pascau, J. A. S. Miranda, F. A. Calvo, A. Bouché, V. Morillo, C. González-San Segundo, C. Ferrer, J. L. Tarjuelo, and M. Desco. An innovative tool for intraoperative electron beam radiotherapy simulation and planning: description and initial evaluation by radiation oncologists. *International Journal of Radiation Oncology* Biology* Physics*, 83(2):e287–e295, 2012.

M. Pérez-Liva. Simulación de aceleradores para radioterapia intraoperatoria. Master's thesis, Advisor: José Manuel Udías, Universidad Complutense de Madrid, 2012.

M. Pimpinella, D. Mihailescu, A. Guerra, and R. Laitano. Dosimetric characteristics of electron beams produced by a mobile accelerator for IORT. *Physics in medicine and biology*, 52(20): 6197, 2007.

N. Reynaert, S. van der Marck, and D. Schaart. Monte Carlo Treatment Planning—An Introduction, Nederlandse Commissie Voor Stralingsdosimetrie, 2006.

T. A. Rich. Intraoperative radiotherapy. *Radiotherapy and oncology*, 6(3):207–221, 1986.

S. Righi, E. Karaj, G. Felici, and F. Di Martino. Dosimetric characteristics of electron beams produced by two mobile accelerators, Novac7 and Liac, for intraoperative radiation therapy through Monte Carlo simulation. *Journal of Applied Clinical Medical Physics*, 14(1), 2013.

M. Rodríguez, S. E. de Física Médica, F. Vicente, and E. Cebrián. *Protocolo para el control de calidad en sistemas de planificación de terapia con radiaciones ionizantes*. Ramírez de Arellano Editores, 2005. ISBN 9788493444815.

M. Rodriguez, J. Sempau, and L. Brualla. PRIMO: a graphical environment for the Monte Carlo simulation of Varian and Elekta linacs. *Strahlentherapie und Onkologie*, 189(10):881–886, 2013.

D. Rogers. Monte Carlo techniques in radiotherapy. *Physics in Canada*, 58(2):63–71, 2002.

D. Rogers. Fifty years of Monte Carlo simulations for medical physics. *Physics in medicine and biology*, 51(13):R287, 2006.

D. Rogers, B. Faddegon, G. Ding, C.-M. Ma, J. We, and T. Mackie. BEAM: a Monte Carlo code to simulate radiotherapy treatment units. *Medical physics*, 22(5):503–524, 1995.

G. Russo, C. Casarino, G. Arnetta, G. Candiano, A. Stefano, F. Alongi, G. Borasi, C. Messa, and M. C. Gilardi. Dose distribution changes with shielding disc misalignments and wrong orientations in breast IOERT: a Monte Carlo–GEANT4 and experimental study. *Journal of Applied Clinical Medical Physics*, 13(5), 2012.

M. Sadeghi, M. Enferadi, A. Shirazi, et al. External and internal radiation therapy: past and future directions. *Journal of cancer research and therapeutics*, 6(3):239, 2010.

F. Salvat, J. M. Fernandez-Varea, J. Baro, and J. Sempau. PENELOPE, an algorithm and computer code for Monte Carlo simulation of electron-photon showers. *Informes Tecnicos CIEMAT*, 799, 1996.

F. Salvat, J. M. Fernández-Varea, and J. Sempau. PENELOPE-2006: A code system for Monte Carlo simulation of electron and photon transport. In *Workshop proceedings*, volume 7, 2006.

F. Schneider, H. Fuchs, F. Lorenz, V. Steil, F. Ziglio, U. Kraus-Tiefenbacher, F. Lohr, and F. Wenz. A novel device for intravaginal electronic brachytherapy. *International Journal of Radiation Oncology* Biology* Physics*, 74(4):1298–1305, 2009a.

F. Schneider, M. Polednik, D. Wolff, V. Steil, A. Delana, F. Wenz, and L. Menegotti. Optimization of the Gafchromic^{TM} EBT protocol for IMRT QA. *Zeitschrift für medizinische Physik*, 19(1):29–37, 2009b.

F. Schneider, F. Greineck, S. Clausen, S. Mai, U. Obertacke, T. Reis, and F. Wenz. Development of a novel method for intraoperative radiotherapy during kyphoplasty for spinal metastases (Kypho-IORT). *International Journal of Radiation Oncology* Biology* Physics*, 81(4):1114–1119, 2011.

F. Schneider, S. Clausen, J. Thölking, F. Wenz, and Y. Abo-Madyan. A novel approach for superficial intraoperative radiotherapy (IORT) using a 50 kV X-ray source: a technical and case report. *Journal of Applied Clinical Medical Physics*, 15(1), 2014.

T. Schneider, M. Rouija, and H. J. Selbach. Absolute Dosimetry for Brachytherapy with the INTRABEAM miniature x-ray devices. *Radiotherapy and Oncology*, 96:S573, 2010.

S. M. Seltzer. Electron-photon Monte Carlo calculations: the ETRAN code. *International Journal of Radiation Applications and Instrumentation. Part A. Applied Radiation and Isotopes*, 42(10):917–941, 1991.

J. Sempau, E. Acosta, J. Baro, J. M. Fernández-Varea, and F. Salvat. An algorithm for Monte Carlo simulation of coupled electron-photon transport. *Nuclear Instruments and Methods in Physics Research Section B: Beam Interactions with Materials and Atoms*, 132(3):377–390, 1997.

J. Sempau, S. J. Wilderman, and A. F. Bielajew. DPM, a fast, accurate Monte Carlo code optimized for photon and electron radiotherapy treatment planning dose calculations. *Physics in medicine and biology*, 45(8):2263, 2000.

J. Sempau, J. M. Fernandez-Varea, E. Acosta, and F. Salvat. Experimental benchmarks of the Monte Carlo code PENELOPE. *Nuclear Instruments and Methods in Physics Research Section B: Beam Interactions with Materials and Atoms*, 207(2):107–123, 2003.

J. Sempau, A. Badal, and L. Brualla. A PENELOPE-based system for the automated Monte Carlo simulation of clinacs and voxelized geometries—application to far-from-axis fields. *Medical physics*, 38(11):5887–5895, 2011.

M. N. Shah, J. R. Leonard, G. Inder, F. Gao, M. Geske, D. H. Haydon, M. E. Omodon, J. Evans, D. Morales, R. G. Dacey, et al. Intraoperative magnetic resonance imaging to reduce the rate of early reoperation for lesion resection in pediatric neurosurgery: Clinical article. *Journal of Neurosurgery: Pediatrics*, 9(3):259–264, 2012.

A. S. Shiu, S. Tung, K. R. Hogstrom, J. W. Wong, R. L. Gerber, W. B. Harms, J. A. Purdy, R. K. Ten Haken, D. L. McShan, and B. A. Fraass. Verification data for electron beam dose algorithms. *Medical physics*, 19(3):623–636, 1992.

J. Siebers, P. Keall, A. Nahum, and R. Mohan. Converting absorbed dose to medium to absorbed dose to water for Monte Carlo based photon beam dose calculations. *Physics in medicine and biology*, 45(4):983, 2000.

I. M. Sobol. *A primer for the Monte Carlo method*. CRC press, 1994.

E. Sperk, G. Welzel, A. Keller, U. Kraus-Tiefenbacher, A. Gerhardt, M. Sütterlin, and F. Wenz. Late radiation toxicity after intraoperative radiotherapy (IORT) for breast cancer: results from the randomized phase III trial TARGIT A. *Breast cancer research and treatment*, 135 (1):253–260, 2012.

J. M. Udías, P. Ibáñez, and M. Vidal. Phase Space generator from dose data. *Intellectual property registration. Submitted*, 2017a.

J. M. Udías, P. Ibáñez, and M. Vidal. Hybrid Monte Carlo. *Intellectual property registration. Submitted*, 2017b.

J. Vaidya, M. Baum, J. S. Tobias, D. P. D'Souza, S. Naidu, S. Morgan, K. Harte, A. Sliski, and E. Thomson. Targeted intra-operative radiotherapy (Targit): an innovative method of treatment for early breast cancer. *Annals of Oncology*, 12(8):1075–1080, 2001.

J. S. Vaidya, D. J. Joseph, J. S. Tobias, M. Bulsara, F. Wenz, C. Saunders, M. Alvarado, H. L. Flyger, S. Massarut, W. Eiermann, et al. Targeted intraoperative radiotherapy versus whole breast radiotherapy for breast cancer (TARGIT-A trial): an international, prospective, randomised, non-inferiority phase 3 trial. *The Lancet*, 376(9735):91–102, 2010.

J. S. Vaidya, F. Wenz, M. Bulsara, J. S. Tobias, D. J. Joseph, M. Keshtgar, H. L. Flyger, S. Massarut, M. Alvarado, C. Saunders, et al. Risk-adapted targeted intraoperative radiotherapy versus whole-breast radiotherapy for breast cancer: 5-year results for local control and overall survival from the TARGIT-A randomised trial. *The Lancet*, 383(9917):603–613, 2014.

M. F. Valdivieso-Casique, R. Rodríguez, S. Rodríguez-Bescós, D. Lardíes, P. Guerra, M. J. Ledesma, A. Santos, P. Ibáñez, M. Vidal, J. M. Udías, et al. RADIANCE—A planning software for intra-operative radiation therapy. *Translational Cancer Research*, 4(2):196–209, 2015.

J. Van Dyk, R. Barnett, J. Cygler, and P. Shragge. Commissioning and quality assurance of treatment planning computers. *International Journal of Radiation Oncology* Biology* Physics*, 26(2):261–273, 1993.

F. Verhaegen, A. Nahum, S. Van De Putte, and Y. Namito. Monte Carlo modelling of radiotherapy kV x-ray units. *Physics in medicine and biology*, 44(7):1767, 1999.

U. Veronesi, R. Orecchia, P. Maisonneuve, G. Viale, N. Rotmensz, C. Sangalli, A. Luini, P. Veronesi, V. Galimberti, S. Zurrida, et al. Intraoperative radiotherapy versus external radiotherapy for early breast cancer (ELIOT): a randomised controlled equivalence trial. *The lancet oncology*, 14(13):1269–1277, 2013.

M. Vidal, P. Ibáñez, J. Cal González, P. Guerra Gutiérrez, and J. M. Udías. Hybrid Monte Carlo dose algorithm for low energy X-rays intraoperative radiation therapy. *Radiotherapy and Oncology*, 111(S1):117–118, 2014a.

M. Vidal, P. Ibáñez, P. Guerra, E. Herranz, and J. M. Udías. Realistic on-the-fly dose calculation for low energy X-rays Intra-Operative Radiation Therapy. *Radiotherapy and Oncology*, 110: S103–S104, 2014b.

M. Vidal, P. Ibáñez, L. Parent, M. Goubert, R. Ferrand, P. Guerra, and J. M. Udias. Optimized Monte-Carlo intra-operative radiotherapy dose prediction for flat and surface applicators. *Radiotherapy and Oncology*, (115):S277–S278, 2015.

X. Wang, S. Spirou, T. LoSasso, J. Stein, C.-S. Chui, and R. Mohan. Dosimetric verification of intensity-modulated fields. *Medical physics*, 23(3):317–327, 1996.

F. Wenz, F. Schneider, C. Neumaier, U. Kraus-Tiefenbacher, T. Reis, R. Schmidt, and U. Obertacke. Kypho-IORT-a novel approach of intraoperative radiotherapy during kyphoplasty for vertebral metastases. *Radiation Oncology*, 5(1):1, 2010.

World Health Organization. Fact sheet N^{o} 297. Technical report, 2015.

World Health Organization. World Cancer Report 2014. Technical report, ISBN: 978-92-832-0443-5, 2014.

Z. Xiao, O. Bin, Z. Wang, B. Huang, and B. Wen. The Dosimetric Characteristics and Potential Limitation in Clinical Application of a Low Energy Photon Intra-Operative Radiotherapy System. *International Journal of Medical Physics, Clinical Engineering and Radiation Oncology*, 4(02):184, 2015.

J. Yanch and K. Harte. Monte Carlo simulation of a miniature, radiosurgery x-ray tube using the ITS 3.0 coupled electron-photon transport code. *Medical physics*, 23(9):1551–1558, 1996.

C. Zeiss. Intrabeam technical specification, Brochure, no. EN-30-010-0158IIs. Technical report, C. Zeiss, 2012.

C. Zeiss. INTRABEAM-Dosimetry. Technical report, Carl Zeiss Meditec AG, 2011.